Understanding galaxy formation and evolution with realistic simulations

Thesis by
Xiangcheng Ma

In Partial Fulfillment of the Requirements for the
Degree of
Doctor of Philosophy

Caltech

CALIFORNIA INSTITUTE OF TECHNOLOGY
Pasadena, California

2018
Defended April 27, 2018

© 2018

Xiangcheng Ma
ORCID: 0000-0001-8091-2349

ACKNOWLEDGEMENTS

At first, I would like to thank my advisor, Phil Hopkins, whom I started to work with on the day after I arrived in the United States, for all his advices and support. Phil has not only taught me technical details about running simulations and writing papers, but also the way to think from the big picture and come up with good research projects. I always admire his broad knowledge on almost every subfield in galaxy formation and evolution and his passion in doing science, which I have benefited a lot from and becomes a standard I will try to reach in the future. I also appreciate all the financial support that Phil has generously provided, for my stipend, buying a laptop, attending conferences, going to job tours, etc.

I am also grateful to be involved in the Feedback in Realistic Environments (FIRE) collaboration. In the past five years, I have been lucky to know and work closely with many greatest scientists, including Daniel Anglés-Alcázar, Michael Boylan-Kolchin, Claude-André Faucher-Giguère, Robert Feldmann, Shea Garrison-Kimmel, Chris Hayward, Dan Kasen, Dušan Kereš, Sasha Muratov, Norman Murray, Eliot Quataert, Paul Torrey, Andrew Wetzel, and many more, from whom I have learned a lot about science. I thank all my collaborators for their constructive comments on my papers, particularly Claude-André Faucher-Giguère and Michael Boylan-Kolchin for their help on subtle text editing and correcting my English.

As the very first graduate student in the Hopkins' group, I have seen the group grow from 3-ish people to ~ 20. I was still enjoying the time when we had small group meetings where there were a lot of in-depth discussions. I enjoyed talking to the postdocs in the group, including Andrew Wetzel, Ji-hoon Kim, Chris Hayward, and Paul Torrey, and I also thank many current group members, Shea Garrison-Kimmel, Anne Medling, Astrid Lamberts, and Cameron Hummels for sacrificing their time on my postdoc applications during the last job season.

Moreover, I thank Evan Kirby, Chuck Steidel, and Eliot Quataert for sitting on my thesis committee. I also thank the Caltech astronomy department for offering great classes (especially Sterl Phinney's Ay 125 and Ay 126 in my first year), for gathering the greatest people in every research field, and for bringing in great visitors almost every day. It has always been helpful talking to the extragalactic observers around, such as Richard Ellis, Chuck Steidel, Evan Kirby, and Nick Scoville. I also thank the administrative staff at Caltech, especially JoAnn Boyd and the international office,

for their effective and efficient work, which is impossible in big universities other than Caltech. Admittedly, being a Chinese (male) graduate student at Caltech or in the United States can be very tough sometimes, when I feel isolated, unfairly treated, or even discriminated against by other graduate students, but these episodes make my life in graduate school more colorful.

Finally, I am grateful for my family, especially my parents who are in their mid-60s, for their understanding and support.

ABSTRACT

Understanding the formation and evolution of galaxies from the Big Bang to the present day is one of the most important questions in modern astronomy. The tremendous amount of observational data accumulated in the past decade that probe various properties of galaxies across cosmic time demand a more detailed theoretical understanding of galaxy formation and evolution.

In this thesis, I will investigate several open question in this field using state-of-the-art cosmological hydrodynamic zoom-in simulations of galaxy formation from the Feedback in Realistic Environments (FIRE) suite. These high-resolution simulations (10–$10^4\,M_\odot$, 0.1–$10\,\mathrm{pc}$) include realistic models of the multi-phase ISM, star formation, and stellar feedback and explicitly capture gas cooling down to $10\,\mathrm{K}$, star formation in dense clumps in giant molecular clouds, and feedback coupling on the smallest resolved scales. These simulations are powerful tools for studying the key physics governing galaxy formation and evolution and understanding the detailed observations of galaxy properties.

The first half of this thesis presents three studies on galactic chemical evolution. Chapter 2 focuses on the origin and evolution of the galaxy mass-metallicity relation (MZR), one of the fundamental properties of galaxies. I will show that the FIRE simulations broadly agree with the observed galaxy MZR from $z = 0$–3. The slope of the MZR is mainly driven by the metal retention fraction in low-mass galaxies, while the amount of redshift evolution of the MZR is mostly determined by the star formation histories of galaxies. Chapter 3 attempts to understanding the diversity of gas-phase metallicity gradients found in intermediate-redshift ($z \sim 0.6$–3) galaxies. I will show that the metallicity gradient in a galaxy varies on small timescales driven by bursty star formation and feedback cycle at early times, naturally resulting in the observed diversity of metallicity gradients in $z \sim 2$ galaxies. The metallicity gradient only reflects the instantaneous dynamics of a galaxy. Chapter 4 will study the structure, stellar age and metallicity gradients, and formation history of Milky Way (MW)-like disk galaxies. At high redshift, star formation happens in a chaotic, bursty mode, which eventually forms a nearly spherical structure by $z = 0$. Since $z \lesssim 1$, a stable gas disk emerged and stars formed in that disk thereafter. The thickness of the gas disk decreases with time due to lowering gas fraction. Stars formed earlier in this disk are kinematically heated to a thicker, flaring disk. Such a formation history leads to the age and stellar metallicity gradients consistent with

what observed in the MW disk.

The second half of this thesis focuses on galaxy formation in the first billion years of the Universe, known as the reionization era. Chapters 5 and 6 study the escape fraction of ionizing photons from galaxies at $z \geq 5$, which is an important, yet poorly constrained parameter for understanding the reionization history. Most ionizing photons are emitted by the youngest stellar populations in the galaxy, which are usually embedded in their 'birth clouds'. Stellar feedback is required to clear these clouds in a few Myr before ionizing photons are allowed escape. In the meanwhile, the ionizing photon budget decreases rapidly as the most massive stars start to die. The competition of timescales between feedback and stellar evolution is thus the most important physics determines f_{esc}. I will show that canonical single-star stellar population models such as STARBURST99 generally yield a f_{esc} far below what is required for cosmic reionization. Binary models, in contrast, produce more ionizing photons at late times than single-star models and thus lead to a much higher f_{esc}. Chapter 7 presents a new suite of high-resolution cosmological zoom-in simulations of $z \geq 5$ galaxies that contains thousands of halos at any time in all zoom-in regions. I will present the stellar mass–halo mass relation, SFR–M_{halo} relation, stellar mass–magnitude relation, stellar mass functions, and multi-band luminosity functions at $z = 5$–12. These prediction agree well with current observational constraints and can be further tested by future observations with the *James Webb Space Telescope*. Using these new simulations, Chapter 8 studies the morphology and size evolution of galaxies at $z \geq 5$. I will show that the rest-frame UV light from $z \geq 5$ galaxies is usually dominated by one or several star-forming clumps that are intrinsically bright and small. Current observations with moderate surface brightness limits tend to only pick up the intrinsically small galaxies or individual clumps but miss the diffuse light in the galaxies. Such a selection effect is likely to result in the extremely small sizes claimed for the faint galaxies in the Hubble Frontier Fields.

PUBLISHED CONTENT AND CONTRIBUTIONS

Ma, X., Hopkins, P. F., Faucher-Giguère, C.-A., et al., 2016, "The origin and evolution of the galaxy mass-metallicity relation", *Monthly Notices of the Royal Astronomical Society*, 456, 2140-2156
DOI: 10.1093/mnras/stv2659
X. Ma involved in developing the idea, did all the analysis, and wrote the manuscript.

Ma, X., Hopkins, P. F., Wetzel, A. R., et al., 2017, "The structure and dynamical evolution of the stellar disc of a simulated Milky Way-mass galaxy", *Monthly Notices of the Royal Astronomical Society*, 467, 2430-2444
DOI: 10.1093/mnras/stx273
X. Ma involved in developing the idea, did all the analysis, and wrote the manuscript.

Ma, X., Hopkins, P. F., Feldmann, R., et al., 2017, "Why do high-redshift galaxies show diverse gas-phase metallicity gradients? ", *Monthly Notices of the Royal Astronomical Society*, 466, 4780-4794
DOI: 10.1093/mnras/stx034
X. Ma developed the idea, did all the analysis, and wrote the manuscript.

Ma, X., Kasen, D., Hopkins, P. F., et al., 2015, "The difficulty of getting high escape fractions of ionizing photons from high-redshift galaxies: a view from the FIRE cosmological simulations", *Monthly Notices of the Royal Astronomical Society*, 453, 960-975
DOI: 10.1093/mnras/stv1679
X. Ma involved in developing the idea, did all the analysis, and wrote the manuscript.

Ma, X., Hopkins, P. F., Kasen, D., et al., 2016, "Binary stars can provide the 'missing photons' needed for reionization", *Monthly Notices of the Royal Astronomical Society*, 459, 3614-3619
DOI: 10.1093/mnras/stw941
X. Ma involved in developing the idea, did all the analysis, and wrote the manuscript.

Ma, X., Hopkins, P. F., Garrison-Kimmel, S., et al., 2018, "Simulating galaxies in the reionization era with FIRE-2: galaxy scaling relations, stellar mass functions, and luminosity functions", *Monthly Notices of the Royal Astronomical Society*, in press
DOI: 10.1093/mnras/sty1024
X. Ma developed the entire project, built and ran the simulations, did all the analysis, and wrote the manuscript.

Ma, X., Hopkins, P. F., Boylan-Kolchin, M., et al., 2018, "Simulating galaxies in the reionization era with FIRE-2: galaxy scaling relations, stellar mass functions, and luminosity functions", *Monthly Notices of the Royal Astronomical Society*, 477, 219-229
DOI: 10.1093/mnras/sty684
X. Ma developed the idea based on his own simulations, did all the analysis, and wrote the manuscript.

TABLE OF CONTENTS

LIST OF ILLUSTRATIONS

LIST OF TABLES

Chapter 1

INTRODUCTION

Galaxies are the building blocks of the Universe. Understanding how galaxies form and evolve from the Big Bang to the present day is one of the most important but challenging problems in modern astronomy. In the past decade, a series of observing campaigns have brought us a large amount of high-quality data that has significantly
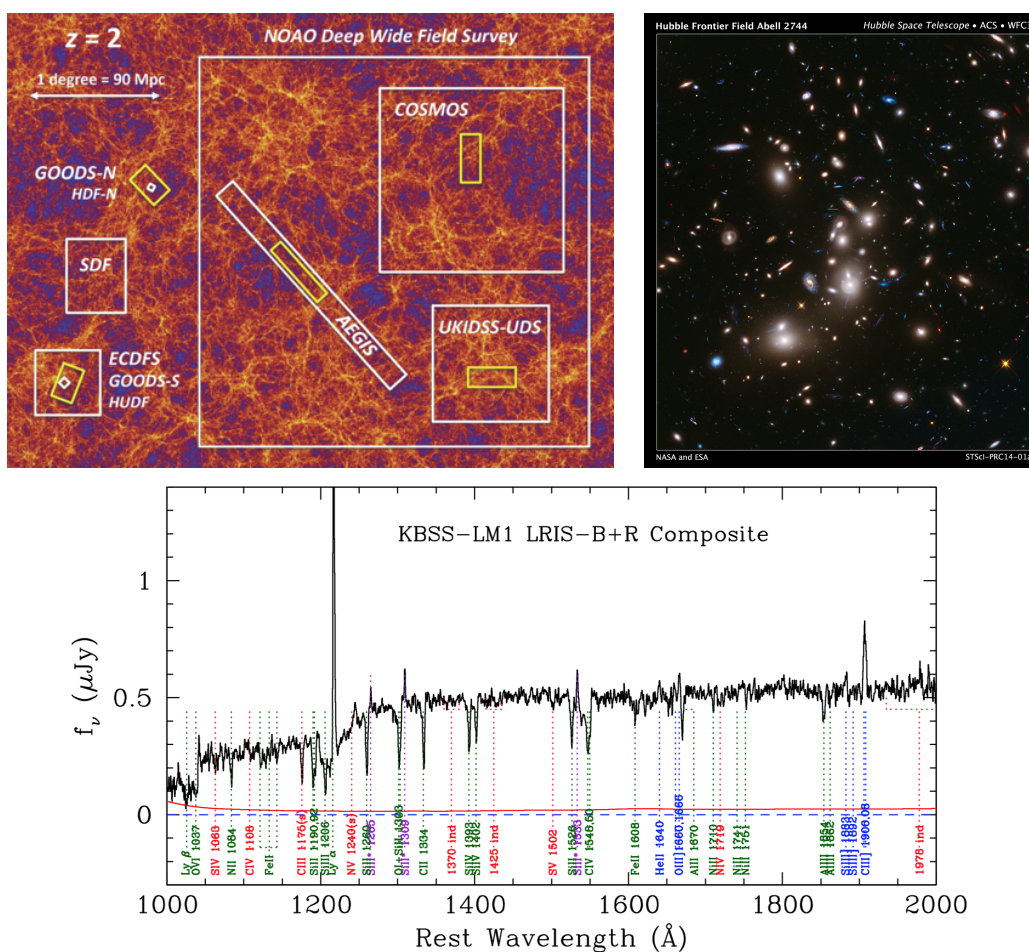
Figure 1.1: Examples of recent observing programs that have produced numerous data of galaxies across cosmic time. *Top left*: Some important surveys of distant galaxies marked by their relative sizes of the regions on the sky, taken from Madau & Dickinson (2014). The yellow boxes represent the CANDELS fields. *Top right*: Abell 2744, one of the HFF galaxy clusters. *Bottom*: Stacked composite rest-frame UV spectrum of 30 galaxies around $\langle z \rangle = 2.4$ from the KBSS sample, taken from Steidel et al. (2016).

improved our understanding of galaxies in a number of ways.

Figure 1.1 shows several examples of recent observing programs. The top left panel illustrates some important surveys of distant galaxies represented by their relative sizes of the regions on the sky (taken from Madau & Dickinson 2014), including the Cosmic Assembly Near-IR Deep Extragalactic Legacy Survey (CANDELS; Grogin et al. 2011, the yellow boxes), which provides multi-band deep images for 250,000 galaxies from $z = 1.5$–8 with *Hubble Space Telescope* (HST). Also shown in this panel is the *Hubble* Ultra Deep Field (HUDF), which yields multi-band data for more than ten thousand galaxies up to $z \sim 10$ over a period of ten years of observations (Illingworth et al. 2013). The top right panel shows Abell 2744, one of the galaxy clusters from the *Hubble* Frontier Fields (HFF; Coe et al. 2015; Lotz et al. 2017). The large magnification due to strong gravitational lensing enables the discovery of thousands of faint galaxies down to $M_{UV} \sim -12$, including tens of galaxies at $z \geq 6$. The bottom panel shows the stacked composite rest-frame ultraviolet (UV) spectrum of 30 galaxies around $\langle z \rangle = 2.4$ from the Keck Baryonic Structure Survey (KBSS; taken from Steidel et al. 2016). These high signal-to-noise-ratio rest-frame UV-to-optical spectra cover a series of nebular emission lines that provide strong constraints on the ionizing spectrum, stellar population, gas-phase and stellar metallicity, and abundance ratios of $z \sim 2$ galaxies (Steidel et al. 2014, 2016; Strom et al. 2017).

1.1 Basic physics in galaxy formation

These detailed observations demand comparably detailed theoretical modeling of galaxy formation and evolution, which is conceivably a very challenging task because it involves a broad range of physical processes on scales across many orders of magnitude (Figure 1.2). Over the past decade, the basic framework of galaxy formation has been established. The key physical ingredients have been well documented in a number of textbooks and review papers (e.g., Longair 2008; Benson 2010; Mo et al. 2010; Silk & Mamon 2012; Somerville & Davé 2015; Naab & Ostriker 2017, and references therein), which I only briefly summarize here.

Gravity and cosmic structure formation. The very early ($z \gtrsim 100$) Universe is fairly homogeneous with small density fluctuations seeded during the inflation. The density contrast grows linearly at first, until gravity overcomes cosmic expansion in the most overdense regions, where dark matter (DM) collapses into self-gravitating halos. Galaxies will form in the central regions of these halos. The mass distribution and spatial correlation of DM halos, described by the halo mass functions
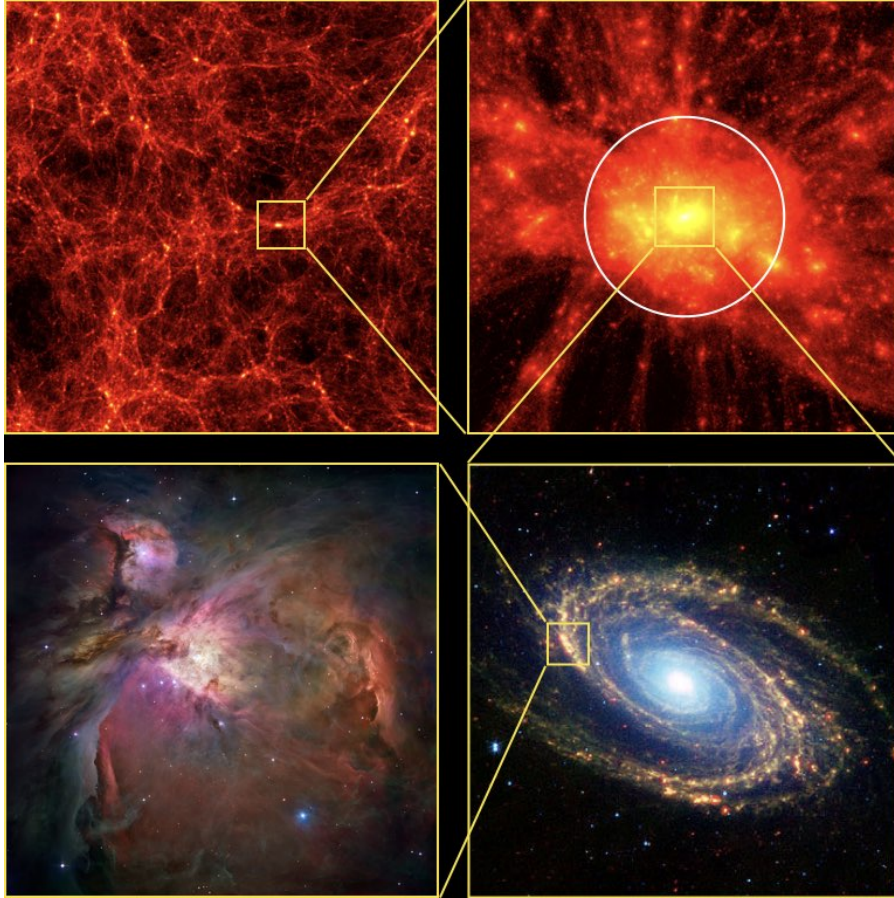
Figure 1.2: Multi-scale physics in galaxy formation. *Top left*: A $20 \times 20\,\mathrm{Mpc}^2$ slice of the cosmic web, showing the large-scale structure of the Universe. *Top right*: A dark matter halo. The white circle shows the halo virial radius ($200\,\mathrm{kpc}$). *Bottom right*: Messier 81. Galaxies form in the central region ($\sim 0.1 R_{\mathrm{vir}}$) of the halo, where the gas can cool efficiently and from stars. *Bottom left*: The Orion nebular, which is an actively star-forming region. Photoionization and radiation pressure feedback acting on small scales is driving turbulence and disrupting the star-forming cloud.

(HMFs) and the correlation functions, respectively, are fully determined by the power spectrum of the primordial density fluctuations. Halo mergers will induce environmental effects (e.g., gas stripping via ram pressure) and galaxy mergers that are important physical processes on galaxy evolution. The cosmic structure formation is well understood with analytic models (e.g., Press & Schechter 1974) and N-body simulations (e.g., Springel et al. 2005a).

Heating and cooling. Gas accretes onto the halo as DM collapses, being heated to the halo virial temperature by accretion shock. The gas needs to cool before it can fall into the central region of the halo and form stars. The most important cooling

mechanisms include bremsstrahlung (free-free, $> 10^6$ K), metal-line cooling (10^5–10^6 K), atomic cooling (H and He, 10^4–10^5 K), fine-structure lines ([C $\textsc{ii}$] and [O $\textsc{i}$]), molecular, and dust cooling ($< 10^4$ K). There are also a number of heating terms, including Compton heating, photoionization and photoelectric heating (from black hole accretion, stellar sources, and the metagalactic ionizing background), cosmic ray heating, and shocks (e.g., supernova ejecta, outflows, accretion shocks). These processes result in the multi-phase nature of the interstellar medium (ISM) and the circumgalactic medium (CGM), where hot ionized gas, warm neutral gas, and cold molecular gas coexist in equipartition.

Star formation and stellar feedback. Gravitational instabilities are responsible for the formation of self-gravitating giant molecular clouds (GMCs) in the ISM. These GMCs are supersonically turbulent, where the parent cloud keeps fragmenting into smaller clouds until forming protostellar cores that will collapse into protostars on scales of 10^{-5} pc, which is far below the scale of DM halos ($\sim 10^5$ pc). The mass distribution of newly formed stars follows some initial mass functions (IMFs; e.g., Salpeter 1955; Kroupa 2002; Chabrier 2003).

Once stars form, they act back to the gas via a number of feedback mechanisms. (1) *Photoionization*. The large number of ionizing photons (above 13.6 eV) produced by O and B stars create ionized H $\textsc{ii}$ regions around them and heat the gas to a temperature about 10^4 K. (2) *Radiation pressure*. The starlight can be absorbed by dust grains in the ISM, depositing momentum to the gas and probably generating outflows (e.g., Thompson et al. 2005). (3) *Supernovae (SNe)*. Each SN ejects a mass of 1–20 $M_\odot$ carrying 10^{51} ergs kinetic energy, corresponding to an initial velocity from 2000–10^4 km s^{-1}. The ejecta run into the ISM, shock-heated to $\gg 10^6$ K. The SN remnant is cooling-inefficient at first, when the hot bubble expands adiabatically and boosts the ejecta momentum by a factor of a few (i.e., the Sedov-Taylor phase). These SN remnants expand and overlap, generating outflows on galactic scale. (4) *Stellar winds*, including both 'fast' winds from O and B stars and 'slow' winds from AGB stars. These winds add mechanical feedback to the ISM in a similar way to SN ejecta. In addition, SNe and stellar winds also inject heavy elements into the ISM, with α-elements mostly produced by Type-II SNe, Fe by Type-Ia SNe, and stellar winds producing a lot C, N, and O (e.g., Woosley & Weaver 1995; Iwamoto et al. 1999; Izzard et al. 2004; Nomoto et al. 2006).

Due to the large dynamic range, it is not possible to explicitly treat the small-scale physics, such as the formation of individual stars or the early evolution of SN ejecta,

in galaxy formation models, but one has to rely on 'sub-grid' recipes. For example, stars are treated as a collection of stellar populations and all the feedback strengths are calculated based on 'IMF-averaged' quantities.

Black hole formation, growth, and feedback. Almost every galaxy hosts a super-massive black hole (SMBH, mass $\gg 10^6\,\mathrm{M_\odot}$) in the center. In local galaxies, the BH mass correlates tightly with the central velocity dispersion and the bulge mass (e.g., McConnell & Ma 2013), suggesting either coevolution or feedback regulation between SMBHs and their host galaxies (e.g., Fabian 2012). However, the formation, growth, and feedback of SMBHs are probably the least understood physical processes in galaxy formation and evolution.

It is believed that BH seeds are formed either via SN explosion of Population III (Pop III) stars (light seeds, $\sim 100\,\mathrm{M_\odot}$) or via direct collapse of a gas cloud (massive seeds, $> 10^4\,\mathrm{M_\odot}$). Some of these seed BHs must sink into the galactic center via dynamical friction and grow by several orders of magnitude in mass via accretion and mergers. The tremendous energy released by BH accretion has a great impact on the host galaxy. The commonly discussed BH feedback mechanisms include accretion disk winds (line-driven winds launched from the accretion disk with initial velocity $\sim 30,000\,\mathrm{km\,s^{-1}}$), radiation pressure, and heating from the relativistic jets. The first two are known as 'quasar-mode' feedback at high accretion rates that drives strong outflows and regulates star formation. The jet heating is also known as 'radio-mode' feedback at low accretion rates, which is mainly invoked to maintain quenching in massive galaxies. All of these processes are poorly understood and have to be treated by empirical prescriptions in galaxy formation models.

Other physics. *Magnetic fields.* The magnetic fields in the Universe are seeded in the early Universe and amplified via cosmic structure formation and by magnetic dynamos in the supersonic ISM and CGM. In dense, star-forming clouds, the magnetic fields are probably dynamically important. *Cosmic rays (CRs).* CRs refer to the relativistic particles, mainly electrons and protons, which are produced in SN explosions, shocks and relativistic jets. CRs provide a major heating mechanism and determine the electron abundances in dense molecular clouds. The anisotropic conduction, viscosity, and CR transport through magnetic fields may hugely impact the phase structure of the ISM, CGM, and the galactic winds. *Dust.* Dust forms in SN ejecta and in AGB winds. Dust grains can grow in cold, dense clouds and be destroyed in shock fronts and in hot gas. Dust is important in galaxy formation in terms of cooling, molecule formation, radiation pressure, etc. Observationally, dust
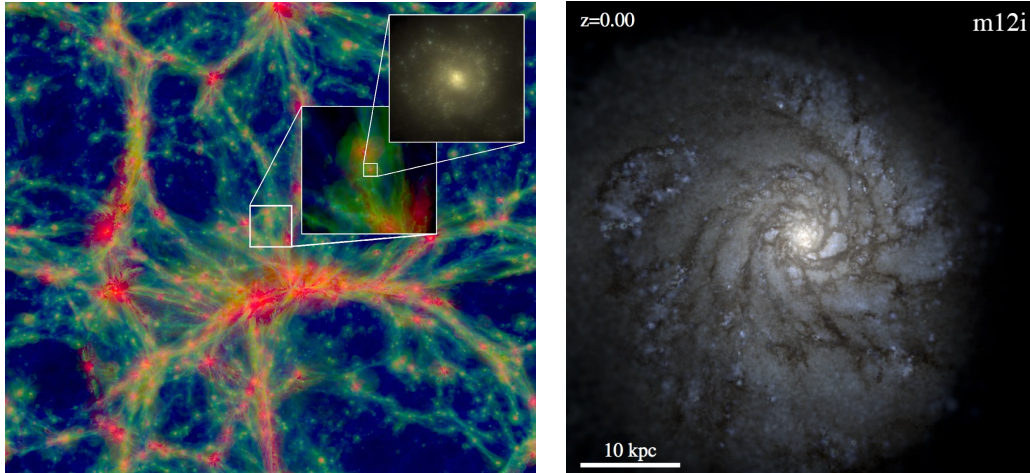
Figure 1.3: Cosmological hydrodynamic simulations of galaxy formation. *Left*: A slice of size $100 \times 100 \times 20 \, \mathrm{cMpc}^3$ from the large-volume cosmological simulation, EAGLE, taken from Schaye et al. (2015). *Right*: Composite $u/g/r$ image of a high-resolution cosmological zoom-in simulation of a MW-like galaxy from the FIRE suite, taken from Hopkins et al. (2017).

obscuration and re-emission are also important for understanding galaxy colors and measuring the star formation rates (SFRs) in dusty galaxies.

1.2 Common tools for modeling galaxy formation

There are two most commonly used tools for modeling galaxy formation and evolution in a cosmological context.

Cosmological hydrodynamic simulations. These types of models explicitly solve the equations of motion, gravity, (magneto)hydrodynamics, and thermodynamics for particles and/or cells representing dark matter, gas, stars, and BHs. All the key physical processes, such as heating and cooling, star formation, BH formation and accretion, and stellar and BH feedback, are numerically implemented as 'sub-grid' prescriptions at the resolution level. Cosmological simulations broadly fall into the following two categories (Figure 1.3).

Large-volume cosmological simulations. These types of simulations follow the structure formation and galaxy evolution in a periodic cosmological box with typical sizes from 50 to a few 100 Mpc along each dimension. These simulations produce large samples of galaxies in their simulation volume that are powerful for studying statistical properties of galaxy populations. As a trade-off due to limited computational resources, these simulations generally have mass resolution $\gg 10^5 \, \mathrm{M}_\odot$ and spatial resolution ~ 1 kpc, so they are not able to resolve smaller-scale physics such

as the formation of GMCs (on scales $\sim 100\,\mathrm{pc}$) and the propagation of individual SN blastwave. As a consequence, these simulations usually adopt empirical models for cold cloud and star formation, SNe energy deposition, velocity and mass rate of galactic outflows, etc. (e.g., Springel & Hernquist 2003; Vogelsberger et al. 2013). Such models usually contain several free parameters that need to be tuned manually to match the observed $z = 0$ galaxy stellar mass function (SMF). State-of-the-art large-volume cosmological simulations include Illustris (Vogelsberger et al. 2014), IllustrisTNG (Pillepich et al. 2018), EAGLE (Schaye et al. 2015), and MUFASA (Davé et al. 2016).

Cosmological zoom-in simulations. These types of simulations take advantage of the well-studied cosmological zoom-in technique (e.g., Bertschinger 2001; Hahn & Abel 2011, and reference therein): it keeps the large-scale tidal forces in a low-resolution cosmological box, but uses much higher resolution in the central zoom-in region (usually selected to form a halo of interest). These zoom-in simulations have much better resolution than large-volume simulations: for example, state-of-the-art zoom-in simulations of Local Group analogs from the ELVIS suite (Garrison-Kimmel et al. 2014) adopt a mass resolution $\sim 3,500\,\mathrm{M}_\odot$ and spatial resolution better than 1 pc. Such resolution allows the simulations to capture the formation of GMCs in the ISM, star formation in cloud clumps, at least late-stage evolution of SN blastwaves, and how galactic winds are launched and propagated from small to large scales. Due to the detailed physics included, these zoom-in simulations are too expensive to run a large sample and thus limited in statistical power. Recent simulations in this category include the MaGICC suite (Brook et al. 2012a), the VELA suite (Ceverino et al. 2014), the NIHAO suite (Wang et al. 2015), and the Feedback in Realistic Environments suite (FIRE; Hopkins et al. 2014, 2017).

Semi-analytic models (SAMs). These types of models do not solve fundamental equations for structure formation and hydrodynamics, but are built upon DM halo merger trees. In SAMs, every galaxy is described by a series of global properties, including stellar mass, hot and cold gas mass, BH mass, SFR, gas-phase and stellar metallicity, disk-to-bulge ratio, size, etc. These models usually adopt parametrized recipes to model how fast gas accretes onto the DM halo, cooling and star formation rates, heating and outflow rates driven by feedback, so on and so forth. SAMs are much computationally cheaper than hydrodynamic simulations, so they can be used to compare different families of models (e.g., Lu et al. 2014b; Knebe et al. 2018) and to explore the relative importance of different physical processes. Similar to

large- volume cosmological simulations, SAMs are also useful for understanding galaxy statistical properties, but one also needs to tune the free parameters in these models to match $z = 0$ observations.

Another commonly used tool for understanding galaxy formation and evolution is the so-called idealized simulations, which are generally conducted for exploring the effects of certain physical processes. For example, recent studies that belong to this category include understanding SN feedback in supersonically turbulent box (e.g., Martizzi et al. 2015), the effects of magnetic fields using isolated disk simulations (e.g., Su et al. 2017b), SMBH growth and feedback in nuclear disk simulations (e.g., Hopkins & Quataert 2010; Hopkins et al. 2016), phase structure of the CGM in hot halo simulations (e.g., Fielding et al. 2017), and many more. Conceivably, it is easy and straightforward to control parameters in these simulations, so that they are able to isolate the effect of individual mechanisms.

1.3 Open questions to be addressed in this thesis

The ultimate goal of galaxy formation theory is to understand the observed galaxy properties and to predict new observations that can tell apart different models. In this thesis, I will primarily focus on two broad topics in galaxy formation and evolution: (1) galactic chemical evolution and (2) the properties of galaxies in the first billion years of the Universe and their contribution to cosmic reionization. The goal of this thesis is to understand several open questions in these fields using the state-of-the-art FIRE cosmological zoom-in simulations suite (Hopkins et al. 2014, 2017).

In this section, I will briefly review the motivation and recent progress for questions that will be addressed in the rest of this thesis. In Chapters 2–8, I will present each problem, with a more detailed introduction, description of the simulation sample and numerical models included, main results, important discussions, and conclusions, in each chapter. In Chapter 9, I will conclude and discuss possible extensions of the studies in this thesis for future work.

1.3.1 Galactic chemical evolution

The abundances and distributions of heavy elements in the galaxies are among the most fundamental galaxy properties. These metals are produced by SNe and AGB winds due to stellar evolution and can be redistributed among different phases and at different locations by locking metals into stars, feedback-driven outflows, and gas recycling. Therefore, metals are powerful tracers of galaxy formation histories and feedback processes. In this thesis, I will study three problems on galactic chemical

evolution: the origin and evolution of the galaxy mass–metallicity relation (Chapter 2), the origin and diversity of radial gas-phase metallicity gradients in intermediate-redshift galaxies ($z \sim 2$; Chapter 3), and the structure, stellar metallicity gradients, and formation history of Milky Way (MW)-like disk galaxies (Chapter 4).

The average galaxy gas-phase and stellar metallicity correlate tightly with galaxy stellar mass, with more massive galaxies more metal enriched. This correlation is known as the galaxy mass–metallicity relation (MZR). The gas-phase MZR has been measured in a wide range of redshift (e.g., $z \sim 0$, Tremonti et al. 2004; $z \sim 0.8$, Zahid et al. 2011; $z \sim 1.4$, Yabe et al. 2014; $z \sim 2.3$, Sanders et al. 2015; $z \sim 3.1$, Mannucci et al. 2009). There is a continuous evolution of the gas-phase MZR with redshift (e.g., Zahid et al. 2013), with high-redshift galaxies being less enriched than low-redshift galaxies at fixed stellar mass. Very recently, Shapley et al. (2017) have pushed the measurement of gas-phase metallicity in a $z \sim 4$ galaxy. Spectroscopic survey with the *James Webb Space Telescope* (JWST) in the near future will enable the constraints on the gas-phase MZR up to $z \sim 10$. Past measurements on the stellar MZR are mostly for nearby galaxies (e.g. Gallazzi et al. 2005; Kirby et al. 2013), while Leethochawalit et al. (2018) have measured the stellar abundances for a sample of quiescent galaxies in a $z \sim 0.4$ galaxy cluster and reported an evolution of the stellar MZR up to $z \sim 2$ based on the derived galaxy quenching time. Pushing the measurements of stellar metallicity to higher redshifts will be an important, but challenging direction for future observations.

As shown by simple analytic galactic chemical evolution models, the metallicity of a galaxy is largely determined by its star formation efficiency (the fraction of gas that turns into stars) and feedback strength (characterized by the so-called mass loading factor, which is defined as the ratio of outflow rate to SFR). A lower star formation efficiency and a stronger feedback strength generally lead to a lower metallicity. The mass loading factor tends to increase dramatically in low-mass galaxies, which sets the slope of the MZR (e.g., Kirby et al. 2011). The redshift evolution of the MZR, on the other hand, largely reflects the star formation histories of galaxies. Therefore, the shape and the amount of evolution of the galaxy MZR is an important property for constraining galaxy formation and feedback models. Cosmological simulations and SAMs with different feedback recipes generally produce very different galaxy MZR (e.g., figure 6 in Somerville & Davé 2015). In Chapter 2, I will present the MZR from $z = 0$–6 for a sample of galaxies from the FIRE simulations, compare the results with observations and other theoretical predictions, and understand the

key physical mechanisms driving the shape and evolution of the MZR.

Metals are not uniformly distributed in the galaxy. In local galaxies, it has been known for a long time that gas in the central regions is more metal-enriched than in the outskirts, which is usually referred as negative metallicity gradients (e.g., Searle 1971; Zaritsky et al. 1994; van Zee et al. 1998; Sánchez et al. 2014; Ho et al. 2015; Belfiore et al. 2017). This can be simply explained by radially dependent star formation efficiency in galactic disks: consider a gas disk with a power-law surface density profile $\Sigma_g \sim R^{-\beta}$, the star formation rate surface density follows the Kennicutt–Schmidt law as $\dot{\Sigma}_* \sim \Sigma_g^{1.4} \sim R^{-1.4\beta}$ (Kennicutt 1998). Following the 'closed-box' model, it is expected that $Z_g \sim -\ln(1 - \Sigma_*/\Sigma) \sim \Sigma_*/\Sigma \sim \dot{\Sigma}_* t/\Sigma \sim R^{-0.4\beta}$ assuming a moderate gas fraction and no efficient metal mixing between annuli. However, at intermediate redshifts ($z \sim 0.6$–3), only a small number of galaxies clearly show strong negative metallicity gradients (e.g., Jones et al. 2010; Yuan et al. 2011), while the majority of galaxies only show weak or flat gradients (e.g., Swinbank et al. 2012; Leethochawalit et al. 2016; Wuyts et al. 2016; Wang et al. 2017). Such a diversity of gas-phase metallicity gradients in intermediate-redshift galaxies is potentially a powerful probe of feedback, as gas can be strongly perturbed by feedback processes. For example, Gibson et al. (2013) have shown that when using a weak feedback model, simulations always produce strong negative metallicity gradients at $z \sim 2$, while the same simulations will instead produce flat gradients when using a strong feedback model. The 'true' feedback strength is likely between the two extreme scenarios. In Chapter 3, I will present the radial gas-phase metallicity gradients for a sample of ~ 30 galaxies at $z \sim 0$–2 from the FIRE suite. I will show that the FIRE simulations reproduce the observed broad distribution of metallicity gradients. The diversity reflects the time variabilities of these gradients due to bursty star formation and feedback cycles in these galaxies.

Metallicity gradients are also widely found in the stellar component of local galaxies (e.g., Sánchez-Blázquez et al. 2014). Particularly, there are rapidly accumulating data from spectroscopic survey of MW stars during the past few years and in the near future, such as APOGEE (Allende Prieto et al. 2008) and Gaia-ESO (Gilmore et al. 2012), from which our knowledge of the MW structure, stellar abundances, and kinematics is dramatically growing on a star-by-star base. The MW stars show a negative radial metallicity gradient near the disk mid-plane, but it gradually flattens and eventually becomes positive at larger heights in the disk (e.g., Cheng et al. 2012). They also show negative vertical metallicity gradients, which appear to be steeper
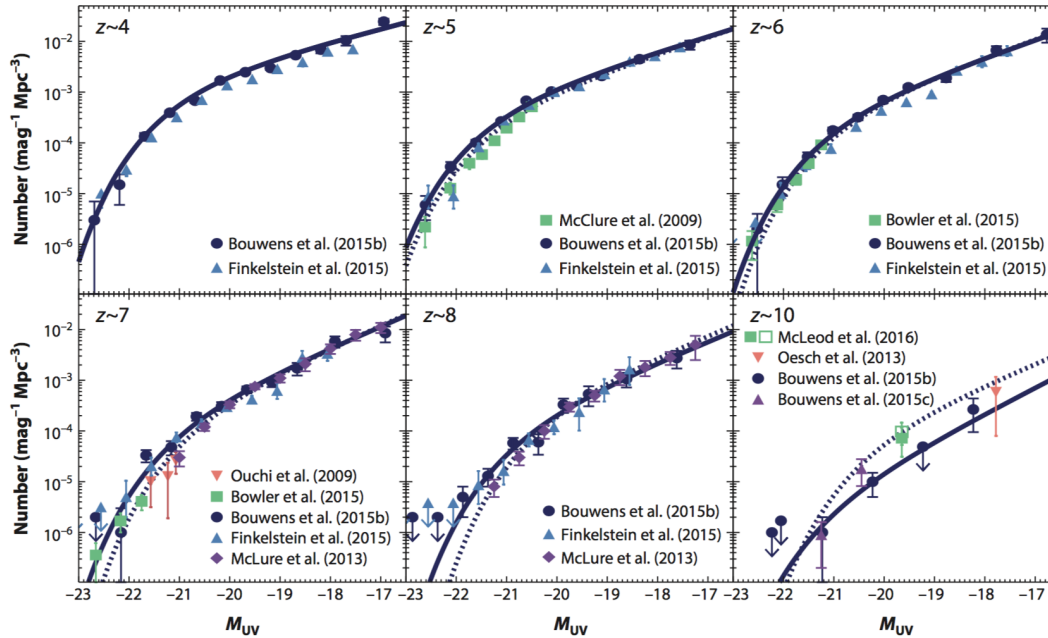
Figure 1.4: Some recent observational constraints on the galaxy UVLFs from $z = 4$–10, taken from Stark (2016). Up to $z \sim 8$, the UVLFs measured by different groups agree well with each other for $M_{UV} < -17$.

at the inner disk than at the outer disk (e.g., Hayden et al. 2014). Such a variance of stellar metallicity gradients across the MW disk is largely associated with the disk formation history. Since Gilmore & Reid (1983), it has been known that the MW disk has two components, namely the 'thin disk' and the 'thick disk'. Such a two-component structure has also been found in other disk galaxies nearby (e.g., Yoachim & Dalcanton 2006). It is still unclear when and how the thin and thick disks form in the MW and in other galaxies. In Chapter 4, I will present a case study using one simulation from the FIRE suite that eventually forms a MW-like galaxy (Figure 1.3), where I will show the disk assembly history, how the two-component structure establishes, how to interpret the thick disk, and how the formation history results in the stellar age and metallicity gradients across the disk.

1.3.2 Galaxies in the first billion years of the Universe

Understanding galaxy formation in the first billion years of the Universe is important for establishing a coherent picture of galaxy evolution across cosmic time. In the past few years, thousands of galaxies at $z \geq 5$ have been discovered by a series of multi-band deep imaging campaigns, which provide first constraints on the galaxy rest-frame UV luminosity functions (LFs) at these redshifts (Figure 1.4; for a recent

review, see Stark 2016). Moreover, these first galaxies are thought to be the dominant sources for cosmic reionization, a phase transition when the diffuse hydrogen in the intergalactic medium (IGM) became fully ionized. However, only a certain fraction of the ionizing photons produced by the massive stars can escape from the galaxy to ionize the IGM. This ionizing photon escape fraction, f_{esc}, is thus an important, yet poorly constrained parameter for understanding the reionization history. It has been suggested that a high $f_{esc} \sim 20\%$ is required for matching the observational constraints such as the integrated electron scattering optical depths (e.g., Finkelstein et al. 2012; Kuhlen & Faucher-Giguère 2012; Robertson et al. 2013, 2015).

In Chapter 5, I will present three high-resolution cosmological zoom-in simulations (mass resolution 20–2000 $M_{\odot}$, spatial resolution 0.1–4 pc) of $z \geq 5$ galaxies from the FIRE suite and post-process them with ionizing photon Monte Carlo radiative transfer calculations to evaluate f_{esc} from these simulated galaxies. According to stellar population synthesis models such as STARBURST99, most of the ionizing photons are emitted in the first few Myr's life of a stellar population, when the stars are still embedded in their 'birth cloud'. It also takes several Myr for early feedback processes to destroy the cloud and allow a large fraction of the ionizing photons to escape. However, the ionizing photon budget decreases dramatically after a few Myr as the most massive stars start to explode. Therefore, the competition between feedback clearing the star-forming cloud and stellar evolution is what determines the f_{esc}. Models that only include single-star evolution usually yield $f_{esc} \sim 5\%$. In Chapter 6, I will show that models including binaries, which produce significantly more ionizing photons after a few Myr than canonical single-star models, can lead to a much higher f_{esc} in these galaxies.

Despite many galaxies at $z \geq 5$ having been discovered lately, their physical properties, including stellar mass, star formation history, dust and metal content, etc., remain poorly understood. Moreover, even with moderate f_{esc}, it is still not clear whether star-forming galaxies are able to fully ionize the Universe. Recent measurements of the IGM ionization states at $z \geq 5$ suggest a non-negligible contribution from rare sources to reionization (e.g., Becker et al. 2015), such as active galactic nuclei (AGNs; e.g., Madau & Haardt 2015), which are SMBHs accreting gas in the center of galaxies. The next decade will be a golden age for studying first galaxies, SMBHs, and their role in cosmic reionization. After the launch of JWST in 2020, for the first time, we will obtain a large amount of high-quality photometric and spectroscopic data of $z \geq 5$ sources in the rest-frame UV and optical. With current and
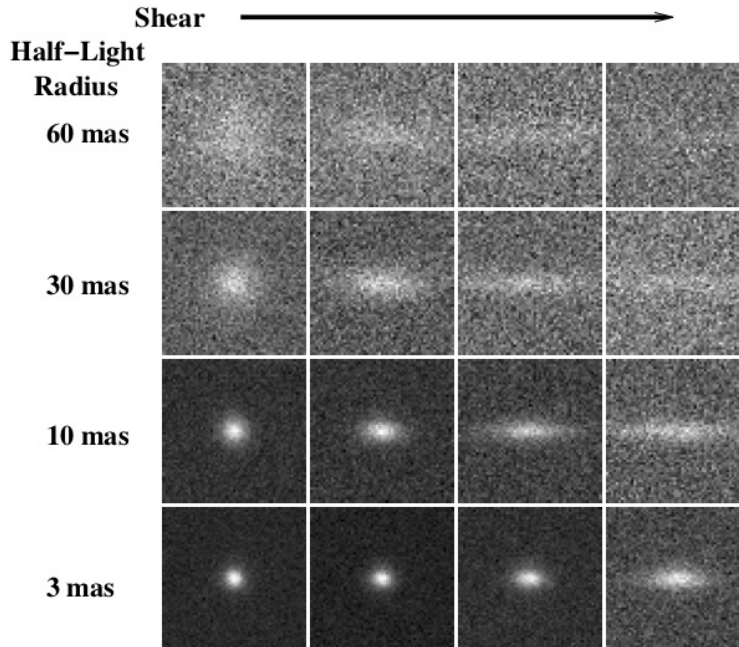
Figure 1.5: Simulated images for galaxies with fixed luminosity but different intrinsic sizes and degrees of shear in the HFFs, taken from Bouwens et al. (2017b). The detectability of galaxies in the HFFs depends strongly on these parameters.

future ground-based facilities in a broad range of wavelengths (e.g., Keck, ALMA, TMT, etc.), wide-field surveys of high-redshift objects, and neutral hydrogen 21-cm experiments, there will be tremendous new data probing high-redshift galaxies and the reionization process. It is thus critical and timely to make theoretical predictions that can be directly connected to these observations.

In Chapter 7, I will present a suite of 15 high-resolution (100–7000 $M_\odot$) cosmological zoom-in simulations using the state-of-the-art FIRE models for the multi-phase ISM, star formation, and stellar feedback (these models do not yet include SMBH physics). These simulations contains thousands of halos from 10^8–$10^{12}\,M_\odot$ from $z = 5$–12 in all the zoom-in regions. Such a moderate sample size allows us to do some statistical analysis. I will present a number of galaxy properties, including the stellar mass–halo mass relation, star formation history, SFR–M_* (M_{halo}) relation, and stellar mass–magnitude relation. I will convolve these scaling relations with the well-known HMFs to predict the galaxy SMFs and multi-band LFs for a broad range of stellar mass and magnitude at these redshifts. I will also show that these predictions agree well with current observational constraints at $z \sim 6$ and can be further tested by future JWST observations.

Current HST deep imaging can only detect galaxies with rest-frame UV magnitude down to $M_{UV} \sim -17$ at $z \geq 5$ in the deep fields. For fainter galaxies, one needs to rely on the large magnifications provided by strong gravitational lensing, which is achievable in the HFFs. However, the detectability of galaxies in the HFFs depends strongly on their intrinsic size and the degree of shear (Figure 1.5), so it is critical to understand the underlying distribution of morphology and sizes for high-redshift faint galaxies in order to reliably constrain the faint-end UVLF at $z \geq 5$. Bouwens et al. (2017b) have claimed that galaxies fainter than $M_{UV} \sim -15$ discovered in the HFFs generally have extremely small sizes (~ 10–$200\,$pc), some of which are even comparable to those of star clusters (e.g., Bouwens et al. 2017a). To address these questions, I will use the new suite of simulations presented in Chapter 7 and study the morphology, size–mass relation, and size evolution for our simulated galaxies. I will show that the rest-frame UV light is usually dominated by one or several bright star-forming clumps with intrinsic sizes $\sim 50\,$pc. Observations with finite surface brightness limits tend to only pick up the intrinsically small galaxies or the brightest clumps in the galaxies. On average, about 50% of the diffuse light in $M_{UV} \sim -15$ galaxies will be missed at a limit comparable to HFF observations. The extremely small sizes found for HFF galaxies are very likely due to such a selection bias. These results will be presented in Chapter 8.

As outlined above, understanding the properties of high-redshift galaxies and the reionization process is a rapidly growing field in today's astronomy. There are many open questions in this field that still lack a satisfactory theoretical understanding: How do the first stars and first galaxies form? What are the detailed properties of these galaxies? How many ionizing photons can each galaxy contribute? How do SMBHs form and grow at these redshifts? Do they play an important role, or even a dominant role in cosmic reionization? What observation signatures can tell apart competing models? In Chapter 9, I will briefly review two broad research topics for future investigations: (1) multi-wavelength spectral modeling of our state-of-the-art simulations of $z \geq 5$ galaxies to directly connect to future observations, and (2) the formation and growth of SMBHs at $z \geq 5$ and their roles in reionization.

C h a p t e r 2

THE ORIGIN AND EVOLUTION OF GALAXY MASS–METALLICITY RELATION

Abstract

We use high-resolution cosmological zoom-in simulations from the Feedback in Realistic Environment (FIRE) project to study the galaxy mass–metallicity relations (MZR) from $z = 0$–6. These simulations include explicit models of the multi-phase ISM, star formation, and stellar feedback. The simulations cover halo masses $M_{halo} = 10^9$–$10^{13}\,M_\odot$ and stellar masses $M_* = 10^4$–$10^{11}\,M_\odot$ at $z = 0$ and have been shown to produce many observed galaxy properties from $z = 0$–6. For the first time, our simulations agree reasonably well with the observed mass–metallicity relations at $z = 0$–3 for a broad range of galaxy masses. We predict the evolution of the MZR from $z = 0$–6, as $\log(Z_{gas}/Z_\odot) = 12 + \log(O/H) - 9.0 = 0.35\,[\log(M_*/M_\odot) - 10] + 0.93\exp(-0.43z) - 1.05$ and $\log(Z_*/Z_\odot) = [Fe/H] + 0.2 = 0.40\,[\log(M_*/M_\odot) - 10] + 0.67\exp(-0.50z) - 1.04$, for gas-phase and stellar metallicity, respectively. Our simulations suggest that the evolution of MZR is associated with the evolution of stellar/gas mass fractions at different redshifts, indicating the existence of a universal metallicity relation between stellar mass, gas mass, and metallicities. In our simulations, galaxies above $M_* = 10^6\,M_\odot$ are able to retain a large fraction of their metals inside the halo, because metal-rich winds fail to escape completely and are recycled into the galaxy. This resolves a long-standing discrepancy between "sub-grid" wind models (and semi-analytic models) and observations, where common sub-grid models *cannot* simultaneously reproduce the MZR and the stellar mass functions.

Keywords: galaxies: evolution – galaxies: formation – cosmology: theory

2.1 Introduction

The galaxy mass–metallicity relation (MZR) is one of the most fundamental properties observed in galaxies. In the local universe, there is a tight correlation between galaxy stellar mass and gas-phase oxygen abundance for star-forming galaxies (e.g., Tremonti et al. 2004), with an intrinsic scatter of only 0.1 dex in log(O/H). This relation has been extended to local dwarf galaxies and found to be a uniform, tight correlation over five orders of magnitude in stellar mass, from $M_* = 10^6$–$10^{11}\,M_\odot$ (Lee et al. 2006). Many different groups have confirmed the MZR to exist not only in the local universe but also at high redshifts up to $z \sim 2.3$ (e.g., Savaglio et al. 2005; Erb et al. 2006; Zahid et al. 2011, 2012; Andrews & Martini 2013; Henry et al. 2013a,b; Yabe et al. 2014; Steidel et al. 2014; Sanders et al. 2015). Zahid et al. (2013) compiled a number of the observed MZR from $z = 0$–2.3 and found that the MZR evolves with redshift, with higher metallicity at low redshift for a given stellar mass. The MZR is also found at $z \gtrsim 3$ (e.g., Maiolino et al. 2008; Mannucci et al. 2009), despite the fact that the results are obtained from very small samples.

Gas-phase metallicities represent the "current" state of chemical enrichment in the galaxies, while stellar metallicities reflect the "time-averaged" galactic metallicity across the whole star formation history. Similarly, an MZR is also found in stellar metallicities. Gallazzi et al. (2005) derived the stellar metallicities for ~44,000 galaxies from SDSS and found a tight correlation between stellar mass and stellar metallicity for galaxies of stellar masses 10^9–$10^{12}\,M_\odot$. Kirby et al. (2013) measured the metallicities of individual stars in a sample of dwarf galaxies within the Local Group and found the SDSS stellar MZR can be continually extended down to $10^3\,M_\odot$. Despite the fact that stellar metallicity is challenging to measure at high redshifts, the stellar MZR provides very important and complimentary insights on the chemical evolution of galaxies, especially for massive quiescent galaxies and satellite galaxies in the local group where the gas-phase metallicities are hard to measure due to their low gas content.

Simple analytic models of galactic chemical evolution, such as the "closed-box", "leaky-box", and "accreting-box" models (e.g., Schmidt 1963; Talbot & Arnett 1971; Searle & Sargent 1972; Edmunds 1990), are often quoted to illustrate the qualitative behavior of the MZR. More complicated models have also been developed to work in cosmological contexts and to connect gas inflows, outflows, and star formation to galactic chemical evolution (e.g., Dalcanton 2007; Finlator & Davé 2008; Davé et al. 2012; Lilly et al. 2013; Lu et al. 2015b). These models indicate that the existence

of MZR is the consequence of an interplay between star formation efficiency, metal loss from gas outflows, and gas recycling and accretion. For example, the stellar mass–halo mass relation (e.g., Moster et al. 2013; Behroozi et al. 2013b) indicates that the star formation efficiency (fraction of baryons turned into stars) is lower in low-mass galaxies than in more massive galaxies, suggesting that low-mass galaxies should be less metal-enriched. Meanwhile, galactic winds are ubiquitous (see e.g., Veilleux et al. 2005, for a recent review), carrying metals away from galaxies. Low mass galaxies have shallow potential wells so they tend to lose a significant fraction of their gas and metals, while massive galaxies have potential wells deep enough to prevent material from escaping the galaxy (e.g., Dekel & Silk 1986). On the other hand, gas inflows bring the metal-poor gas in the galactic halo and/or in the intergalactic medium (IGM) inwards, diluting the metal content in the interstellar medium (ISM) and supplying new material for star formation (e.g., Kereš et al. 2005; Faucher-Giguère & Kereš 2011). During this process, a considerable fraction of the gas and metals that have been formerly ejected via outflows eventually come back to the galaxy (e.g., Bertone et al. 2007; Oppenheimer et al. 2010). Galaxy mergers and AGN activity could also be important, in the sense that they can trigger violent starburst, drive intensive gas outflows, and ultimately quench the star formation in the galaxy (e.g., Springel et al. 2005b; Hopkins et al. 2013a).

Analytical models usually rely on simplified assumptions such as perfect mixing and adopt simple analytic prescriptions describing star formation, gas accretion, and outflows. In reality, these physical processes are tightly connected to each other and therefore must be treated self-consistently to understand the complete picture of galactic chemical evolution. Semi-analytic models (SAMs) of galaxy formation follow cosmological halo growth and halo mergers and include physically and/or empirically motivated prescriptions of heating and cooling, star formation, metal enrichment, gas accretion and outflows, recycling, and AGN feedback (e.g., Croton et al. 2006; Somerville et al. 2008; Benson 2012; Guo et al. 2013; Yates et al. 2013; Lu et al. 2011, 2014b, 2015a; Henriques et al. 2013, 2015). They are much less computationally expensive to run than hydrodynamic simulations and are able to reproduce a number of galaxy properties for a broad range of stellar mass. However, one major challenge for SAMs is *simultaneously* reproducing observed stellar masses, star formation rates (SFRs), and metallicities. The metallicities of low-mass galaxies are particularly sensitive to the galactic wind model because strong outflows are required to suppress star formation in low-mass systems (see e.g., Lu et al. 2014b, for a detailed comparison and discussion). Moreover, even

though different SAMs have been successfully tuned to match the $z = 0$ stellar mass function (SMF), many of them fail to match the observed the SMFs at high redshifts (e.g., Somerville & Davé 2015). At the same time, these models typically fail to match high-redshift MZR measurements and also diverge from one another in their MZR predictions. Nonetheless, it is encouraging that recently improved SAMs are able to reconcile stellar masses, colors, and SFRs of galaxies from $z = 0$–3 (e.g., Henriques et al. 2013, 2015).

Large-volume cosmological hydrodynamic simulations produce large samples of galaxies and are powerful tools for statistical studies of galaxy properties (e.g., Bertone et al. 2007; Davé et al. 2011b; Torrey et al. 2014; Schaye et al. 2015). These simulations, however, usually have relatively poor mass and spatial resolution. They cannot explicitly resolve the multi-phase structure of the interstellar medium (ISM), when and where star formation takes place, how galactic winds are launched by stellar feedback, and how the winds interact with the circumgalactic medium (CGM). Approximate, empirical "sub-grid" models of the ISM structure, star formation, and stellar feedback are required and used. For example, Davé et al. (2011a) implemented a momentum-driven wind model, with wind mass loading factors and velocities prescribed as a function of bulk galaxy properties. In their implementation, hydrodynamic interactions are temporarily suppressed as gas from the ISM is "kicked" into the galactic wind. Simulations using such simple prescriptions reveal similar problems to the SAMs. Torrey et al. (2014) found a steeper slope than observed at the low-mass end of the MZR. These authors attributed it to the low metal retention efficiency in the presence of strong outflows, which were required in their model in order to prevent low-mass galaxies from forming too many stars. They further emphasized the tension between suppressing star formation and retaining enough metals in low-mass galaxies. Furthermore, the star formation histories in these simulations are very different and not all consistent with observations at high redshifts. Many cosmological simulations tend to form *too many* stars at early times (e.g., Davé et al. 2011a; Sparre et al. 2015; Fiacconi et al. 2015; for a review, see Somerville & Davé 2015). Such problems are also common in SAMs. They are likely the result of imperfect star formation and stellar feedback models implemented in those simulations (cf. Scannapieco et al. 2012). Consequently, these simulations predict very different evolution of the MZR.

Therefore, when using cosmological hydrodynamic simulations to understand the MZR and its evolution, one is required to capture the "correct" behavior of star

formation, stellar feedback, gas outflows, and the mixing and interaction of galactic winds with the CGM on all relevant scales. Encouragingly, Obreja et al. (2014) presented a suite of cosmological zoom-in simulations from the MaGICC project using an improved star formation and SNe feedback model. Their model includes an empirical prescription to approximate the effects of stellar feedback mechanisms operating before the first SNe explode. These authors showed that their simulations match the stellar mass–halo mass relation and the observed MZR from $z = 0$–3, for the eight galaxies in their sample. In this work, the first of a series, we will study the chemical evolution of galaxies using the FIRE (Feedback in Realistic Environment) simulations (Hopkins et al. 2014). The FIRE project[1] is a series of cosmological zoom-in simulations that are able to follow galaxy merger history, interactions of galaxies with the IGM, and many other important processes. These simulations include a full set of realistic physical models and explicitly resolve the multi-phase structure of the ISM, star formation, and stellar feedback, with *no* need to tune parameters. The FIRE simulations successfully reproduce many observed galaxy properties, including the stellar mass-halo mass relation, star formation histories, the Kennicutt-Schmidt law, and the star-forming main sequence, from $z = 0$–6, for a broad range of galaxy masses in $M_* = 10^4$–10^{11} $M_\odot$ (Hopkins et al. 2014). Also, the FIRE simulations predict reasonable covering fractions of neutral hydrogen in the halos of $z = 2$–3 Lyman Break Galaxies (LBGs; Faucher-Giguère et al. 2015) and self-consistently generate galactic winds with velocities and mass loading factors broadly consistent with observational requirements (Muratov et al. 2015). These results further justify the reliability to study galactic chemical evolution using the FIRE simulations.

This paper focuses on the galaxy mass–metallicity relation. In companion papers, we will also study the stellar metallicity distribution functions and [α/Fe] abundance ratio variation in dwarf galaxies, metallicity gradients and their origins, metal outflows and recycling. We start by describing the simulations in Section 2.2 and present the mass–metallicity relation at different redshifts in Section 2.3. In Section 2.4, we discuss the key processes that drive the shape and evolution of the MZR. We summarize and conclude in Section 2.5.

---

[1]FIRE project website: http://fire.northwestern.edu

Table 2.1: Simulations analyzed in this chapter.

Name	M_{halo} (M$_\odot$)	m_b (M$_\odot$)	ϵ_b (pc)	m_{dm} (M$_\odot$)	ϵ_{dm} (pc)	Merger History	Notes
m09	2.5e9	2.6e2	1.4	1.3e3	30	normal	isolated dwarf
m10	0.8e10	2.6e2	3.0	1.3e3	30	normal	isolated dwarf
m10lr	0.8e10	2.1e3	2.1	1.0e4	35	normal	low resolution
m10v	0.8e10	2.1e3	7.0	1.0e4	70	violent	–
m11	1.4e11	7.0e3	7.0	3.5e4	70	quiescent	–
m11v	3.3e11	5.6e4	7.0	3.0e5	140	violent	–
m12v	6.3e11	3.9e4	10	2.0e5	140	violent	several $z < 2$ mergers
m12q	1.2e12	7.1e3	10	2.8e5	140	late merger	–
m12i	1.1e12	5.0e4	14	2.8e5	140	normal	large ($\sim 10\,R_{\mathrm{vir}}$) box
m13	6.0e12	3.6e5	21	2.2e6	210	normal	small group mass
z2h350	7.9e11	5.9e4	9	2.9e5	143	normal	–
z2h400	7.9e11	5.9e4	9	2.9e5	143	quiescent	–
z2h450	8.7e11	5.9e4	9	2.9e5	143	normal	–
z2h506	1.2e12	5.9e4	9	2.9e5	143	violent	–
z2h550	1.9e11	5.9e4	9	2.9e5	143	quiescent	–
z2h600	6.7e11	5.9e4	9	2.9e5	143	violent	–
z2h650	4.0e11	5.9e4	9	2.9e5	143	normal	–
z2h830	5.4e11	5.9e4	9	2.9e5	143	normal	–
z5m09	7.6e8	16.8	0.14	81.9	5.6	quiescent	ultra-high resolution
z5m10	1.3e10	131.6	0.4	655.6	7	normal	ultra-high resolution
z5m10mr	1.4e10	1.1e3	1.9	5.2e3	14	normal	–
z5m11	5.6e10	2.1e3	4.2	1.0e4	14	normal	–

Parameters describing the initial conditions for our simulations (units are physical):
(1) Name: Simulation designation.
(2) M_{halo}: Approximate mass of the main halo at $z = 0$ (mxx series), $z = 2$ (z2hxxx series), or $z = 6$ (z5mxx series).
(3) m_b: Initial baryonic (gas and star) particle mass in the high-resolution region.
(4) ϵ_b: Minimum baryonic force softening (minimum SPH smoothing lengths are comparable or smaller. Force softening is adaptive (mass resolution is fixed).
(5) m_{dm}: Dark matter particle mass in the high-resolution region.
(6) ϵ_{dm}: Minimum dark matter force softening (fixed in physical units at all redshifts).

2.2 The Simulations

2.2.1 Simulation Details

This work is part of the FIRE project. A full description of the numerical methods and physics included in our simulations is presented in (Hopkins et al. 2014, and references therein). We summarized their main features here. All the simulations use the newly developed GIZMO code (Hopkins 2015) in P-SPH mode. P-SPH adopts a Lagrangian pressure-entropy formulation of the smoothed particle hydrodynamics (SPH) equations (Hopkins 2013), which eliminates the major differences between SPH, moving-mesh, and grid codes, and resolves many well-known issues in traditional density-based SPH formulations. The gravity solver is a heavily modified version of the GADGET-3 code (Springel 2005); and P-SPH also includes substantial improvements in the artificial viscosity, entropy diffusion, adaptive time-stepping, smoothing kernel, and gravitational softening algorithm.

We use the multi-scale "zoom-in" initial conditions generated with the MUSIC code (Hahn & Abel 2011), using second-order Lagrangian perturbation theory. The first set of simulations have been run down to $z = 0$ and cover halo masses 10^9–10^{13} $M_\odot$ and stellar masses 10^4–10^{11} $M_\odot$ at $z = 0$ (mxx series). Most of them have been presented in Hopkins et al. (2014). The simulations m09 and m10 are isolated dwarfs, constructed using the method from Oñorbe et al. (2014). Simulations m10v, m11, m11v, m12q, m12i, and m13 are chosen to match the initial conditions from the AGORA project (Kim et al. 2014), which will enable future comparisons with a wide range of simulation codes and physics implementations. Simulation m12v is based on the initial conditions studied in Kereš & Hernquist (2009) and Faucher-Giguère & Kereš (2011). The simulations with a label 'v' have relatively violent merger histories at $z < 2$, while the rest have more typical merger histories. The resolution of these simulations is chosen to scale with the mass of the system to ensure we are able to resolve the giant molecular clouds (GMCs). We also include a separate set of simulations run to $z = 2$ (z2hxxx series), which are presented in (Faucher-Giguère et al. 2015). Their main halos are chosen to host Lyman break galaxies (LBG) and cover halo masses 1.9×10^{11}–1.2×10^{12} $M_\odot$ at $z = 2$. Finally, we include another series of simulations only run to $z \sim 6$, but with extremely high resolutions (z5mxx series). These simulations are presented in Ma et al. (2015). Their main halos cover halo masses from 7.7×10^8–5.6×10^{10} $M_\odot$ at $z = 6$ and these galaxies are believed to contribute most to the cosmic reionization (e.g., Kuhlen & Faucher-Giguère 2012; Robertson et al. 2013). The initial conditions of all the simulations are summarized in Table 2.1.

In our simulations, gas follows an ionized+atomic+molecular cooling curve from 10–10^{10} K, including metallicity-dependent fine-structure and molecular cooling at low temperatures and high-temperature metal-line cooling followed species-by-species for 11 separately tracked species (H, He, C, N, O, Ne, Mg, Si, S, Ca, and Fe; see Wiersma et al. 2009a). At each timestep, the ionization states and cooling rates are determined from a compilation of CLOUDY runs, including a uniform but redshift-dependent photo-ionizing background tabulated in Faucher-Giguère et al. (2009), and photo-ionizing and photo-electric heating from local sources. Gas self-shielding is accounted for with a local Jeans-length approximation, which is consistent with the radiative transfer calculations in Faucher-Giguère et al. (2010).

Star formation is allowed only in dense, molecular, and self-gravitating regions with hydrogen number density above some threshold $n_{th} = 10$–$100\,\mathrm{cm}^{-3}$ (Hopkins et al. 2013b). Stars form at 100% efficiency per free-fall time when the gas meets these criteria. The self-gravity criterion is physically required to obtain the correct spatial star formation distribution in galaxies (Padoan & Nordlund 2011; Hopkins et al. 2013b), but the galaxy-averaged star formation efficiency is regulated by feedback at much lower values ($\sim 1\%$ per dynamical time, e.g., Faucher-Giguère et al. 2013). We stress that changing these parameters in a reasonable range only yields small and random variations to the global star formation history, as long as feedback is active (see Hopkins et al. 2011, 2012a).

Once a star forms, it inherits the metallicity of each tracked species from its parent gas particle. Every star particle is treated as a single stellar population with known mass, age, and metallicity. Then all the feedback quantities, including ionizing photon budgets, luminosities, stellar spectra, supernovae (SNe) rates, mechanical luminosities of stellar winds, metal yields, etc., are directly tabulated from the stellar population models in STARBURST99 (Leitherer et al. 1999), assuming a Kroupa (2002) initial mass function (IMF) from 0.1–$100\,\mathrm{M}_\odot$[2]. We account for several different stellar feedback mechanisms, including (1) local and long-range momentum flux from radiative pressure, (2) energy, momentum, mass and metal injection from SNe and stellar winds, and (3) photo-ionization and photo-electric heating. We follow Wiersma et al. (2009b) and include the metal yields from Type-II SNe, Type-I SNe, and stellar winds. We note that the Type-II SNe yield table from Woosley

---

[2]In principle, the "IMF-averaged" approximation does not hold for the ultra-high resolution simulations in the z5mxx series, where the mass of a star particle is only 10–$100\,\mathrm{M}_\odot$. Nevertheless, we confirmed that these simulations predict similar global galaxy properties to those of much poorer resolutions (see Ma et al. 2015).

& Weaver (1995) adopted in our simulations produce Mg roughly ~ 0.4 dex below the typical values in modern models (e.g., Nomoto et al. 2006). This will have little effect on the galaxy properties in our simulations, as Mg is not an important coolant. Nevertheless, we will add 0.4 dex to the Mg abundance to correct this in the analysis below.

All simulations adopt a standard flat ΛCDM cosmology with cosmological parameters consistent with $H_0 = 70.2 \, \text{km s}^{-1} \, \text{Mpc}^{-1}$, $\Omega_\Lambda = 0.728$, $\Omega_m = 1 - \Omega_\Lambda = 0.272$, $\Omega_b = 0.0455$, $\sigma_8 = 0.807$ and $n = 0.961$ (e.g., Hinshaw et al. 2013).

2.2.2 Halo Identification, Stellar Mass and Metallicity

We use the Amiga Halo Finder (AHF; Gill et al. 2004; Knollmann & Knebe 2009) to identify galactic halos and galaxies in our simulations. The AHF code uses the adaptive mesh refinement method and identifies halos and subhalos as groups of *bound* particles (dark matter, gas, and stars). In this work, we only consider those "well-resolved" halos that include more than 10^5 bound particles, have at most 10% of their mass contaminated by low-resolution particles, and contain at least 100 gas and 100 star particles, respectively. These criteria are somewhat arbitrary; but varying these numbers within a reasonable range will have little effect on our conclusions. If none of the halos meets these criteria in a snapshot (this happens in some snapshots at high redshifts ($z \sim 6$), where the galaxy progenitors are too small to contain so many particles), we will take the most massive halo in the high-resolution region in our analysis. We do not include subhalos/satellite galaxies in this work. The centre of a halo is located at the centre of mass of the finest refinement level. We adopt the virial overdensity from Bryan & Norman (1998), which evolves with cosmic time.

We only consider the main galaxy in each halo. To remove the contamination of satellite galaxies, we exclude any gas/star particle that is bound to a subhalo in the analysis below. We measure the galaxy stellar mass (M_*) by summing over the mass of all star particles that belong to the main galaxy. Then we define its stellar metallicity (as well as the abundance of each tracked species) as mass-averaged metallicity (abundance) of all star particles. To separate halo gas and the ISM, we apply a simple temperature criteria and select all gas particles below 10^4 K as the ISM. In our simulations, this is equivalent to selecting gas above some density threshold of a few $0.1 \, \text{cm}^{-3}$ (we explicitly check the gas distribution in the density–temperature plane), which is comparable to the mean gas density within

a few stellar effective radii. It naturally picks warm ionized and cold neutral gas. We define the gas-phase metallicity as the mass-weighted metallicity of all gas particles that belong to the ISM (we compare and discuss three different definitions of gas-phase metallicity in Appendix A)[3].

In this work, we use $Z_{\rm gas}$ and Z_* to refer to the mass fraction of all heavy elements in gas and stars, respectively. In Section 2.3, we will primarily use oxygen abundance $12 + \log({\rm O/H})$ to present gas-phase metallicities, which is defined in terms of number ratio of oxygen to hydrogen atoms, in order to directly compare with observations. For stellar metallicity, we will primarily use Z_* in the rest of this work. In the literature, gas-phase metallicity and stellar metallicity are also sometimes referred as $Z_{\rm gas}$ and iron abundance [Fe/H] (in solar units), respectively. For these reasons, we provide the conversion between these quantities for our simulated galaxies. We will show the calibration in Appendix B but directly give the results here. For a solar metallicity of 0.02 and a solar iron abundance 0.00173 (both in mass fraction), we obtain $12 + \log({\rm O/H}) = \log(Z_{\rm gas}/Z_\odot) + 9.00$ and $[{\rm Fe/H}] = \log(Z_*/Z_\odot) - 0.20$. We emphasize that these relations may suffer from systematic uncertainties that originate from (1) Type-II and Type-I SNe rates, (2) metal yields of tracked species from different channels, and (3) the solar abundances we adopt in our simulations. However, the shape and evolution of the MZR should be robust to these uncertainties.

2.3 The Mass–Metallicity Relation

In this section, we present both the gas-phase and stellar MZR from $z =$0–6 and compare our results with observations and other simulations. We will further explore the most important factors that shape the MZR and drive its evolution in the Section 2.4.

2.3.1 The MZR at $z = 0$

We begin by showing the gas-phase MZR at $z = 0$. In Figure 2.1, we present the stellar mass–gas-phase oxygen abundance relation for our mxx series simulations at $z = 0$. For comparison, we also present the median and 2σ dispersion of the SDSS MZR from Tremonti et al. (2004, red solid and dashed lines) and the data of individual local dwarf galaxies compiled in Lee et al. (2006, open circles) in

---

[3]In many cosmological simulations with "sub-grid" models, gas-phase metallicity is usually defined as star-formation-rate-averaged metallicity. However, our simulations explicitly resolve multi-phase ISM structures and include realistic models of star formation and feedback. Individual gas particles are very sensitive to local feedback processes. For these reasons, we do not apply SF-averaged gas-phase metallicity to our simulations.
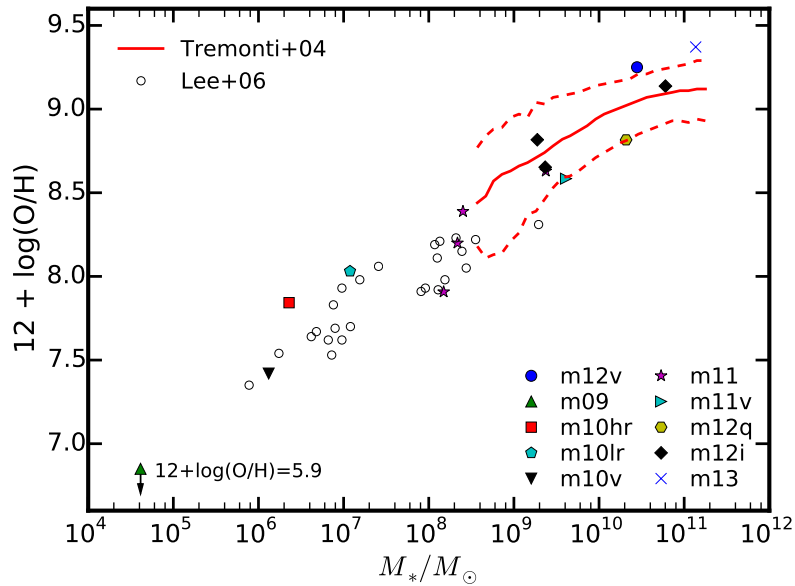
Figure 2.1: Stellar mass–gas-phase oxygen abundance relation at $z = 0$. The red solid and dashed curves represent the median and 2σ dispersion of the SDSS MZR at $z \sim 0.1$ (Tremonti et al. 2004). The open circles denote the data of the dwarf galaxy sample from Lee et al. (2006). Our simulations are in good agreement with observations from $M_* = 10^6$–10^{11} $M_\odot$.
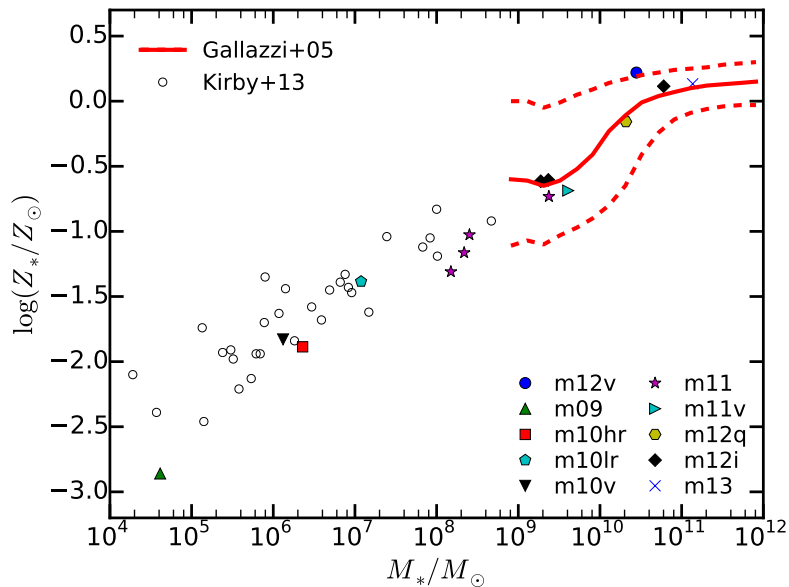
Figure 2.2: Stellar mass–stellar metallicity relation at $z = 0$. The red solid and dashed curves are the median and 1σ dispersion of the SDSS MZR in the local universe (Gallazzi et al. 2005). The open circles represent the values of [Fe/H] of individual dwarfs from Kirby et al. (2013). Again, the agreement is good from 10^4–10^{11} $M_\odot$.

Figure 2.1. We remind the reader that these observed gas-phase oxygen abundances are derived from the relative strength of strong nebulae emission lines produced by photo-ionization from young massive stars, so that the observed gas-phase MZR only holds for star-forming galaxies. Also, we emphasize that the overall shape of gas-phase MZR strongly depends on which empirical calibration it uses and the normalization of this relation differs by at most 0.7 dex between different calibrations (Kewley & Ellison 2008, see also Figure 2.6). For these reasons, we do not apply any correction to these observed data but keep them in their original forms.

In general, our simulations agree reasonably well with observations across stellar mass from $M_* = 10^6$–$10^{11}\,M_\odot$. However, our simulations do not show evidence for flattening at the high-mass end of the gas-phase MZR. The gas-phase metallicity increases with stellar mass up to $M_* \sim 10^{11}\,M_\odot$ in our sample. The simulations predict slightly higher metallicities than the observed relation from Tremonti et al. (2004) at $M_* = 10^{11}\,M_\odot$. The most significant discrepancy is due to our m13 run, which is a somewhat lower resolution simulation of a massive galaxy and which did not include the possible effects of AGN feedback. For example, as it has been shown in Hopkins et al. (2014), the main galaxy in m13 have the cooling flow problem and never quenches at low redshift. The SFR of this galaxy is $3\,M_\odot\,\mathrm{yr}^{-1}$, which is fairly low in its star formation history, but significantly higher than observationally inferred values below $z \sim 1$. Consequently, this galaxy might be over-enriched at low redshift. If so, this suggests that additional physics, such as AGN feedback, is probably required to fully understand the chemical evolution in massive galaxies, at least in the sense of quenching star formation. Alternatively, it has also been proposed that the observed MZR could continue to rise at the high-metallicity end when using new metallicity diagnostics that account for non-equilibrium electron energy distributions (see e.g., Dopita et al. 2013; Nicholls et al. 2013). Furthermore, we note that the "flatness" of MZR at the high-mass end behaves very differently when applying different empirical calibrations (e.g., Kewley & Ellison 2008). Therefore, we do not further quantitatively discuss the discrepancy between our simulations and observations at the massive-end of MZR, but rather focus on galaxies below $M_* = 10^{11}\,M_\odot$ where our simulations are most robust. A larger sample of simulations with improved resolution at the massive end is required to make a robust comparison.

Most of our simulated galaxies are still forming stars (at least very weakly) at $z = 0$, except for m09. The m09 is a low-mass isolated dwarf galaxy (comparable to the

ultra faint dwarfs around the Milky Way), in which star formation has been shut down since $z = 3$ by cosmic reionization (Oñorbe et al. 2015). At $z = 0$, this galaxy has lost almost all metals it produced (see Section 2.4). Although its gas-phase metallicity is an order of magnitude lower than the extrapolation of the observed MZR down to $M_* = 10^4\,M_\odot$, it is not contradictory to observations in the sense that the gas-phase metallicity of such galaxies cannot be measured due to lack of strong nebular emission lines.

In Figure 2.2, we show the stellar mass–stellar metallicity relationship at $z = 0$ and compare our simulations with the SDSS sample from Gallazzi et al. (2005, red solid and dashed curves) and the dwarf galaxies from Kirby et al. (2013, open circles). Note that the stellar metallicities from Gallazzi et al. (2005) are measured from absorption features of galaxy-integrated spectra (mostly Mg and Fe lines), while the metallicities from Kirby et al. (2013) are derived from Fe abundances of individual stars. The conversion between different methods and their systematic uncertainties is complex and beyond the scope of this paper. For our purposes, we avoid any correction to these observations but present them in their original values[4].

Our simulations match these observations quite well over the whole mass coverage from $M_* = 10^4$–$10^{11}\,M_\odot$. The simulated sample shows a flatness in the stellar MZR around $M_* = 10^{11}\,M_\odot$ at $z = 0$, consistent with the observed SDSS MZR from Gallazzi et al. (2005). This is the consequence of the fact that the growth of the more massive galaxies in our simulations is dominated by mergers and accretion of low-mass metal-poor satellites rather than *in situ* star formation at low redshifts. Therefore, the average stellar metallicities do not strongly evolve despite the fact that the stellar masses may grow considerably at low redshifts (see also Choi et al. 2014).

2.3.2 Evolution of the MZR

Figure 2.3 and 2.4 show the gas-phase and stellar MZR, respectively, from $z = 0$–6. We note that for $z \gtrsim 2$ and $z = 6$, we include the z2hxxx and z5mxx simulations in our analysis. The stellar MZR is tighter than the gas-phase MZR, i.e., the gas-phase MZR has larger scatter than stellar MZR at fixed stellar mass. This is because in our simulations, especially at high redshifts, star formation is dominated by multiple bursts, which drives bursts of gas outflows (Muratov et al. 2015). As a consequence, instantaneous gas-phase metallicities may have considerable time

---

[4]In Figure 2.2, we plot the values of [Fe/H] from Kirby et al. (2013), avoiding the complicated conversion between [Fe/H] and $Z_*/Z_\odot$ for the observed sample.
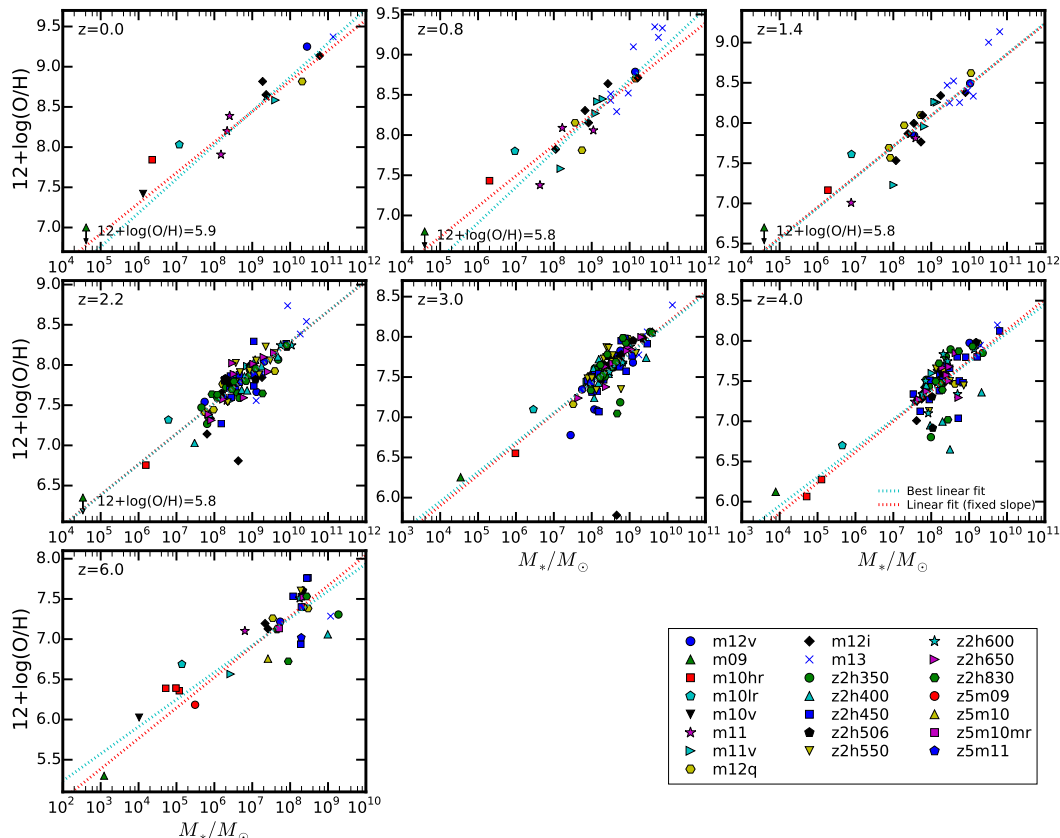
Figure 2.3: Stellar mass–gas-phase metallicity relation at all redshifts. Cyan dotted lines show the best linear fit $\log(Z_{gas}/Z_\odot) = 12 + \log(O/H) - 9.0 = \gamma_g[\log(M_*/M_\odot) - 10] + Z_{g,10}$. The red dotted lines show the best fit for a fixed slope $\gamma_g = 0.35$. Note that a constant slope provides a very good fit, where the zero point evolves by ~ 1 dex from $z = 0$–6.

fluctuations associated with gas inflows, outflows, and mergers. This effect is larger at high redshifts when the galaxy progenitors are of much lower masses and galaxy mergers are more common, resulting in some outliers that deviate from the main MZR at high redshifts. Despite the short-time-scale fluctuations, both the gas-phase and stellar metallicities increase with time on cosmological time-scales. At all times, gas-phase metallicities are higher than stellar metallicities, since gas-phase metallicities represent the current state of metal enrichment in the galaxies, while stellar metallicities reflect the average galactic metallicities across the whole time. Both metallicities should converge at high redshifts.

To illustrate this quantitatively, we fit the gas-phase and stellar MZR at different redshifts for our simulated galaxies with simple linear functions $\log(Z_{gas}/Z_\odot) = 12 + \log(O/H) - 9.0 = \gamma_g[\log(M_*/M_\odot) - 10] + Z_{g,10}$ and $\log(Z_*/Z_\odot) = [Fe/H] + 0.2 =$
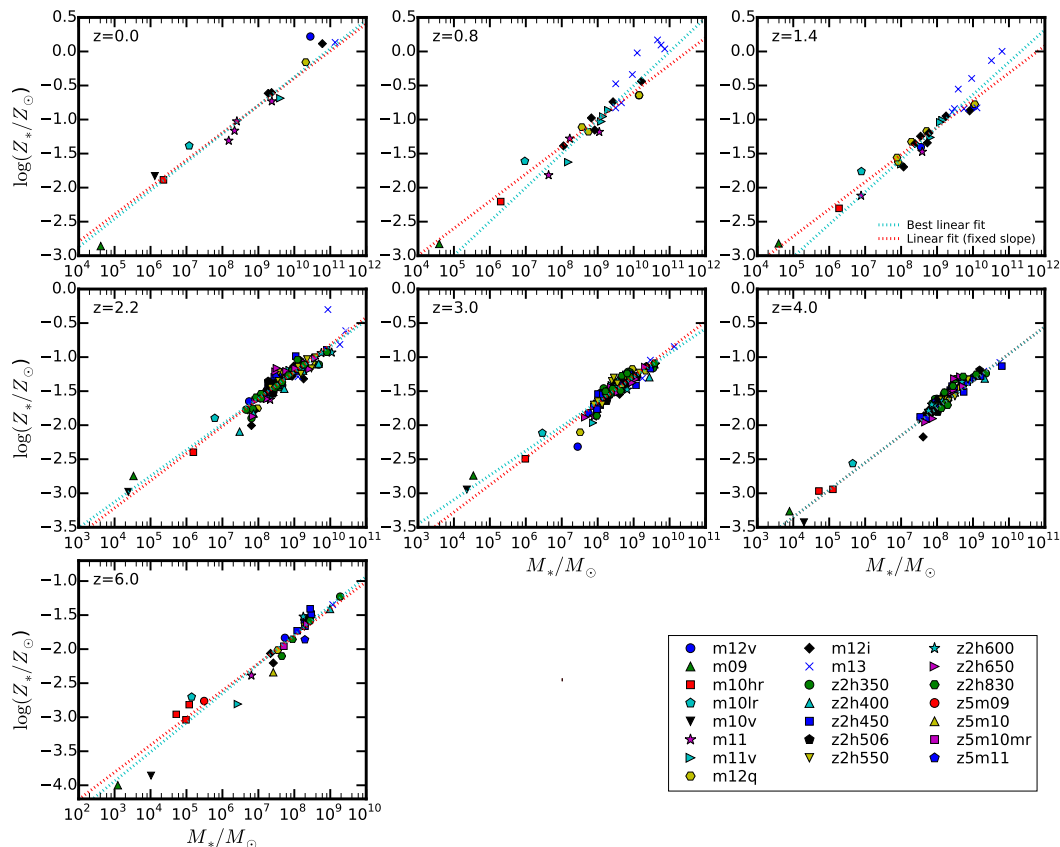
Figure 2.4: Stellar mass–stellar metallicity relation at all redshifts. Cyan dotted lines show the best linear fit at each redshift $\log(Z_*/Z_\odot) = [Fe/H] + 0.2 = \gamma_*[\log(M_*/M_\odot) - 10] + Z_{*,10}$. The red dotted lines show the best fit for a fixed slope $\gamma_* = 0.40$. Again, the slope is approximately constant, while the normalization evolves by ~ 1 dex.

$\gamma_*[\log(M_*/M_\odot) - 10] + Z_{*,10}$, where γ_g and γ_* are the slopes and $Z_{g,10}$ and $Z_{*,10}$ represent the typical gas-phase metallicity and stellar metallicity at $M_* = 10^{10} M_\odot$. Although simple linear function do not capture the flatness of stellar metallicity above $M_* \sim 10^{11} M_\odot$ at $z < 1$, it is sufficient for our purposes here. We use least-squares fitting to obtain the best fit (the cyan dotted lines in Figure 2.3 and 2.4). In principle, both the slopes and zero points should be functions of redshift. Nevertheless, the MZR at different redshifts have very similar slopes. For simplicity, we pick the mean slope of each relation and redo the linear fit using fixed slopes. We choose $\gamma_g = 0.35$ and $\gamma_* = 0.40$ (red dotted lines in Figure 2.3 and 2.4) and confirm that both the best linear fit and the fixed-slope fit describe the simulations reasonably well. We then attribute the evolution of MZR to the evolution of $Z_{g,10}$ and $Z_{*,10}$ with redshift, which we show in Fig-
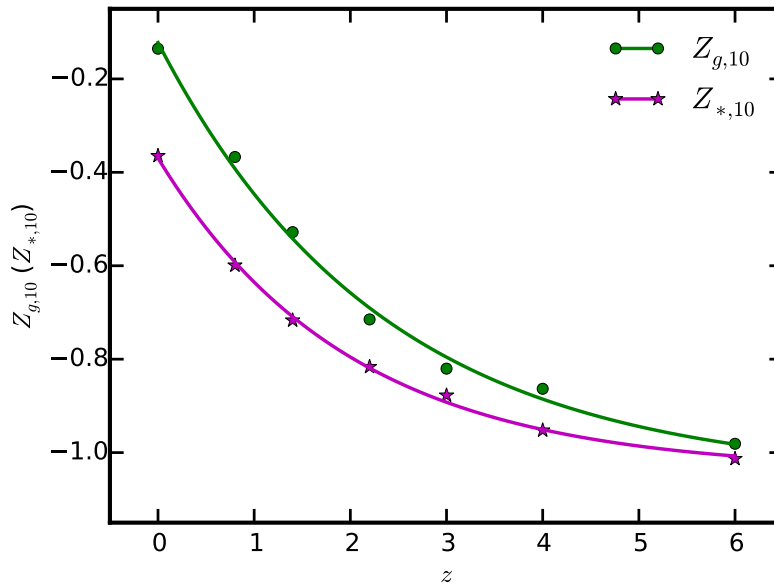
Figure 2.5: The gas-phase and stellar metallicity at $M_* = 10^{10}\,M_\odot$, $Z_{g,10}$ and $Z_{*,10}$ as a function of redshift. The solid lines are the best fit of exponential functions $Z_{g,10} = 0.93 \exp(-0.43z) - 1.05$ and $Z_{*,10} = 0.67 \exp(-0.50z) - 1.04$.

ure 2.5. We fit these parameters as a function of redshift by an exponential function $F(z) = A \exp(-Bz) + C$. The best fit gives $Z_{g,10} = 0.93 \exp(-0.43z) - 1.05$ and $Z_{*,10} = 0.67 \exp(-0.50z) - 1.04$, respectively (the green and magenta lines in Figure 2.5). These give the gas-phase and stellar MZR from $z = 0$–6 as $\log(Z_{\mathrm{gas}}/Z_\odot) = 12 + \log(O/H) - 9.0 = 0.35\,[\log(M_*/M_\odot) - 10] + 0.93 \exp(-0.43z) - 1.05$ and $\log(Z_*/Z_\odot) = [\mathrm{Fe/H}] + 0.2 = 0.40\,[\log(M_*/M_\odot) - 10] + 0.67 \exp(-0.50z) - 1.04$, respectively.

In general, the fitting functions above represent the gas-phase and stellar MZR fairly well for our simulated galaxies, except for the flattening of the stellar MZR above $M_* \sim 10^{11}\,M_\odot$ at $z = 0$. We emphasize that these results have systematic uncertainties from Type-II and Type-Ia SNe rates, the solar abundance, and the metal yield tables we implement in our simulations. When using these fitting functions, one should notice the uncertainties and make adjustments accordingly.

2.3.3 Comparison with Observations and Other Models

In Figure 2.6, we compare the gas-phase MZR between our simulations and a number of observations at multiple redshifts. We show the observed MZR at $z \sim 0$ (Tremonti et al. 2004), $z \sim 0.8$ (Zahid et al. 2011), $z \sim 2.2$ (Erb et al. 2006; Steidel et al. 2014; Sanders et al. 2015), and $z \sim 3.1$ (Mannucci et al. 2009). We recall
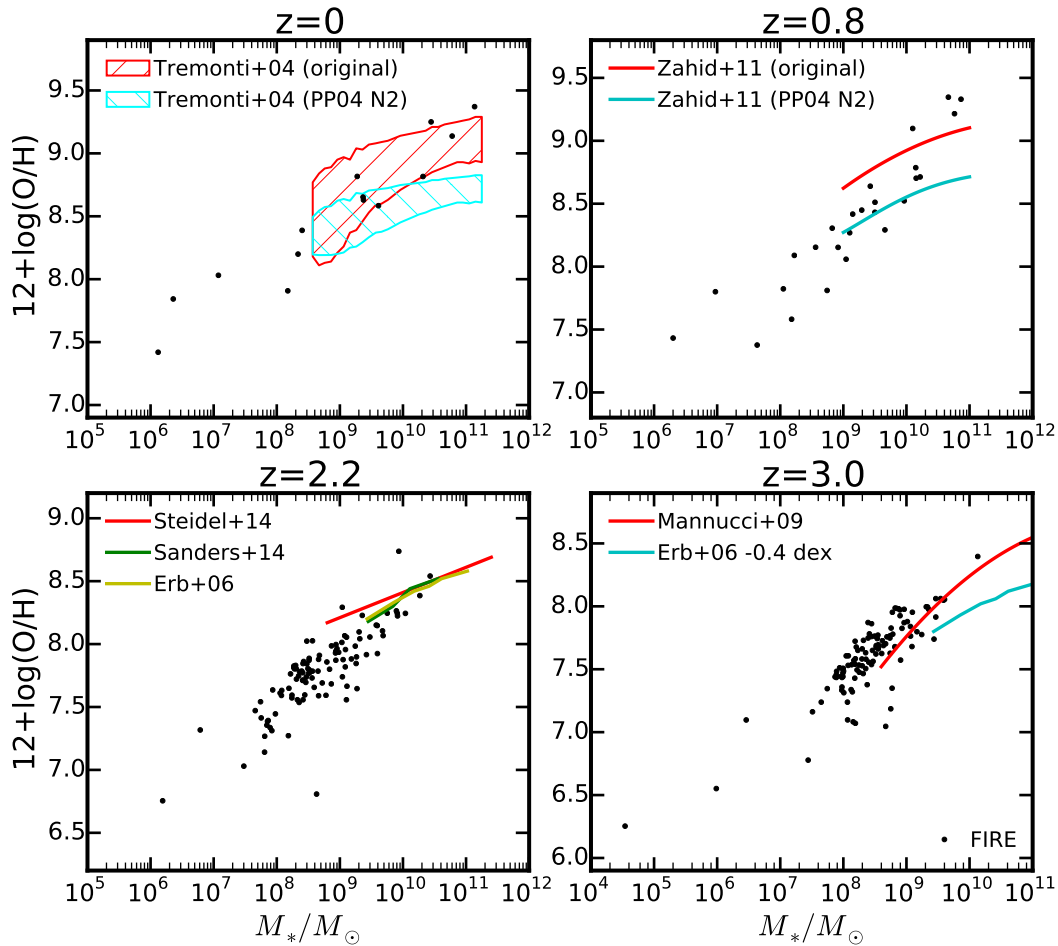
Figure 2.6: Stellar mass–gas-phase oxygen abundance relations at $z = 0, 0.8, 2.2$, and 3.0, as compared with a number of observations at these redshifts. In the upper panels, we show both the original relations (red lines) from Tremonti et al. (2004, $z \sim 0$) and Zahid et al. (2011, $z \sim 0.8$) and the relations converted to PP04 N2 calibration (cyan lines) following Kewley & Ellison (2008). In the lower left panel, we show the observed MZR at $z \sim 2.3$ from Steidel et al. (2014, the red line), Sanders et al. (2015, the green line), and Erb et al. (2006, the yellow line). In the lower right panel, we show the best fitting from Mannucci et al. (2009, $z \sim 3.1$). We also shift the Erb et al. (2006) data downward by 0.4 dex for a comparison as motivated by figure 5 in Mannucci et al. (2009). Our simulations are broadly consistent with observations over a wide range of stellar mass from $z = 0$–3, given the significant systematic uncertainties observational determinations of metallicities.

that these observed relations are originally obtained using different calibrations and the systematic uncertainty between different metallicity diagnostics could be up to 0.7 dex (Kewley & Ellison 2008). To illustrate this point, we also convert all the observed relation to the N2 calibration from Pettini & Pagel (2004, PP04 hereafter) unless their original data are already presented using this calibration. For Tremonti et al. (2004) and Zahid et al. (2011), we do the conversion following the formula from Kewley & Ellison (2008, table 3 therein). In either case, we present both their original relations and the converted relations using PP04 N2 calibration in Figure 2.6. At $z \sim 2.2$, the observed relations are at already presented in PP04 N2 calibration (e.g., Erb et al. 2006; Steidel et al. 2014; Sanders et al. 2015). Mannucci et al. (2009) adopted a very different metallicity calibration, which is established using $z \gtrsim 3$ galaxy samples only. Figure 5 in Mannucci et al. (2009) suggests that the MZR evolves by ~ 0.4 dex from $z \sim 3.1$ to $z \sim 2.2$. Motivated by their results, we also move the $z \sim 2.2$ MZR from Erb et al. (2006) downward by 0.4 dex for a comparison (lower right panel in Figure 2.6).

In general, our simulations are in reasonable agreement with these observations in a broad range of stellar mass at $z = 0$–3, especially when the observed relations are in their original forms. We emphasize that the empirical calibrations developed from the local universe are not necessarily valid for high-redshift galaxies (e.g., Steidel et al. 2014; Kewley et al. 2015). Given the large systematic uncertainties, we do not provide a detailed quantitative discussion of the discrepancies between our simulations and observations. Our results on the evolution of the MZR in Section 2.3.2 are predictions that can be tested more accurately as our understanding of the observational systematic uncertainties improves.

In Figure 2.7, we also compare the MZR from our simulations with other cosmological simulations and semi-analytic models. We compare our results with two other simulations, Torrey et al. (2014, red lines) and Davé et al. (2011b, green lines), and three semi-analytic models from Lu et al. (2014b, the Lu model, magenta; the Somerville model, cyan; the Croton model, yellow). These models adopt "sub-grid" empirical models of galactic winds and stellar feedback, which couple some fraction of energy and/or momentum from SNe to the gas, and force certain amount of the gas to escape the galaxy. Note that the metal yields and solar abundance used in different works are not exactly the same, we renormalize all the $z = 0$ MZR to $12 + \log(O/H) = 8.9$ at $M_* = 10^{10}\,M_\odot$ for comparison. At $z = 0$, Torrey et al. (2014) and the Lu model show steeper slopes at the low-mass end, due to the low
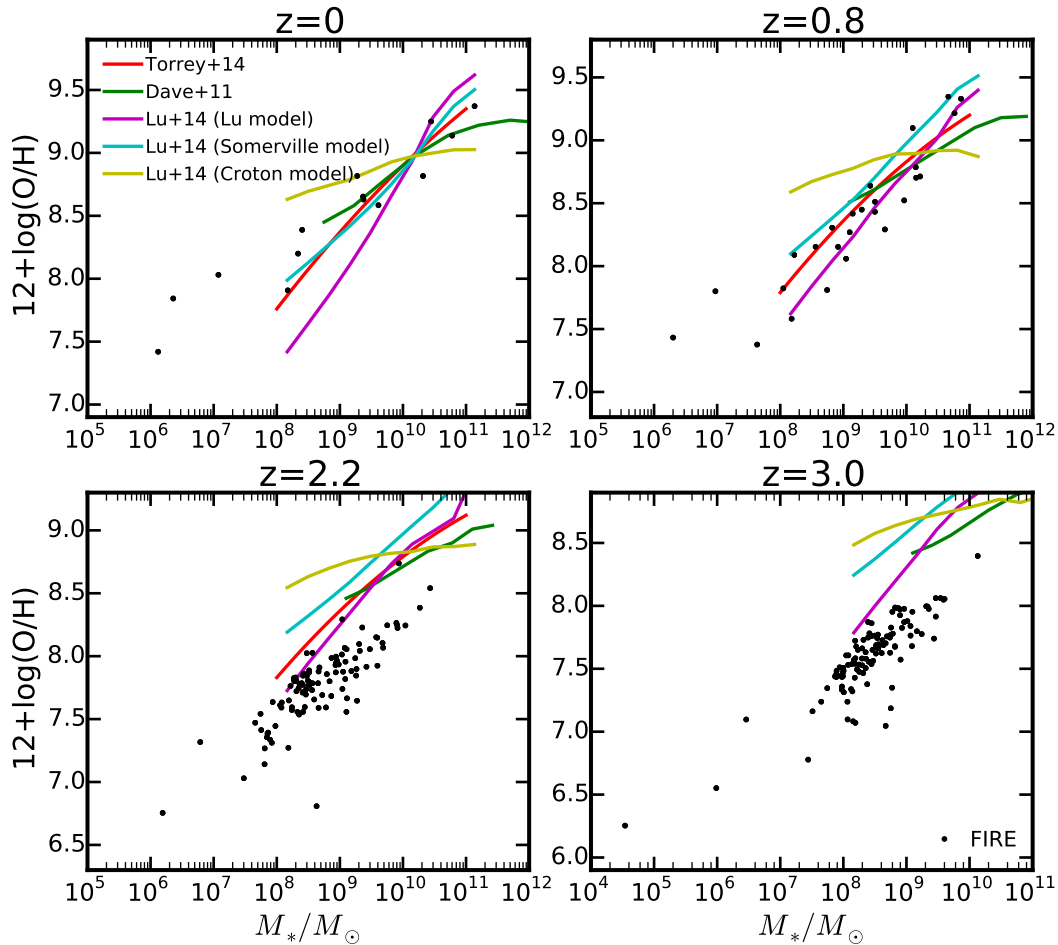
Figure 2.7: Stellar mass–gas-phase oxygen abundance relation at $z = 0$, 0.8, 2.2, and 3.0, as compared with other numerical simulations and semi-analytic models. We renormalize other works to $12 + \log(O/H) = 8.9$ at $M_* = 10^{10}\,M_\odot$ at $z = 0$ with respect to our simulations. Red and green lines show the results from cosmological simulations presented in Torrey et al. (2014) and Davé et al. (2011b), respectively, which used popular "sub-grid" models for galactic winds. Magenta, cyan, and yellow lines show the predictions of three semi-analytic models from Lu et al. (2014b, the Lu model, the Somerville model, and the Croton model, respectively). All of these models reproduce the correct $z = 0$ stellar mass function, but none of them correctly reproduces the slope or the redshift evolution of the MZR.

metal retention efficiency in low-mass galaxies, a consequence of invoking strong outflows to suppress star formation in these galaxies[5]. Some models predict higher metallicities at the most massive end. Furthermore, these models show significant discrepancies at $z \gtrsim 2$. Our simulations predict much stronger evolution of MZR from $z = 3$–0 than any other models. Particularly, the Somerville model and the Croton model predict inverse evolution trends – the gas-phase metallicity decreases at lower redshifts at fixed stellar mass – in contrast with observations and other models. We recall that although these models are tuned to match the observed stellar mass function at $z = 0$, they tend to predict systematically higher stellar mass functions than the observed ones for $M_* \lesssim 10^{11} \, M_\odot$ at $z > 0$ (Somerville & Davé 2015), a consequence of the fact that galaxies in these models form *too* many stars at early time (e.g., Davé et al. 2011a; Sparre et al. 2015; Fiacconi et al. 2015). In Section 2.4.4, we further explore how the different star formation histories between these models cause the discrepancies in the MZR at high redshifts.

2.4 Discussion

We showed above that the gas-phase and stellar MZR in our simulations agree broadly with available observations at different redshifts. We also found that our predictions diverge significantly from those of several large-volume cosmological hydrodynamical simulations and semi-analytic models. In this section, we explore the key factors that drive the shape and evolution of the MZR and discuss why our predictions differ from some other models.

2.4.1 Where are the metals?

Our simulations produce much higher metallicities for galaxies of stellar mass $M_* < 10^9 \, M_\odot$ than Torrey et al. (2014) and the Lu model in Lu et al. (2014b), indicating that our low-mass galaxies retain more metals compared to those models, despite the fact that these galaxies have high wind mass loading factors up to 100. To explicitly show this, we present in Figure 2.8 the metal mass fraction retained within R_{vir} as a function of stellar mass for the simulated sample at $z = 0$. The numbers are

---

[5]This can be simply illustrated using the "leaky box" model (e.g., Schmidt 1963). Assuming the outflow rate is proportional to the star formation rate ($\dot{M}_{\mathrm{out}} = \eta \cdot \mathrm{SFR}$, where η is the mass loading factor), the metallicity is inversely proportional to $1 + \eta$. Low-mass galaxies are very efficient in driving outflows and thus have high mass loading factors compared to massive galaxies. In SAMs and some simulations with "sub-grid" feedback models, it is often assumed that either the metals are well mixed in the system or that the outflowing gas has a metallicity comparable to the metallicity in the ISM. As a consequence, low-mass galaxies tend to lose a large fraction not only of their gas but also of their metals, and therefore end up with very low metallicities.
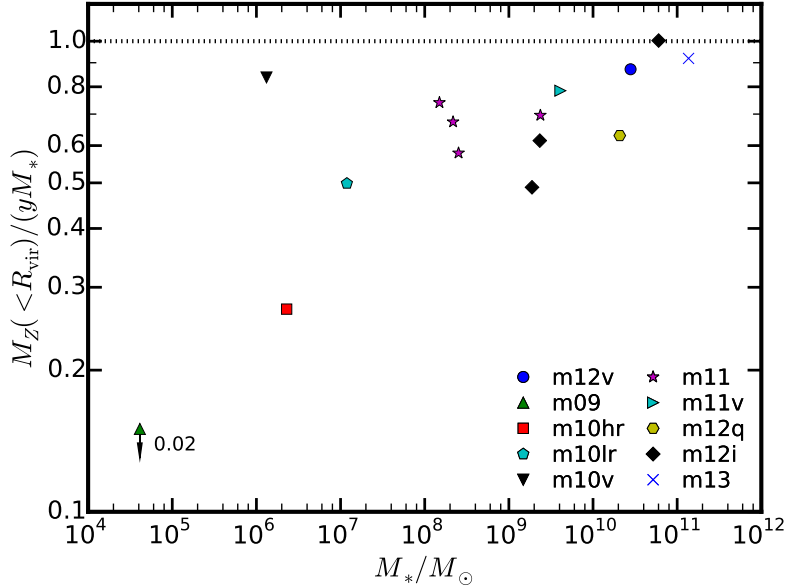
Figure 2.8: Metal retention fraction for our simulated galaxies at $z = 0$. $M_Z(< R_{\rm vir})$ is the total amount of metals retained (in both gas and stars) within the virial radius. yM_* (y is the mean effective yield) is the total metal mass produced by stars in the galaxies. The retained fraction of metal in the halo increases with stellar mass, from 30% at $M_* = 10^6 \, M_\odot$ to about unity at $M_* > 10^{10} \, M_\odot$. However, the ultra-faint dwarfs (e.g., m09) are only able to retain 2% of their metals in the halo.

obtained as follows. First, we estimate the effective yield y for every simulation as the ratio between total metal mass (in both gas and stars) and the total stellar mass in the whole simulation volume. Then the metal retention fraction for a galaxy is simply the ratio between the total metal mass within the virial radius, $M_Z(< R_{\rm vir})$, and yM_*, where M_* is the galaxy stellar mass as defined in Section 2.2.2. Thus, yM_* represents the total amount of metal ever produced by the stars in the galaxy. As shown in Figure 2.8, the metal retention fraction generally increases with stellar mass. In our simulated sample, galaxies above $M_* = 10^{10.5} \, M_\odot$ are able to keep almost all metals they have produced. At much lower masses ($M_* = 10^6$–$10^7 \, M_\odot$), they can still retain at least 30% to a half of their metals within the halo. In contrast, the ultra-faint dwarf in our sample, m09 ($M_* = 4 \times 10^4 \, M_\odot$), only retains 2% of its metals within $R_{\rm vir}$ at $z = 0$.

To quantify in more detail how metals are retained in galaxy halos, we show in Figure 2.9 the cumulative metal retention fraction, as a function of radius, for different gas phases (cool gas with $T < 10^4 \, K$ and warm gas with $10^4 \, K < T < 4 \times 10^5 \, K$)[6]. At

---

[6]In our simulations, most of the diffuse ($n_H < 0.1 \, {\rm cm}^{-3}$) gas has temperature $T > 10^4 \, K$, so a
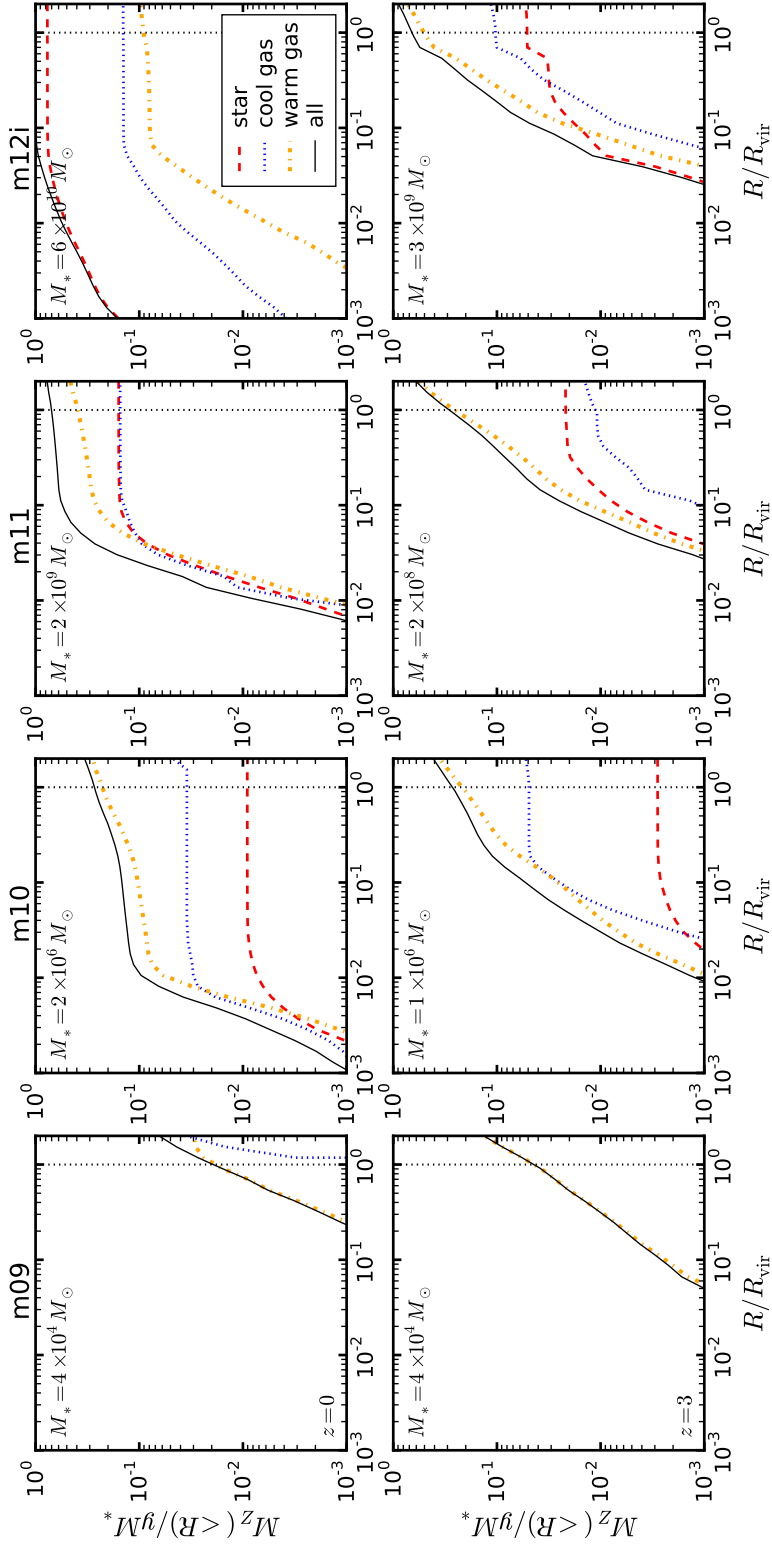
Figure 2.9: Cumulative metal mass in selected simulated halos at z = 0 (top) and z = 3 (bottom), normalized by the total metal mass produced by stars (yM∗). The red dashed, blue dotted, orange dash-dotted, and black solid lines show the metal mass in stars, cool gas (T < 10⁴ K), warm gas (10⁴ K < T < 4×10⁵ K), and total, respectively. The stellar mass of each galaxy is indicated at the top left corner of each panel and the black dotted lines show the virial radius. At z = 0, most of the metals in our more massive simulated galaxies such as m12i are in stars and within 0.1 $R_{\rm vir}$ of the halo center, while in low-mass galaxies, the majority of metals are found in the warm CGM. In low-mass galaxies at z = 0 and in high-redshift galaxies, a larger fraction of the metals are found at larger radii from the halo center, consistent with the fact that galactic outflows are more powerful in these systems.

$z = 0$ (top row), low-mass galaxies such as m10 ($M_* = 2 \times 10^6 \, M_\odot$) have most of their metals in the warm CGM, while in massive galaxies like m12i ($M_* = 6 \times 10^{10} \, M_\odot$), the majority of the metals are found in stars. This trend is qualitatively consistent with the empirical halo metal budget presented in Peeples et al. (2014, figure 6). In most cases, we find that only a small fraction of the total metal mass is found in hotter ($T > 4 \times 10^5 \, K$) gas. Our results are in contrast with the large-volume simulations of Ford et al. (2016) based on a parameterized galactic wind model, in which stars, ISM, and the cool CGM contain comparable metal masses for halos of mass similar to our m12i run.

For a comparison, we also show the cumulative metal distribution for the progenitors of these galaxies at $z = 3$ (the bottom panel in Figure 2.9). Similar to $z = 0$, a significant fraction of metals are still retained in R_{vir} at $z = 3$, although metals are more uniformly distributed from the centre to a few virial radii. These galaxies have much lower mass than their low-redshift decedents, and thus they are more efficient in driving gas outflows from star-forming regions throughout the halo.

2.4.2 Circumgalactic O VI

Although this paper is primarily focused on the metallicity of gas and stars inside galaxies, it is useful to check whether our simulations are consistent with observed CGM metal absorption. In addition to the overall metal budget discussed above, the COS-Halos program has provided useful measurements of O VI absorption around $\sim L^*$ galaxies at $z \approx 0.1 - 0.4$ (Tumlinson et al. 2011). Figure 2.10 shows the O VI column density map around our m12i simulated halo at $z = 0$. For this comparison, we assume that a fraction $f_{\mathrm{OVI}} = 0.2$ of the oxygen is in O VI and only include warm and hot gas ($T > 10^4 \, K$) in the halo. $f_{\mathrm{OVI}} = 0.2$ is the maximum expected if the oxygen is in collisional ionization equilibrium, though it is possible that O VI is also photo-ionized and/or subject to non-equilibrium effects (e.g., Oppenheimer & Davé 2009; Oppenheimer & Schaye 2013) so that this ionization fraction is not a strict upper limit. The figure shows that for m12i the characteristic N_{OVI} drops from $\sim 10^{15} \, \mathrm{cm}^{-2}$ at impact parameter $b = 20 \, \mathrm{kpc}$ from the central galaxy to $\sim 10^{13.5} \, \mathrm{cm}^{-2}$ at $b = 200 \, \mathrm{kpc}$. The simulation agrees well with the O VI columns measured by Tumlinson et al. (2011) around low-redshift $\sim L^*$ star-forming galaxies at impact parameters $b < 50 \, \mathrm{kpc}$ but appears to underestimate O VI columns by a factor of a few at larger impact parameters. Overall the agreement with observed O VI columns

---

temperature cut at $T = 10^4 \, K$ also effectively separates ISM and CGM gas, justifying our approach of using gas with $T < 10^4 \, K$ to evaluate gas-phase ISM metallicities.
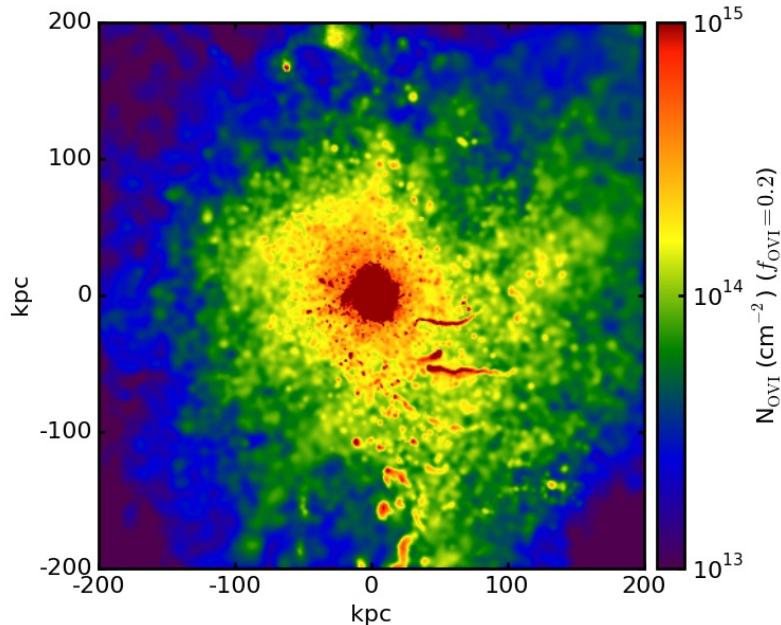
Figure 2.10: O ᴠɪ column density map for the m12i halo at $z = 0$. We crudely assume that a fraction $f_{\rm OVI} = 0.2$ of the oxygen is in O ᴠɪ and only include warm and hot gas ($T > 10^4$ K) in the halo. The characteristic $N_{\rm OVI}$ drops from $\sim 10^{15}$ cm^{-2} at impact parameter $b = 20$ kpc from the central galaxy to $\sim 10^{13.5}$ cm^{-2} at $b = 200$ kpc. The simulation agrees well with the O ᴠɪ columns measured by COS-Halos Tumlinson et al. (2011) around low-redshift $\sim L^*$ star-forming galaxies at impact parameters $b < 50$ kpc but appears to underestimate O ᴠɪ columns by a factor of a few at larger impact parameters. Overall the agreement with observed O ᴠɪ columns is reasonable given the uncertainties in ionization correction.

is reasonable given the uncertainties in ionization correction. More systematic and detailed comparisons of CGM metal statistics from the FIRE simulations with observations will be reported in future papers (Hafen et al. 2017).

2.4.3 Metal outflows, inflows, and recycling

SAMs and large-volume cosmological simulations require "sub-grid" models of galactic winds, which often incorporate fairly crude approximations. In this subsection, we further examine the metal inflow and outflow rates and the metallicities of gas inflows and outflows in our simulations and compare with the assumptions of common "sub-grid" models.

We follow Faucher-Giguère et al. (2011) and Muratov et al. (2015) and define the
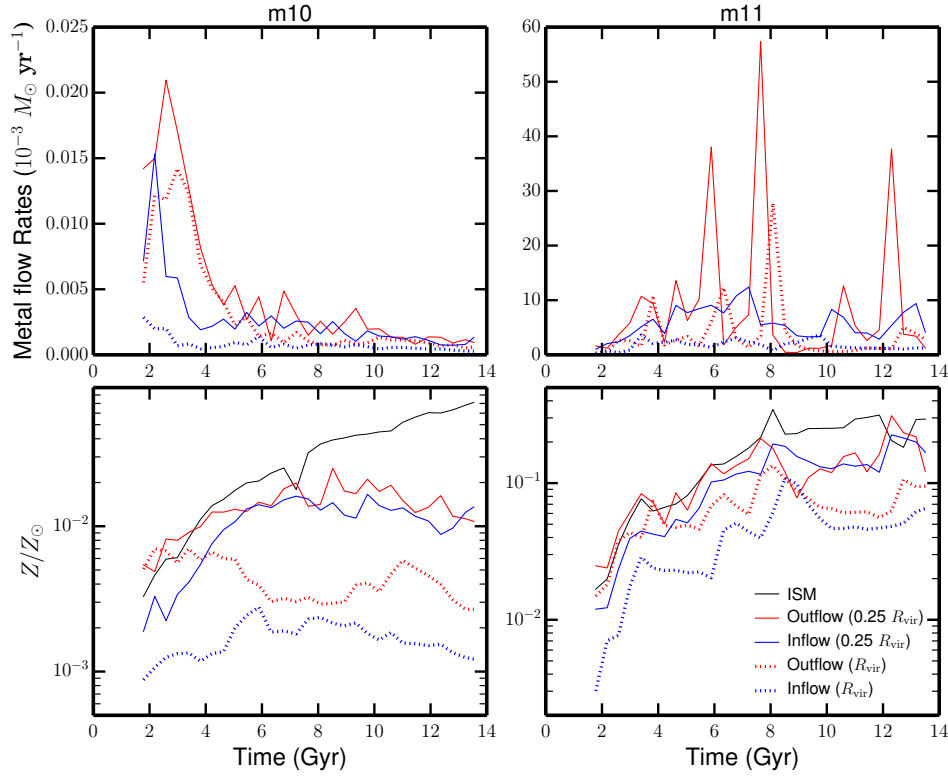
Figure 2.11: *Upper*: Metal inflow (blue) and outflow rates (red) from $z = 0$–4. Solid and dotted lines show the metal inflow/outflow rates measured at $0.25\,R_{\mathrm{vir}}$ and R_{vir}, respectively. *Bottom*: Metallicities of inflowing/outflowing gas. The black line shows the metallicity of the ISM. All quantities are averaged over a time-scale of 400 Myr. Metals are efficiently ejected in fountains reaching $0.25\,R_{\mathrm{vir}}$, but they do not usually reach R_{vir} – they are either deposited in the halo or recycled efficiently in galactic fountains. Outflowing gas that escapes from the halo at R_{vir} tends to be less enriched than the gas in the ISM.

gas outflow rates, metal outflow rates, and metallicities of outflow gas as

$$\frac{\partial M}{\partial t} = \sum_i \vec{v} \cdot \frac{\vec{r}}{|r|} M_i / \mathrm{d}L, \tag{2.1}$$

$$\frac{\partial M_{\mathrm{metal}}}{\partial t} = \sum_i \vec{v} \cdot \frac{\vec{r}}{|r|} Z_i \, M_i / \mathrm{d}L, \tag{2.2}$$

$$Z_{\mathrm{outflow}} = \frac{\partial M_{\mathrm{metal}}}{\partial t} / \frac{\partial M}{\partial t}, \tag{2.3}$$

where M_i and Z_i are the mass and metallicity of the ith gas particle within the shell of thickness $\mathrm{d}L = 0.1\,R_{\mathrm{vir}}$ with radial velocity outwards $\vec{v} \cdot \frac{\vec{r}}{|r|} > 0$. The inflow rates and inflow metallicities are defined in the same way but for gas particles with

inward radial velocity $\vec{v} \cdot \frac{\vec{r}}{|r|} < 0$. The upper panels in Figure 2.11 show the metal inflow/outflow rates at $0.25 \, R_{\mathrm{vir}}$ (blue/red solid lines) and at R_{vir} (blue/red dotted lines) for our m10 (left) and m11 (right) simulations. We average the inflow/outflow rates on a time-scale of 400 Myr. In either case, the net metal outflow rates are considerably lower at R_{vir} than at $0.25 \, R_{\mathrm{vir}}$, indicating that the metals are either deposited in the halo or returned back to the ISM. At high redshifts, metals ejected in outflows can be more easily driven to R_{vir} than at low redshifts. At $0.25 \, R_{\mathrm{vir}}$, metal inflow rates are comparable to metal outflow rates, suggesting a high efficiency of metal recycling. The lower panels in Figure 2.11 show the average metallicities of inflows and outflows at both $0.25 \, R_{\mathrm{vir}}$ and at R_{vir}, as compared to the metallicity of the ISM (black solid lines). The outflow metallicities are much lower at R_{vir} than at $0.25 \, R_{\mathrm{vir}}$ (and even more so than in the ISM), because outflowing gas sweeps up and mixes with more metal-poor gas in the halo as it propagates outwards. This is particularly important for low-mass galaxies, such as m10 ($M_* = 2 \times 10^6 \, M_\odot$), which can have wind mass loading factors up to ~ 100, yet retain a large fraction of the metals they produced in their halos.

Our analysis calls into question a number of assumptions and approximations often adopted in analytic, semi-analytic, and large-volume cosmological hydrodynamic models of galaxy formation. First of all, unlike often assumed in analytic and semi-analytic models, metals are generally not well-mixed in galaxy halos (e.g., Figure 2.9). In particular, in many "sub-grid" galactic wind models, wind gas is assumed to have a metallicity directly related to the ISM metallicity (e.g., Davé et al. 2011a; Torrey et al. 2014), an assumption that oversimplifies the complex mass and metal loading that takes places in our more explicit simulations. Our simulations also indicate that metal re-accretion onto galaxies (recycling) is important on small scales, an effect which is not well captured in semi-analytic models and in "sub-grid" models that either assume that the ejected gas never returns to the galaxy, or which ignore hydrodynamical interactions between the wind and the gas close to the galaxy.

Recently, Lu et al. (2015a) compared three different SAM feedback models — one including only gas ejection, one including both gas ejection and recycling, and the other including a model of "preventive" feedback. Lu et al. (2015a) found that none of these models could *simultaneously* reproduce the MZR, the distribution of metals in different phases, and the SFR observed at $z = 0$–3. This finding is consistent with the picture suggested by our high-resolution simulations that the

chemical evolution of galaxies is a complex process and that it is necessary to self-consistently model galaxy-halo interactions in order to capture it faithfully. It is encouraging that our cosmological simulations with explicit stellar feedback and hydrodynamical interactions tracked at all times appear to produce a low-mass-end slope of the MZR that is closer to observations than most previous models, without the need for parameter tuning. Our results are broadly consistent with those of Brook et al. (2014), who also highlighted the importance of metal mixing with the CGM and recycling for explaining the MZR. The simulations of Brook et al. (2014) also provide a fair match to the observed MZR at $z = 0$–3 (Obreja et al. 2014)).

2.4.4 Why the MZR evolves with redshift?

Another major difference between our simulations and other theoretical work is we predict much stronger evolution of the MZR from $z = 3$–0 (e.g., the stellar metallicity increases by 0.5 dex at fixed stellar mass, see Figure 2.5). Observations and some theoretical models suggest a fundamental metallicity relation (FMR) between stellar mass, star formation rate, and metallicity that holds for star-forming galaxies both in the local universe and at high redshifts (e.g., Mannucci et al. 2010, 2011; Lilly et al. 2013; Obreja et al. 2014; Cullen et al. 2014; Zahid et al. 2014). Motivated by these results, we attempt to qualitatively illustrate what might be the primary factor that drives the evolution of MZR in this section. We start by reviewing the simplest chemical evolution model, i.e., the "closed box" model, which predicts the stellar and gas-phase metallicities as a function of stellar mass fraction, $f_* = M_*/(M_{\mathrm{gas}} + M_*)$ as the following:

$$Z_* = y \left[\frac{1 - f_*}{f_*} \ln(1 - f_*) + 1 \right], \tag{2.4}$$

$$Z_g = -y \ \ln(1 - f_*), \tag{2.5}$$

where y is the effective metal yield (e.g., Schmidt 1963; Talbot & Arnett 1971; Searle & Sargent 1972). The parameter f_* describes the fraction of baryons that have been turned into stars, and $1 - f_*$ is the "gas fraction". In Figure 2.12, we show the relation between stellar and gas-phase metallicities and f_*, respectively (the middle and right panels), for our mxx series simulations at $z = 0$ and $z = 3$ (black and red points). We emphasize that we account for *both* the halo gas *and* the ISM in the total gas mass when calculating f_*, since halo gas is actively involved in supplying star formation and metal exchange in most cases. For consistency, the gas-phase metallicities shown in Figure 2.12 are the average metallicity of *all* gas in the halo. For illustrative purposes, we also show the simple predictions from the
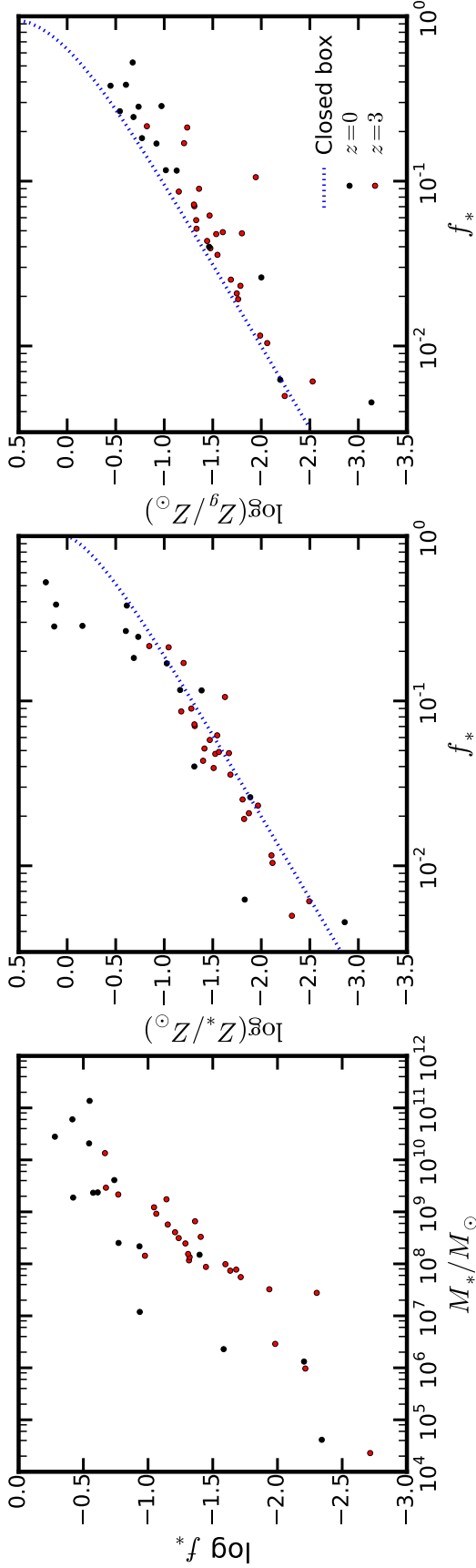
Figure 2.12: *Left*: Stellar mass fraction $f_* = M_*/(M_{\rm gas} + M_*)$ as a function of stellar mass. $M_{\rm gas}$ here is the total gas mass in the *halo* (not only in the galaxy). *Middle*: Stellar metallicity Z_* as a function of f_*. *Right*: Gas-phase metallicity $Z_{\rm gas}$ as a function of f_*. For consistency, $Z_{\rm gas}$ here is the average metallicity of *all* gas in the halo (including *both* the ISM *and* the halo gas). Black points and red points show the primary FIRE simulations at $z = 0$ and $z = 3$, respectively. Blue dotted lines show the simple "closed box" model predictions assuming an effective metal yield of $y = 0.02$. The $z = 0$ and $z = 3$ galaxies share the same Z_*-f_* and $Z_{\rm gas}-f_*$ relations, but the f_*-M_* relation evolves by ~ 0.5 dex from $z = 3$–0. This indicates that the evolution of the MZR is associated with the evolution of f_* (at a fixed stellar mass) at different redshifts. The major offset between our simulations and the predictions of the "closed box" model is largely due to the fact that the metals are not perfectly mixed throughout the halo. Especially in massive galaxies, gas tends to be more metal-enriched in the central star-forming regions than in the outer halo, so stellar metallicities tend to be higher and gas-phase metallicities (including the halo gas) are lower than the predictions of the "closed box" model.

"closed box" model, assuming an effective metal yield of $y = 0.02$ (blue dotted lines in Figure 2.12).

The simulated data at $z = 0$ and $z = 3$ overlap with each other in the Z_*–f_* and Z_{gas}–f_* diagrams. In the left panel of Figure 2.12, we also show the relation between f_* and M_* for these galaxies at both redshifts. There is a systematic offset (~0.5 dex) in the f_*–M_* relation between galaxies at $z = 0$ and 3. Note that in the limit of $f_* \ll 1$, one has $Z_*, Z_{\mathrm{gas}} \propto f_*$. Therefore, the 0.5 dex offset in f_*–M_* relation propagates to the 0.5 dex evolution of the MZR from $z = 3$ to 0. This suggests that the evolution of the MZR is associated with the evolution of f_* (at a fixed stellar mass) within the *halo* at different redshifts, providing a first hint of a universal metallicity relation between stellar mass, gas mass, and metallicities (cf. Bothwell et al. 2013; Zahid et al. 2014, for observational evidences). In simulations with "sub-grid" feedback models and semi-analytic models, where the $z = 0$ stellar mass functions are tuned to match observations, galaxies tend to form a large fraction of their stars at high redshift and therefore their evolution is weaker at lower redshift (e.g., Somerville & Davé 2015), as opposed to observations and our simulations. In other words, these models produce higher f_* than our simulations at fixed stellar mass at $z > 0$ and an f_*–M_* relation barely evolving from $z = 3$–0. Therefore, galaxies in those models are more metal-enriched at high redshifts and the evolution of the MZR is weaker than our simulations.

Our simulations are qualitatively consistent with the simple "closed box" predictions applied to *halo* quantities[7]. This is not unreasonable because a large fraction (order unity) of metals are retained within the virial radius at both redshifts (see e.g., Figure 2.9). However, we emphasize that one should not think our simulated galaxies are closed boxes, because the metals are not perfectly well-mixed in the galactic halo. This explains the major offset between the "closed box" model and our simulations (middle and right panels in Figure 2.12), especially in the most massive systems where this effect is stronger. Since gas in the centre of the galaxy tends to be more metal-enriched than gas in the outer halo and stars preferentially form in the central region, stellar metallicities tend to be higher and the gas-phase metallicities (including the halo gas) are lower than the predictions of the closed box model (applied to halo quantities). The mixing of metals is very complex and

---

[7]We emphasize that in the analog of Figure 2.12 where we measure f_* using *only* the gas in the galaxy (i.e., excluding the halo gas), all the galaxies are well below the predictions of the closed box model and there is no well-defined relation, indicating that galaxies themselves are far from closed boxes. This suggests the necessity of accounting for halo gas as reservoirs in galaxy evolution.

associated with galactic fountains on different scales. Although the "closed box" model gives a natural relation between stellar mass, gas mass, and the metallicities, the parameterization of a universal metallicity relation for galactic quantities (i.e., excluding the halo) is more complicated than the simple model. This is worth further investigation in more detail in future work.

2.5   Conclusion

We use a series of high-resolution cosmological zoom-in simulations spanning halo masses 10^9–10^{13} $M_\odot$ and stellar masses 10^4–10^{11} $M_\odot$ at $z = 0$ from the FIRE project to study the galaxy mass–metallicity relations at $z = 0$–6. These simulations include explicit models of multi-phase interstellar medium, star formation, and stellar feedback. As has been shown in previous papers, these simulations successfully reproduce many observed galaxy properties, including the stellar mass–halo mass relation, star-forming main sequence, the Kennicutt-Schmidt law, star formation histories, etc., for a wide range of galaxies at many redshifts (Hopkins et al. 2014). These simulations also predict reasonable covering fractions of neutral hydrogen in the halos of $z = 2$–3 LBGs (Faucher-Giguère et al. 2015) and self-consistently generate galactic winds with velocities and mass loading factors broadly consistent with observational requirements (Muratov et al. 2015). These simulations adopt "standard" stellar population models and metal yield tables from Type-I and Type-II supernovae and stellar winds, following species-by-species for 11 separately tracked elements. Our key conclusions include the following.

(i) The simulations predict galaxy mass–metallicity relations that agree reasonably well with a number of observations from $z = 0$–3 for a broad range of stellar masses. Both gas-phase and stellar metallicities evolve monotonically from $z = 0$–6, with higher metal abundance at low redshifts at fixed stellar mass. The best linear fits of the MZR for our simulated galaxies as a function of redshift are $\log(Z_{\mathrm{gas}}/Z_\odot) = 12 + \log(\mathrm{O/H}) - 9.0 = 0.35\,[\log(\mathrm{M}_*/\mathrm{M}_\odot) - 10] + 0.93\exp(-0.43z) - 1.05$ and $\log(Z_*/Z_\odot) = [\mathrm{Fe/H}] + 0.2 = 0.40\,[\log(\mathrm{M}_*/\mathrm{M}_\odot) - 10] + 0.67\exp(-0.50z) - 1.04$, for gas-phase metallicity and stellar metallicity, respectively. We emphasize that the normalizations may have systematic uncertainties that originate from the SNe rates, yield tables, and solar abundance we adopt, but the evolution of the MZR is robust to these uncertainties.

(ii) The stellar MZR becomes flat around $\mathrm{M}_* \sim 10^{11}\,\mathrm{M}_\odot$ since $z = 0$, because the most massive galaxies in our simulations evolve via mergers and accretion

of satellites rather than *in situ* star formation at low redshifts. Therefore, the stellar metallicity does not increase despite the fact that the stellar mass grows considerably. We do not see the flatness in the gas-phase MZR at the high-mass end seen in observations, because gas continues to be enriched by non-negligible star formation. This apparent discrepancy may be due to the more limited resolution in our m13 run or to the lack of AGN feedback in our simulations. AGN might be required to quench star formation below $z \sim 1$ in such massive galaxies.

(iii) The evolution of MZR is associated with the evolution of the gas/stellar mass fraction within the inner halo (not just inside the galaxy effective radius) at different redshifts. This provides a first hint of a universal metallicity relation between stellar mass, gas mass, and metallicities, but its parameterization for galactic quantities (as opposed to for halo quantities, which behave more like a closed box) is much more complicated than simple analytic models. We will investigate this in more detail in future work.

(iv) Galaxies above $M_* \sim 10^6 \, M_\odot$ can retain a large fraction of their metals in the halo even up to $z = 3$. The net metal outflow rates near the virial radius are always lower than those near the galaxy, indicating that the metals either get deposited in the halo or return back to the ISM. The high metal inflow rates and the high metallicity of inflowing gas at 0.25 $R_{\rm vir}$ suggest a high efficiency of metal recycling (a finding that we have confirmed using particle tracking; Anglés-Alcázar et al. 2017a). On average, the outflows at outer radii are much less metal-enriched than those at the inner radius. This effect helps resolve the tension between the need for strong gas outflows and high metal retention fractions in low-mass galaxies.

(v) These differential recycling and metal retention effects are not properly accounted for in most semi-analytic and early generation of "sub-grid" feedback models that are popular in cosmological simulations. As a result, these simplified models cannot simultaneously reproduce the galaxy mass function and the slope and redshift evolution of the MZR. By explicitly resolving the "missing physics" in these models, we reconcile the long-standing discrepancy, and provide a clear way forward to improve the sub-grid and semi-analytic models.

Nevertheless, our simulations are still limited in sample size. In the near future, we will expand our simulations to include more dwarf galaxies covering halo mass from $M_{\rm halo} = 10^8$–$10^{11} \, M_\odot$ and to enlarge our sample at the most massive end to better understand whether the flattening of the MZR is real and what drives the flatness. This may depend critically on AGN feedback. We will provide quantitative analysis

on metal outflow rates, outflow metallicities, metal recycling, and their relation with galaxy properties in future work (Muratov et al. 2017; Anglés-Alcázar et al. 2017a).

Acknowledgments

Appendix A: Different Definitions of Gas-phase Metallicity

In this work, the gas-phase metallicity is defined as the mass-weighted average metallicity of all gas particles below 10^4 K, which we refer as the ISM gas. In principle, there are many alternative approaches to define gas-phase metallicities. In this section, we discuss three definitions and compare them with each other: (1) the average metallicity of all gas particles below 10^4 K in the galaxy (our default definition), (2) the average metallicity of all gas particles within $0.1\,R_{\rm vir}$, and (3) the average metallicity of all gas particles with temperature between 7,000–15,000 K and density above $0.5\,{\rm cm}^{-3}$. In Figure 2.13, we compare definition (1) and (2) in the left panel and (1) and (3) in the right panel for all galaxies presented in Figure 2.3.

Definition (1) is designed to automatically select all the warm ionized gas and cold neutral gas (the ISM), definition (2) aims to pick the gas in the star-forming regions, and definition (3) is observationally motivated to select the nebular gas which produce the strong nebular emission lines in star-forming galaxies. In general, these definitions are consistent with each other. Most of the galaxies lie very close to the
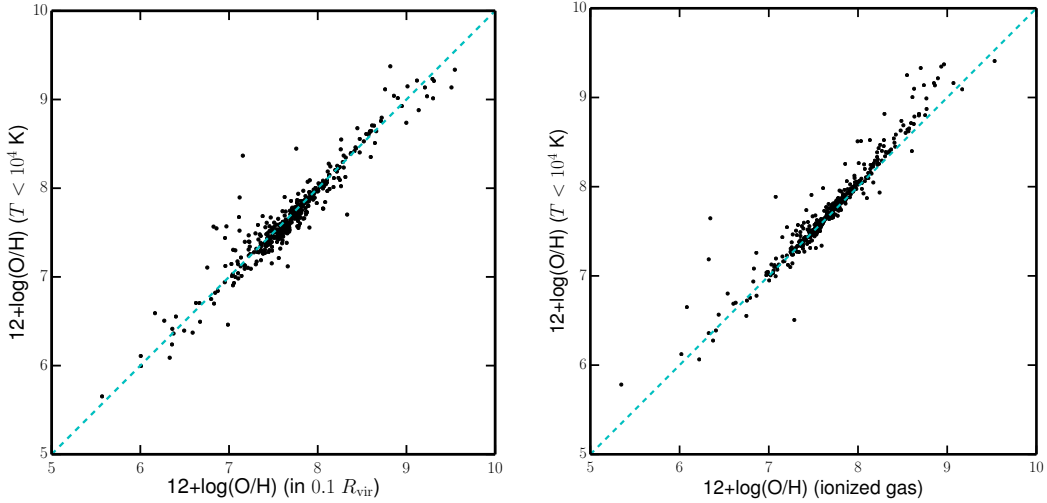
Figure 2.13: Gas-phase oxygen abundances in different definitions. *Left:* The relation of gas oxygen abundances between definition (1) the average metallicity of all gas particles below 10^4 K and (2) the average metallicity of all gas particles within $0.1\,R_{\mathrm{vir}}$. *Right*: The relation of gas oxygen abundances between definition (1) and (3) the average metallicity of all gas particles with temperature between 7,000–15,000 K and density above $0.5\,\mathrm{cm}^{-3}$. The cyan dashed lines show the $y = x$ relation. The black points show all the data presented in Figure 2.3. Different definitions agree well, and have *no* qualitative effect on any of our conclusions. Most of the "outliers" are caused by transient, stochastic time variability.
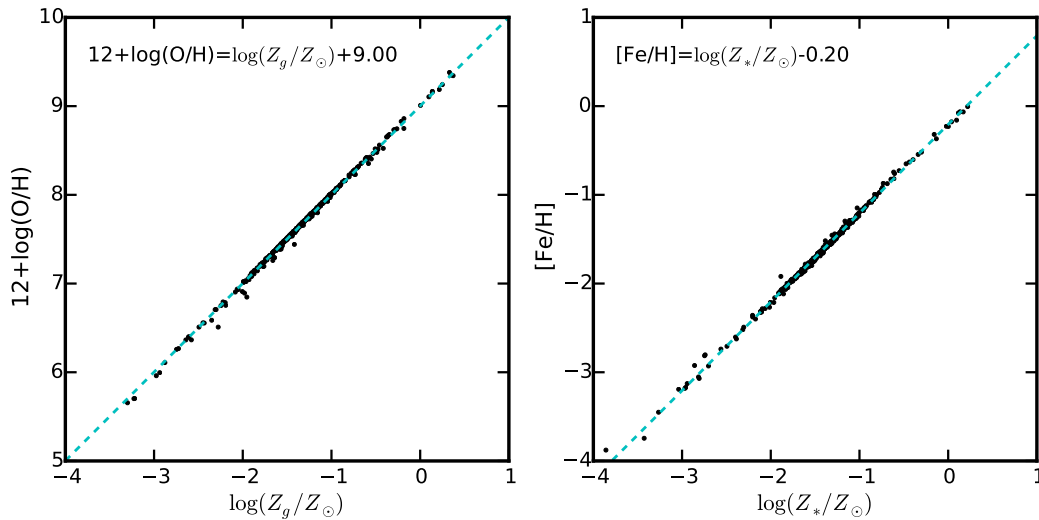
Figure 2.14: Relations between different forms of metallicities. *Left*: Gas-phase oxygen abundance $12 + \log(\mathrm{O/H})$ vs. gas-phase metallicity (mass fraction of all metals) Z_{gas}. *Right*: Stellar iron abundance [Fe/H] vs. stellar metallicity Z_*. Black dots collect all the data points presented in this work. The cyan lines represent the best fits of these relations with slope unity. These definitions give essentially identical results, and are equivalent, for all of our results in this paper.

$y = x$ relation in each panel of Figure 2.13. However, there are a few outliers in these diagrams. Definition (2) can be problematic in merging systems, where the halo centre may deviate far from the stellar bulk and thus $0.1\,R_{\mathrm{vir}}$ does not necessarily probe the star-forming region. Definition (3) is largely affected by abundance variance between gas particles, since there are usually not many gas particles at any single instant that meet the temperature and density criteria. However, a time-averaged version of definition (3) removes most of the outliers. Therefore, we argue that our default definition is more adaptive and flexible than other definitions.

Appendix B: Metallicities in Different Forms

In this work, we primarily use $12 + \log(\mathrm{O/H})$ and Z_* to present gas-phase metallicity and stellar metallicity, respectively. In the literature, gas-phase metallicity and stellar metallicity are sometimes presented in terms of Z_{gas} and [Fe/H]. Therefore, we also provide the conversion between these different forms of metallicities for comparison. We emphasize these conversions are obtained from our simulations only and there are systematic uncertainties originating from the uncertain relative metal yields between species and solar abundances we adopt.

In Figure 2.14, we show the relations between $12 + \log(\mathrm{O/H})$ and $\log(Z_{\mathrm{gas}}/Z_{\odot})$ (left panel) and the relation between [Fe/H] and $\log(Z_*/Z_{\odot})$ (right panel), where we adopt a solar metallicity $Z_{\odot} = 0.02$ and a solar iron abundance of 0.00173, both in mass fraction. In both panels, we collect data of all the simulated galaxies at all epochs we present earlier in this paper. Both relations are extremely tight and have slope unity, which ensures the validity, at least to the first order, to use either quantity to represent metallicities interchangeably. The best fits for our simulations are $12 + \log(\mathrm{O/H}) = \log(Z_{\mathrm{gas}}/Z_{\odot}) + 9.0$ and $[\mathrm{Fe/H}] = \log(Z_*/Z_{\odot}) - 0.20$. We emphasize that there relations may suffer from systematic uncertainties that originate from (1) Type-II and Type-I SNe rates, (2) metal yields of tracked species from different channels, and (3) the solar abundances we adopt in our simulations.

Chapter 3

WHY DO HIGH-REDSHIFT GALAXIES SHOW DIVERSE GAS-PHASE METALLICITY GRADIENTS?

Abstract

Recent spatially resolved observations of galaxies at $z \sim 0.6$–3 reveal that high-redshift galaxies show complex kinematics and a broad distribution of gas-phase metallicity gradients. To understand these results, we use a suite of high-resolution cosmological zoom-in simulations from the Feedback in Realistic Environments (FIRE) project, which include physically motivated models of the multi-phase ISM, star formation, and stellar feedback. Our simulations reproduce the observed diversity of kinematic properties and metallicity gradients, broadly consistent with observations at $z \sim 0$–3. Strong negative metallicity gradients *only* appear in galaxies with a rotating disk, but not *all* rotationally supported galaxies have significant gradients. Strongly perturbed galaxies with little rotation always have flat gradients. The kinematic properties and metallicity gradient of a high-redshift galaxy can vary significantly on short time-scales, associated with starburst episodes. Feedback from a starburst can destroy the gas disk, drive strong outflows, and flatten a pre-existing negative metallicity gradient. The time variability of a single galaxy is statistically similar to the entire simulated sample, indicating that the observed metallicity gradients in high-redshift galaxies reflect the instantaneous state of the galaxy rather than the accretion and growth history on cosmological time-scales. We find weak dependence of metallicity gradient on stellar mass and specific star formation rate (sSFR). Low-mass galaxies and galaxies with high sSFR tend to have flat gradients, likely due to the fact that feedback is more efficient in these galaxies. We argue that it is important to resolve feedback on small scales in order to produce the diverse metallicity gradients observed.

Keywords: galaxies: formation – galaxies: evolution – cosmology: theory

3.1 Introduction

Metallicity is a fundamental property of galaxies. In the local Universe, galaxy stellar mass correlates tightly with both gas-phase metallicity (e.g., Tremonti et al. 2004; Lee et al. 2006) and stellar metallicity (e.g., Gallazzi et al. 2005; Kirby et al. 2013), known as the galaxy mass–metallicity relation (MZR). The MZR also exists at higher redshifts up to $z \sim 3$ (e.g., Erb et al. 2006; Maiolino et al. 2008; Mannucci et al. 2009; Zahid et al. 2011; Yabe et al. 2014; Steidel et al. 2014; Sanders et al. 2015). The MZR evolves smoothly with redshift, with galaxies being more metal-enriched at lower redshift (e.g., Zahid et al. 2013). The MZR results from the interplay between gas accretion and recycling, star formation, and feedback-driven outflows (e.g., Edmunds 1990; Davé et al. 2012; Lilly et al. 2013; Feldmann 2013; Lu et al. 2015b), so it is widely used to constrain feedback models in cosmological simulations and semi-analytic models of galaxy formation (e.g., Davé et al. 2011b; Torrey et al. 2014; Lu et al. 2014b; Ma et al. 2016a).

Historically, galaxy metallicity is usually measured in the central regions despite the presence of metallicity gradients. Since Searle (1971), it has been known that galaxies in the local Universe tend to have negative gas-phase metallicity gradients, which means that galaxies are more metal-enriched in the central region than at the outskirt (e.g., Zaritsky et al. 1994; van Zee et al. 1998; Sánchez et al. 2012, 2014). The slope of metallicity gradients of non-interacting galaxies, if normalized to some characteristic radius (e.g., the effective radius), does not depend strongly on galaxy properties, such as morphology, the existence of bars, magnitude, stellar mass, etc. (e.g., Zaritsky et al. 1994; Sánchez et al. 2014; Ho et al. 2015; however, see Vila-Costas & Edmunds 1992). This can be understood by a simple model where gas and stellar disks co-evolve under virtually closed-box assumptions (Ho et al. 2015). Interacting galaxies are under-abundant in their central regions (e.g., Kewley et al. 2006; Peeples et al. 2009) and show evidence of shallower gas-phase metallicity gradients than isolated galaxies of similar masses (e.g., Vila-Costas & Edmunds 1992; Kewley et al. 2010; Rupke et al. 2010b), owing to strong radial inflow of low-metallicity gas from the outskirts toward the galactic center (e.g., Rupke et al. 2010a; Torrey et al. 2012).

It is only in the past few years that gas-phase metallicity gradients have been directly measured in galaxies beyond the local Universe. Early attempts include resolved studies of several strongly lensed galaxies at redshift $z \sim$ 1.5–2.4 (e.g., Yuan et al. 2011; Jones et al. 2010, 2013). Four out of five of these galaxies show well-

ordered rotation and have steeper slopes (in dex kpc^{-1}) in metallicity gradient than those of galaxies in the local Universe. In addition, Maciel et al. (2003) measured the abundances of planetary nebulae in the Milky Way (MW) generated by stars spanning a broad age interval and suggested that the MW had steeper metallicity gradients back to $z \sim 1.5$. These results support the so-called "inside-out" growth model of galaxy formation (e.g., Bouwens et al. 1997). In this scenario, the central galactic bulge formed rapidly at early times, building a steep radial metallicity gradient at high redshift. The size of the disk gradually grows with time via gas infall. The metallicity gradient gradually weakens via star formation in the outer disk and radial gas mixing. Such a picture is also seen in some cosmological hydrodynamic simulations (e.g., Pilkington et al. 2012; Gibson et al. 2013), where the metallicity gradients are steepest at high redshift and gradually flatten at late times.

Recently, Leethochawalit et al. (2016) have studied 11 gravitationally lensed galaxies at redshift $z \sim 1.4$–2.5 and found a broad distribution of kinematics and abundance patterns (see also Jones et al. 2015; Wang et al. 2017). Most galaxies in their sample show no features of well-ordered rotation and tend to have flat gas-phase metallicity gradient, in contrast to earlier statements that high-redshift galaxies tend to have stronger metallicity gradients (Jones et al. 2013). Moreover, large samples of non-lensed galaxies at redshift $z \sim 0.6$–3 also show diverse metallicity gradients (e.g., Cresci et al. 2010; Queyrel et al. 2012; Swinbank et al. 2012; Stott et al. 2014; Wuyts et al. 2016), with slope varying from negative to flat and positive. For example, Wuyts et al. (2016) have found that only 15 out of 180 galaxies that have spatially resolved measurements of abundances in a sample of galaxies at $z \sim 0.6$–2.7 show statistically significant non-zero slope of metallicity gradients. These results complicate the simple 'inside-out' growth picture.

Various studies have pointed out the necessity of strong feedback in order to avoid steep metallicity gradients in high-redshift galaxies in cosmological hydrodynamic simulations (e.g., Pilkington et al. 2012; Gibson et al. 2013; Anglés-Alcázar et al. 2014). For example, Gibson et al. (2013) compared two cosmological simulations run with different feedback models and showed that their 'enhanced' feedback model produces constantly flat metallicity gradients at high redshift, whereas their 'conservative' feedback model tends to follow the simple 'inside-out' growth scenario and produce steep metallicity gradients. However, they do not reproduce the diverse range of metallicity gradients in high-redshift galaxies (only one or the other). In

addition, many simulations used empirical feedback models where galactic winds are generated by manually kicking particles and enforcing these wind particles to be temporarily decoupled from hydrodynamics (e.g., Davé et al. 2011b; Torrey et al. 2014; Anglés-Alcázar et al. 2014) or artificially preventing SNe bubbles from cooling for much longer time (e.g., Stinson et al. 2013a). Such models do not properly resolve the launch and propagation of galactic winds from the ISM scale and tend to artificially mix metals on larges scales and prevent strong metallicity gradients from forming.

In this work, we study the origin and evolution of galaxy metallicity gradients using 32 cosmological zoom-in simulations from the Feedback In Realistic Environments project (FIRE; Hopkins et al. 2014)[1]. These simulations include physically motivated models of the multi-phase interstellar medium (ISM), star formation, and stellar feedback, with sufficient spatial and mass resolution down to giant molecular cloud (GMC) scales to explicitly resolve the launch and propagation of galactic winds. This is essential in studying metallicity gradients using simulations. In previous studies, it has been shown that these simulations reproduce many observed scaling relations, such as the stellar mass–halo mass relation, the Kennicutt–Schmidt relation, the star-forming main sequence (Hopkins et al. 2014), and the MZR (Ma et al. 2016a), for a broad range of halo mass and redshift, *without* the need for fine-tuning. These simulations also predict a reasonable covering fraction of neutral absorbers in the circum-galactic medium (CGM) at both low and high redshift (Faucher-Giguère et al. 2015, 2016; Hafen et al. 2017), mass loading factor of galactic outflows (Muratov et al. 2015), and density profiles, kinematics, and chemical abundances of local dwarf galaxies (Oñorbe et al. 2015; Chan et al. 2015), all broadly consistent with observational constraints. All of these demonstrate the validity of using the FIRE simulations to study metallicity gradients.

Almost all galaxies in the FIRE simulations at high redshift ($z > 0.5$) show strong variability (burstiness) in star formation rates (SFRs) on short time-scales of order $10\,\mathrm{Myr}$ (Hopkins et al. 2014; Sparre et al. 2017; Muratov et al. 2015; Feldmann et al. 2017). In these systems, rapid gas inflows trigger starbursts in the galactic center (Torrey et al. 2017). In turn, feedback from newly formed stars injects sufficient energy and momentum into the ISM to destroy the gas disk and launch galactic winds. At lower redshift ($z < 0.5$), on the other hand, massive galaxies ($M_* \gtrsim 10^{10}\,M_\odot$) have calmed down, with star formation in the disk being regulated

---

[1] http://fire.northwestern.edu

by gas infall and feedback to more stable rates (e.g., Faucher-Giguère et al. 2013), and feedback can no longer damage the disk nor drive strong gas outflows (Muratov et al. 2015). This transition is likely due to a combination of decreasing galaxy merger rates (e.g., Hopkins et al. 2010) and decreasing gas fractions in galaxies (e.g., Hayward & Hopkins 2017) at low redshift. In this paper, we show that the FIRE simulations reproduce the diversity of kinematics and metallicity gradients observed in high-redshift galaxies. We also show that bursty star formation can produce the observed diversity – a galaxy may change kinematic properties and metallicity gradient between starburst episodes. This is important for the interpretation of the observed metallicity gradients in high-redshift galaxies.

The paper is organized as follows. We start by introducing the simulations and describing the methods to measure kinematic properties and gas-phase metallicity gradient in the simulated galaxies in Section 3.2. We present the main results in Section 3.3 and discuss and conclude in Section 3.4.

We adopt a standard flat ΛCDM cosmology with cosmological parameters $H_0 = 70.2 \, \mathrm{km \, s^{-1} \, Mpc^{-1}}$, $\Omega_\Lambda = 0.728$, $\Omega_m = 1 - \Omega_\Lambda = 0.272$, $\Omega_b = 0.0455$, $\sigma_8 = 0.807$ and $n = 0.961$, broadly consistent with observations (e.g., Hinshaw et al. 2013; Planck Collaboration et al. 2014).

3.2 Methodology

3.2.1 Simulation Details

In this work, we use a suite of simulations from the FIRE project that have been presented in previous studies (Hopkins et al. 2014; Faucher-Giguère et al. 2015; Chan et al. 2015; Feldmann et al. 2016; Hafen et al. 2017). These are cosmological "zoom-in" simulations that are run using GIZMO (Hopkins 2015) in P-SPH mode (Hopkins 2013). Because of computational expense, some of them are only run to $z = 2$, and span a halo mass 10^{11}–$10^{13} \, \mathrm{M_\odot}$ at that redshift. For those that are run to $z = 0$, we only include the ones above $z = 0$ halo mass $10^{11} \, \mathrm{M_\odot}$ in this study, since smaller galaxies lack observational probes at high redshift. All the simulations used in this paper, along with the mass of the most massive halo in the zoom-in region, the initial mass of baryonic and dark matter particles, minimum force softening lengths, and the reference where the simulation is first presented, are listed in Tables 3.1 and 3.2. We briefly summarize the physical models below for completeness, but refer to Hopkins et al. (2014, and references therein) for more detailed description.

In our simulations, gas follows an molecular-atomic-ionized cooling curve from

Table 3.1: Simulation analyzed in the chapter.

Name	M_{halo} ($z = 0$) (M$_\odot$)	M_{halo} ($z = 2$) (M$_\odot$)	m_b (M$_\odot$)	ϵ_b (pc)	m_{dm} (M$_\odot$)	ϵ_{dm} (pc)	Reference
m11	1.4e11	3.8e10	7.1e3	7.0	3.5e4	70	(1)
m12v	6.3e11	2.0e11	3.9e4	10	2.0e5	140	(1)
m12q	1.2e12	5.1e11	7.1e3	10	2.8e5	140	(1)
m12i	1.1e12	2.7e11	5.0e4	14	2.8e5	140	(1)
m13	6.0e12	8.4e11	3.6e5	21	2.2e6	210	(1)
m11h383	1.6e11	4.1e9	1.7e4	10	8.3e4	100	(2)
m11.4a	2.6e11	8.9e10	3.3e4	9	1.7e5	140	(3)
m11.9a	8.4e11	1.3e11	3.4e4	9	1.7e5	140	(3)
MFz0_A2	1.0e13	2.2e12	3.0e5	9	1.4e6	140	(3)
z2h350	–	7.9e11	5.9e4	9	2.9e5	143	(4)
z2h400	–	7.9e11	5.9e4	9	2.9e5	143	(4)
z2h450	–	8.7e11	5.9e4	9	2.9e5	143	(4)
z2h506	–	1.2e12	5.9e4	9	2.9e5	143	(4)
z2h550	–	1.9e11	5.9e4	9	2.9e5	143	(4)
z2h600	–	6.7e11	5.9e4	9	2.9e5	143	(4)
z2h650	–	4.0e11	5.9e4	9	2.9e5	143	(4)
z2h830	–	5.4e11	5.9e4	9	2.9e5	143	(4)

Parameters describing the initial conditions for our simulations (units are physical):
(1) Name: Simulation designation.
(2) M_{halo}: Approximate mass of the main halo (most massive halo), at $z = 0$ and $z = 2$.
(3) m_b: Initial baryonic (gas and star) particle mass in the high-resolution region.
(4) ϵ_b: Minimum baryonic Plummer-equivalent force softening (minimum SPH smoothing lengths are comparable or smaller). Force softening is adaptive (mass resolution is fixed).
(5) m_{dm}: Dark matter particle mass in the high-resolution region.
(6) ϵ_{dm}: Minimum dark matter Plummer-equivalent force softening (fixed in physical units at all redshifts).
(7) Reference: Where the simulation is first presented. (1) Hopkins et al. (2014), (2) Chan et al. (2015), (3) Hafen et al. (2017), (4) Faucher-Giguère et al. (2015), and (5) Feldmann et al. (2016).
Note: Detailed physical properties of these galaxies are presented in Appendix.

Table 3.2: Simulation analyzed in the chapter – continued.

Name	M_{halo} ($z = 0$) (M$_\odot$)	M_{halo} ($z = 2$) (M$_\odot$)	m_b (M$_\odot$)	ϵ_b (pc)	m_{dm} (M$_\odot$)	ϵ_{dm} (pc)	Reference
A1:0	–	2.3e12	3.3e4	10	1.7e5	143	(5)
A2:0	–	2.9e12	3.3e4	10	1.7e5	143	(5)
A3:0	–	2.4e12	3.3e4	10	1.7e5	143	(5)
A4:0	–	2.8e12	3.3e4	10	1.7e5	143	(5)
A5:0	–	2.3e12	3.3e4	10	1.7e5	143	(5)
A6:0	–	2.6e12	3.3e4	10	1.7e5	143	(5)
A7:0	–	2.5e12	3.3e4	10	1.7e5	143	(5)
A8:0	–	3.5e12	3.3e4	10	1.7e5	143	(5)
A9:0	–	2.8e12	3.3e4	10	1.7e5	143	(5)
A10:0	–	3.2e12	3.3e4	10	1.7e5	143	(5)
B1:0	–	8.3e12	3.3e4	10	1.7e5	143	(5)
B2:0	–	9.0e12	3.3e4	10	1.7e5	143	(5)
B3:0	–	9.7e12	3.3e4	10	1.7e5	143	(5)
B4:0	–	8.5e12	3.3e4	10	1.7e5	143	(5)
B5:0	–	9.1e12	3.3e4	10	1.7e5	143	(5)

10–10^{10} K, including metallicity-dependent fine-structure and molecular cooling at low temperatures and high-temperature metal-line cooling followed species-by-species for 11 separately tracked species (H, He, C, N, O, Ne, Mg, Si, S, Ca, and Fe; see Wiersma et al. 2009a). At each timestep, the ionization states and cooling rates are determined following Katz et al. (1996) for primordial abundances and from a compilation of CLOUDY runs for metals, including a uniform but redshift-dependent photo-ionizing background tabulated in Faucher-Giguère et al. (2009), and photo-ionizing and photo-electric heating from local sources. Gas self-shielding is accounted for with a local Jeans-length approximation.

We allow star formation to take place only in dense, molecular, and self-gravitating regions with hydrogen number density above a threshold $n_{th} = 5$–$50\,\text{cm}^{-3}$ (Hopkins et al. 2013b). Stars form at 100% efficiency per local free-fall time when the gas meets these criteria and there is no star formation elsewhere. A star particle inherits the metallicity of each tracked species from its parent gas particle. Every star particle is treated as a single stellar population with known mass, age, and metallicity, assuming a Kroupa (2002) initial mass function (IMF) from 0.1–100 M$_\odot$. Then the ionizing photon budgets, luminosities, Type II supernova rates, mechanical luminosities of stellar winds, etc., are directly tabulated from the stellar population models in STARBURST99 (Leitherer et al. 1999). The Type Ia SN rates follow the

time delay distribution from Mannucci et al. (2006). We account for the following stellar feedback mechanisms, including (1) local and long-range momentum flux from radiative pressure, (2) energy, momentum, mass and metal injection from SNe and stellar winds, and (3) photo-ionization and photo-electric heating. We follow Wiersma et al. (2009b) and account for metal production from Type-II SNe, Type-Ia SNe, and stellar winds using the metal yields in Woosley & Weaver (1995), Iwamoto et al. (1999), and Izzard et al. (2004), respectively. We do not include a sub-resolution metal diffusion model, but the simulations explicitly resolve the metal mixing by advection of gas particles.

3.2.2 Galaxy Identification and Definitions

We use Amiga's Halo Finder (AHF; Knollmann & Knebe 2009) to identify halos in the simulations. The approximate halo mass at $z = 2$ and $z = 0$ (if applicable) for the most massive (best-resolved) halo in each simulation are listed in Tables 3.1 and 3.2, where we adopt the redshift-dependent virial parameter from Bryan & Norman (1998). In this paper, we only study the central galaxy in the most massive halo in each simulation. The entire simulated sample is only studied at four redshifts $z = 2$, 1.4, 0.8, and 0 (if applicable). The physical properties of these galaxies (as described below) at these redshifts are presented in Appendix.

We define the center of each galaxy by iteratively finding the geometric center of all star particles within a sphere of decreasing radius from 20 kpc to 1 kpc. This generally corresponds closely to the location of maximum stellar mass density. The stellar mass (M_*) and the star formation rate (SFR) for the central galaxy are measured within 10 kpc from this center, where we remove the contamination of satellite galaxies if necessary. The SFRs are averaged over 200 Myr to mimic the observational measurements based on far-ultraviolet luminosity (e.g., Sparre et al. 2017). Next, we define a characteristic radius R_{90}, which encloses 90% of the star formation within 10 kpc. Such definition of galactic center and characteristic radius appears to be most numerically stable, given that a considerable fraction of galaxies in our simulated sample have clumpy and irregular morphologies (especially those at high redshifts). The stellar mass, SFR, and R_{90} for the entire simulated sample are listed in the Appendix. Our sample covers a stellar mass range 10^8–10^{11} $M_\odot$.

For simplicity, we define the z-axis to be aligned with the total angular momentum of all gas particles within R_{90} and the x-axis to be an arbitrary direction perpendicular to z-axis. We refer to face-on and edge-on views when observing along the z- and
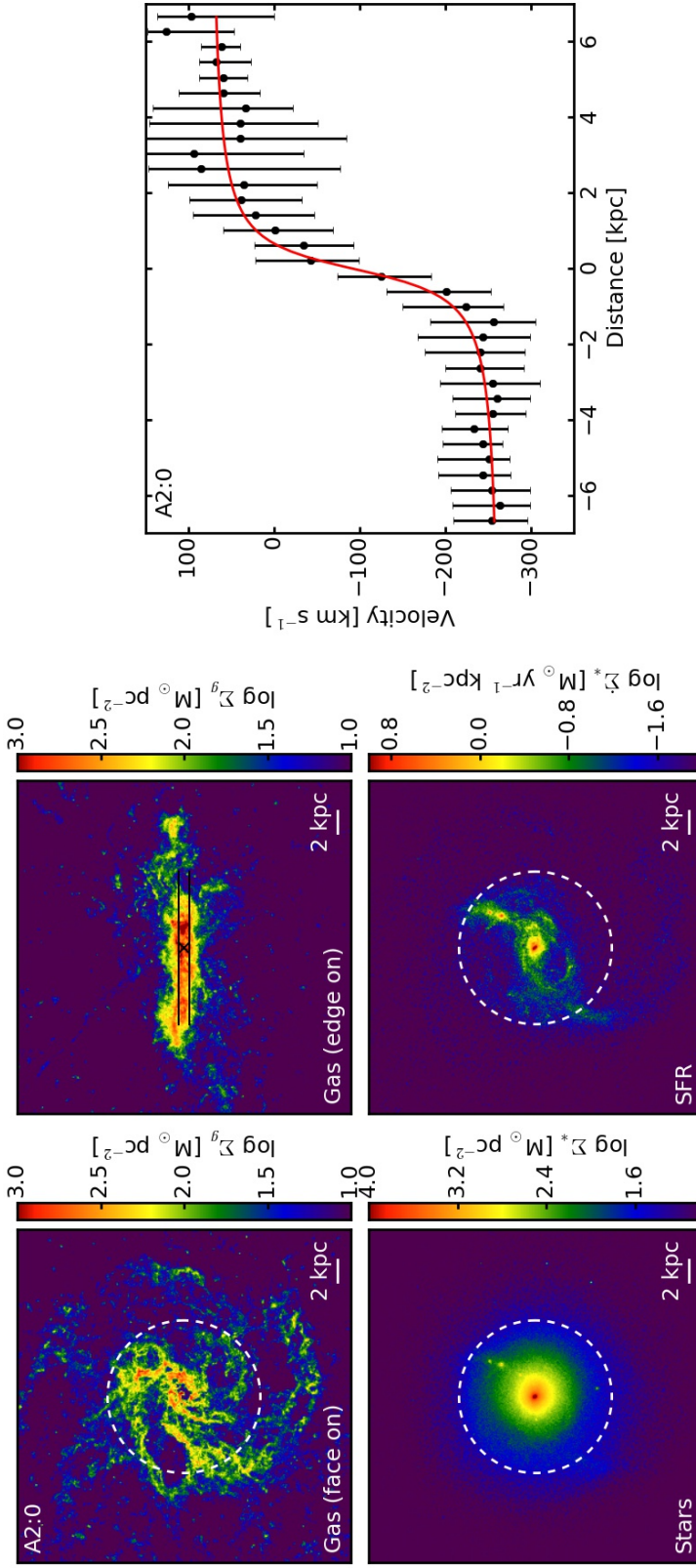
Figure 3.1: *Left:* Example images from our simulated sample, including face-on gas surface density (upper left), edge-on gas surface density (upper right), stellar surface density (lower left), and star formation surface density (lower right). We show A2:0 (top) and A8:0 (middle) at $z = 2$ and m12i (bottom) at $z = 0$ (see Tables 3.1 and 3.2 for details). The white circles show R_{90} as defined in Section 3.2.3. The black lines on the edge-on gas images show the long slits where we extract the gas velocity curve. *Right:* Velocity curve extracted from the slit. The symbols and errorbars show the line-of-sight velocity and velocity dispersion, respectively. The red lines show the best fit from the arctan function given by Equation (3.1). A2:0 and m12i have well-ordered rotating disk, while A8:0 is a merging system with no evidence of rotation.
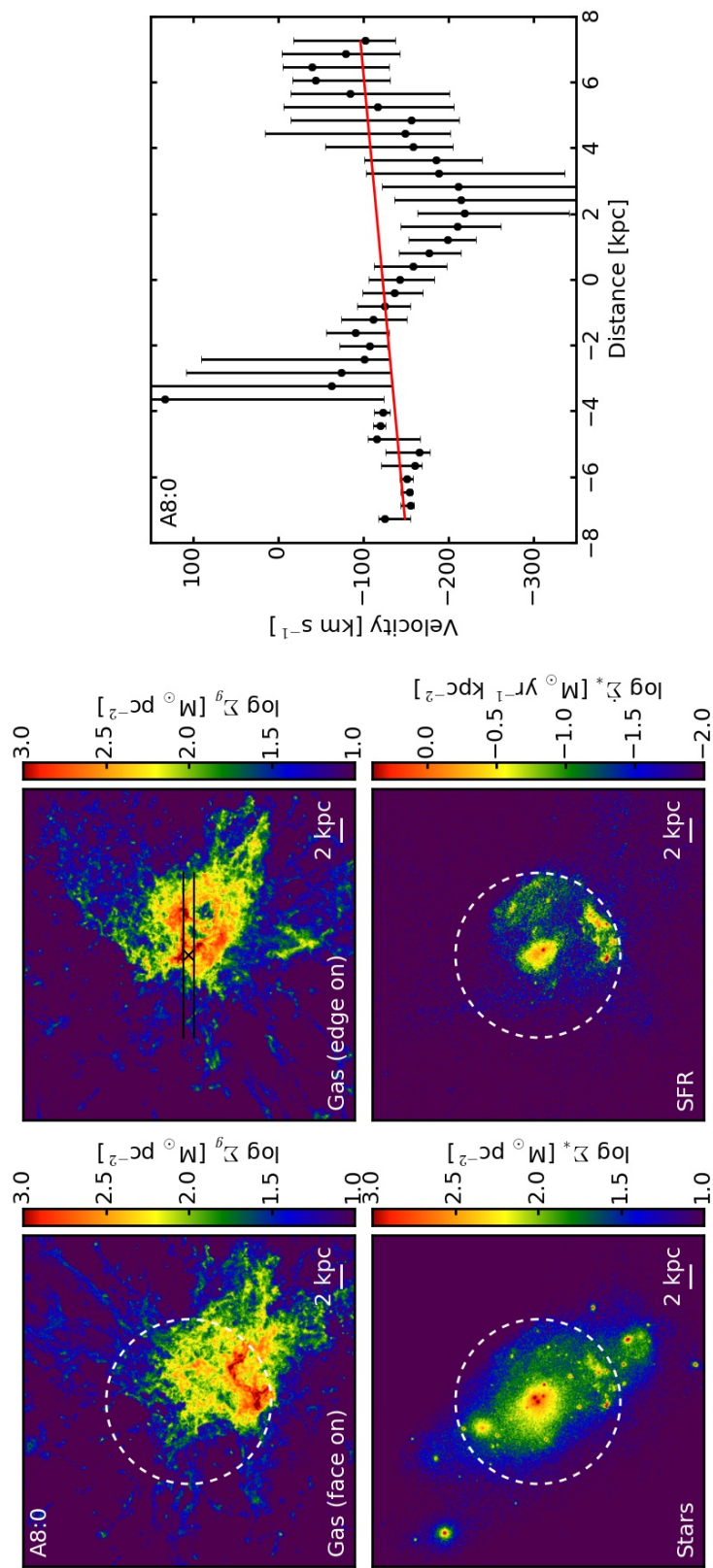
Figure 3.2: Figure 3.1 – continued.
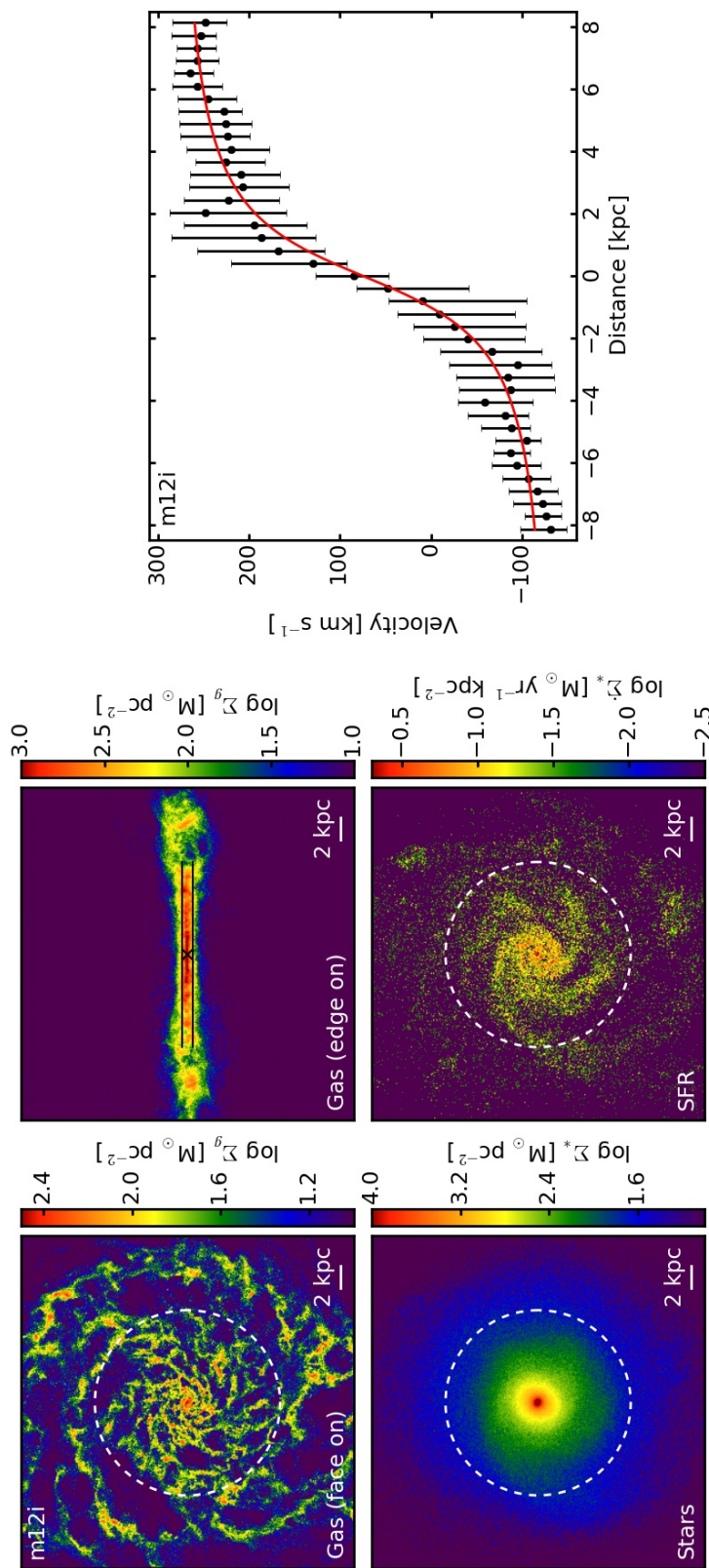
Figure 3.3: Figure 3.1 – continued.

x-axis, respectively. In Figs. 3.1–3.3 (left two columns), we show example images for three galaxies in our sample, A2:0 at $z = 2$ (top), A8:0 at $z = 2$ (middle), and m12i at $z = 0$ (bottom). For each galaxy, we show a face-on gas image (*x-y* plane, top left) and edge-on gas image (*y-z* plane, top right), face-on stellar image (bottom left), and face-on SFR map (bottom right, averaged over 200 Myr). The dashed white circles on all face-on images show the characteristic R_{90} of each galaxy. A8:0 is a merging system that has clumpy, irregular morphology, while A2:0 and m12i have star-forming gas disks.

3.2.3 Kinematics

Before we present the gas-phase metallicity gradients for our simulated sample, we first measure the kinematic properties of these galaxies, as commonly done in observational studies (e.g., Yuan et al. 2011; Jones et al. 2013; Leethochawalit et al. 2016). We do so by mimicking the widely-used long-slit spectroscopy technique. The mock slit is placed along the *y*-axis (edge-on) along the mid-plane with a vertical width of 1 kpc, as illustrated by the black lines on the edge-on gas images in Fig. 3.1. We then extract the one-dimensional velocity curve along the slit. We measure the line-of-sight gas velocity and 1σ velocity dispersion in the range $-R_{90} < y < R_{90}$ with a spatial resolution of $\Delta y = 0.4$ kpc, by taking into account all gas particles with number density $n > 1\,\mathrm{cm}^{-3}$ in every pixel. This allows us to primarily select interstellar gas and eliminate contamination by foreground/background gas in the circumgalactic/intergalactic medium. Example velocity curves of the three galaxies, A2:0, A8:0 (at $z = 2$), and m12i (at $z = 0$), are shown in the right column of Figs. 3.1–3.3, with the black points and errorbars representing the line-of-sight velocity and velocity dispersion along the slit.

We fit the one-dimensional velocity curve with the following analytic form

$$V(R) = V_0 + V_c \frac{2}{\pi} \arctan\left(\frac{R}{R_t}\right), \tag{3.1}$$

as motivated by the simple disk model commonly adopted in various studies (e.g., Jones et al. 2010; Swinbank et al. 2012; Stott et al. 2014; Leethochawalit et al. 2016). For our simulated galaxies, V_0 accounts for the peculiar velocity in the simulation box and V_c gives the asymptotic circular velocity at large radii. Example fits for the three galaxies are shown by the red lines in Fig. 3.1. The velocity curves of A2:0 and m12i can be well described by the arctan function, reaffirming that these galaxies have well-ordered rotating disks. However, the chaotic system, A8:0, returns a bad fit (as reflected by unphysical values of V_c). We have visually checked all of
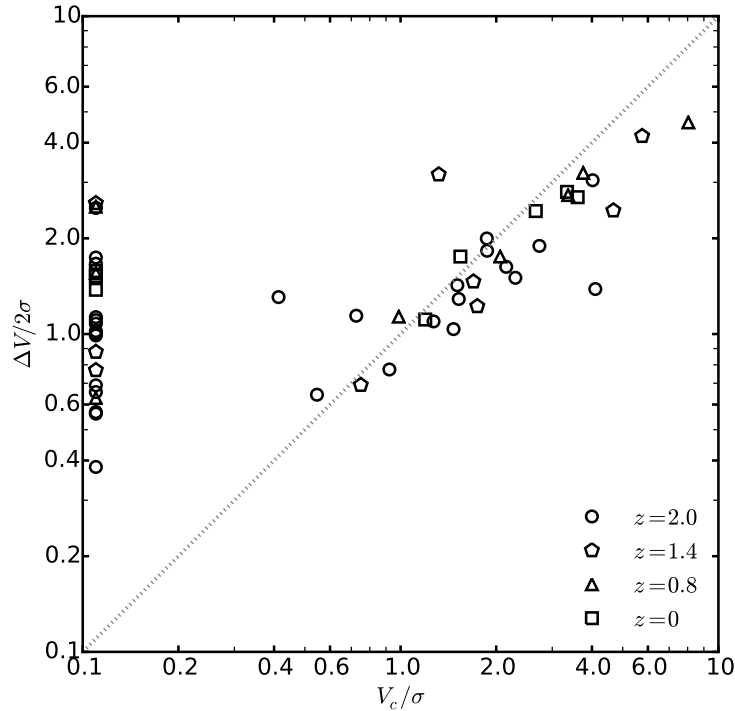
Figure 3.4: Comparison between V_c/σ and $\Delta V/2\sigma$ for our simulated galaxies. V_c is the rotation velocity given by the best fit of the velocity curve by the arctan function in Equation (3.1), while ΔV is the peak-to-peak velocity difference. σ is the maximum velocity dispersion (see Figures 3.1–3.3 for examples). Galaxies that cannot be well fitted by an arctan function are plotted at $V_c/\sigma \sim 0.1$. V_c/σ and $\Delta V/2\sigma$ are broadly consistent with each other for galaxies with $V_c/\sigma \geq 1$, indicating that they have well-ordered rotation by either criterion. However, galaxies with $V_c/\sigma < 1$ show $\Delta V/2\sigma \sim 0.4$–3. This suggests that $\Delta V/2\sigma$ is ambiguous for non-rotationally supported systems.

our simulations and find that bad fits occur when a galaxy has clumpy, irregular morphology and shows little evidence of rotation. For these galaxies, V_c cannot be properly defined. We also follow Leethochawalit et al. (2016) and measure the "peak-to-peak" velocity difference ΔV along the slit. Any galaxy can give a finite ΔV despite its kinematic properties. For a rotating disk, ΔV equals $2V_c$ in the asymptotic limit and is thus a proxy for the rotation velocity. We define the velocity dispersion of the galaxy σ as the maximum velocity dispersion along the slit. V_c, ΔV, and σ for the entire simulated sample are presented in Appendix. Note that some galaxies in our sample are temporarily quenched, with little gas in the central region. The kinematic properties for these galaxies cannot be properly determined.

The degree of rotational support of a galaxy can be defined as either V_c/σ or

$\Delta V/2\sigma$. In Fig. 3.4, we compare V_c/σ and $\Delta V/2\sigma$ for our simulated galaxies. For illustrative purposes, we plot those whose velocity curve cannot be well fitted by Equation 3.1 at $V_c/\sigma \sim 0.1$, as they do not have well-ordered rotation. The criterion for rotationally supported system is commonly taken to be $V_c/\sigma \geq 1$ or $\Delta V/2\sigma \geq 0.4$ (e.g., Förster Schreiber et al. 2009; Leethochawalit et al. 2016). Most of our simulated galaxies with $V_c/\sigma \geq 1$ have consistent values of $\Delta V/2\sigma$, reaffirming that these galaxies are rotationally supported. However, galaxies with $V_c/\sigma < 1$ span a wide range of $\Delta V/2\sigma$, mostly from 0.4–3 for our simulated sample. These galaxies have little evidence of rotation as shown by the velocity curve and confirmed by our visual inspection, but they would be classified as rotating systems by the criterion $\Delta V/2\sigma \geq 0.4$. We caution that $\Delta V/2\sigma$ is an ambiguous indicator in practice, especially for those galaxies with little rotation.

3.2.4 Metallicity Gradients

We now present the metallicity gradients for our simulated sample. In the top panel of Fig. 3.5, we show the face-on metallicity map for the same galaxies as in Figs. 3.1–3.3, with a pixel size of 100 pc. We measure the mass-weighted metallicity of all gas particles in each pixel. We only show pixels where the gas surface density is above $\Sigma_g \geq 10\,\mathrm{M}_\odot\,\mathrm{pc}^{-2}$. Such threshold is roughly the surface density above which fragmentation and star formation occurs in these simulations and observations (Orr et al. 2017), so these pixels are likely to have observationally detectable nebular emission lines. This also reduces the shot noise from low surface density pixels where the metallicities are determined by individual gas particles. In the bottom panels, we plot the gas-phase metallicity as a function of projected radius for individual pixels (grey points). Again, only pixels above surface density $10\,\mathrm{M}_\odot\,\mathrm{pc}^{-2}$ are shown. We measure the median metallicity and its 1σ dispersion at every 0.2 kpc in a certain radius interval, as illustrated by the red points and errorbars (in 0.25–$1R_{90}$, our fiducial interval) in Fig. 3.5. We require a minimum number of 20 pixels in a 0.2 kpc bin to obtain a reliable measurement at this radius. We fit the metallicity profile with a linear function (the blue dotted lines in Fig. 3.5)

$$\log(Z/Z_\odot) = \alpha R + \beta, \tag{3.2}$$

to obtain the slope of the metallicity gradient α (in dex kpc^{-1}).

Equation 3.2 is motivated by the fact that metallicity gradients are most commonly measured in $\mathrm{d}\log Z/\mathrm{d}R$ (in dex kpc^{-1}) in the literature, although the metallicity profile of a galaxy may deviate from a linear function in reality. In Fig. 3.6,
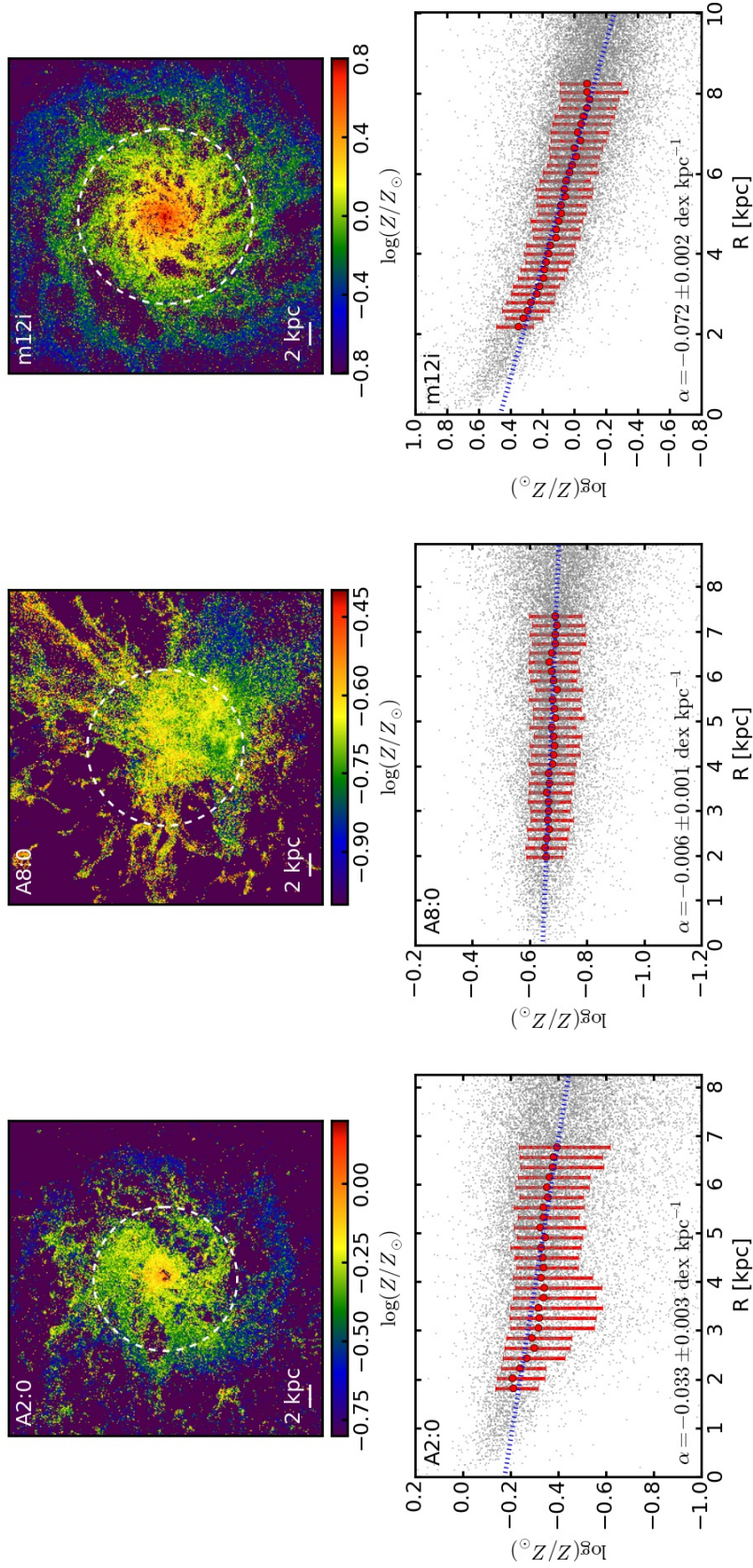
Figure 3.5: *Top:* Face-on gas-phase metallicity map for the three example galaxies in Figs. 3.1–3.3. *Bottom:* Metallicity profile. The grey points show individual pixels, and the red points and errorbars show the median and 1σ dispersion of metallicity at every 0.2 kpc in $0.25-1R_{90}$. The blue lines show the best linear fit $\log(Z/Z_{\odot}) = \alpha R + \beta$, where α gives the slope of metallicity gradient in dex kpc^{-1}.
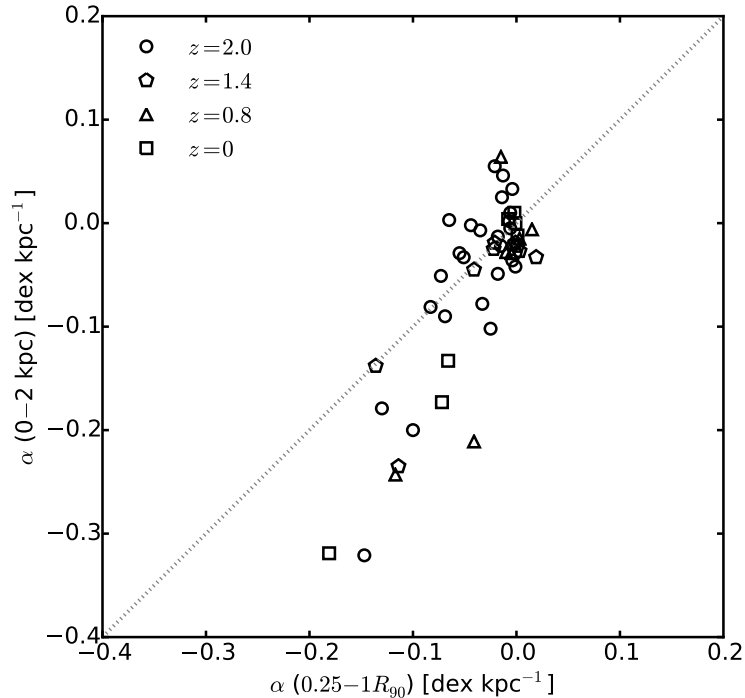
Figure 3.6: Metallicity gradients measured in the radial interval 0.25–1R_{90} vs. metallicity gradients measured in the central 0–2 kpc. The difference is small when the gradient is flat, because the gas-phase metallicity is almost uniform in the ISM (e.g., simulation A8:0). On the other hand, the slopes measured over 0–2 kpc are much steeper than those measured over 0.25–1R_{90} in galaxies that show strong negative metallicity gradients (e.g., simulations A2:0 and m12i shown in Figs. 3.1, 3.3, and 3.5). They show rapidly increasing metallicity profiles toward the galactic center.

we compare the slopes of the metallicity gradients measured over 0.25–1R_{90} and over 0–2 kpc, respectively. Both slopes are qualitatively consistent with each other. The difference is small when the gradient is close to flat, because the metals are nearly uniformly mixed within the ISM (e.g., simulation A8:0). On the other hand, galaxies with strong negative metallicity gradients tend to have a rapidly increasing metallicity profile toward the center (e.g., simulations A2:0 and m12i in Figs. 3.1, 3.3 and 3.5), as reflected by the fact that the slopes measured in 0–2 kpc are much steeper than those measured in 0.25–1R_{90}. This happens in our simulations because the galactic centers can reach very high gas surface densities ($\Sigma_g \gtrsim 10^3 \, \mathrm{M_\odot \, pc^{-2}}$) during a starburst, and the star formation efficiency may increase dramatically with gas surface density (e.g., Burkert & Hartmann 2013; Torrey et al. 2017; Grudić et al. 2016), resulting in rapid metal enrichment toward the center. Such a picture

is consistent with previous studies on the formation of cusp elliptical galaxies via mergers (e.g., Hopkins et al. 2009), which reproduce the observed steep metallicity gradients in the central region of early-type galaxies (e.g., Reda et al. 2007; Sánchez-Blázquez et al. 2007). In this work, we primarily focus on the metallicity gradients measured over 0.25–$1 R_{90}$. The slopes of metallicity gradient for the entire simulated sample are listed in Appendix. We note that all of our results presented below are qualitatively consistent if one uses the gradients measured in 0–$2\,\text{kpc}$. A detailed discussion on the full metallicity profile is beyond the scope of this study, but worth further investigations in future work.

3.3 Results

3.3.1 Metallicity gradients: general properties

As illustrated by the visual examples in Fig. 3.5 and more quantitative results shown in Appendix, our simulations produce a variety of kinematic properties and metallicity distributions. Simulations A2:0 and m12i have obvious negative metallicity gradients, with the center being more metal-enriched than the outskirts, consistent with the observed metallicity patterns in local and some high-redshift galaxies (e.g., Zaritsky et al. 1994; van Zee et al. 1998; Yuan et al. 2011; Jones et al. 2013; Sánchez et al. 2014). Both of them have a rotationally supported, star-forming disk as shown in Fig. 3.1. In contrast, simulation A8:0 is a merging system that has a clumpy, irregular gas morphology with no well-ordered gas motion, and a relatively uniform metallicity distribution, with metallicity gradient close to flat. Intuitively, these examples indicate that strong negative metallicity gradients are more likely to occur in galaxies with a rotating disk, while strongly perturbed galaxies tend to have flat gradients.

Strong perturbations, mostly induced by mergers, rapid gas infall, and strong outflows, can stir the gas and drive galactic-scale motion in the ISM, with typical velocities up to several hundred $\text{km}\,\text{s}^{-1}$. This causes gas/metal re-distribution on galactic scales of $\lesssim 10\,\text{kpc}$ on relatively short time-scales ~ 10–$50\,\text{Myr}$, leading to kinematically hot gas motion and flat metallicity gradients[2]. In simulation A8:0, the perturbation is induced by a series of minor mergers (see Fig. 3.2). Besides, strong stellar feedback can also drive galaxy-scale motion in the ISM, resulting in irregular gas motion and morphology (e.g., Agertz & Kravtsov 2016). Gibson et al. (2013)

---

[2]Here we do not consider metal mixing on scales below our resolution limit, but rather focus on re-distribution of metals driven by largest-scale motion. This is justified by more detailed studies of diffusion processes in supersonically turbulent media like the ISM, which show that diffusion is most efficient on large scales (e.g., Colbrook et al. 2017).
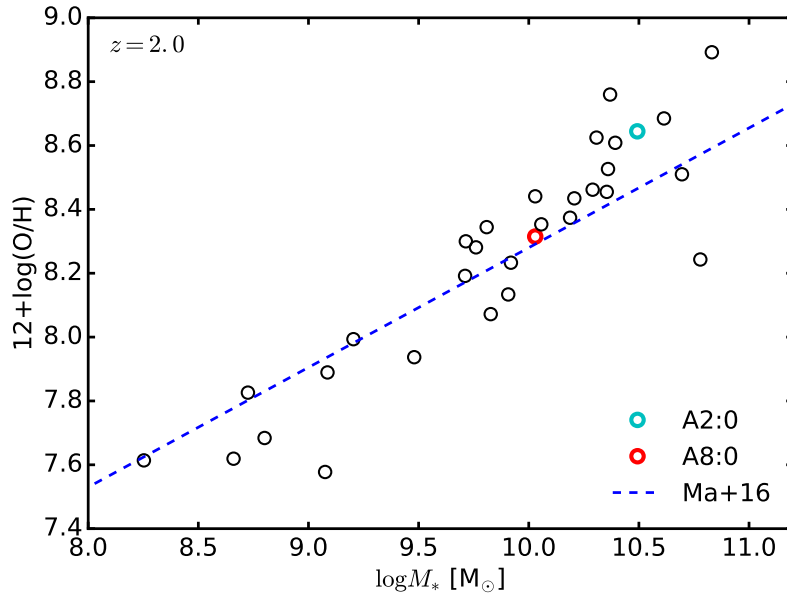
Figure 3.7: Gas-phase oxygen abundance vs. stellar mass for our simulated sample at $z = 2$. Galaxies A2:0 and A8:0 (see also Figs. 3.1, 3.2 and 3.5) are indicated by the thick cyan and red circles, respectively. The simulations analyzed in this work cover a stellar mass range 10^8–$10^{11}\,\mathrm{M_\odot}$. The blue dashed line shows the fit from Ma et al. (2016a), which is derived from a sample covering a stellar mass range 10^4–$10^{10}\,\mathrm{M_\odot}$ at this redshift.

show that simulations with strong feedback produce flat metallicity gradients, while those with weak feedback tend to produce steep gradients. The high resolution and physically motivated models of stellar feedback adopted in the FIRE simulations enable us to explicitly resolve the launch and propagation of galactic winds from small scales (tens of pc) to galactic scales, which is essential to study gas-phase metallicity gradients.

The rest of this section is organized as follows. Before going into details about metallicity gradients in our simulated galaxies, we first show where our sample lies on the galaxy MZR in Section 3.3.2. In Section 3.3.3, we will study the dependence of metallicity gradient on stellar mass and specific star formation rate (sSFR). In Section 3.3.4, we will examine the relation between metallicity gradient and the degree of rotational support. In Section 3.3.5, we will present the redshift dependence on metallicity gradient. In Section 3.3.6, we will perform a case study on simulation m12i and explore how stellar feedback can change metallicity gradients on short time-scales ($\lesssim$ Gyr), which has a great effect on the interpretations of the observed metallicity gradients in high-redshift galaxies.

3.3.2 The mass-metallicity relation (MZR)

We follow Ma et al. (2016a) and define the gas-phase metallicity as mass-weighted mean metallicity of all gas particles below 10^4 K in the central galaxy (satellites excluded). In Fig. 3.7, we show the gas-phase MZR for our simulated sample at $z = 2$, where we define the oxygen abundance as $12 + \log(\text{O/H}) = \log(Z/Z_\odot) + 9.0$. Galaxies A2:0 and A8:0 shown in Figs. 3.1 and 3.5 are indicated with thick cyan and red circles, respectively. They have typical gas-phase metallicities for our sample. In Ma et al. (2016a), we extensively studied the MZR in a sample of FIRE simulated galaxies at $z = 1.4$, 0.8, and 0. In that work, we showed that m12i lies on the observed median gas-phase and stellar MZR from Tremonti et al. (2004) and Gallazzi et al. (2005) at $z = 0$. The blue dashed line shows the linear fit to the simulations from Ma et al. (2016a). We note that Ma et al. (2016a) used a sample that covered the stellar mass range from 10^4–10^{10} M$_\odot$ at $z = 2$, while the new simulations from Feldmann et al. (2016) included in this work allow us to extend our analysis to 10^{11} M$_\odot$.

3.3.3 Metallicity gradient vs stellar mass and sSFR

We start by examining the correlation between gas-phase metallicity gradient (measured over 0.25–1R_{90}) and galaxy properties. In Fig. 3.8, we show the dependence of metallicity gradient on stellar mass (left) and specific star formation rate (sSFR, right) for the simulated sample at four redshifts $z = 2.0$, 1.4, 0.8, and 0. We do not find significant differences between redshifts except perhaps for massive galaxies at $z \sim 0$, consistent with recent observations (e.g., Wuyts et al. 2016). The shaded regions show 2σ linear fits to the simulated data. We find a weak anti-correlation between metallicity gradient and stellar mass. Low-mass galaxies tend to have flat gradients, because feedback is very efficient in driving outflows and thus mixing metals in low-mass systems (Muratov et al. 2015, 2017). Note that the FIRE project also includes simulations of isolated dwarf galaxies with stellar masses M$_*$ $\sim$ 10^4–10^8 M$_\odot$ (e.g., Hopkins et al. 2014; Chan et al. 2015), but we do not consider these dwarfs in this work, because observations probe only galaxies more massive than 10^9 M$_\odot$. Nevertheless, they also have very weak (flat) metallicity gradients (El-Badry et al. 2016), because they are bursty, feedback-dominated galaxies, consistent with the argument above. We also find a weak correlation between metallicity and sSFR. Most galaxies with high sSFR have undergone rapid gas inflows that trigger starbursts, and feedback in turn drives strong outflows. Such violent gas infall and outflows can stir the gas in the ISM and mix metals on galactic scales efficiently,
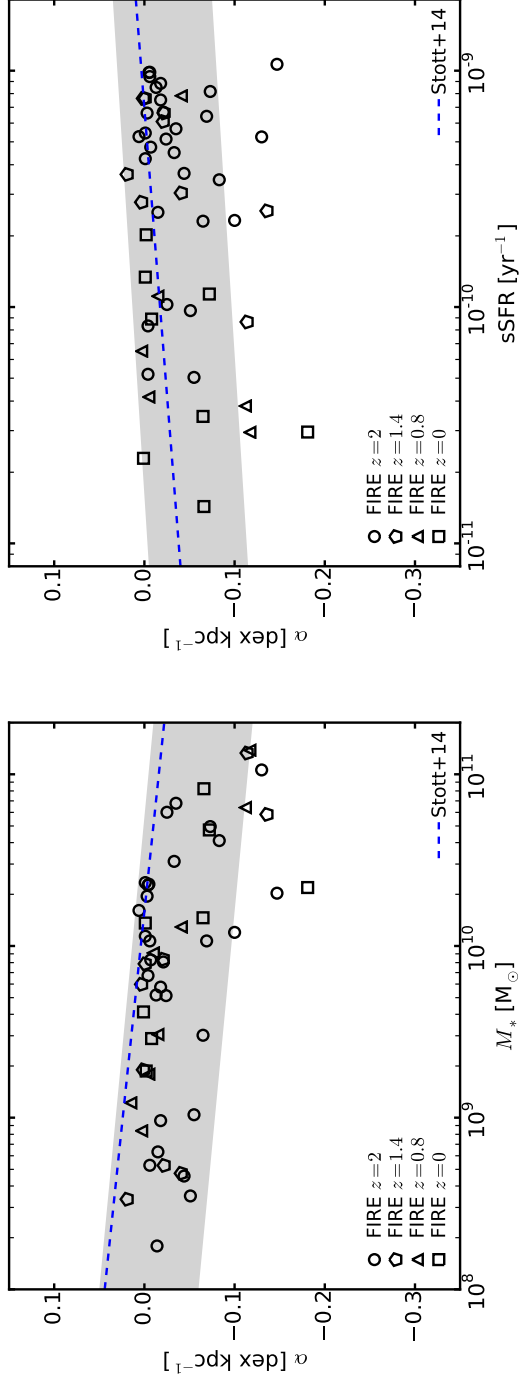
Figure 3.8: *Left:* Metallicity gradient (measured over 0.25–1R_{90}) *vs.* stellar mass. *Right:* Metallicity gradient vs sSFR. The shaded regions show the 2σ interval of the linear fit to the simulated data. The blue dashed lines show the linear fit to a compilation of observational data at $z = 0$–2.5 from Stott et al. (2014). There is weak dependence of metallicity gradient on both stellar mass and sSFR. Low-mass galaxies or those with high sSFR tend to have flat metallicity gradients, due to the fact that feedback is more efficient in such galaxies.

resulting in a flat metallicity gradient. In Fig. 3.8, we also show the linear fits to a compilation of observational data at redshifts $z = 0$–2.5 from Stott et al. (2014, blue dashed lines). These trends are in qualitative agreement with our simulations, but we note that both observations and our simulations only show weak trends with stellar mass and sSFR (within 3σ, the data are consistent with no trend).

3.3.4 Metallicity gradient vs kinematic properties

In the left panel of Fig. 3.9, we show the relation between gas-phase metallicity gradient (measured over 0.25–$1R_{90}$) and degree of rotational support, V_c/σ, for the entire simulated sample. Again, galaxies whose V_c cannot be properly determined are plotted at $V_c/\sigma \sim 0.1$. In general, our simulated sample can be divided into three populations that occupy three different regions on the α–V_c/σ diagram: (1) significant negative metallicity gradients *only* occur in galaxies with rotationally supported disks ($V_c/\sigma \geq 1$), (2) strongly perturbed galaxies, with no evidence of rotation ($V_c/\sigma < 1$, including those with undetermined V_c), tend to have flat metallicity gradients, and (3) there is also a population that show flat or mildly positive metallicity gradients ($\alpha \sim 0$) while being rotationally supported ($V_c/\sigma \geq 1$). The existence of population (3) reflects the observed complex relation between metallicity gradient and galaxy kinematics (e.g., Jones et al. 2015; Leethochawalit et al. 2016). We emphasize that our sample only predicts that galaxies with a strong negative metallicity gradient *must* be rotationally supported, but *not* vice versa. We do *not* find any galaxy in our simulated sample that has a significant negative metallicity gradient ($\alpha < -0.05$ dex kpc^{-1}) but is strongly perturbed ($V_c/\sigma < 1$).

The connection between negative metallicity gradients and rotating disks can be understood from the coevolution of the gas disk and stellar disk (e.g., Ho et al. 2015). A simple toy model is useful for illustrative purposes. Start from a pristine gas disk with an exponential surface density profile $\Sigma_g \sim \exp(-R/R_d)$, where R_d is the disk scale length. Stars form in the disk at higher efficiencies in regions with higher surface densities, following the Kennicutt–Schmidt law $\dot{\Sigma}_* \sim \Sigma_g^{1.4} \sim \exp(-1.4R/R_d)$ (Kennicutt 1998). If the metals do not mix efficiently between annuli (i.e., the local 'closed-box' assumption), the gas-phase metallicity is $Z_g \sim -\ln(1 - f_*)$, where f_* is the mass fraction of stars (note that both f_* and Z_g are functions of radius). If the gas fraction is not too low, $Z_g \sim f_* \sim \Sigma_*/\Sigma \sim \dot{\Sigma}_* t/\Sigma \sim \exp(-0.4R/R_d)$. This naturally gives a negative metallicity gradient $\mathrm{d}\log Z_g/\mathrm{d}R = -0.17/R_d$ dex kpc^{-1} (if R_d is in kpc), although the slope can be altered by the exact disk surface density
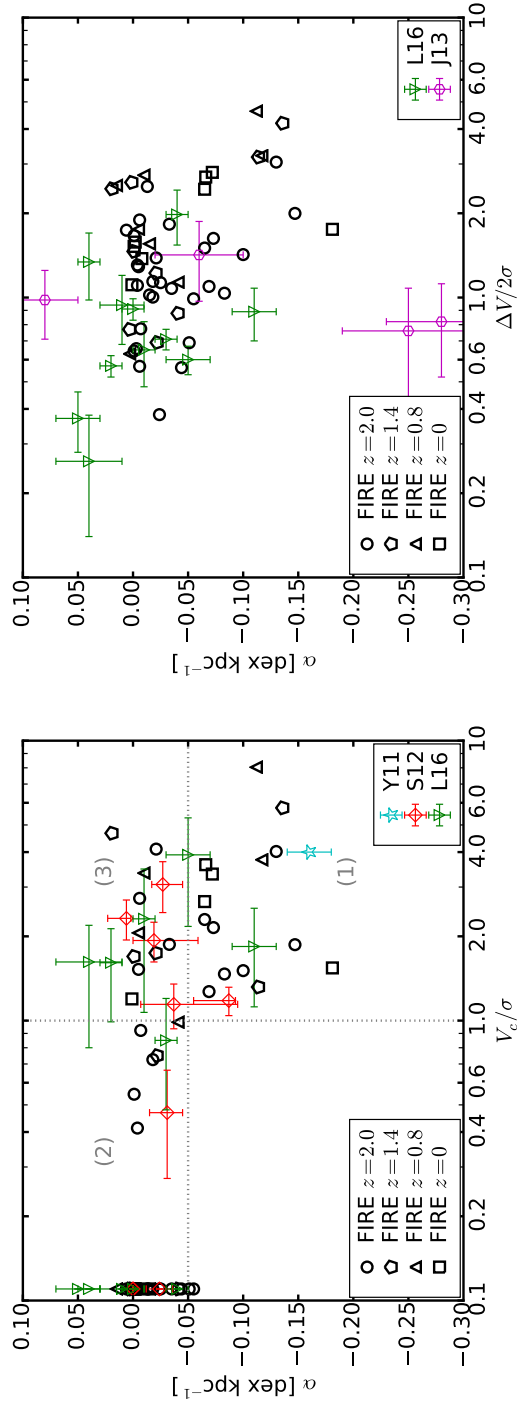
Figure 3.9: Metallicity gradient (measured over 0.25–1R_{90}) vs. degree of rotational support. *Left:* α–V_c/σ. As in Fig. 3.4, galaxies for which V_c cannot be properly determined are plotted at $V_c/\sigma \sim 0.1$. The simulated sample can be divided into three populations: (1) strong negative metallicity gradients *only* appear in rotationally supported galaxies ($V_c/\sigma \geq 1$), (2) highly perturbed galaxies with no rotation ($V_c/\sigma < 1$) tend to have flat gradients, and (3) there is also a population of rotationally supported galaxies that have flat metallicity gradients. We do *not* find any strongly perturbed galaxy that has a strong negative metallicity gradient. *Right:* α–$\Delta V/2\sigma$. Similarly, strong negative gradients *only* occur in galaxies with $\Delta V/2\sigma \geq 1$. Symbols with errorbars show observational data from Yuan et al. (2011, Y11), Swinbank et al. (2012, S12), Jones et al. (2013, J13), and Leethochawalit et al. (2016, L16). Our simulations reproduce the observed complexity in metallicity gradient and kinematic properties.

profile[3], pre-enrichment in the disk, the strength of radial mixing, etc. Population (2) galaxies are strongly perturbed via violent processes, such as mergers, rapid gas inflows, and strong feedback-driven outflows, which can destroy any pre-existing rotating disk and cause efficient gas re-distribution on galactic scales. Galaxies in region (3) may be in a transition phase, e.g., during a gas infall before a strong negative metallicity gradient builds up at a later time. In Section 3.3.6, we will further show that the metallicity gradient and kinematic properties of a galaxy can vary on $\lesssim$ Gyr time-scales, causing the galaxy to move across the three regions on the α–V_c/σ relation.

In the right panel of Fig. 3.9, we show the relation between metallicity gradient and $\Delta V/2\sigma$. Similarly, strong negative metallicity gradients *only* appear in galaxies with $\Delta V/2\sigma \geq 1$, consistent with the results we find with V_c/σ. Again, we caution that $\Delta V/2\sigma$ may not be a robust indicator of whether a galaxy is rotationally supported or strongly perturbed (see Fig. 3.4). In Fig. 3.9, we also compare our simulations with observational data from Yuan et al. (2011, Y11), Swinbank et al. (2012, S12), Jones et al. (2013, J13), and Leethochawalit et al. (2016, L16). Note that we follow Leethochawalit et al. (2016) and only adopt the V_c/σ for those that can be reliably fitted by a simple disk model ($\chi^2_{\rm red} < 20$ in their table 3), while we regard the rest of their sample as non-rotationally supported (V_c undetermined). Our simulations reproduce the observed complexity in the relationship between metallicity gradient and kinematic properties. Remarkably, the simulated sample and the observed sample, although both small in sample size, occupy almost identical parameter space in these relations.

3.3.5 Metallicity gradient vs redshift

In Fig. 3.10, we plot the metallicity gradients for all simulated galaxies in our sample as a function of redshift, at $z = 2$, 1.4, 0.8, and 0. The black points present the metallicity gradients measured from 0.25–$1R_{90}$. We also compare a variety of observations from Maciel et al. (2003, M03), Yuan et al. (2011, Y11), Swinbank et al. (2012, S12), Jones et al. (2013, J13), Jones et al. (2015, J15),

---

[3]If the initial gas disk has a power-law surface density profile $\Sigma_g \sim R^{-\beta}$, where $\beta > 0$ is the power-law index, following the same argument above, the gas-phase metallicity profile will be $Z_g \sim R^{-0.4\beta}$. A power-law profile might be a better description to our simulations (e.g., Hopkins et al. 2009) and the observed metallicity profiles in early-type galaxies (e.g., Reda et al. 2007; Sánchez-Blázquez et al. 2007). In such case, the slope of metallicity gradients, if defined in d log Z_g/dR (in dex kpc^{-1}), also depends on the range where the gradient is measured. This may account for the steep metallicity gradients (~ -0.3 dex kpc^{-1}) observed in high-redshift galaxies (e.g., Jones et al. 2013, also see Fig. 3.10).
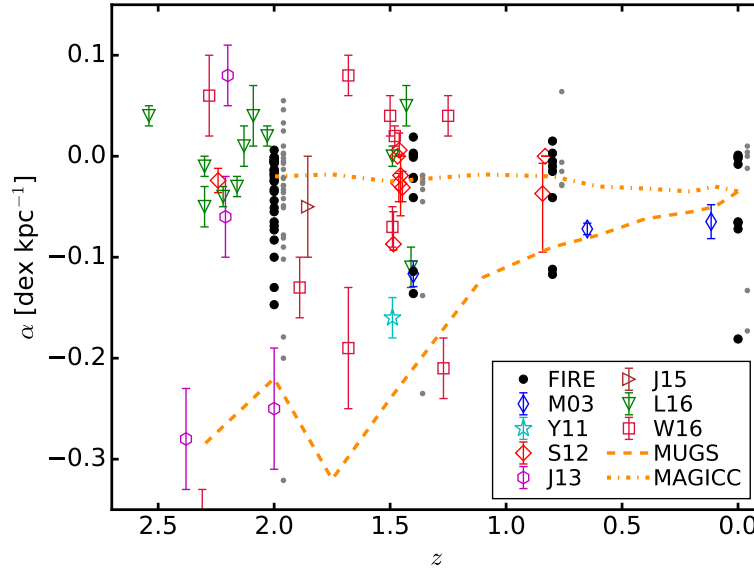
Figure 3.10: Metallicity gradient vs. redshift. The black points show the metallicity gradients measured in $0.25–1R_{90}$ for the entire FIRE sample at four redshifts. The smaller grey points show the slopes measured in 0–2 kpc. The grey points are shifted slightly right along the x-axis for better illustration. Symbols with errorbars show a compilation of observations from Maciel et al. (2003, M03), Yuan et al. (2011, Y11), Swinbank et al. (2012, S12), Jones et al. (2013, J13), Jones et al. (2015, J15), Leethochawalit et al. (2016, L16), and Wang et al. (2017, W16). The green lines show the predictions from the sub-grid 'conservative' (weak) feedback model used in MUGS simulations (dashed) and the 'enhanced' (strong) feedback used in MAGICC simulations (dotted) from Gibson et al. (2013). Our simulations agree well with the wide range of metallicity gradients observed over the $z = 0–2.5$ redshift range – in some circumstances (e.g., starbursts), feedback is predicted to be effectively 'strong' to produce flatten metallicity gradients, while in others, it is sufficiently 'weak' to allow a strong negative gradient.

Leethochawalit et al. (2016, L16), and Wang et al. (2017, W16). Our simulations are broadly consistent with the observed diversity of metallicity gradients at redshifts $z = 0.5–2.5$. For example, at $z \sim 2$, our sample covers metallicity gradients from $\alpha = -0.15–0.05$ dex kpc^{-1}, in reasonably good agreement with observational data at that epoch. Note that we measure the metallicity gradient from $0.25–1R_{90}$ by default, whereas there is no universal standard for the radial limits used to define the metallicity gradients in observations. If we instead use the metallicity gradient in the central 0–2 kpc in our simulations, as shown by the small grey points in Fig. 3.10, we obtain a similar result, but with somewhat larger scatter, with the slope ranging from $-0.3–0.1$ dex kpc^{-1}. This is in better agreement with the

steep slopes and positive metallicity gradients in some of the observational samples (e.g., Jones et al. 2013; Leethochawalit et al. 2016). A more rigorous comparison would require matching precisely the galaxy selection function and observational metallicity gradient measurement method of each observed sample, which is beyond the scope of this paper.

We also compare our results with the MUGS simulation ('conservative' feedback) and the MAGICC simulation ('enhanced' feedback) from Gibson et al. (2013). In the 'enhanced' feedback model, gas heated by SNe is kept hot artificially for much longer than the Sedov-Taylor phase to generate efficient outflows (Stinson et al. 2013a), in contrast to much simpler 'sub-grid' models which effectively suppress bursty star formation. These feedback models also require fine-tuning certain parameters to match the observed galaxy properties. The 'conservative' (weak) feedback model in Gibson et al. (2013) always predicts the so-called 'inside-out' growth picture. In this scenario, a compact core formed rapidly at the center of the galaxy, building up a steep negative metallicity gradient at high redshift. Then the galaxy gradually grows in size and the metallicity gradient flattens as the galaxy evolves. Their 'enhanced' (strong) feedback model, on the other hand, always produces a flat metallicity gradient that shows little evolution with redshift. In contrast, our sample produces more diverse distribution of metallicity gradients in good agreement with observations, including both strong negative gradients and flat/weak positive gradients. This confirms that metallicity gradients in cosmological simulations are sensitive to the treatment of feedback. The physics adopted in FIRE explicitly resolves feedback processes on sub-kpc scales which allows galaxies to 'switch' between weak and strong outflows based on their local conditions. As a consequence, our simulations produce both strong and weak gradients, even in the same galaxy at slightly different times in its evolution. This leads to a diversity of gradients in good agreement with observations, and in contrast to simpler 'sub-grid' feedback models.

3.3.6 The effects of feedback: a case study

In this section, we will show how feedback results in the complex relation between galaxy gas-phase metallicity gradients and kinematic properties. To this end, we perform a case study on simulation m12i, which produces a Milky Way-mass disk galaxy by $z = 0$. In the top panel of Fig. 3.11, we show the metallicity gradient (measured from $0.25–1R_{90}$) as a function of cosmic time at redshifts $z = 0–1.1$ (the black solid line). Note that prior to $z = 1.1$, this is a clumpy, low-mass galaxy that
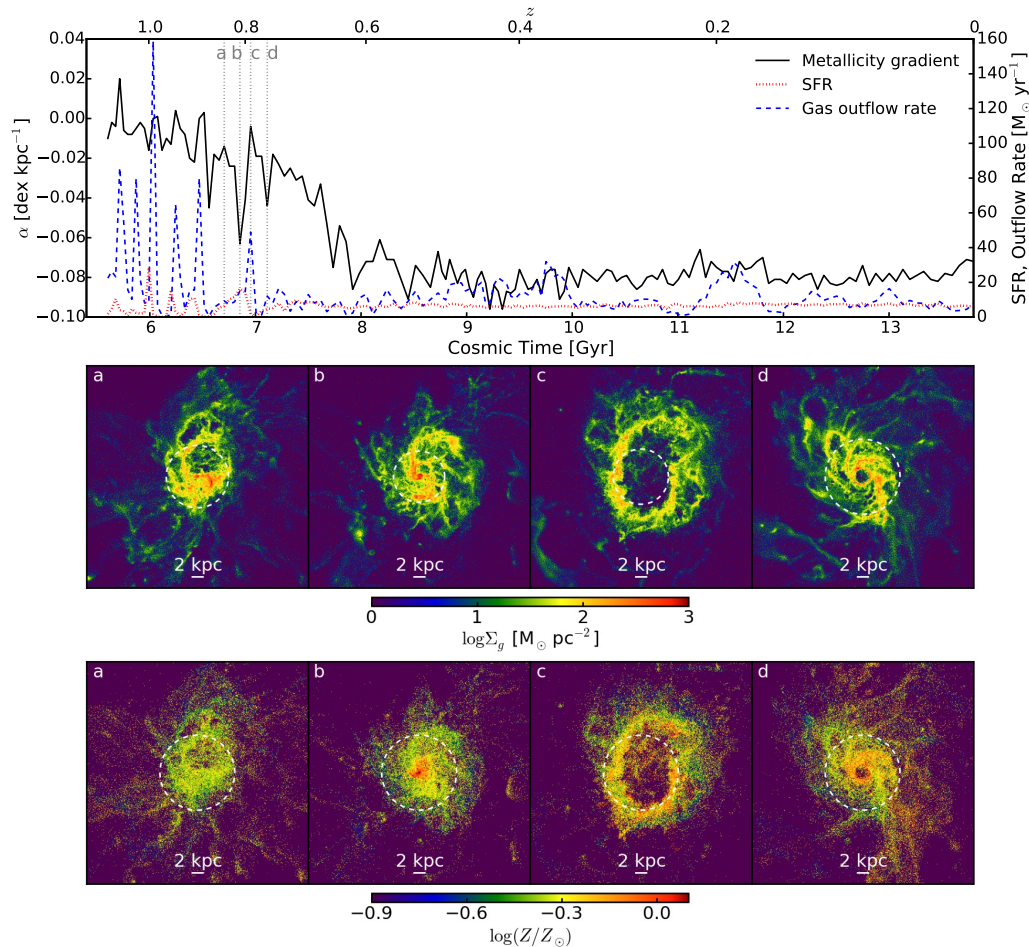
Figure 3.11: *Top:* Metallicity gradient in the galaxy m12i (measured from 0.25–1R_{90}) as a function of cosmic time at redshifts $z = 0$–1.1 (black solid). The SFR (red dotted) and gas outflow rate measured at 10 kpc (blue dashed) are also shown for comparison. *Middle:* Gas morphology at the four epochs labeled by the vertical grey dotted lines in the top panel (a–d). *Bottom:* Metallicity map at the four epochs. At $z > 0.7$, the metallicity gradient shows considerable time fluctuations, associated with starburst episodes. The examples illustrate this process: (a) gas flows in rapidly and forms a disk, (b) a negative metallicity gradient builds up during star formation, (c) strong feedback from starburst drives intense gas outflow and flattens the metallicity gradient, and (d) gas falls back and reforms a disk. The peaks in gas outflow rate match the "peaks" in metallicity gradients (where the gradients are flat). This explicitly shows the effect of feedback flattening the metallicity gradient. At $z < 0.7$, the disk has 'calmed down', and stellar feedback is no longer strong enough to disrupt the gas disk. A negative metallicity gradient then develops rapidly, and does not evolve significantly with time after this.

has chaotic, bursty star formation, with little rotation and flat metallicity gradients (Ma et al. 2017c), so we do not show it here. For comparison, we also show the instantaneous SFR (averaged over 10 Myr, the red dotted line)[4] and the gas outflow rate at 10 kpc (the blue dashed line) during the same period. We follow Faucher-Giguère et al. (2011) and Muratov et al. (2015) and calculate the gas outflow rate as

$$\frac{\partial M}{\partial t} = \frac{1}{L} \sum_i m_i \frac{\mathbf{v}_i \cdot \mathbf{r}_i}{|\mathbf{r}_i|}, \tag{3.3}$$

where we sum over all gas particles that have radial velocity $v_r = \mathbf{v} \cdot \mathbf{r}/|\mathbf{r}| > 100 \, \mathrm{km \, s^{-1}}$ within the central $L = 10 \, \mathrm{kpc}$ in the galaxy.

At $z > 0.7$, both the gas outflow rate and SFR show significant time variability. The outflow rates are much higher than the SFRs (high mass loading factors), implying that feedback is very efficient at these times (Muratov et al. 2015)[5]. At the same time, the metallicity gradient also shows significant fluctuations. Interestingly, the peaks in gas outflow rates coincide with the 'peaks' in metallicity gradients (i.e., when the gradient is flat, since a strong gradient has a negative slope). To further illustrate the process, we show example gas images and metallicity maps in the middle and bottom panels in Fig. 3.11, respectively, at four selected times labeled by (a)–(d), as shown by the grey vertical dotted lines in the top panel of Fig. 3.11. First, gas flows in rapidly and forms a rotating gas disk (a). Rapid gas infall triggers a starburst in the disk, and a negative metallicity gradient builds up quickly (b, see the argument in Section 3.3.4). Next, feedback from the starburst drives strong outflows, which destroy the gas disk and mix the metals on galactic scales, flattening the pre-existing negative metallicity gradient in the disk (c). Finally, gas falls back, reforming a disk, and the next episode starts (d).

We repeat the analysis in Section 3.3.4 and measure the degree of rotational support V_c/σ for 50 successive snapshots from simulation m12i, from $z = 0.6–1.1$, before the metallicity gradient becomes stable. In Fig. 3.12, we plot the relation between metallicity gradient and V_c/σ for the 50 epochs considered here (blue circles) and compare the results with the entire FIRE sample as shown in Fig. 3.9 (grey points). Remarkably, the time variability of a single galaxy occupies almost identical parameter space as the entire simulated sample in the α–V_c/σ relation. Again,

---

[4]Note that the SFRs shown here are different from those defined in Section 3.2.2 and listed in Appendix (where the SFRs are averaged over 200 Myr), because we want to emphasize the short-time-scale fluctuations in this section.

[5]Note that while the outflow rates in Fig. 3.11 are qualitatively similar to those in Muratov et al. (2015), they different quantitively because of different radial and velocity range considered.

significant negative metallicity gradients *only* appear when there is a well-ordered rotating disk, while the gradients are flat when the galaxy is strongly perturbed and shows little rotation. At the epochs when the galaxy has a flat metallicity gradient but is rotationally supported, it is mostly in the early stage of gas infall before a strong metallicity gradient builds up later (e.g., epoch (a) shown in Fig. 3.11). These results suggest that a single galaxy can rapidly (in a few 100 Myr) traverse the range of observed metallicity gradients and kinematic properties, indicating that the observed metallicity gradients at high redshifts may be more of an indicator of the *instantaneous* ($\lesssim$ Gyr time-scale) dynamical state of the galaxy, *not* the long-term galaxy formation, accretion, or growth history.

Almost all the simulated galaxies show significant burstiness in SFR and undergo strong bursts of feedback-driven outflows at high redshift ($z \gtrsim 0.5$), even for the most massive galaxies at $z \sim 2$ (Hopkins et al. 2014; Sparre et al. 2017; Muratov et al. 2015). The central galaxy in simulation m12i calms down after $z \sim 0.7$, and there is always a well-ordered, rotationally supported gas disk thereafter (Ma et al. 2017c). Stars form in the disk at a nearly constant rate that is set by the nearly constant gas accretion rate and regulated by stellar feedback. The feedback is no longer sufficient to drive strong gas outflows and destroy the gas disk. A negative metallicity gradient builds up quickly as soon as the disk calms down and stays almost unchanged after this time. A similar transition is also seen in other simulations that produce a galaxy more massive than $M_* = 10^{10}\,M_\odot$ by $z = 0$, as these galaxies also cannot drive strong gas outflows at late times (Muratov et al. 2015). Such a transition is likely due to a combination of decreasing merger rates at lower redshifts (e.g., Hopkins et al. 2010) and decreasing gas fractions in massive galaxies (Hayward & Hopkins 2017). Therefore, it is expected that massive galaxies in the local Universe mostly have stable negative metallicity gradients, except for strongly perturbed (e.g., merging) galaxies.

3.4 Discussion and Conclusions

In this paper, we use 32 high-resolution cosmological zoom-in simulations from the FIRE project to study the gas-phase metallicity gradient in galaxies and its relation with galaxy properties. Our simulated sample includes 32 galaxies at $z = 2$, covering a halo mass range 10^{11}–$10^{13}\,M_\odot$ and stellar mass range 10^9–$10^{11}\,M_\odot$. A sub-sample has been run to $z = 0$, spanning a halo mass range 10^{11}–$10^{13}\,M_\odot$ and stellar mass range 10^9–$10^{11}\,M_\odot$ at $z = 0$. The FIRE simulations include physically motivated models of the multi-phase ISM, star formation, and stellar feedback and
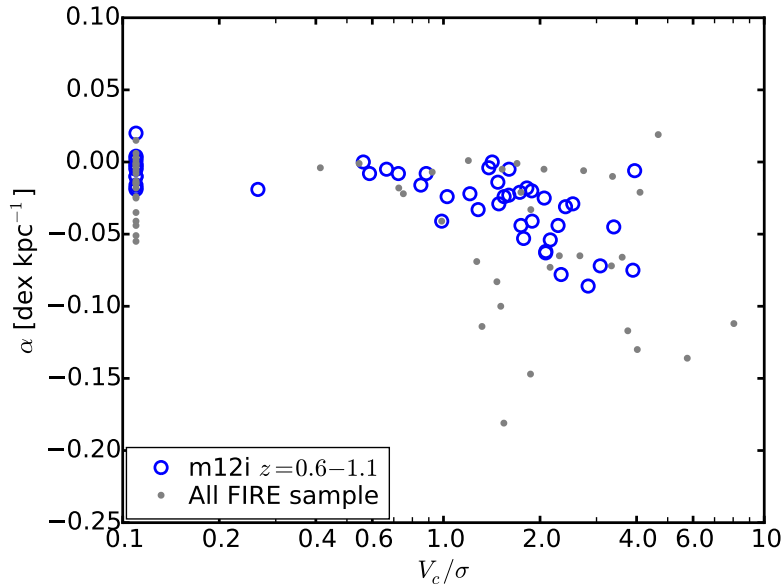
Figure 3.12: Metallicity gradient vs degree of rotational support (α–V_c/σ) for 50 successive snapshots from simulation m12i during $z = 0.6$–1.1 (blue circles). The grey points show the entire FIRE sample presented in Figure 3.9. A single galaxy measured at different time occupies similar parameter space to an ensemble of galaxies – strong negative metallicity gradients *only* appear when there is well-ordered rotation, while the gradient tends to be flat when the galaxy is strongly perturbed. This implies that the observed gradients more closely reflect the instantaneous state of the galaxy than its cosmological growth history.

have been shown to reproduce a number of observed properties of galaxies for a broad range of stellar mass at redshift $z = 0$–6. These simulations explicitly resolve the launching and propagation of galactic winds on sub-kpc scales and can thus capture the effects of stellar feedback on metallicity gradients. Our main conclusions are as follows.

(i) The simulations produce a diverse range of kinematic properties and metallicity gradients, broadly consistent with observations at all redshifts. Our simulated sample includes merging galaxies, starbursts with gas morphologies disturbed by feedback, as well as relatively stable, rotation-dominated disk galaxies.

(ii) Strong negative metallicity gradients *only* appear in galaxies with a gas disk, as reflected by well-ordered rotation ($V_c/\sigma \geq 1$), while strongly perturbed galaxies ($V_c/\sigma < 1$) always have flat gradients. In a gas disk, the star formation efficiency is higher toward the center due to increasing gas surface density, so metal enrichment is faster in the central region, leading to a negative metallicity gradient. Strong

perturbations driven by rapid gas infall, mergers, or violent outflows, can stir the gas in the ISM, causing metal re-distribution on galactic scales and flattening metallicity gradients. Not *all* rotationally supported galaxies have strong negative metallicity gradients.

(iii) The metallicity gradient and kinematic properties of a high-redshift galaxy can vary on $\lesssim$ Gyr time-scales, associated with starburst episodes. The time variability of a single galaxy is statistically similar to the overall simulated sample. A negative metallicity gradient can build up quickly as a starburst is triggered in a gas disk formed via gas infall. Strong feedback from the starburst drives intense outflows, which destroy the gas disk and cause metal re-distribution on galactic scales, resulting in flat metallicity gradients. Gas recycles in fountains (Anglés-Alcázar et al. 2017a), and negative gradients may re-establish quickly. This has important consequences for the interpretation of metallicity gradients observed in high-redshift galaxies. They may *not* well-correlate with the accretion or growth history of the galaxy on cosmological time-scales, but rather reflect the 'instantaneous' state of gas dynamics.

(iv) There is weak dependence of metallicity gradient on both stellar mass and sSFR. Low-mass galaxies, and/or galaxies with high sSFR tend to have flat metallicity gradients, owing to efficient feedback in such systems, which keeps them in the 'bursty' star formation mode.

(v) Because of the important role of stellar feedback, it is essential to resolve feedback from sub-kpc to galactic scales in sufficiently high-resolution simulations, to reproduce the observed diversity of kinematic properties and metallicity gradients in high-redshift galaxies. Our results are in contrast to simulations with simple 'sub-grid' feedback models, which tend to predict either 'all strong' or 'all weak' metallicity gradients.

Our results suggest that the bursty star formation in our simulations can change the kinematic properties and gas-phase metallicity gradients in these galaxies on relatively short time-scales ($\sim 10^8$–10^9 yr), which can at least partly explain the diverse kinematics and gradients observed in high-redshift galaxies. One intriguing question we leave open is when and why a galaxy shows such bursty star formation. A detailed answer of this question may require a larger sample of simulations. Nonetheless, the current sample of the FIRE simulations have suggested that at high redshift ($z > 2$), all galaxies show significant burstiness in the SFR, even in the most massive galaxies in the simulated sample (Sparre et al. 2017; Faucher-Giguère et al.

2015; Feldmann et al. 2017). At late times, low-mass galaxies ($M_* < 10^{10}\,M_\odot$) still have bursty star formation down to $z \sim 0$ (Wheeler et al. 2017; El-Badry et al. 2016), while more massive galaxies ($M_* \gtrsim 10^{10}\,M_\odot$) tend to have a transition from bursty to relatively stable star formation at intermediate redshift ($z \sim 0.5$–1, Muratov et al. 2015). Hayward & Hopkins (2017) provide an analytic model and argue that such transition happens at a gas fraction threshold of $f_{\mathrm{gas}} \sim 0.3$, above which the ISM is highly turbulent and star formation is sufficiently violent that feedback can efficiently blow out a large fraction of low-density gas from the disk. At lower gas fractions, turbulence becomes weaker, and feedback is no longer sufficient to drive strong outflows.

In our simulations, stellar metallicity gradients develop coherently with gas-phase metallicity gradients as stars form in the disk (also see the argument in Section 3.3.4), but stellar metallicity gradients are much less vulnerable to strong feedback than their gas-phase counterparts, especially in massive galaxies (El-Badry et al. 2016). Stellar migration in the disk can flatten metallicity gradients, but it may only have a weak net effect over a few Gyr time-scale (Ma et al. 2017c). Therefore, we propose that our predictions for the short-time-scale variation of gas-phase metallicity gradients can be tested with stellar metallicity gradients. One would expect that a large fraction of massive high-redshift galaxies have significant negative *stellar* metallicity gradients, even if they show a broad range of kinematic properties and gas-phase metallicity gradients. We say massive because the galaxy must have had a gas disk at some point to build up a stellar metallicity gradient, which is not the case in small dwarf galaxies. Negative stellar metallicity gradients have been observed in local galaxies (e.g., Sánchez-Blázquez et al. 2014), although it is challenging to measure stellar metallicities at higher redshifts. It will be interesting to study stellar metallicity gradients in these simulations in more details in future work.

Nevertheless, our simulations only have a moderate sample size and are limited in statistical power. We show in Section 3.3.4 that our simulated sample can be divided into three populations based on their kinematic properties and metallicity gradients, but we leave a number of open questions. What fractions of galaxies at a given redshift are rotationally supported and strongly perturbed, respectively? How often are strong perturbations driven by internal feedback vs. external processes? What fraction of rotationally supported galaxies show strong negative gas-phase metallicity gradients? What fraction of galaxies in each population are associated with mergers? These questions are important for understanding high-redshift galaxy

populations and worth further investigations, which we hope to explore with larger ensembles of simulations in the future.

Acknowledgments

Appendix: Galaxy properties

In this section, we list the galaxy properties (stellar mass, star formation rate, and R_{90}, Section 3.2.2), kinematic properties (V_c, $\Delta V/2$, and σ, Section 3.2.3), and gas-phase metallicity gradient measured in 0.25–1R_{90} (Section 3.2.4), for the entire simulated sample studied in this paper (Figs. 3.8–3.10). A machine-readable version of this table is available at http://www.tapir.caltech.edu/~xchma/data/metal_grad.txt.

Table 3.3: Galaxy properties, kinematics, and metallicity gradients of the simulated sample.

Name	z	M_* ($M_\odot$)	SFR ($M_\odot\,\mathrm{yr}^{-1}$)	R_{90} (kpc)	V_c ($\mathrm{km\,s}^{-1}$)	$\Delta V/2$ ($\mathrm{km\,s}^{-1}$)	σ ($\mathrm{km\,s}^{-1}$)	α ($\mathrm{dex\,kpc}^{-1}$)
m11	2.0	1.9e8	–	–	–	–	–	–
m12v	2.0	1.0e9	0.05	4.37	–	76.7	77.5	-0.055 ± 0.007
m12q	2.0	3.0e9	0.70	2.51	85.4	55.8	37.2	-0.065 ± 0.007
m12i	2.0	5.3e8	0.52	4.57	44.2	30.6	16.2	-0.006 ± 0.005
m13	2.0	2.0e10	2.2	3.07	157.8	168.8	84.5	-0.147 ± 0.008
m11h383	2.0	3.5e8	0.04	2.8	–	8.3	12.0	-0.051 ± 0.007
m11.4a	2.0	4.6e8	0.17	3.4	–	16.6	29.6	-0.044 ± 0.006
m11.9a	2.0	6.3e8	0.16	4.1	–	21.3	20.9	-0.015 ± 0.005
MFz0_A2	2.0	1.1e11	55.6	4.6	482.4	365.6	120.0	-0.130 ± 0.008

Galaxy properties studied in this paper (units are physical):
(1) Name: Simulation designation.
(2) z: redshift where the properties here are measured.
(3) M_*: Stellar mass within the central 10 kpc of the galaxy at the given redshift.
(4) SFR: Star formation rate within the central 10 kpc of the galaxy (averaged over 200 Myr).
(5) R_{90}: Defined in Section 3.2.2, as the radius that encloses 90% of the stars younger than 200 Myr within 10 kpc.
(6) V_c: Rotation velocity given by the arctan fit from Equation (3.1) to the gas velocity curve (see Section 3.2.3).
(7) ΔV: Peak-to-peak velocity difference in the gas velocity curve (see Section 3.2.3).
(8) σ: Maximum velocity dispersion of gas (see Section 3.2.3).
(9) α: Gas-phase metallicity gradient measured over 0.25–$1\,R_{90}$ from Equation (3.2).
Note: If a galaxy is temporarily quenched and near gas depletion in the central 10 kpc, its gas kinematic properties (V_c, $\Delta V/2$, and σ) and gas-phase metallicity gradient (α) cannot be properly measured. If a galaxy has been quenched for more than 200 Myr, its SFR and R_{90} are also not defined.

Table 3.4: Table 3.3 – continued.

Name	z	M_* ($M_\odot$)	SFR ($M_\odot\,\mathrm{yr}^{-1}$)	R_{90} (kpc)	V_c ($\mathrm{km\,s}^{-1}$)	$\Delta V/2$ ($\mathrm{km\,s}^{-1}$)	σ ($\mathrm{km\,s}^{-1}$)	α ($\mathrm{dex\,kpc}^{-1}$)
z2h350	2.0	6.4e9	9.4	3.44	–	–	–	–
z2h400	2.0	5.8e9	4.3	4.89	67.9	106.8	93.5	−0.018 ± 0.002
z2h450	2.0	6.7e9	0.35	9.42	–	114.1	103.2	−0.004 ± 0.002
z2h506	2.0	8.1e9	5.4	7.85	116.5	39.4	28.4	−0.021 ± 0.003
z2h550	2.0	9.6e8	0.85	3.77	–	25.6	25.5	−0.018 ± 0.004
z2h600	2.0	1.1e10	6.2	7.67	–	59.6	35.8	−0.001 ± 0.002
z2h650	2.0	5.2e9	4.4	6.46	–	31.1	12.5	−0.013 ± 0.003
z2h830	2.0	5.1e9	2.6	5.32	–	3.0	7.8	−0.029 ± 0.011
A1:0	2.0	2.3e10	9.9	2.90	72.4	85.5	132.7	−0.001 ± 0.013
A2:0	2.0	3.1e10	14.0	6.88	171.7	167.7	91.7	−0.033 ± 0.003
A3:0	2.0	1.1e10	6.9	2.98	148.8	128.4	117.2	−0.069 ± 0.008
A4:0	2.0	1.2e10	2.8	2.43	167.6	158.2	111.1	−0.100 ± 0.015
A5:0	2.0	1.6e10	28.5	6.67	–	115.5	66.4	0.007 ± 0.004
A6:0	2.0	2.3e10	1.9	5.83	50.5	159.8	122.3	−0.004 ± 0.003
A7:0	2.0	2.0e10	12.9	8.02	–	67.6	103.0	−0.003 ± 0.001
A8:0	2.0	1.1e10	10.1	7.46	–	67.0	118.0	−0.006 ± 0.001
A9:0	2.0	8.3e9	3.9	3.80	23.9	20.0	25.9	−0.007 ± 0.007
A10:0	2.0	2.3e10	22.5	6.62	76.1	64.3	49.9	−0.003 ± 0.004
B1:0	2.0	6.8e10	38.5	6.50	–	253.7	235.4	−0.035 ± 0.002
B2:0	2.0	6.0e10	6.2	7.30	–	280.3	248.0	−0.025 ± 0.002
B3:0	2.0	5.0e10	40.5	8.26	428.0	323.9	199.1	−0.073 ± 0.003
B4:0	2.0	2.5e10	45.3	8.00	–	–	–	–
B5:0	2.0	4.1e10	14.2	5.39	202.5	143.0	138.0	−0.083 ± 0.002

83

Table 3.5: Table 3.3 – continued.

Name	z	M_* (M$_\odot$)	SFR (M$_\odot$ yr^{-1})	R_{90} (kpc)	V_c (km s^{-1})	$\Delta V/2$ (km s^{-1})	σ (km s^{-1})	α (dex kpc^{-1})
m11	1.4	3.4e8	0.12	7.1	30.6	16.0	6.6	0.019 ± 0.003
m12v	1.4	7.9e9	6.0	7.36	83.2	71.8	49.2	-0.001 ± 0.001
m12q	1.4	8.4e9	5.1	3.68	119.0	83.5	68.2	-0.021 ± 0.004
m12i	1.4	6.0e9	1.7	4.44	5.7	52.2	67.9	0.003 ± 0.004
m13	1.4	5.8e10	14.9	5.39	344.3	251.0	59.8	-0.136 ± 0.006
m11h383	1.4	4.7e8	0.14	1.9	–	61.8	70.4	-0.041 ± 0.011
m11.4a	1.4	5.3e8	0.35	2.5	17.3	15.9	23.0	-0.022 ± 0.008
m11.9a	1.4	1.9e9	1.4	8.1	–	70.4	27.3	0.001 ± 0.001
MFz0_A2	1.4	1.3e11	11.5	4.3	537.6	392.8	123.7	-0.114 ± 0.008
m11	0.8	8.4e8	0.05	4.8	–	14.3	22.7	0.003 ± 0.005
m12v	0.8	9.1e9	0.004	4.13	133.8	108.8	39.8	-0.010 ± 0.004
m12q	0.8	1.1e10	0.001	4.56	–	–	–	–
m12i	0.8	1.3e10	10.1	4.12	76.6	88.0	77.6	-0.041 ± 0.004
m13	0.8	6.4e10	2.4	7.04	435.7	251.0	54.2	-0.112 ± 0.013
m11h383	0.8	1.2e9	0.01	2.6	–	27.3	10.9	0.015 ± 0.010
m11.4a	0.8	1.8e9	0.07	6.4	62.3	53.1	30.3	-0.005 ± 0.002
m11.9a	0.8	3.0e9	0.4	4.4	–	41.6	26.8	-0.015 ± 0.004
MFz0_A2	0.8	1.4e11	4.1	5.3	411.9	352.4	109.7	-0.117 ± 0.004
m11	0	1.9e9	0.4	6.4	–	24.1	15.3	-0.002 ± 0.002
m12v	0	2.2e10	0.65	4.28	141.7	161.0	91.9	-0.181 ± 0.008
m12q	0	1.5e10	0.50	7.71	141.8	129.8	53.3	-0.065 ± 0.005
m12i	0	4.7e10	5.4	8.35	215.2	180.4	64.4	-0.072 ± 0.002
m13	0	8.2e10	1.2	3.81	324.3	242.3	89.9	-0.066 ± 0.005
m11h383	0	2.9e9	0.3	5.0	–	37.2	27.0	-0.008 ± 0.002
m11.4a	0	4.1e9	0.1	8.8	55.2	51.2	46.1	0.001 ± 0.001
m11.9a	0	1.4e10	1.8	8.4	–	59.6	39.2	-0.001 ± 0.002
MFz0_A2	0	1.5e11	–	–	–	–	–	–

Chapter 4

THE STRUCTURE AND DYNAMICAL EVOLUTION OF THE STELLAR DISK OF A SIMULATED MILKY WAY-MASS GALAXY

Abstract

We study the structure, age and metallicity gradients, and dynamical evolution using a cosmological zoom-in simulation of a Milky Way-mass galaxy from the Feedback in Realistic Environments project. In the simulation, stars older than 6 Gyr were formed in a chaotic, bursty mode and have the largest vertical scale heights (1.5–2.5 kpc) by $z = 0$, while stars younger than 6 Gyr were formed in a relatively calm, stable disk. The vertical scale height increases with stellar age at all radii, because (1) stars that formed earlier were thicker 'at birth', and (2) stars were kinematically heated to an even thicker distribution after formation. Stars of the same age are thicker in the outer disk than in the inner disk (flaring). These lead to positive vertical age gradients and negative radial age gradients. The radial metallicity gradient is negative at the mid-plane, flattens at larger disk height $|Z|$, and turns positive above $|Z| \sim 1.5$ kpc. The vertical metallicity gradient is negative at all radii, but is steeper at smaller radii. These trends broadly agree with observations in the Milky Way and can be naturally understood from the age gradients. The vertical stellar density profile can be well-described by two components, with scale heights 200–500 pc and 1–1.5 kpc, respectively. The thick component is a mix of stars older than 4 Gyr which formed through a combination of several mechanisms. Our results also demonstrate that it is possible to form a thin disk in cosmological simulations even with strong stellar feedback.

Keywords: galaxies: abundances – galaxies: evolution – galaxies: formation – cosmology: theory

4.1 Introduction

Gilmore & Reid (1983) first discovered that the vertical stellar density profile in the solar neighborhood in the Milky Way (MW) can be described by two exponential components with scale heights ~ 300 pc and ~ 1450 pc, respectively, and identified them as the thin disk and the thick disk. Such a two-component profile is also seen in external edge-on disk galaxies (e.g., Yoachim & Dalcanton 2006; Comerón et al. 2011, 2012). However, it remains unclear whether the thin and thick disks are two distinct components or one single structure that varies continuously above the disk plane.

Several mechanisms have been proposed to explain the formation of the thick disk, despite the ambiguity of whether it is a discrete component or not. Some popular scenarios, all motivated by theory or observations, include: (1) kinematic heating from a pre-existing thin disk during minor mergers (e.g., Quinn et al. 1993; Kazantzidis et al. 2008; Hopkins et al. 2008; Villalobos & Helmi 2008; Purcell et al. 2009; Qu et al. 2011), (2) star formation at high redshift from chaotic gas accretion during hierarchical assembly (Brook et al. 2004) or in a turbulent, gas-rich disk (Bournaud et al. 2009; Haywood et al. 2013), (3) radial migration of stars from the inner disk to the outer disk (Schönrich & Binney 2009b; Loebman et al. 2011), and (4) accretion of stars from SMC-like satellites (Abadi et al. 2003). Nonetheless, it is still unclear which mechanism (or combination of mechanisms) is responsible for the formation of thick disks in the MW and other galaxies.

Thanks to spectroscopic surveys of stars in the MW, such as RAVE (Steinmetz et al. 2006), SEGUE (Yanny et al. 2009), APOGEE (Allende Prieto et al. 2008), and Gaia-ESO (Gilmore et al. 2012), one can now combine three-dimensional position, velocity, and chemical abundance information for large samples (for a recent review, see Rix & Bovy 2013). Many groups have claimed that there are two distinct sub-populations, named α-rich and α-poor stars, as revealed by the gap in the [α/Fe]–[M/H] plane ([M/H] represent total stellar metallicity relative to solar abundance) or the bimodality of the [α/Fe] distribution at fixed [M/H]. These two populations are attributed to the thick and thin disks (e.g., Adibekyan et al. 2013; Bensby et al. 2014; Anders et al. 2014; Nidever et al. 2014; Mikolaitis et al. 2014; Kordopatis et al. 2015). Nonetheless, some samples show a much less significant gap in the [α/Fe]–[M/H] plane than others (e.g., Mikolaitis et al. 2014; Kordopatis et al. 2015), or no gap at all (e.g., Boeche et al. 2014). Also, in some cases, the bimodality appears in certain α elements but disappears in others (e.g.,

Bensby et al. 2014; Mikolaitis et al. 2014). Such discrepancies are likely due to large uncertainties in abundance measurements in some studies. The bimodality, if real, implies that the MW may have a hiatus in its star formation history at high redshift (e.g., Chiappini et al. 1997; Brook et al. 2012b; Nidever et al. 2014). Also, it is not clear whether such feature is common in other galaxies.

Various groups have confirmed a negative radial metallicity gradient with a slope $d[M/H]/dR \sim -0.06\,dex\,kpc^{-1}$ in MW stars near the disk plane (height $|Z| <$ $0.5\,kpc$), with $d[M/H]/dR$ gradually flattening above the mid-plane and turning positive at and above $|Z| > 1.5\,kpc$ (e.g., Cheng et al. 2012; Boeche et al. 2013, 2014; Anders et al. 2014; Hayden et al. 2014; Mikolaitis et al. 2014). A negative vertical metallicity gradient is also found in the MW disk from the mid-plane to $|Z| \sim 3\,kpc$, but the slope varies dramatically in the literature (e.g., Carrell et al. 2012; Boeche et al. 2014; Hayden et al. 2014). Hayden et al. (2014) found that the vertical metallicity gradient is steeper at inner Galactocentric radii than at outer radii.

Nevertheless, using the data at a single epoch alone is not sufficient to identify the mechanism for MW thick disk formation. Cosmological simulations of MW analogs are useful for this problem as they allow one to trace the evolution of the galaxy as well as understand the underlying implications in the observational data. For example, Stinson et al. (2013b) found that older stars tend to have larger scale heights but shorter scale lengths than younger stars in their MW analog simulation, which also supported the observationally motivated conjecture in Bovy et al. (2012) that mono-abundance populations (MAPs; stars with certain [Fe/H] and [α/Fe]) are good proxies for single age populations (see also Matteucci & Brocato 1990; Fuhrmann 1998). Likewise, many authors have also found a two-component disk structure and similar MAP properties in their simulations (e.g., Brook et al. 2012b; Bird et al. 2013; Minchev et al. 2013; Martig et al. 2014a; Minchev et al. 2017). Most of these simulations show that the thick disk was formed kinematically hot at high redshift, although it has been debated whether heating is important in disk evolution. For instance, Bird et al. (2013) argued that the thick-disk structure is predominantly determined 'at birth', while others suggested that kinematic heating at late times is also significant (e.g., Minchev et al. 2013; Martig et al. 2014b).

Additionally, Minchev et al. (2013) developed a chemo-dynamical model of disk galaxy evolution which reconciled the structure, formation history, and the variation of metallicity gradients in the disk (see also Minchev et al. 2014, 2015). However,

Miranda et al. (2016) pointed out that the metallicity gradients in the disk strongly rely on the treatment of (simplified) feedback in these simulations and only certain recipes produced similar behavior to the MW in their simulations. Therefore, it is important to include realistic models of the interstellar medium (ISM) and stellar feedback to understand the formation of galactic disks.

In this paper, we study a simulation from the Feedback in Realistic Environments project (FIRE; Hopkins et al. 2014)[1], which produces a disk galaxy with stellar mass similar to the MW at $z = 0$, to study the structure and abundance pattern of stars in the galactic disk. We present the structure and dynamical evolution of the stellar disk, compare the metallicity gradients and their variation with recent observations, and show how the metallicity gradients can be understood from the disk structure. The FIRE project is a suite of cosmological zoom-in simulations with detailed models of the multi-phase ISM, star formation, and stellar feedback taken directly from stellar evolution models and it produces reasonable galaxy properties broadly consistent with observations from $z = 0$–6, such as the stellar mass–halo mass relation (Hopkins et al. 2014; Feldmann et al. 2016), the Kennicutt–Schmidt law (Orr et al. 2017), neutral hydrogen covering fractions around galaxies at both low and high redshift (Faucher-Giguère et al. 2015, 2016; Hafen et al. 2017), the stellar mass–metallicity relation (Ma et al. 2016a), mass-loading factors of galactic winds (Muratov et al. 2015), metal budgets and CGM metal content (Muratov et al. 2017), galaxy sizes (El-Badry et al. 2016), and the population of satellite galaxies around MW-mass galaxies (Wetzel et al. 2016). We briefly summarize the simulation in Section 4.2, present our main results in Section 4.3, discuss our findings in Section 4.4, and conclude in Section 4.5.

We adopt a standard flat ΛCDM cosmology with cosmological parameters $H_0 = 70.2\,\mathrm{km\,s^{-1}\,Mpc^{-1}}$, $\Omega_\Lambda = 0.728$, $\Omega_m = 1 - \Omega_\Lambda = 0.272$, $\Omega_b = 0.0455$, $\sigma_8 = 0.807$ and $n = 0.961$, broadly consistent with observations (e.g., Hinshaw et al. 2013; Planck Collaboration et al. 2014).

4.2 Simulation and Methods

In this work, we perform a case study using galaxy m12i, a disk galaxy with mass comparable to the Milky Way at $z = 0$, from the FIRE project. We pick this simulation because it has been well-studied in previous work (e.g., Hopkins et al. 2014; Muratov et al. 2015, 2017; El-Badry et al. 2016; Anglés-Alcázar et al. 2017a;

---

[1]http://fire.northwestern.edu

Ma et al. 2017b) and has a morphology that is closest to the MW in our suite. A detailed description of the simulations, numerical recipes, and physics included is presented in Hopkins et al. (2014, and references therein). We briefly summarize their main features here. The simulation is run using GIZMO (Hopkins 2015), in P-SPH mode, which adopts a Lagrangian pressure-entropy formulation of the smoothed particle hydrodynamics (SPH) equations that improves the treatment of fluid-mixing instabilities (Hopkins 2013).

The cosmological 'zoom-in' initial conditions for m12i are adopted from the AGORA project (Kim et al. 2014). The zoom-in region is about one Mpc in radius at $z = 0$. The initial particle masses for baryons and dark matter are $m_{\rm b} = 5.7 \times 10^4 \, {\rm M}_\odot$ and $m_{\rm dm} = 2.8 \times 10^5 \, {\rm M}_\odot$, respectively. The minimum force softening lengths for gas and star particles are $\epsilon_{\rm gas} = 14 \, {\rm pc}$ and $\epsilon_{\rm star} = 50 \, {\rm pc}$ (Plummer-equivalent). The force softening lengths for the gas particles are fully adaptive (Price & Monaghan 2007). The most massive halo in the zoom-in region has a halo mass of $M_{\rm halo} = 1.4 \times 10^{12} \, {\rm M}_\odot$ and a stellar mass around $M_* = 6 \times 10^{10} \, {\rm M}_\odot$ at $z = 0$.

In our simulation, gas follows a molecular-atomic-ionized cooling curve from 10–10^{10} K, including metallicity-dependent fine-structure and molecular cooling at low temperatures and high-temperature metal-line cooling followed species-by-species for 11 separately tracked species (H, He, C, N, O, Ne, Mg, Si, S, Ca, and Fe; see Wiersma et al. 2009a). At each timestep, the ionization states and cooling rates are determined from a compilation of CLOUDY runs, including a uniform but redshift-dependent photo-ionizing background tabulated in Faucher-Giguère et al. (2009), and approximate models of photo-ionizing and photo-electric heating from local sources. Gas self-shielding is accounted for with a local Jeans-length approximation, which is consistent with the radiative transfer calculations in Faucher-Giguère et al. (2010).

We follow the star formation criteria in Hopkins et al. (2013b) and allow star formation to take place only in locally self-gravitating, self-shielding/molecular gas which also exceeds a hydrogen number density threshold $n_{\rm th} = 5 \, {\rm cm}^{-3}$. Stars form on the local free-fall time when the gas meets these criteria and there is no star formation elsewhere. Once a star forms, it inherits the metallicity of each tracked species from its parent gas particle. Every star particle is treated as a single stellar population with known mass, age, and metallicity, assuming a Kroupa (2002) initial mass function (IMF) from 0.1–$100 \, {\rm M}_\odot$. All the feedback quantities, including ionizing photon budgets, luminosities, supernovae (SNe) rates, mechanical luminosities of

stellar winds, etc., are then directly tabulated from the stellar population models in STARBURST99 (Leitherer et al. 1999). We account for several different stellar feedback mechanisms, including (1) local and long-range momentum flux from radiative pressure, (2) energy, momentum, mass and metal injection from SNe and stellar winds, and (3) photo-ionization and photo-electric heating. We follow Wiersma et al. (2009b) and account for metal production from Type-II SNe, Type-Ia SNe, and stellar winds using the metal yields in Woosley & Weaver (1995), Iwamoto et al. (1999), and Izzard et al. (2004), respectively. The rates of Type-II and Type-Ia SN are separtately computed from STARBURST99 and following Mannucci et al. (2006), respectively.

We note that the Mg yield from Type II SN in Woosley & Weaver (1995) is ~ 0.4 dex lower than typical values in more recent models (e.g., Nomoto et al. 2006). Therefore, we manually add 0.4 dex to all Mg abundances in our simulation to compare with observations more accurately. This will have little effect on global galaxy properties, since Mg is not an important coolant (it is simply a "tracer species"). Also, the total number of Type Ia SNe calculated from Mannucci et al. (2006) is lower than that derived from Maoz et al. (2010) by a factor of a few for a stellar population older than 1 Gyr; this may lead to predictions of lower Fe, but we cannot simply renormalize the Fe abundances in the simulation. We do not include a sub-resolution metal diffusion model in the simulation; all mixing above the resolution scale is explicitly resolved.

We use the Amiga Halo Finder (AHF; Knollmann & Knebe 2009) to identify halos in the simulated box, where we adopt the time-dependent virial overdensity from Bryan & Norman (1998). In this work, we only study the most massive (hence best-resolved) halo in the zoom-in region, which hosts a disk galaxy of very similar properties to the MW at $z = 0$. At each epoch, we define the galactic center at the density peak of most stars and find the stellar half-mass radius as the radius within which the stellar mass equals to a half of the stellar mass within 0.1 virial radius. Then the Z-axis is defined to be aligned with the total angular momentum of the gas within 5 stellar half-mass radii. In this paper, we will primarily focus on the stellar component. We do not perform a kinematic decomposition for the stellar content, but take all star particles in the analysis to form an unbiased sample.

A list of symbols used in this paper and their descriptions are presented in Table 4.1. In the rest of this paper, we always mean the $z = 0$ age when we quote stellar ages and will predominantly use lookback time (t_{lookback}) when referring to an epoch

Table 4.1: A list of symbols used in this chapter.

Symbol	Description
z	Redshift
t_{lookback}	Lookback time
age	Stellar age at $z = 0$
X, Y, Z	Cartesian coordinates
R	Galactocentric radius
$|Z|$	Height from the mid-plane
[M/H]	Total metallicity (relative to solar)
[Fe/H]	Fe abundance (relative to solar)
[Mg/Fe]	Mg to Fe abundance ratio (relative to solar)

Table 4.2: Lookback time vs redshift.

Lookback Time (t_{lookback}, in Gyr)	Redshift (z)
0	0
1	0.076
2	0.162
3	0.258
4	0.369
5	0.497
6	0.649
7	0.834
8	1.068
10	1.812

in the simulation. In Table 4.2, we list the conversion between lookback time and redshift at selected epochs for reference.

4.3 Results

4.3.1 General Picture

At high redshifts, the galaxy accretes gas rapidly and undergones multiple mergers, producing violent, bursty star formation, until a final minor merger finished at $z \sim 0.7$ (corresponding to a look-back time of $t_{\text{lookback}} \sim 6$ Gyr). Since then, a calm, stable gas disk was formed and maintained, with stars forming in the disk at a nearly constant rate ($\sim 7 \, M_\odot \, \text{yr}^{-1}$, integrated across the entire disk) regulated by stellar feedback.

The top panel in Fig. 4.1 illustrates the stellar morphologies at $z = 0$ for stars in the
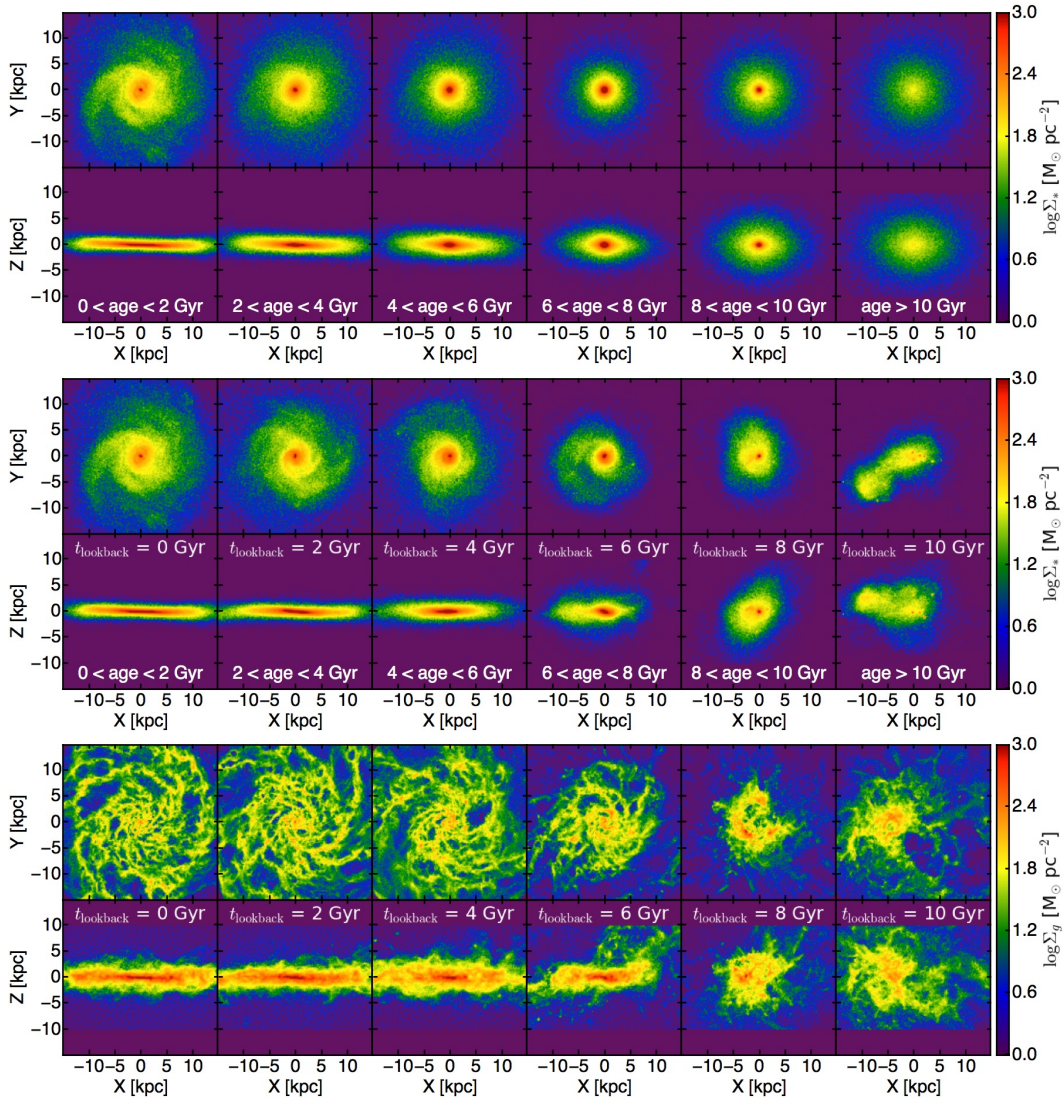
Figure 4.1: *Top:* Morphology of stars in different age intervals at $z = 0$. The thickness increases with stellar age, but the scale length first decreases with stellar age in $0 < \text{age} < 6\,\text{Gyr}$ and then increases in $\text{age} > 8\,\text{Gyr}$, leaving stars of age $\sim 6\,\text{Gyr}$ the most radially concentrated (owing to a merger-driven nuclear starburst about this time). *Middle:* Morphology of the same stars from each $z = 0$ age interval in the top panel, but viewed at the epoch when they just formed (labeled by lookback time) in the galaxy progenitor. Stars younger than $6\,\text{Gyr}$ at $z = 0$ were formed in a relatively calm disk. Stars older than $8\,\text{Gyr}$ at $z = 0$ were formed in a violent, bursty mode and relax by $z = 0$. *Bottom:* Morphology of gas, viewed at the same epochs as in the middle panel. At early time, the gas is highly irregular and chaotic. By $t_{\text{lookback}} \sim 6\,\text{Gyr}$ ($z \sim 0.7$), the gas eventually formed a disk.

galaxy in six different $z = 0$ age intervals. The top and bottom panels show the stellar surface density viewed face-on and edge-on, respectively. The thickness increases with stellar age, from a thin disk-like structure to more spheroidal morphology, broadly consistent with the MW (Bovy et al. 2012) and other simulations (e.g., Brook et al. 2012b; Bird et al. 2013; Stinson et al. 2013b; Minchev et al. 2013; Martig et al. 2014a). On the other hand, the radial morphology first shrinks with increasing age ('inside-out' growth), but then becomes less concentrated for ages greater than 8 Gyr, leaving intermediate-age stars (age $\sim$ 6 Gyr) the most radially concentrated. This is in contrast with the results in Bovy et al. (2012) and other simulations where the scale length decreases monotonically with stellar age (oldest stars have the smallest scale lengths). This directly owes to a minor merger in the simulation around lookback time $t_{\mathrm{lookback}} \sim 6$ Gyr ($z \sim 0.7$), which drove a concentrated nuclear starburst. Afterwards, the disk formed inside out.

The middle panel in Fig. 4.1 shows the stellar morphologies for the same stars shown in the top panel (divided into the same $z = 0$ age intervals), but viewed at the epoch when they just formed (labeled by look-back time). In other words, we trace the galaxy back to these epochs, and show the young stars in the main progenitor galaxy at that time. Stars older than 8 Gyr were born to be a chaotic, non-disk-like structure. For illustrative purposes, we also show gas morphologies at the same epochs in the bottom panel in Fig. 4.1. During the early stage of galaxy assembly when the stellar mass was sufficiently low, this galaxy experienced bursty, chaotic star formation (Sparre et al. 2017). Starbursts drive bursts of gas outflows with high efficiency (Muratov et al. 2015), and the bursty outflows in turn modify the potential and cause radial migration of stars, resulting in radial expansion and quasi-spherical morphology for stars older than 8 Gyr (El-Badry et al. 2016). A gas disk is formed by $t_{\mathrm{lookback}} \sim 6$ Gyr ($z \sim 0.7$). Below $t_{\mathrm{lookback}} \lesssim 6$ Gyr, star formation takes place in a relatively calm mode, with stars forming in a relatively stable disk at a rate self-regulated by feedback, and there are no longer large scale outflows (Muratov et al. 2015; Anglés-Alcázar et al. 2017a). Hayward & Hopkins (2017) proposed an analytic model and argued that such bursty-to-calm transition is expected in massive galaxies at late times, due to the change of ISM structure at low gas fractions.

We estimate the fraction of stars that comes from mergers or tidally disrupted satellites, i.e., stars formed outside the main progenitor galaxy, using the particle tracking technique developed by and presented in Anglés-Alcázar et al. (2017a). We find that only $\lesssim 10\%$ of the stellar mass in the $z = 0$ galaxy was formed *ex situ* and

this contribution is only significant far above the galactic plane ($|Z| \gtrsim 5\,\mathrm{kpc}$). For example, during the last minor merger at $t_{\mathrm{lookback}} \sim 6\,\mathrm{Gyr}$ ($z \sim 0.7$), the passing-by satellite has been tidally disrupted and its stars are re-distributed in the diffuse halo. Within the galactic disk, which we select to be in galactocentric radius $R = 4$–$14\,\mathrm{kpc}$ and $|Z| < 3\,\mathrm{kpc}$ (to exclude bulge and halo stars), stars that were formed *ex situ* contribute no more than a few percent of the stellar mass, so we will ignore them in the analysis below.

4.3.2 Disk Structure

One common argument for the presence of a thick disk in the MW and nearby disk galaxies is that the stellar density profile along the $|Z|$-direction cannot be well-described by a single-component profile

$$\rho_*(|Z|) = \rho_*(0)\,\mathrm{sech}^2\left(\frac{|Z|}{2Z_H}\right), \tag{4.1}$$

where Z_H is the scale height, but requires a second component

$$\rho_*(|Z|) = \rho_{*,1}(0)\,\mathrm{sech}^2\left(\frac{|Z|}{2Z_{H,1}}\right) + \rho_{*,2}(0)\,\mathrm{sech}^2\left(\frac{|Z|}{2Z_{H,2}}\right) \tag{4.2}$$

(e.g., Gilmore & Reid 1983; Yoachim & Dalcanton 2006; Comerón et al. 2011, 2012). In Fig. 4.2, we show the vertical stellar density profile $\rho_*(|Z|)$ at $R \sim 8\,\mathrm{kpc}$ in our simulation (black dots) at $z = 0$ and fit it with a single-component profile (grey dotted line) and a two-component profile (black dashed line), respectively. The dark green and brown lines show the thin- and thick-components, respectively.

We find that a two-component profile provides a much better fit than a single-component profile. The two components, which we refer as the 'thin' and 'thick' disks, have scale heights of $Z_{H,1} \sim 300\,\mathrm{pc}$ and $Z_{H,2} \sim 1.1\,\mathrm{kpc}$, respectively, close to the observed MW-disk scale heights around the solar neighborhood ($300\,\mathrm{pc}$ and $1450\,\mathrm{pc}$, e.g., Gilmore & Reid 1983). Derived from the profile fitting, the thick disk component contributes 36% of the stellar mass at $R = 8\,\mathrm{kpc}$, broadly in agreement with measurements of nearby edge-on disk galaxies (e.g., Yoachim & Dalcanton 2006) as well as other simulations (e.g., Brook et al. 2012b; Bird et al. 2013; Minchev et al. 2013). Note that this is far greater than the fraction of stars that were formed *ex situ*, which is $\lesssim 5\%$ at $R = 8\,\mathrm{kpc}$, so the 'thick disk' in our simulation does not originate from accreted satellite galaxies.

In Fig. 4.2, we further decompose the density profile into five bins according to stellar age (open symbols). Qualitatively, the thickness of stars increases with age,
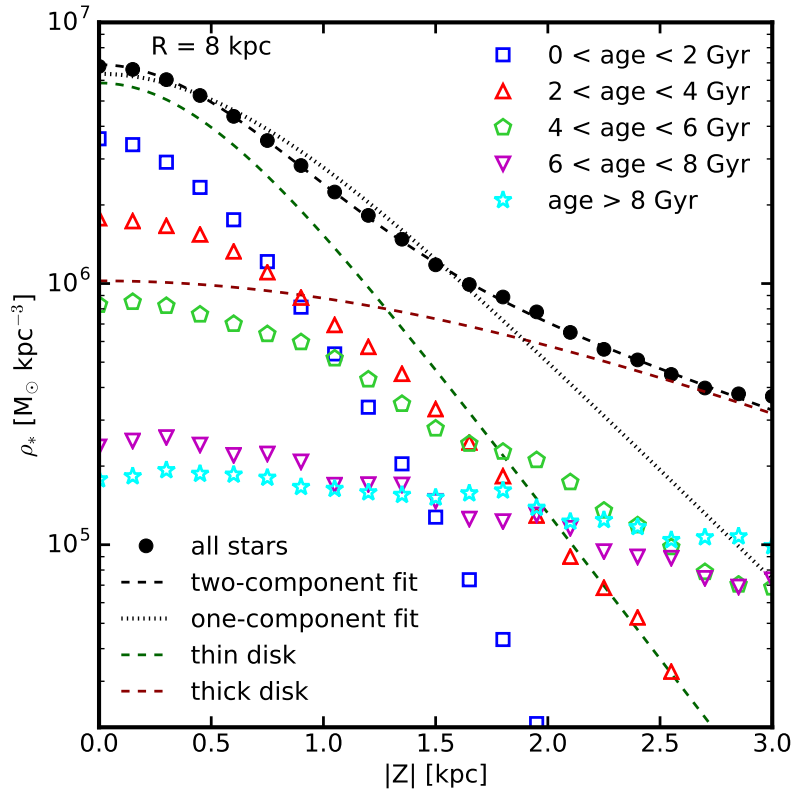
Figure 4.2: Vertical stellar density profile $\rho_*(|Z|)$ at $R = 8$ kpc (black points) in the simulation at $z = 0$. The density profile cannot be well described by a single-component profile (Eqn. 4.1, black dotted line), while a two-component profile provides a good fit (Eqn. 4.2, black dashed line). The dark green and brown dashed lines show the thin- and thick-disk profiles from the fitting. The 'thin' and 'thick' disks have scale heights of 300 pc and 1.1 kpc, respectively, close to the MW scale heights around the solar neighborhood (300 pc and 1450 pc, e.g., Gilmore & Reid 1983). The 'thick disk' contributes 36% of the total stellar mass around $R = 8$ kpc. Note that the stellar densities, thin- and thick-disk scale heights, and the mass fraction of the thick disk in our simulation are in good agreement with observations and other simulations in the literature. The open symbols show the density of stars in different age intervals. Stars younger than 4 Gyr contribute more than 90% of the mass in the 'thin disk', while the 'thick disk' is made almost entirely of stars older than 4 Gyr.
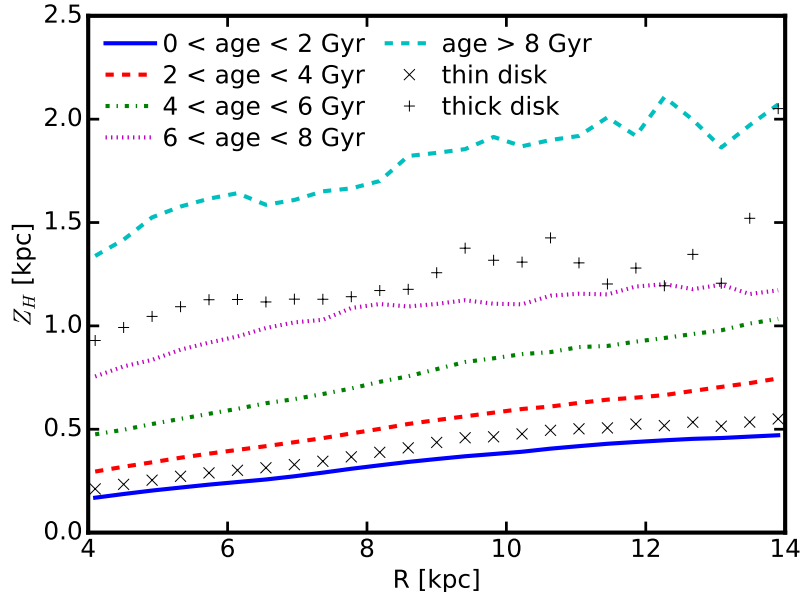
Figure 4.3: Scale heights of stars in five age intervals, as a function of galactocentric radius in the disk. Each population can be well-described by a single-component profile from Equation (4.1). At fixed radius, Z_H increases with stellar age. For a given population, Z_H increases with R. The cross and plus symbols show the scale heights of the thin- and thick-disk component, respectively. At all radii, the 'thin disk' has a scale height close to that of stars younger than 4 Gyr.

with youngest stars being most concentrated to the mid-plane and the oldest stars being most vertically extended. This is consistent with the visualization shown in Fig. 4.1. We find that over 90% of the mass in the 'thin disk' is contributed by stars younger than 4 Gyr, while the 'thick disk' is made of stars older than 4 Gyr. Note that our thin-to-thick disk decomposition is purely based on the mass density at this point. In Section 4.4.1, we will further discuss the formation mechanisms of both components.

Stars in each age interval in Fig. 4.2 can be well-described by a single-component profile from Equation 4.1 (see also, e.g., Bird et al. 2013; Martig et al. 2014a; Minchev et al. 2013, 2015). In Fig. 4.3, we further show Z_H as a function of R for stars in all five age intervals. Only $R = 4$–14 kpc is shown to minimize contamination from the bulge component, which is important within $R < 4$ kpc. Stars older than 8 Gyr have very large scale heights ($Z_H > 1.5$ kpc), since they were formed during the chaotic phase and have relaxed to be quasi-spherical by $z = 0$. Stars younger than 6 Gyr have considerably smaller scale heights, since they were formed in a disk. Even for these stars, the scale heights increase with stellar age at

any radius. For example, the scale heights of stars with age 4–6 Gyr are larger than those of stars with age < 2 Gyr by a factor of 2. Note that this is equivalent to the observed age–velocity dispersion relation (e.g., Nordström et al. 2004), since the vertical velocity dispersion is proportional to disk thickness as expected from disk equilibrium. For comparison, we also show the scale heights of the 'thin' and 'thick' disks as a function of galactocentric radius (black cross and plus symbols). At all radii, the 'thin disk' scale heights are comparable to those of stars younger than 4 Gyr ($Z_{H,1}$ = 200–500 pc), while the 'thick disk' represents a median stellar age of 8 Gyr ($Z_{H,2}$ = 1–1.5 kpc). Moreover, the disk is flaring for stars younger than 6 Gyr – the scale height increases with R, with Z_H being a factor of 2 larger at R = 14 kpc than that at R = 4 kpc. The disk flaring broadly agrees with observations in the MW stellar disk (e.g., Momany et al. 2006; Kalberla et al. 2014; López-Corredoira & Molgó 2014; Bovy et al. 2016).

4.3.3 Age and Metallicity Gradients

In Fig. 4.4, we show the median stellar age as a function of galactocentric radius R and height $|Z|$ (upper panel) for R = 0–15 kpc and $|Z|$ = 0–5 kpc in our simulation at z = 0. At each radius, the median stellar age increases with $|Z|$, resulting in a significant positive vertical age gradient in the disk. Moreover, there is also a moderate negative radial age gradient above the mid-plane, as the median stellar age decreases with R at fixed $|Z|$. These features naturally follow the disk structure presented above: (1) differential scale heights of stars in different age intervals and (2) the disk flaring for any single-age stellar population. These results are in line with predictions from Minchev et al. (2015) and observations from Martig et al. (2016). In Fig. 4.4, we also show the mass-weighted mean stellar metallicity as a function of R and $|Z|$ (bottom panel). Qualitatively, the stellar metallicity is higher at the inner disk and near the mid-plane than at the outer disk and large heights.

In Fig. 4.5, we further show the radial metallicity gradient d[M/H]/dR as a function of height $|Z|$ (left panel) and vertical metallicity gradient d[M/H]/d$|Z|$ as a function of galactocentric radius R (right panel). The black dashed lines show the values measured in the z = 0 snapshot of our simulation. The radial metallicity gradient at a certain $|Z|$ is measured using stars in a layer of thickness $\Delta|Z|$ = 0.5 kpc and by fitting the radial metallicity profile from R = 4–14 kpc with a simple linear function. For vertical metallicity gradients, we use stars in annuli of ΔR = 1 kpc and fit the vertical metallicity profile from $|Z|$ = 0–2.5 kpc with a linear function. We take all star particles into account.
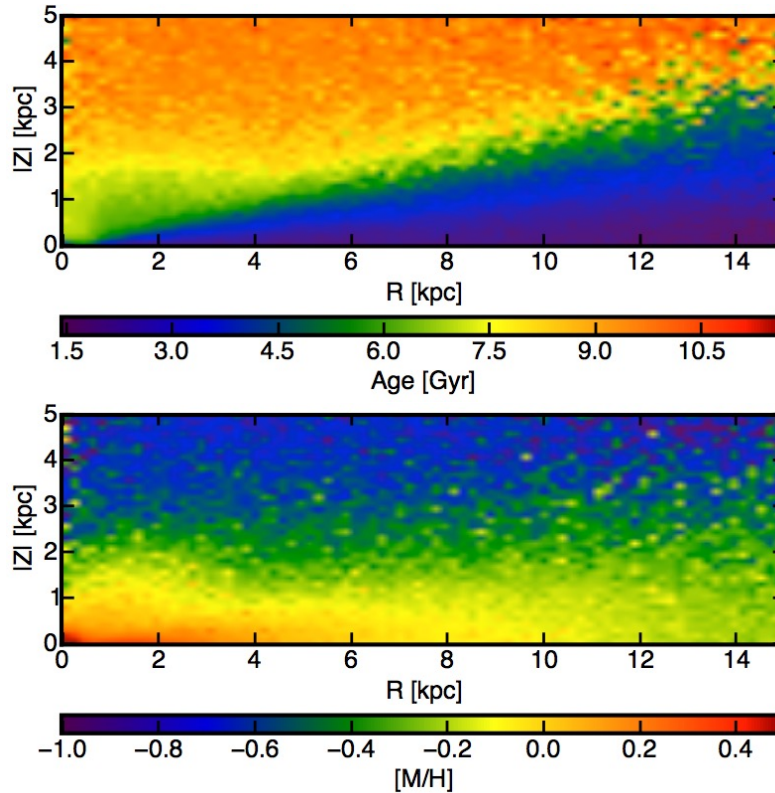
Figure 4.4: *Top:* Median stellar age as a function of R and $|Z|$. The median stellar age naturally follows the disk structure. At fixed radius, stellar age increases with $|Z|$. Above the mid-plane, the stellar age decreases with R due to disk flaring. *Bottom:* Stellar metallicity in the disk. [M/H] is higher at the inner disk and near the mid-plane than at the outer disk and large heights.

In Fig. 4.5, we also compare our results with published radial and vertical metallicity gradients measured from different samples of MW stars in the literature (Cheng et al. 2012; Carrell et al. 2012; Boeche et al. 2014; Anders et al. 2014; Hayden et al. 2014). The horizontal error bars show the R or $|Z|$ interval where the metallicity gradient is measured. Our simulation is qualitatively consistent with observations, despite the fact that the slopes are not identical – d[M/H]/dR = -0.03 dex kpc^{-1} at $|Z| < 0.5$ kpc is shallower than the canonical MW value of -0.06 dex kpc^{-1}, but is close or slightly steeper than that of -0.02 dex kpc^{-1} in M31 (e.g., Gregersen et al. 2015). It is difficult to know whether this discrepancy is meaningful, without a large, statistically significant sample (both simulated and observed). We find that the radial gradient is negative and steepest near the mid-plane, gradually flattens, and finally becomes positive above $|Z| \gtrsim 1.5$ kpc, as observed in the MW (e.g., Cheng et al. 2012; Boeche et al. 2014; Anders et al. 2014) and predicted in other
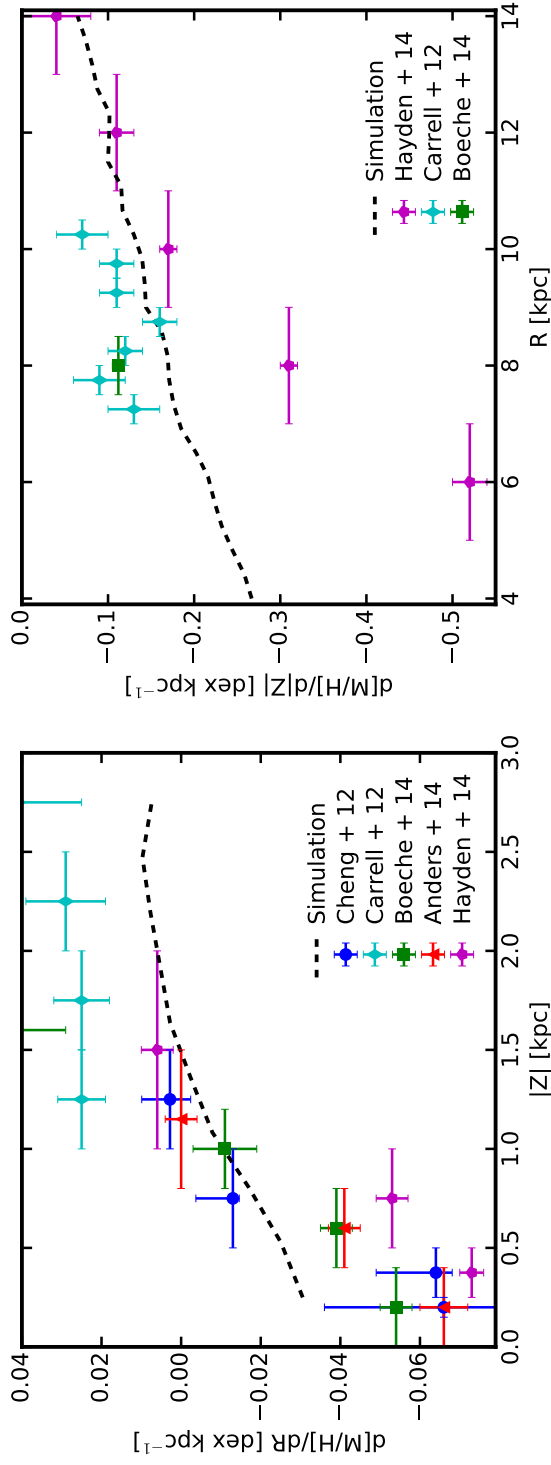
Figure 4.5: *Left:* Radial metallicity gradient d[M/H]/d*R* as a function of height |Z|. *Right:* Vertical metallicity gradient d[M/H]/d|Z| as a function of galactocentric radius *R*. d[M/H]/d*R* is negative at all radii, but is stronger at smaller radii. d[M/H]/d|Z| is negative at the mid-plane, gradually increases with |Z|, and eventually becomes positive above |Z| ~ 1.5 kpc. A number of observations in the MW disk. These trends are qualitatively consistent with observations in the MW disk. A number of observations are shown, including Cheng et al. (2012), Carrell et al. (2012), Boeche et al. (2014), Anders et al. (2014), and Hayden et al. (2014).

simulations (e.g., Minchev et al. 2014, 2015). The vertical gradient is negative at any radius between $R = 4$–14 kpc, but is steeper at inner radii. This trend is qualitatively consistent with observations in Hayden et al. (2014).

To understand why the metallicity gradients have such behavior, in Fig. 4.6, we break down the radial (top panels) and vertical (bottom panels) metallicity profiles into four age intervals: age < 2 Gyr (blue dashed lines), $2 <$ age < 4 Gyr (red dotted lines), $4 <$ age < 6 Gyr (green dash-dotted lines), and age > 6 Gyr (magenta dashed lines). The black lines show the metallicity profile of all stars. To leading order, metallicity is a proxy of stellar age, with young stars being more metal-enriched than old stars (also see Section 4.4.3). The top panels in Fig. 4.6 show the radial metallicity profiles from $R = 4$–14 kpc in three layers: $0 < |Z| < 0.5$ kpc, $1.0 < |Z| < 1.5$ kpc, and $2.0 < |Z| < 2.5$ kpc. The flattening and inversion of the radial metallicity gradient can be naturally understood from the negative age gradient at large heights. For example, in the $2.0 < |Z| < 2.5$ kpc layer, old, metal-poor stars dominate at $R = 4$ (where the disk scale heights of young stars are small, i.e., $Z_H \sim 0.3$ kpc), while younger, more metal-enriched stars take over at much larger radius (where the young stellar disk is thicker in absolute units, e.g., $Z_H \sim 1$ kpc at $R = 14$ kpc). This leads to an overall positive radial metallicity gradient at this fixed height. Note that our interpretations here agree well with the chemo-dynamical model in Minchev et al. (2014, fig. 10). The bottom panels in Fig. 4.6 show the vertical metallicity profile at $R = 6$, 10, and 14 kpc, respectively. The reasons why the vertical metallicity gradient flattens at large radius are twofold: (1) the metallicity of young stars is lower at larger radius than at small radius and (2) the age gradient is much weaker at larger radius.

The negative radial metallicity gradient for stars younger than 6 Gyr (those formed in a disk) near the mid-plane is inherited from the parent star-forming gas disk (Ma et al. 2017b). A negative radial metallicity gradient is expected from the coevolution between the gas disk and stellar disk (e.g., Ho et al. 2015). In short, suppose a pure gas disk has formed with an exponential surface density profile and begun to form stars. The star formation efficiency is higher at the inner disk than at the outer disk according to the observed Kennicutt–Schmidt law (Kennicutt 1998). Under the local closed-box assumption, the inner disk would be enriched more rapidly than the outer disk, leading to a negative radial metallicity gradient in the disk. Nonetheless, the slope of such a gradient can be affected by disk scale length, radial inflow and mixing, disk pre-enrichment, etc. A comprehensive analysis of the radial metallicity
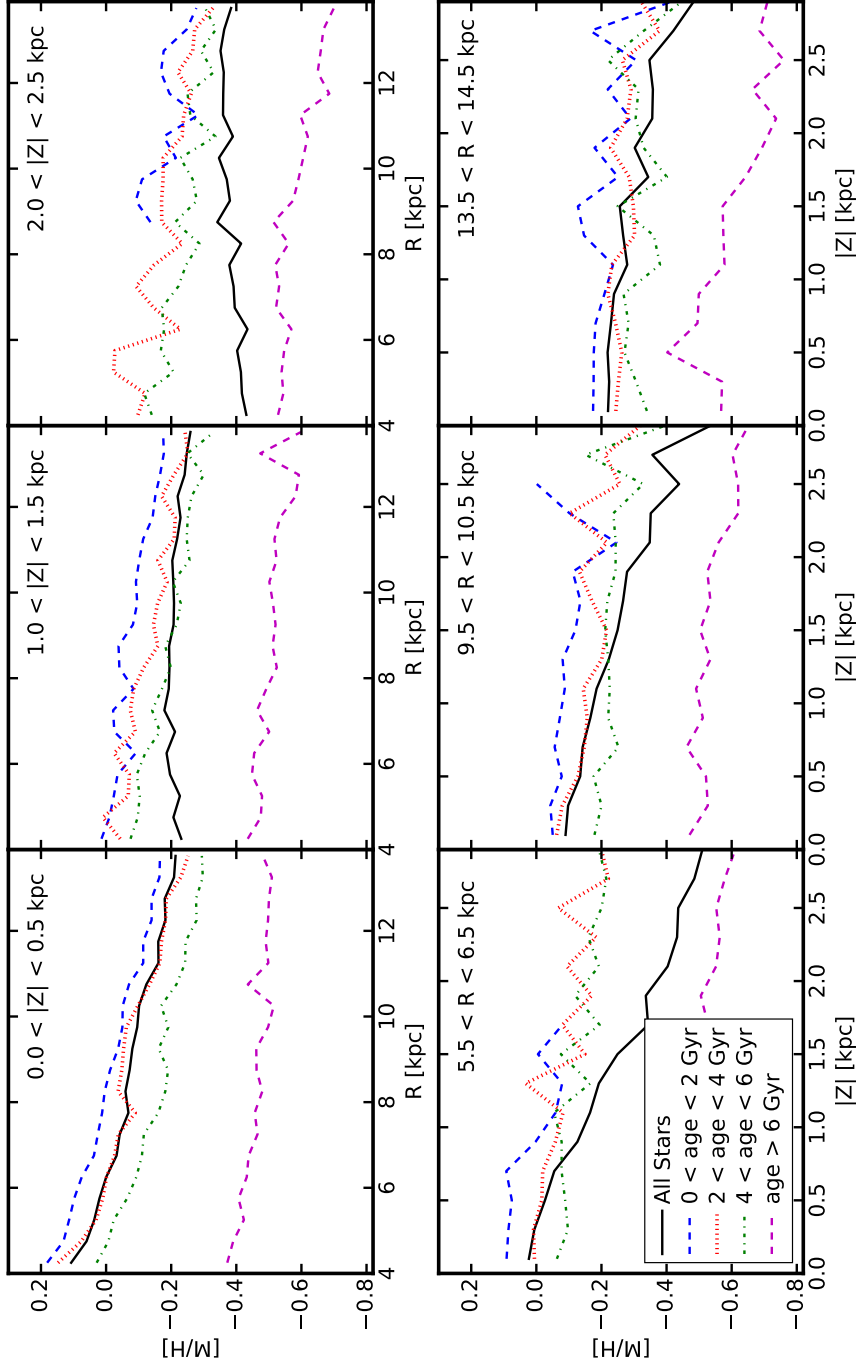
Figure 4.6: *Top:* Radial metallicity profile in layers with $|Z| = 0$–0.5, 1.0–1.5, and 2.0–2.5 kpc. *Bottom:* Vertical metallicity profile at radii $R = 6$, 10, 14 kpc. We show the metallicity profiles for all stars (black solid lines) as well as in bins of different stellar ages. The flattening and inversion of the radial metallicity gradient at high $|Z|$ follows the negative age gradient at these heights. The steepening of the vertical metallicity gradient at smaller radii results from a stronger age gradient. The stellar age gradient is a natural consequence of disk structure. These results are in line with the predictions in Minchev et al. (2014, fig. 10).

gradient and its dependence on galaxy properties with a larger sample of simulations is presented in a companion study (Ma et al. 2017b).

4.3.4 Dynamical Evolution of the Stellar Disk

In Section 4.3.2, we show that even for stars that are initially formed in a disk (i.e., stars younger than age ~ 6 Gyr by $z = 0$), by $z = 0$, their scale height increases with stellar age at all radii (Fig. 4.3). To explain this, we first explore the scale heights of stars at the time when they just formed. In the left panel in Fig. 4.7, we show the scale heights for stars in three $z = 0$ age intervals: 0–2 Gyr, 2–4 Gyr, and 4–6 Gyr, but measured just after their formation time (labeled by lookback time). In other words, these stars are younger than 2 Gyr at the time we measure their scale heights. The newly formed stars inherit the scale heights and velocity dispersion from the cold star-forming gas in the disk where they were born. In general, stars formed earlier (which are older today) were born with larger scale heights than stars formed at late times. For example, stars with $z = 0$ age 4–6 Gyr (formation time at $t_{\mathrm{lookback}} = 4$ Gyr) were born with a scale height of $Z_H \sim 0.4$ (0.8) kpc at $R = 4$ (14) kpc at this epoch, larger by a factor of ~ 2 compared to the 'at birth' scale heights of stars formed at $z = 0$. This naturally follows the evolution of the gas disk, because the thickness of a star-forming disk, where self-regulation by feedback yields a Toomre parameter $Q \sim 1$, is proportional to its gas fraction (e.g., Thompson et al. 2005; Faucher-Giguère et al. 2013), which is higher at early times.

We now examine how the scale height evolves over time. In the right panel in Fig. 4.7, we show the scale heights at three post-formation epochs (labeled by lookback time), for stars in the $z = 0$ age interval 4–6 Gyr. At all radii, the scale height increases by $\sim 30\%$ (or ~ 0.2 kpc in absolute units) over the 4 Gyr from their formation time to $z = 0$. During the same period, the vertical velocity dispersion has also increased consistently. Our simulation shows that kinematic heating plays a non-negligible role in the formation of the thick disk, in line with the predictions in Minchev et al. (2013) and Martig et al. (2014b), but in contrast with the argument in Bird et al. (2013).

Several mechanisms have been proposed to cause such kinematic heating, including (1) bars and spiral arms (e.g., Sellwood & Carlberg 1984; Minchev & Quillen 2006; Saha et al. 2010; Faure et al. 2014; Yurin & Springel 2015; Grand et al. 2016), (2) radial migration (e.g., Schönrich & Binney 2009b; Loebman et al. 2011; however, see e.g., Minchev et al. 2012; Vera-Ciro et al. 2014; Grand et al. 2016), (3)
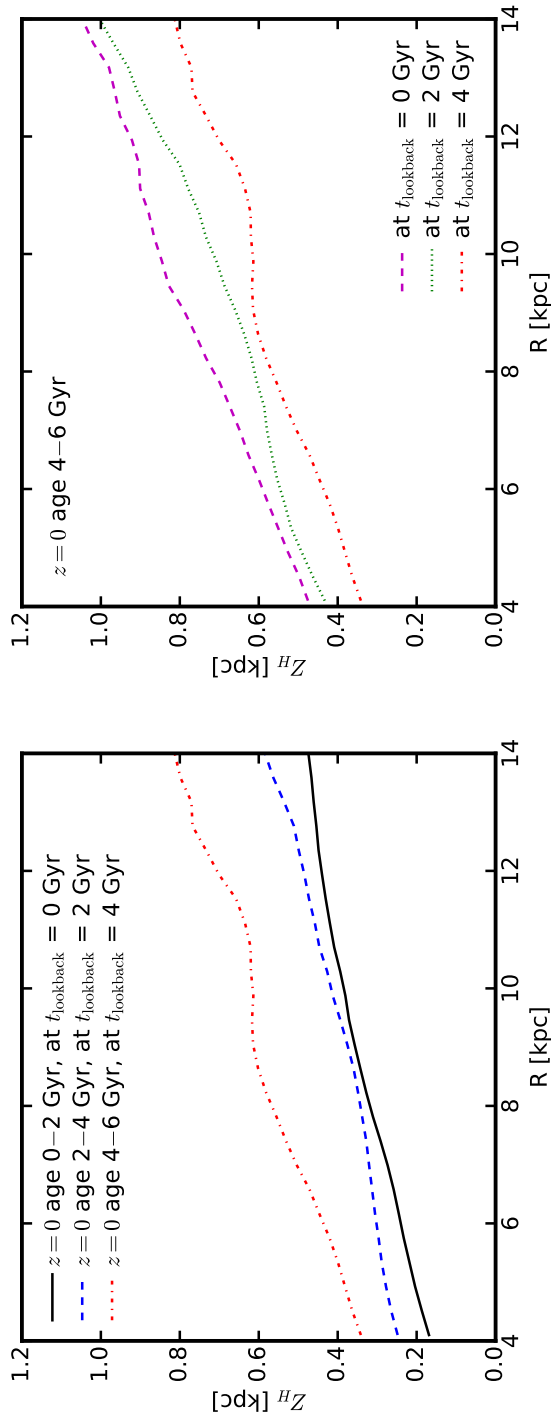
Figure 4.7: *Left*: Scale heights of stars in three $z = 0$ age intervals (0–2, 2–4, 4–6 Gyr), measured at the epoch when the stars formed (labeled by lookback time). *Right*: The evolution of scale heights for stars of age 4–6 Gyr at $z = 0$, as they would be observed at three different epochs (labeled by lookback time) after their formation. Stars formed at an early epoch were born in a thicker disk than those formed at later times, because the star-forming disk was more gas-rich and therefore turbulent. The scale heights of those populations then increase with time due to kinematic heating.

perturbation of satellites and sub-halos (e.g., Quinn et al. 1993; Kazantzidis et al. 2008; Purcell et al. 2009; Gómez et al. 2013), and (4) scattering by giant molecular clouds (GMCs) or star clusters (e.g., Spitzer & Schwarzschild 1951, 1953; Aumer et al. 2016). In a cosmological context, these mechanisms are usually combined and difficult to isolate in practice. For example, gravitational perturbation of satellites can induce bars and spiral arms (e.g., Purcell et al. 2011), which further result in kinematic heating and radial migration (Lynden-Bell & Kalnajs 1972). Scattering by massive GMCs is also needed to redistribute the energy between planar and vertical motions (Carlberg 1987). In our simulation, the increase of disk thickness and velocity dispersion is roughly a linear function of time, indicating that spiral arms may be the dominant heating mechanism, as suggested by an analysis of a large sample of disk galaxy simulations (Grand et al. 2016).

The flaring of the stellar disk is present 'at birth' and preserved during kinematic heating. At their formation time, stars inherited the flaring of their parent gas disk, which is likely to be a natural consequence of hydrostatic equilibrium in a galactic potential (e.g., Olling 1995; O'Brien et al. 2010; Allaert et al. 2015), although disk flaring may also be induced and enhanced by mergers (e.g., Bournaud et al. 2009; Purcell et al. 2011) and radial migration (e.g., Minchev et al. 2012).

4.4 Discussion

In this section, we discuss some observational and theoretical implications of our simulation. Although our analysis in Section 4.3 is based on a single simulation, preliminary analysis of several other MW-mass disk galaxy simulations indicates that the disk structure and dynamic evolution are similar in other systems, including one using 8 times higher mass resolution from Wetzel et al. (2016, see Appendix for more details), despite the fact that these simulations are run with a different hydrodynamic method and slightly modified numerical implementations of the feedback model (the FIRE-2 code, see Hopkins et al. 2017). This suggests that the results presented in Section 4.3 are typical in similar systems and insensitive to resolution and numerical method, as implied also by the good agreement between our results and many other simulations (e.g., Brook et al. 2012b; Minchev et al. 2013, 2014; Martig et al. 2014a,b). This is expected since our key results are derived from global processes and can be understood with simple analytic models, including (1) star formation is bursty at high redshift and becomes relatively stable at late times, (2) the thickness of the star-forming gas disk decreases at low gas fraction, and (3) the kinematic heating is continuously present from spiral structure, bars, GMCs, etc. Therefore,

Figure 4.8: Scale heights as a function of stellar age at $R = 5$, 9, and 13 kpc. The cross and plus symbols show the scale heights of the 'thin' and 'thick' components obtained from the profile fitting (e.g., see Fig. 4.2) at three radii, but we intentionally select their x-coordinates to match the curve. At all radii, the scale heights increase dramatically above stellar age 6 Gyr, since these stars were formed in a chaotic, bursty mode. In terms of mass density, the thin and thick disks can be separated by stars younger and older than 4 Gyr, as illustrated by the vertical dotted line. The thick disk defined in this way contains two distinct populations of stars: (1) stars older than 6 Gyr which were formed in the chaotic, bursty mode and (2) stars in 4–6 Gyr age interval that were formed in a gas-rich disk and kinematically heated after their formation. Note that the gas disk evolved smoothly during the past 6 Gyr, so there is no sharp transition at 4 Gyr ago when the thin disk at $z = 0$ started to form.

they should be independent of the subtle difference in the numerical details of small-scale physics. A comprehensive analysis on disk morphology and its dependence on galaxy formation history using an enlarged sample of galaxies will be the subject of a future study.

4.4.1 The thin and thick disks

In Section 4.3.2, we show that the vertical stellar density profile in the simulation can be well described by a two-component function (Fig. 4.2), which we refer to as the traditional thin disk ($Z_H \sim 200$–500 pc) and thick disk ($Z_H \sim 1$–1.5 kpc) (e.g., Gilmore & Reid 1983). In terms of mass density, the thin and thick disks in our simulation can be roughly divided into stars younger and older than 4 Gyr,

respectively.

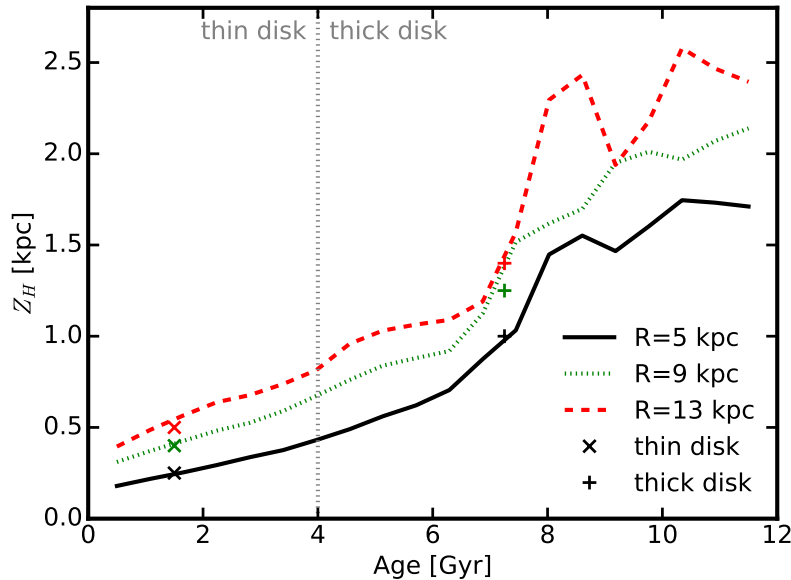We first discuss the formation mechanisms of the thick disk. In Fig. 4.8, we show the scale heights as a function of stellar age at three radii $R = 5$, 9, and 13 kpc. The cross and plus symbols represent the scale heights of the thin and thick components, respectfully, as obtained from profile fitting. The vertical dotted line located at 4 Gyr illustrates the separation of the thin and thick disks. The thick disk contains two distinct populations. First, about two thirds of the stars in the thick disk are older than 6 Gyr (formation redshift $z \gtrsim 0.7$). These were formed during the chaotic, bursty phase in the galaxy progenitor (Fig. 4.1). This agrees with the picture proposed in Brook et al. (2004). These stars have very large scale heights, as shown in Fig 4.8. Second, the other 1/3 of the stars in the thick disk are in the 4–6 Gyr age interval, which were formed in a relatively calm, stable disk. The disk was more gas-rich and turbulent at early times, however, so the stars were formed thick 'at birth', as proposed in Bournaud et al. (2009). Furthermore, these stars continued to be kinematically heated into a thicker spatial distribution after forming. Therefore, the thick disk in our simulation is a mix of stars older than 4 Gyr, which formed through a combination of several mechanisms.

Regarding the formation of the thin disk, we note that the gas disk smoothly became thinner down to $z = 0$, thus forming the thin disk at late times. There is no sharp transition about 4 Gyr ago when the thin disk at $z = 0$ started to form.

In the literature, some authors have claimed that there is a tension between preserving thin disks and the necessity of strong stellar feedback to prevent galaxies from forming too many stars in cosmological simulations (e.g., Roškar et al. 2014). However, our simulation simultaneously forms a thin-disk component while producing a reasonable stellar mass and star formation history in good agreement with observational constraints (Hopkins et al. 2014). These results demonstrate that it is possible to form thin disks in cosmological simulations, even in the presence of strong stellar feedback. This is due to the fact that (1) our simulation has sufficient spatial resolution (smoothing length far less than the vertical scale heights of the thin disk), (2) we allow gas to cool to very low temperatures to explicitly resolve the cold, star-forming gas, and (3) the high resolution and the physically motivated star formation and feedback models adopted in the simulation allow one to explicitly resolve the launching and venting of galactic winds without disrupting the entire galaxy. Likewise, Agertz & Kravtsov (2015, 2016) also found that their simulation can form a thin disk when using feedback recipes similar to ours but fail to do so

using other feedback models.

4.4.2 Stellar Migration in the Disk

It has been proposed that radial migration of stars in the disk due to angular momentum exchange may be an important mechanism of disk heating that also flattens the stellar metallicity gradients (e.g., Schönrich & Binney 2009a,b; Loebman et al. 2011). Recent numerical calculations suggest, however, that radial migration has little impact on the disk thickening (e.g., Minchev et al. 2012; Martig et al. 2014b; Vera-Ciro et al. 2014; Grand et al. 2016; Aumer et al. 2016). Nonetheless, radial migration can still occur when spiral arms and bars are present (via corotation resonance of transient spirals, e.g., Lynden-Bell & Kalnajs 1972; Sellwood & Binney 2002, or induced by long-lived spiral- or bar-like structures, e.g., Minchev & Famaey 2010; Minchev et al. 2011), while spiral arms and bars are suggested to be the dominant mechanism of disk heating (e.g., Grand et al. 2016).

In our simulation, stars older than $8\,\text{Gyr}$ show strong radial migration, because the bursty gas outflows driven by stellar feedback generate large fluctuations in the galactic potential, causing old stars to migrate toward large radius (El-Badry et al. 2016). This is important to shape the global structure of the disk (e.g., Minchev et al. 2015). However, this is a very different mechanism from the standard radial migration within a stable disk. To test the standard migration scenario, we study stars in the $z = 0$ age interval 4–6 Gyr. First, we go back to the snapshot at $t_{\text{lookback}} = 4\,\text{Gyr}$ and select stars in three annuli centered at $R = 5, 9$, and $13\,\text{kpc}$ with 1 kpc width near the disk plane ($|Z| < 0.5\,\text{kpc}$) at that epoch. In the left panel in Fig. 4.9, we show the distribution of galactocentric radius R for these stars by $z = 0$. Stars in a given annulus 4 Gyr ago have a wide distribution in R by $z = 0$. Only a small fraction (less than 10%) of stars have migrated to very large radii ($\Delta R > 5\,\text{kpc}$), while more than half of the stars have migrated inward ($\Delta R < 0$). This is expected from the exchange of angular momentum between stars, because outward-migrating stars carry more angular momentum, so more stars migrate inward. In the right panel, we show the stellar surface density and metallicity profiles in $R = 4$–14 kpc for all stars with $z = 0$ age 4–6 Gyr, measured at three epochs ($t_{\text{lookback}} = 0, 2$, and 4 Gyr). The surface density does not change by more than 0.05 dex during the past 4 Gyr (stellar mass loss is subdominant). The average stellar metallicity has increased at large radii, resulting in a flattening of metallicity gradient by $0.01\,\text{dex}\,\text{kpc}^{-1}$. Our results suggest that radial migration is common, but only has a weak net effect on the late-time global properties (mass density, metallicity profiles) of the galactic disk,
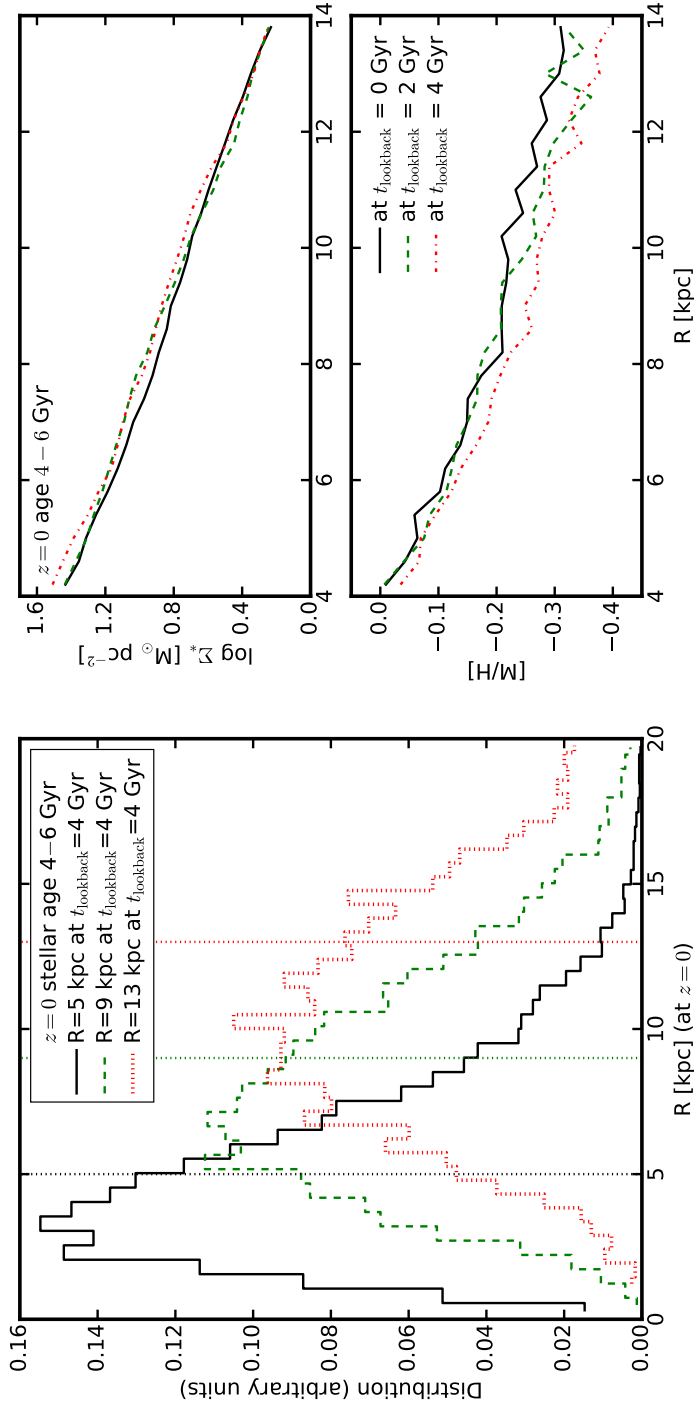
Figure 4.9: *Left:* Distribution of galactocentric radius at z = 0 for stars in the age interval 4–6 Gyr that were located in three annuli centered at R = 5, 9, and 13 kpc (of 1 kpc width) near the disk mid-plane ($|Z| < 0.5$ kpc) at $t_{lookback} = 4$ Gyr. Stars in a given annulus 4 Gyr ago have a wide distribution in R by z = 0. A small fraction (less than 10%) of stars have migrated to very large radii ($\Delta R > 5$ kpc), while more than half of the stars have moved inward ($\Delta R < 0$), as expected from exchange of angular momentum. *Right:* Stellar surface density (top) and metallicity (bottom) profiles from R = 4–14 kpc for all stars with z = 0 age 4–6 Gyr, but measured at three epochs ($t_{lookback} = 0$, 2, and 4 kpc). The surface density does not change more than 0.05 dex, while the average stellar metallicity slightly increased at large radii, but the net effect of stellar migration on the properties of a galactic disk is weak at late times, in line with the results from other simulations (e.g., Minchev et al. 2013; Grand & Kawata 2016).

consistent with predictions from other works (e.g., Minchev et al. 2013; Grand & Kawata 2016).

4.4.3 Abundance Patterns and Mono-abundance Populations

In the literature, several authors have suggested that mono-abundance populations (stars with certain [M/H] and [α/Fe]) are proxies for single-age populations in the MW (e.g., Bovy et al. 2012; Rix & Bovy 2013). This is important because one cannot infer the assembly history of the MW without reliable information on stellar ages. We first examine the abundance patterns in our simulation. In Fig. 4.10, we show the stellar age–metallicity relation in the left panel for all stars with $R = 4$–14 kpc and $|Z| < 3$ kpc, color-coded by the total stellar mass in each pixel (in logarithmic scale). The white dashed line shows the median relation. In the right panel, we show the distributions of these stars in the [Mg/Fe]–[M/H] plane. Stellar age, metallicity, and [Mg/Fe] correlate with each other to leading order, but with considerable scatter (over 1 dex in [M/H] at a given age). The scatter mainly comes from the presence of metallicity gradients in the disk and non-uniform distribution of metals in the galaxy. We have explicitly checked that including sub-resolution metal diffusion in our simulation (as in Shen et al. 2010) does not dramatically reduce the scatter.

In the left panel in Fig. 4.11, we show the mass-weighted age distribution of stars from four mono-abundance populations selected within a tolerance in metallicity and abundance ratio of Δ[M/H] $= 0.06$ and Δ[Mg/Fe] $= 0.04$. In general, low-metallicity, α-rich populations represent old stars, while high-metallicity, α-poor stars are more biased toward younger populations. In the right panel, we compare three mono-abundance populations at fixed [M/H] but different [Mg/Fe]. We find that low-α populations contain more young stars than α-rich populations. These results marginally support the idea that chemical abundances might represent stellar ages to leading order. However, we caution that for any mono-abundance population, the age distribution is wide (see also Minchev et al. 2017). For example, the most metal-poor and α-rich population still contains a non-negligible fraction of young stars with age 2–6 Gyr. As a consequence, if we repeat our analysis in this paper by breaking the stars into several bins of metallicity instead of stellar age, we obtain more complicated results due to age blending effects. Independent constraints on stellar age are required to break the degeneracy.

Recent observations reveal that MW stars fall into two distinct populations on the
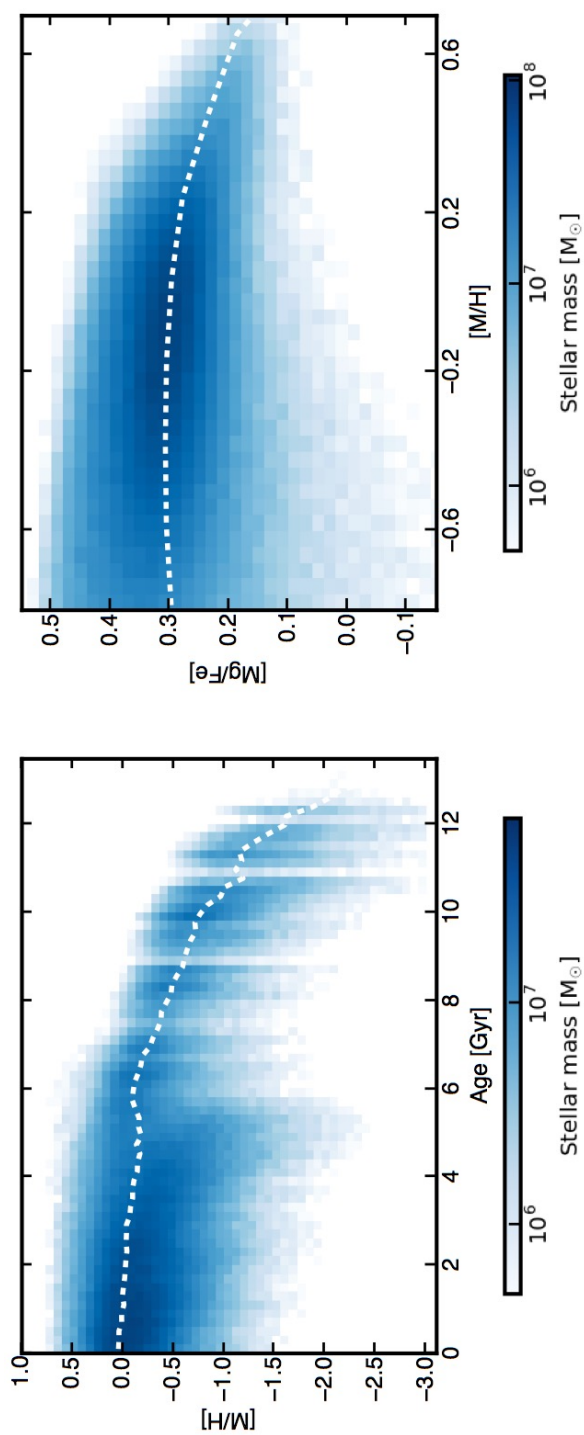
Figure 4.10: *Left*: Stellar age–metallicity relation. *Right*: [Mg/Fe]–[M/H] relation. Colors show the total stellar mass in each pixel (in logarithmic scale). The white dashed lines show the median for each relation. To leading order, stellar age, metallicity, and [Mg/Fe] correlate with each other, but there is large scatter (over 1 dex in [M/H] at a given age).

110
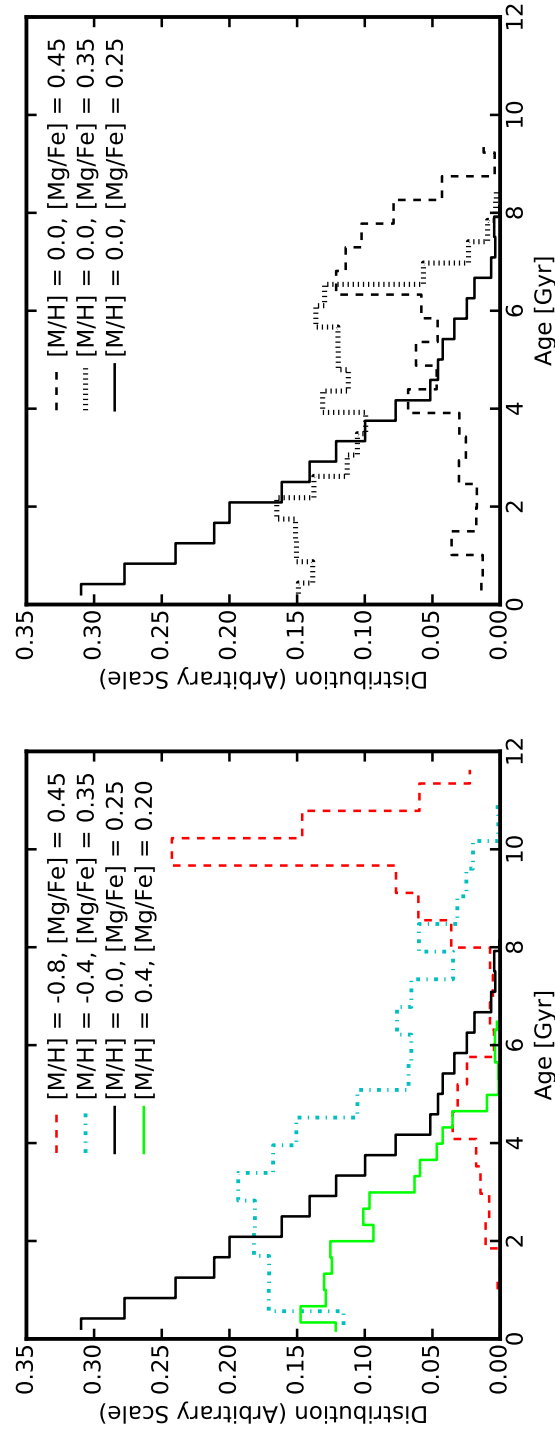
Figure 4.11: Stellar age distribution of six mono-abundance populations in narrow bins with Δ[M/H] = 0.06 and Δ[Mg/Fe] = 0.04. In general, metal-poor, α-rich stars represent older populations than metal-rich, α-poor stars (left panel). At fixed metallicity, α-poor stars are more biased toward younger populations (right panel). However, the age distribution of a mono-abundance population is wide.

[Mg/Fe]–[M/H] plane, known as the high- and low-α populations (e.g., Adibekyan et al. 2013; Bensby et al. 2014; Anders et al. 2014; Nidever et al. 2014; Mikolaitis et al. 2014; Kordopatis et al. 2015). Such feature is difficult to explain and cannot be reproduced by current cosmological simulations (see Nidever et al. 2014, and reference therein), including ours. Nidever et al. (2014) proposed several tentative models to explain how the two populations may form, but all require fine-tuned parameters to match the observed abundance pattern. Nevertheless, we show that in our simulation, star formation has undergone two distinct modes – chaotic, bursty mode at high redshift and relatively calm, stable mode at late times. It is possible that such two-mode formation history may lead to a bimodality in the abundance pattern in very restricted conditions, while in other conditions the two populations may simply merge. Alternatively, the MW may have a very different assembly history from our simulation. In future work, we will study a large sample of simulations of MW-size halos with diverse assembly history and explore if and how such two populations form. Also, spectroscopic survey of stars in extragalactic galaxies with next generation of observational facilities may also reveal whether this is common in MW-mass galaxies or just a unique feature in the MW.

4.4.4 [α/Fe] gradients

There is evidence indicating the presence of an [α/Fe] gradient in the MW disk (e.g., Boeche et al. 2014; Anders et al. 2014; Recio-Blanco et al. 2014), despite the fact that such measurements have large uncertainties. It is clear that the [α/Fe] gradient varies with $|Z|$ in the opposite way to [Fe/H] gradient and that $\mathrm{d}[\alpha/\mathrm{Fe}]/\mathrm{d}R$ is negative at large $|Z|$, but the sign of $\mathrm{d}[\alpha/\mathrm{Fe}]/\mathrm{d}R$ in the disk mid-plane are not fully consistent between various studies. Future spectroscopic surveys that include much larger samples will provide a more robust measurement. Here we use our simulation to make qualitative predictions for [α/Fe] gradients. In Fig. 4.12, we show the radial gradient of [Mg/Fe] as a function of height $|Z|$ (left panel) and the vertical gradient of [Mg/Fe] as a function of radius R (right panel). We find that $\mathrm{d}[\mathrm{Mg/Fe}]/\mathrm{d}R$ is positive near the mid-plane, gradually decreases to zero at about $|Z| = 1.3\,\mathrm{kpc}$, and turns negative at larger heights. Moreover, $\mathrm{d}[\mathrm{Mg/Fe}]/\mathrm{d}|Z|$ is positive at all radii, but is larger at the inner disk than at the outer disk. These are qualitatively similar to the trends of metallicity gradient presented in Section 4.3.3, with the sign flipped following the anti-correlation between [Mg/Fe] and [M/H], as found also in other simulations (e.g., Minchev et al. 2013, 2014). The gradient of [Mg/Fe] is also a consequence of the age gradient in the disk.
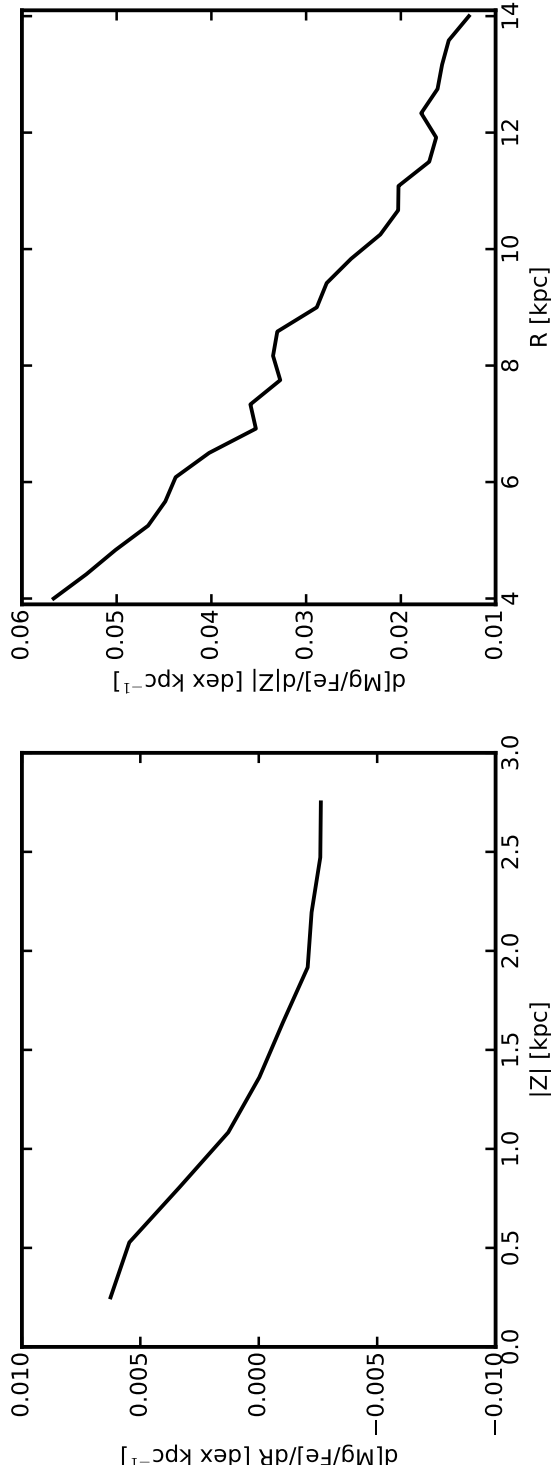
Figure 4.12: *Left*: d[Mg/Fe]/dR as a function of $|Z|$. *Right*: d[Mg/Fe]/d$|Z|$ as a function of R. The radial gradient in [Mg/Fe] is positive at the mid-plane, flattens and becomes negative at larger heights. The vertical gradient in [Mg/Fe] is positive, but is steeper at inner radii than at outer radii. These trends are similar to those of metallicity gradient, but with flipped sign due to the anti-correlation between [Mg/Fe] and metallicity. Both of them arise from the age gradient in the disk, in line with predictions from other simulations (e.g., Minchev et al. 2013, 2014).

4.5 Conclusions

In this work, we have studied the structure, age and metallicity gradients, and dynamical evolution of the stellar disk via a case study of one simulation from the FIRE project, chosen to be a disk galaxy of similar mass to the MW at $z = 0$. The simulation is a cosmological zoom-in simulation that includes physically motivated models of the multi-phase ISM, star formation, and stellar feedback, with parameters taken directly from stellar evolution models. Our main findings include the following:

(i) Stars older than 6 Gyr (formation redshift $z \gtrsim 0.7$) were formed in a violent, bursty mode in a clumpy galaxy progenitor with powerful episodic outflows, and thus have round, puffy morphologies at $z = 0$. Stars younger than 6 Gyr were formed in a relatively calm, well-maintained star-forming disk. By $z = 0$, stars that formed in the chaotic mode have the largest scale heights. Even for those that formed in a disk at late times, their scale heights increase with stellar age at any radius; stars of the same age have larger scale heights in the outer disk than in the inner disk (flaring). As a consequence, the median stellar age increases with $|Z|$ at a fixed radius, but decreases with R in a constant-$|Z|$ layer.

(ii) The radial metallicity gradient is negative at the mid-plane, gradually flattens when moving to larger $|Z|$, and ultimately turns positive at about $|Z| > 1.5$ kpc. The vertical metallicity gradient is negative at all radii, but is stronger at small radii. These trends are qualitatively consistent with observations in the MW. Such variation of metallicity gradient naturally follows the age gradient in the disk, since stellar age, metallicity, and $[\alpha/\text{Fe}]$ all correlate with each other. Similar trends also exist in $[\alpha/\text{Fe}]$ gradients, but with a flipped sign due to the anti-correlation between $[\alpha/\text{Fe}]$ and metallicity.

(iii) For stars that formed within the past 6 Gyr, in a disk, those that formed earlier were thicker 'at birth' than those formed later, because the star-forming disk was more gas-rich and therefore more turbulent and thicker at earlier times (a factor of ~ 2 thicker at 6 Gyr ago). After each population formed, their scale height was further increased via kinematic heating (by $\sim 40\%$ during the past 6 Gyr). In our simulation, the two factors have comparable effect in absolute units on the differential scale heights by $z = 0$.

(iv) The vertical stellar density at $z = 0$ can be well described by a two-component profile, defined as the traditional 'thin disk' (scale heights $Z_H \sim 200$–500 pc) and 'thick disk' ($Z_H \sim 1$–1.5 kpc). The thin and thick disks can be roughly separated

by stars younger and older than 4 Gyr. Two thirds of the stars in the thick disk are formed during the chaotic, bursty phase; the other 1/3 stars in the thick disk are formed in a gas-rich star-forming disk and then were further thickened via kinematic heating. The gas disk smoothly evolves during the past 6 Gyr and forms the thin disk at late times. Therefore, the thick disk is a mix of stars that formed via different mechanisms, while the formation is continuous at the transition time (around 4 Gyr ago) when the $z = 0$ thin-disk stars started to form.

(v) Our simulation demonstrates that it is possible to form a thin disk in sufficiently high-resolution cosmological simulations even in the presence of strong stellar feedback.

Although we only study one simulation in this paper, our main results here are derived from global processes that can be understood with simple analytic arguments, including (1) star formation is bursty at high redshift and becomes relatively stable at late times, (2) the thickness of the star-forming gas disk decreases at low gas fraction, and (3) kinematic heating is continuously present from spiral structure, bars, GMCs, etc. In fact, some of our results agree very well with previous studies by other authors. For instance, almost all simulations of MW analogs show violent merger history at high redshift but relatively quiescent merger history at late times. Most of them form a separate thin and thick disk by $z = 0$, with their scale heights and mass fractions similar to ours (e.g., Brook et al. 2012b; Bird et al. 2013; Minchev et al. 2013; Martig et al. 2014a). Some models also successfully reproduce the observed MW abundance distribution and the variation of stellar metallicity gradients, and attribute these results to the disk formation history (e.g., Minchev et al. 2013, 2014). Therefore, our results further confirm that the physical processes we proposed are common in the assembly histories of disk galaxies, regardless of numerical details and feedback model.

One key prediction of our simulation is that the thick disk does *not* form from a single channel, but it is rather a mixture of stars that formed and evolved in three different ways (see conclusion (iv) and Section 4.4.1 for details). This scenario can be tested by future observations of MW stars if an independent constraint on stellar age can be obtained. For example, we expect the age separation between thin- and thick-disk stars is different from the one between stars that formed in the chaotic mode and in the calm mode. The latter can be identified by a sudden jump in the velocity dispersion as a function of stellar age.

Nevertheless, our simulation is not designed or chosen in any way to be identical

to the MW and differs from it in several aspects. The radial metallicity gradient is $-0.03\,\mathrm{dex\,kpc^{-1}}$ in the disk mid-plane in our simulation, shallower than the $-0.06\,\mathrm{dex\,kpc^{-1}}$ slope in the MW disk (e.g., Cheng et al. 2012). This can be affected by disk scale length, disk pre-enrichment at formation time, the extent of radial mixing, and specific merger or accretion events in the past. Also, our simulation does not show any bimodality in the $[\alpha/\mathrm{Fe}]$–$[\mathrm{M/H}]$ relation, in contrast to some observations of MW stars (e.g., Nidever et al. 2014). Moreover, our simulation does not show a prominent central bar, with which we expect that kinematic heating would be stronger (e.g., Grand et al. 2016). Such differences may originate from details in the assembly history. In future work, we will further explore the disk formation, morphology, and metallicity profile and their dependence on galaxy formation history using an enlarged sample of disk galaxy simulations.

Acknowledgments

Appendix: Resolution test

In this paper, we performed a case study of a cosmological zoom-in simulation that produces a MW-mass disk galaxy at $z = 0$. This simulation is originally presented
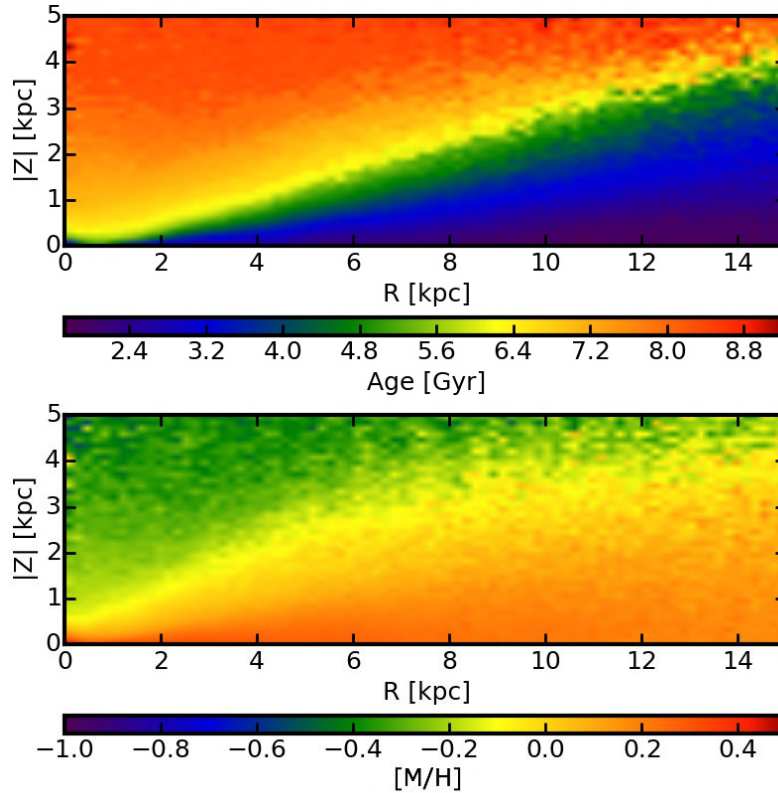
Figure 4.13: The same as Fig. 4.4, but for the ultra-high-resolution simulation presented in Wetzel et al. (2016). The disk structure does not significantly differ from the simulation studied in the paper, although this run has eight times better mass resolution and uses a more accurate hydrodynamic solver.

in Hopkins et al. (2014) and has been thoroughly studied in other work (van de Voort et al. 2015; Faucher-Giguère et al. 2015; Muratov et al. 2015; Ma et al. 2017b, 2016a; El-Badry et al. 2016). Recently, Wetzel et al. (2016) have re-run this simulation with eight times better mass resolution and higher spatial resolution ($\epsilon_{\mathrm{gas}} = 1$ pc and $\epsilon_{\mathrm{star}} = 4$ pc), but using the mesh-less finite-mass (MFM) hydrodynamics method in GIZMO and FIRE-2, an improved numerical implementation of the FIRE model (see Hopkins et al. 2017, for details). We repeat our analysis on the new run and find all the results presented in the paper remain qualitatively unchanged. Particularly, the thin-to-thick disk decomposition, disk scale heights, and the amount of disk thickening at late times are consistent within 10%. As one explicit example, in Fig. 4.13, we show the median stellar age and average stellar metallicity as a function of R and $|Z|$ in the new run. The disk structure and metallicity profile are very similar to the simulation analyzed in the paper (Fig. 4.4). This suggests that our results are independent of resolution and numerical details, because most of the physics we

consider in the paper are global processes and can be understood by simple analytic considerations. Nevertheless, there are some quantitative differences between the two runs. In the new run, the star-forming disk formed and stabilized at a later time ($t_{\mathrm{lookback}} \sim 4\,\mathrm{Gyr}$), due to stochastic effects during the last minor merger. The gas disk is more metal-enriched at formation time, so the radial metallicity gradient on the mid-plane is weaker. Moreover, the disk is more strongly flared, so the radial metallicity gradient turns positive at a lower height ($|Z| \sim 1\,\mathrm{kpc}$). This suggests that a large statistical sample is needed to make rigorous statements about quantitative details, as opposed to the robust qualitative trends we have focused on here.

Chapter 5

THE DIFFICULTY OF GETTING HIGH ESCAPE FRACTIONS OF IONIZING PHOTONS FROM HIGH-REDSHIFT GALAXIES

Abstract

We present a series of high-resolution (20–2000 $M_\odot$, 0.1–4 pc) cosmological zoom-in simulations at $z \gtrsim 6$ from the Feedback In Realistic Environment (FIRE) project. These simulations cover halo masses 10^9–$10^{11}\,M_\odot$ and rest-frame ultraviolet magnitude $M_{\rm UV} = -9$ to -19. These simulations include explicit models of the multi-phase ISM, star formation, and stellar feedback, which produce reasonable galaxy properties at $z = 0$–6. We post-process the snapshots with a radiative transfer code to evaluate the escape fraction ($f_{\rm esc}$) of hydrogen ionizing photons. We find that the instantaneous $f_{\rm esc}$ has large time variability (0.01%–20%), while the time-averaged $f_{\rm esc}$ over long time-scales generally remains $\lesssim 5\%$, considerably lower than the estimate in many reionization models. We find no strong dependence of $f_{\rm esc}$ on galaxy mass or redshift. In our simulations, the intrinsic ionizing photon budgets are dominated by stellar populations younger than 3 Myr, which tend to be buried in dense birth clouds. The escaping photons mostly come from populations between 3–10 Myr, whose birth clouds have been largely cleared by stellar feedback. However, these populations only contribute a small fraction of intrinsic ionizing photon budgets according to standard stellar population models. We show that $f_{\rm esc}$ can be boosted to high values, if stellar populations older than 3 Myr produce more ionizing photons than standard stellar population models (as motivated by, e.g., models including binaries). By contrast, runaway stars with velocities suggested by observations can enhance $f_{\rm esc}$ by only a small fraction. We show that "sub-grid" star formation models, which do not explicitly resolve star formation in dense clouds with $n \gg 1\,{\rm cm}^{-3}$, will dramatically over-predict $f_{\rm esc}$.

Keywords: galaxies: formation – galaxies: evolution – galaxies: high-redshift – cosmology: theory

5.1 Introduction

Star-forming galaxies at high redshifts are thought to be the dominant source of hydrogen reionization (e.g., Madau et al. 1999; Faucher-Giguère et al. 2008; Haardt & Madau 2012). Therefore, the escape fraction of hydrogen ionizing photons (f_{esc}) from these galaxies is an important, yet poorly constrained, parameter in understanding the reionization history.

Models of cosmic reionization are usually derived from the galaxy ultraviolet luminosity function (UVLF; e.g., Bouwens et al. 2011; McLure et al. 2013), Thomson scattering optical depths inferred from Cosmic Microwave Background (CMB) measurements (Hinshaw et al. 2013; Planck Collaboration et al. 2014), Lyα forest transmission (e.g., Fan et al. 2006). They often require high f_{esc} in order to match the ionization state of the intergalactic medium (IGM) by $z = 6$ (e.g., Ouchi et al. 2009; Kuhlen & Faucher-Giguère 2012; Finkelstein et al. 2012; Robertson et al. 2013). For example, Finkelstein et al. (2012) and Robertson et al. (2013) suggested $f_{esc} > 13\%$ and $f_{esc} > 20\%$, respectively, assuming all the ionization photons are contributed by galaxies brighter than $M_{UV} = -13$. However, such constraints on f_{esc} are always entangled with the uncertainties at the faint end of UVLF, since low-mass galaxies can play a dominant role in providing ionizing photons due to their dramatically increasing numbers. For example, Finkelstein et al. (2012) derived that reionization requires a much higher escape fraction $f_{esc} > 34\%$ if one only accounts for the contribution of galaxies brighter than $M_{UV} = -18$. Also, Kuhlen & Faucher-Giguère (2012) showed that even applying a cut off on UV magnitude at $M_{UV} = -13$, the required escape fraction at $z = 6$ varies from 6%–30% when changing the faint-end slope of UVLF within observational uncertainties. Furthermore, it is also not clear how f_{esc} depends on galaxy mass and evolves with redshift, which makes the problem more complicated.

Therefore, independent constraints on f_{esc} are necessary to disentangle these degeneracies. Star-forming galaxies at lower redshifts should provide important insights into their high-redshift counterparts. In the literature, high escape fractions from 10% up to unity have been reported in various samples of Lyman break galaxies (LBGs) and Lyα emitters (LAEs) around $z \sim 3$ (e.g., Steidel et al. 2001; Shapley et al. 2006; Vanzella et al. 2012; Nestor et al. 2013). These measurements are based

on detection of *rest-frame* Lyman continuum (LyC) emission from either individual galaxies or stacked samples, so the exact value of f_{esc} depends on uncertain dust and IGM attenuation correction. Similar observations at lower redshifts always show surprisingly low escape fractions. In the local universe, the only two galaxies which have confirmed LyC detection suggest f_{esc} to be only $\sim 2\%$–3% (Leitet et al. 2011, 2013). At $z \sim 1$, stacked samples have been used to derive upper limits as low as $f_{esc} < 1\%$–2% (e.g., Cowie et al. 2009; Siana et al. 2010; Bridge et al. 2010). Even at $z \sim 3$, low escape fractions ($< 5\%$) have also been reported in some galaxy samples (e.g., Iwata et al. 2009; Boutsia et al. 2011). Recent careful studies have revealed that a considerable fraction of specious LyC detection at $z \sim 3$ is due to contamination from foreground sources (Vanzella et al. 2010; for a very recent study, see Siana et al. 2015), which could at least partly account for the apparent contradiction between these observations. Nevertheless, given the large uncertainty in these studies, no convincing conclusion can be reached so far from current observations.

Previous numerical simulations of galaxy formation also predict a broad range of f_{esc}, and even contradictory trends of the dependence of f_{esc} on halo mass and redshift. For example, Razoumov & Sommer-Larsen (2010) found f_{esc} decreases from unity to a few precent with increasing halo mass from $10^{7.8}$–$10^{11.5}\,M_{\odot}$. Similarly, Yajima et al. (2011) also found their f_{esc} decreases from 40% at halo mass $10^9\,M_{\odot}$ to 7% at halo mass $10^{11}\,M_{\odot}$. On the other hand, Gnedin et al. (2008) found increasing f_{esc} with halo mass in 10^{10}–$10^{12}\,M_{\odot}$. They also reported significantly lower escape fraction of $1\% - 3\%$ for the most massive galaxies in their simulations and $< 0.1\%$ for the smaller ones. Razoumov & Sommer-Larsen (2010) also found f_{esc} decreases from $z = 4$–10 at fixed halo mass, while Yajima et al. (2011) found no dependence of f_{esc} on redshift. At lower masses, Wise & Cen (2009) found $f_{esc} \sim 5\%$–40% and $f_{esc} \sim 25\%$–80% by invoking a normal initial mass function (IMF) and a top-heavy IMF, respectively, for galaxies of halo mass in $10^{6.5}$–$10^{9.5}\,M_{\odot}$; whereas Paardekooper et al. (2011) reported lower escape fraction of 10^{-5}–0.1 in idealized simulations of galaxy masses 10^8–$10^9\,M_{\odot}$.

Most of the intrinsic ionizing photons are produced by massive stars of masses in 10–$100\,M_{\odot}$, which are originally born in giant molecular clouds (GMCs). The majority of the ionizing photons are instantaneously absorbed by the dense gas in the GMCs and generate H II regions. These "birth clouds" must be disrupted and dispersed by radiation pressure, photoionization, H II thermal pressure, and supernovae before a considerable fraction of ionizing photons are able to escape (e.g., Murray et al. 2010;

Kim et al. 2013; Paardekooper et al. 2015). Therefore, to study the escape fraction of ionizing photons using simulations, one must resolve the multi-phase structure of the interstellar medium (ISM) and "correctly" describe star formation and stellar feedback. Many previous simulations adopt very approximate or "sub-grid" ISM and feedback model, which can lead to many differences between those studies. Recent studies have noted the importance of resolving the ISM structure around the stars and started to adopt more detailed treatments of the ISM and stellar feedback physics (Kim et al. 2013; Kimm & Cen 2014; Wise et al. 2014; Paardekooper et al. 2013, 2015). For example, Wise et al. (2014) performed radiative hydrodynamical simulations with state-of-art ISM physics and chemistry, star formation, and stellar feedback models and found f_{esc} drops from 50% to 5% with increasing halo mass in 10^7–$10^{8.5}$ $M_\odot$ at $z > 7$. They conclude that more massive galaxies are not likely to have high escape fractions, but are unable to simulate more massive systems. Kimm & Cen (2014) explored more physically motivated models of supernovae (SN) feedback and found average escape fraction of $\sim 11\%$ for galaxies in 10^8–$10^{10.5}$ $M_\odot$. Paardekooper et al. (2015) argued that the dense gas within 10 pc from young stars provides the main constraint on the escape fraction. They found in their simulation that about 70% of the galaxies of halo mass above 10^8 $M_\odot$ have escape fraction below 1%. But none of these simulations has been run to $z = 0$ to confirm that the models for star formation, feedback, and the ISM produce reasonable results in comparison to observations.

The Feedback in Realistic Environment (FIRE) project[1] (Hopkins et al. 2014) is a series of cosmological zoom-in simulations that are able to follow galaxy merger histories, interaction of galaxies with IGM, and many other processes. The simulations include a full set of realistic models of the multi-phase ISM, star formation, and stellar feedback. The first series of FIRE simulations run down to $z = 0$ reproduce reasonable star formation histories, the stellar mass-halo mass relation, the Kennicutt–Schmidt law, and the star-forming main sequence, for a broad range of galaxy masses ($M_* = 10^4$–10^{11} $M_\odot$) from $z = 0$–6 (Hopkins et al. 2014). Cosmological simulations with the FIRE stellar feedback physics self-consistently generate galactic winds with velocities and mass loading factors broadly consistent with observational requirements (Muratov et al. 2015) and are in good agreement with the observed covering fractions of neutral hydrogen in the halos of $z = 2$–3 LBGs (Faucher-Giguère et al. 2015). In previous studies of isolated galaxy simulations, these models have also been shown to reproduce many small scale observations,

---

[1]FIRE project website: http://fire.northwestern.edu

including the observed multi-phase ISM structure, density distribution of GMCs, GMC lifetimes and star formation efficiencies, and the observed Larson's law scalings between cloud sizes and structural properties, from scales < 1 pc to > kpc (e.g., Hopkins et al. 2011, 2012a). A realistic model with these properties is *necessary* to study the production and propagation of ionizing photons inside a galaxy.

In this work, we present a separate set of cosmological simulations at $z > 6$, performed with the same method and models at extremely high resolution (particle masses 20–2000 $M_\odot$, smoothing lengths 0.1–4 pc). These simulations cover galaxy halo masses 10^9–10^{11} $M_\odot$ and rest-frame ultraviolet magnitudes $M_{UV} = -9$ to -19 at $z = 6$. We then evaluate the escape fraction of ionizing photons with Monte Carlo radiative transfer calculations. We describe the simulations and present the properties of our galaxies in Section 5.2 and 5.3. In Section 5.4, we describe the Monte Carlo radiative transfer code and compile our main results on the escape fractions and there dependence on galaxy mass and cosmic time. In Section 5.5, we show how the UV background and star formation prescriptions affect our results. We also discuss the effects of runaway stars and extra ionizing photon budgets contributed by intermediate-age stellar populations, as motivated by recent observations and stellar models. We summarize and conclude in Section 5.6.

5.2 The Simulations

This work is part of the FIRE project (Hopkins et al. 2014). All the simulations use the newly developed GIZMO code (Hopkins 2015) in P-SPH mode. P-SPH adopts a Lagrangian pressure-entropy formulation of the smoothed particle hydrodynamics (SPH) equations (Hopkins 2013), which eliminates the major differences between SPH, moving-mesh, and grid codes, and resolves many well-known issues in traditional density-based SPH formulations. The gravity solver is a heavily modified version of the GADGET-3 code (Springel 2005); and P-SPH also includes substantial improvements in the artificial viscosity, entropy diffusion, adaptive time-stepping, smoothing kernel, and gravitational softening algorithm. We refer to Hopkins (2013, 2015) for more details on the numerical recipes and extensive test problems. A list of the simulations in this work is presented in Table 5.1, while the parameters there will be introduced in the rest of this section.

The simulations in this work are of a separate series from other FIRE simulations. A large cosmological box was first simulated at low resolution down to $z = 5$, and then halos of masses in 10^9–10^{11} $M_\odot$ at that time were picked and re-simulated

in a smaller box at much higher resolution with the multi-scale "zoom-in" initial conditions generated with the MUSIC code (Hahn & Abel 2011), using second-order Lagrangian perturbation theory. The resolution of the simulations in this work can be roughly divided into two categories, which we refer as "high resolution" (HR) and "medium resolution" (MR), although the specific initial particle mass may vary according to the size of the system. Some initial conditions we adopt in the simulations and general properties of the galaxies at $z = 6$ are listed in Table 5.1. We will show in Section 5.3 that they are typical in most of their properties and thus can be considered as "representative" in this mass range.

In our simulations, gas follows an ionized+atomic+molecular cooling curve from 10–10^{10} K, including metallicity-dependent fine-structure and molecular cooling at low temperatures and high-temperature metal-line cooling followed species-by-species for 11 separately tracked species (Wiersma et al. 2009a). We do not include a primordial chemistry network nor try to model the formation of Pop III stars, but apply a metallicity floor of $Z = 10^{-4}\,Z_\odot$ in the simulations. Therefore, we will focus our analysis at $z \lesssim 11$, when our galaxies are sufficiently metal-enriched.

At each timestep, the ionization states are determined from the photoionization equilibrium equations described in Katz et al. (1996) and the cooling rates are calculated from a compilation of CLOUDY runs, by applying a uniform but redshift-dependent photo-ionizing background tabulated in Faucher-Giguère et al. (2009)[2], and photo-ionizing and photo-electric heating from local sources. Gas self-shielding is accounted for with a local Jeans-length approximation, which is consistent with the radiative transfer calculation in Faucher-Giguère et al. (2010). In this work, we also post-process the simulations with full radiative transfer calculation and re-compute the ionization states. We find consistent results between the post-processing and on-the-fly calculations (see Appendix A for details).

The models of star formation (SF) and stellar feedback implemented in the FIRE simulations are developed and presented in a series of papers (Hopkins et al. 2011, 2012a, 2013b, 2014, and references therein). We briefly summarize their main features here and refer to the references for more details and discussion. We follow the SF criteria developed in Hopkins et al. (2013b) and allow stars to form only in molecular and self-gravitating gas clouds with number density above some threshold $n_{\rm th}$. We choose $n_{\rm th} = 100\,{\rm cm}^{-3}$ as the fiducial value. It corresponds to the typical

---

[2]The photo-ionizing background stars to kick in at $z = 10.6$ and is available at http://galaxies.northwestern.edu/uvb/.

density of GMCs and is much larger than the mean ISM density in our simulations[3]. In z5m10h, we set $n_{\rm th} = 1000\,{\rm cm}^{-3}$ for a convergence test. SF occurs at 100% efficiency per free-fall time when the gas meets these criteria (i.e., $\dot{\rho}_* = \rho/t_{\rm ff}$). This SF prescription adaptively selects the largest over-densities and automatically predicts clustered SF (Hopkins et al. 2013b). It is also motivated by much higher-resolution, direct simulations of dense, star-forming clouds (Padoan & Nordlund 2011; Vázquez-Semadeni et al. 2011; Federrath et al. 2011). A star particle inherits the metallicity of each tracked species from its parent gas particle, and its age is determined by its formation time in subsequent timesteps.

The z5m10e run is intentionally designed to mimic "sub-grid" star formation models as commonly adopted in low-resolution simulations that cannot capture the star formation in dense gas clouds. In this run, we lower $n_{\rm th}$ to $1\,{\rm cm}^{-3}$ and allow stars to form at 2% efficiency per free-fall time in *all* gas above $1\,{\rm cm}^{-3}$ but not self-gravitating (still 100% efficiency in self-gravitating gas). This will result in a wide spatial and density distribution of SF and means that stars do not need to form in high-density structures.

Every star particle is treated as a single stellar population with known age, metallicity, and mass. Then all the quantities associated with feedback, including ionizing photon budgets, luminosities, stellar spectra, supernovae (SNe) rates, mechanical luminosities of stellar winds, metal yields, etc., are directly tabulated from the stellar population models in STARBURST99 (Leitherer et al. 1999), assuming a Kroupa (2002) initial mass function (IMF) from 0.1–100 $M_\odot$. In principle, this "IMF-averaged" approximation breaks down in our HR simulations, where the mass of a star particle is only 10–100 $M_\odot$. Previous studies showed that it has little effect on global galaxy properties (e.g., Hopkins et al. 2014, and references therein). We also test and confirm that this approximation does not affect our results on escape fraction (see Section 5.4).

We account for different mechanisms of stellar feedback, including (1) local and long-range momentum flux from radiative pressure, (2) energy, momentum, mass and metal injection from SNe and stellar winds, and (3) photoionization and photoelectric heating. We apply the Type-II SNe rates from STARBURST99 and Type-Ia SNe rates following Mannucci et al. (2006), when a star particle is older than 3 Myr and 40 Myr, respectively. We assume that every SN ejecta has an initial kinetic en-

---

[3]On the other hand, the threshold is much less than the highest density these simulations can resolve, to save computational expense.

ergy of 10^{51} ergs, which is coupled to the gas as either thermal energy or momentum, depending on whether the cooling radius can be resolved (see Hopkins et al. 2014; Martizzi et al. 2015, for more details). We also follow Wiersma et al. (2009b) and adopt Type-II SNe yields from Woosley & Weaver (1995) and Type-Ia yields from Iwamoto et al. (1999). We do not model SNe and metal enrichment from Pop III stars.

We emphasize that the on-the-fly photoionization is treated in an approximate way in our simulations – we move radially outwards from the star and ionize each nearest neutral gas particle until the photon budget is exhausted. This treatment allows ionizing regions to overlap and expand, and is qualitatively reasonable in intense star-forming regions. However, when the gas distribution is highly asymmetric around an isolated star particle, their ionization states might not be accurately captured in the simulations. Nonetheless, as we will post-process our simulations with full radiative transfer code to trace the propagation of ionizing photons and re-compute the ionization states (Section 5.4), this approximation will have little effect on the escape fraction we evaluate. Also, in the region where the gas density is extremely high, photoionization may not be well-captured due to resolution limits. But we confirm that this neither has strong dynamical effect on gas structure in high-density regions nor affects the escape fraction[4].

The simulations described in Table 5.1 adopt a standard flat ΛCDM cosmology with cosmological parameters $H_0 = 70.2 \, \mathrm{km} \, s^{-1} \, Mpc^{-1}$, $\Omega_\Lambda = 0.728$, $\Omega_m = 1 - \Omega_\Lambda = 0.272$, $\Omega_b = 0.0455$, $\sigma_8 = 0.807$ and $n = 0.961$, which are within the uncertainty of current observations (e.g., Hinshaw et al. 2013; Planck Collaboration et al. 2014).

---

[4]In our simulations, star particles have similar mass to gas particles. Applying a (Kroupa 2002) IMF and standard stellar population model, in regions with $n_{\mathrm{th}} \sim 100 \, \mathrm{cm}^{-3}$, the ionizing photons emitted from a young star particle can ionize the mass of two gas particles. However, some clouds reach densities $\gtrsim 2000 \, \mathrm{cm}^{-3}$, where one needs to collect the ionizing photon budgets from 10 young star particles to fully ionize a single gas particle. In the code, the on-the-fly estimate of HII photoionization feedback treats this limit stochastically (see Hopkins et al. 2011), so we might risk underestimating the dynamical effects of photo-heating. Therefore, we run a simulation where we artificially boost the ionizing photon budget by a factor of 10, which is not physical but dramatically reduces the stochastic variations. We find that the typical gas density of star-forming clouds and the average escape fractions (computed from our post-processing radiative transfer, see Section 5.4) are very similar to our standard runs. Therefore, we confirm that the on-the-fly photoionization feedback approximation in our simulations does not strongly affect our results.

Table 5.1: Simulations studied in this chapter.

Name	Boxsize (h^{-1} Mpc)	M_{halo} ($M_\odot$)	m_b ($M_\odot$)	ϵ_b (pc)	m_{dm} ($M_\odot$)	ϵ_{dm} (pc)	n_{th} (cm^{-3})	M_* ($h^{-1}\,M_\odot$)	M_{UV} (AB mag)	Resolution
z5m09	1	7.6e8	16.8	0.14	81.9	5.6	100	3.1e5	-10.1	HR
z5m10	4	1.3e10	131.6	0.4	655.6	7	100	2.7e7	-14.8	HR
z5m10mr	4	1.5e10	1.1e3	1.9	5.2e3	14	100	5.0e7	-17.5	MR
z5m10e^a	4	1.3e10	1.1e3	1.9	5.2e3	14	1	2.4e7	-16.1	MR
z5m10h	4	1.3e10	1.1e3	1.9	5.2e3	14	1000	6.6e7	-16.4	MR
z5m11	10	5.6e10	2.1e3	4.2	1.0e4	14	100	2.0e8	-18.5	MR

Initial conditions of our simulations and simulated galaxy properties at z = 6:

(1) Name: Simulation designation.

(2) Boxsize: Zoom-in box size of our simulations.

(3) M_{halo}: Halo mass of the primary galaxy at z = 6.

(4) m_b: Initial baryonic (gas and star) particle mass in the high-resolution region.

(5) ϵ_b: Minimum baryonic force softening (minimum SPH smoothing lengths are comparable or smaller). Force softening is adaptive (mass resolution is fixed).

(6) m_{dm}: Dark matter particle mass in the high-resolution regions.

(7) ϵ_{dm}: Minimum dark matter force softening (fixed in physical units at all redshifts).

(8) n_{th}: Density threshold of star formation (see Section 5.2).

(9) M_*: Stellar mass of the primary galaxy at z = 6.

(10) M_{UV}: Galaxy UV magnitude (absolute AB magnitude at 1500 Å).

(11) Resolution: Whether a simulation is of ultra-high resolution (HR) or of medium resolution (MR).

Note:

^{a} This simulation is intentionally designed to mimic "sub-grid" star formation models that are usually adopted in low-resolution cosmological simulations. We not only lower the star formation density threshold to $n_{th} = 1\ cm^{-3}$, but also allow star formation at 2% efficiency per free-fall time if gas reaches n_{th} but is not self-gravitating.
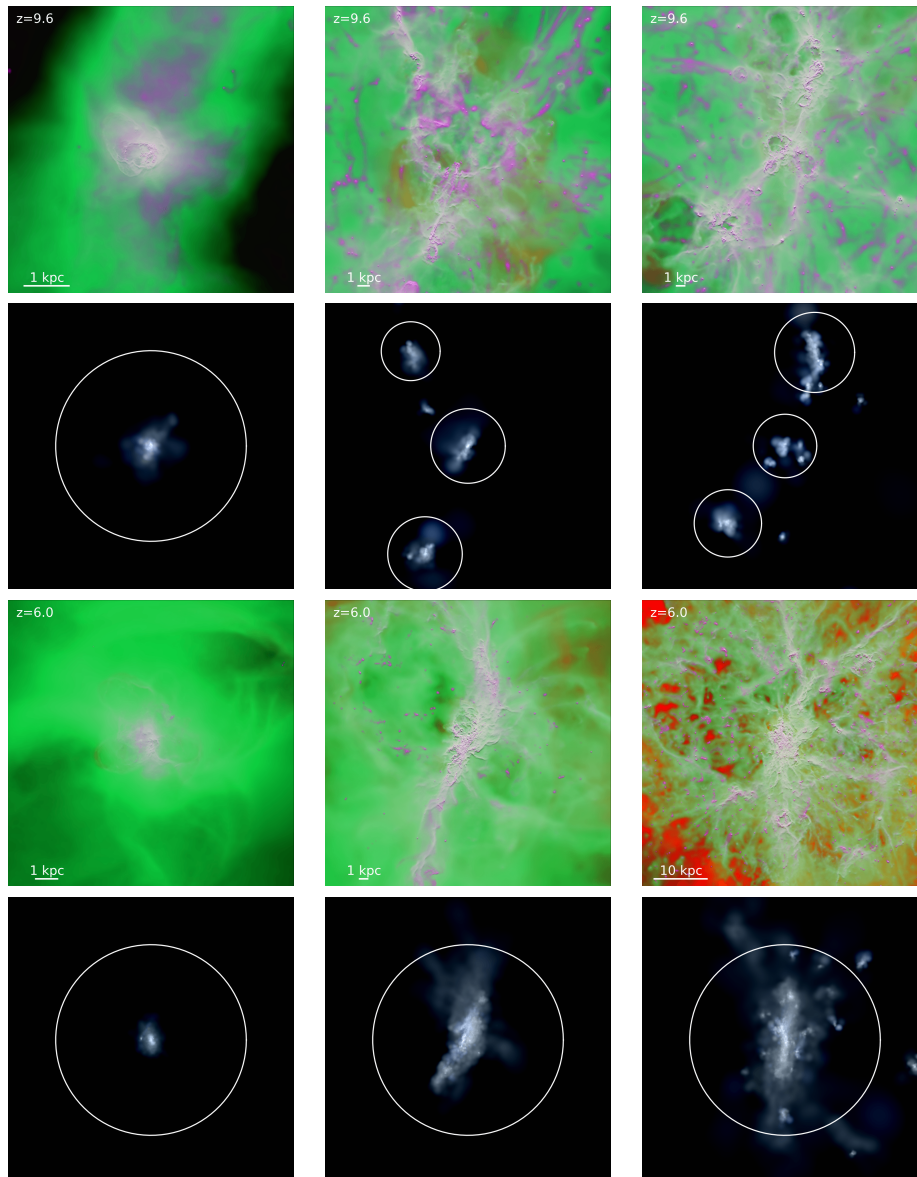
Figure 5.1: Gas and stars in z5m09 (left column), z5m10mr (middle column), and z5m11 (right column), at $z = 9.6$ (upper panels) and $z = 6.0$ (lower panels), respectively. Gas images show log-weighted projected gas density. Magenta shows cold molecular/atomic gas ($T < 1000$ K), green shows warm ionized gas ($10^4 \leq T \leq 10^5$ K), and red shows hot gas ($T > 10^6$ K) (see Hopkins et al. 2014 for details). Stellar images are mock $u/g/r$ composites. We use STARBURST99 to determine the SED of each star particle from its known age and metallicity, and then ray-tracing the line-of-sight flux, attenuating with a MW-like reddening curve with constant dust-to-metals ratio for the abundance at each point. White circles show the position and halo virial radii of each main galaxy (see text) identified by the AHF code. Gas and star images of the same snapshot use the same projection and the same box size along each direction. We can clearly see a complicated, multi-phase ISM structure, with inflows, outflows, mergers, and star formation in dense clouds all occurring at the same time.

5.3   Galaxy Properties

5.3.1   Halo Identification

The galaxies in our simulations have different assembly histories at high redshifts. The smallest galaxy, z5m09, evolves primarily via accretion and passive evolution, while the more massive ones have undergone multiple mergers at earlier times. We use the Amiga Halo Finder (AHF; Gill et al. 2004; Knollmann & Knebe 2009) to identify halos in the simulations. The AHF code uses an adaptive mesh refinement method. We choose the center of a halo as the center of mass of all particles in the finest refinement level and adopt the virial overdensity from Bryan & Norman (1998). In this work, we only consider the main galaxies that are well-resolved in the simulations. We exclude those that are contaminated by low-resolution paticles, not sufficiently resolved (contain less than $10^5/10^6$ bound particles in MR/HR runs, or have stellar mass lower than 10% of the most massive galaxy in each snapshot), and subhalos/satellite galaxies. Some example images of gas and stars at different redshifts are presented in Figure 5.1. The white circles show the virial radius of each halo. As the figure shows, the more massive systems were assembled by merging several smaller halos at early time.

5.3.2   Multi-phase ISM Structure

One advantage of our simulation is that we are able to explicitly resolve a realistic multi-phase ISM, star formation, and stellar feedback. Figure 5.1 shows the distribution cold, warm, and hot phase of gas on galactic scale. In Figure 5.2, we show some examples of ISM structure on sub-kpc scale around star particles of different ages from z5m10mr. The left column is the density and temperature maps around a star particle of age 1 Myr (before the first SNe explode at ∼ 3 Myr). As expected from our star formation criteria, newly formed stars are embedded in their dense "birth" clouds. Within the central few pc around the star particle, the dense gas is ionized and heated by ionizing photons from the star and an H II region forms[5]. The middle column shows the ISM structure around an intermediate-age star particle (3–10 Myr), where there has just been a SN explosion (the example is 5 Myr old). The birth cloud has been largely dispersed and cleared by radiation pressure and SN feedback, opening a large covering fraction of low-density regions. In contrast, old star particles (right column, ∼ 40 Myr) tend to be located in a warm, ambient medium. The ISM structures around star particles of different ages are very

---

[5]For a typical gas density of $100 \, \mathrm{cm}^{-3}$ and an ionizing photo budget $10^{49.5} \, \mathrm{s}^{-1}$ in this simulation, the Strömgren radius is around 5 pc.
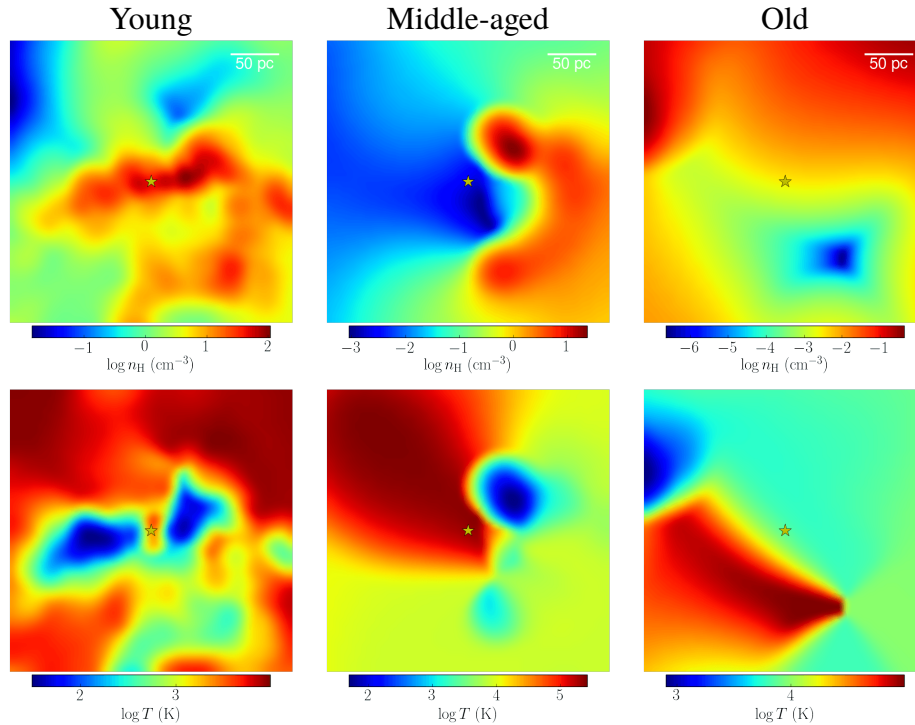
Figure 5.2: ISM structure in a random star neighborhood. We show density (top panels) and temperature (bottom panels) maps of a slice around a(n) young (~ 1 Myr, left column), middle-aged (~ 5 Myr, middle column), and old (~ 40 Myr, right column) star particle. Each box is 300 pc along each direction. The yellow stars represent the position of the star particle. We clearly see that young stars – which produce most of the ionizing photons – are buried in H II regions inside their dense birth clouds. By $\gtrsim 10$ Myr, the clouds are totally destroyed and most sightlines to the stars have low column densities, but these stars no longer produce many ionizing photons.

important in understanding the propagation of ionizing photons.

5.3.3   Galaxy Masses, Stellar Mass Assembly, and Star Formation History

As has been shown in Hopkins et al. (2014), with the stellar feedback models described here (with no tuned parameters), the FIRE simulations predict many observed galaxy properties from $z = 0$–6: the stellar mass–halo mass relation, the Kennicutt–Schimidt law, star formation histories (SFHs), and the star-forming main sequence. The simulations in this work are of much higher resolution and focus on higher redshifts than those in Hopkins et al. (2014). We extend their analysis and present the stellar mass-halo mass relation at $z = 6, 7, 8$, and 9.6 for our simulated galaxies in Figure 5.3. We compare our results with the simulations from Hopkins et al. (2014) at $z = 6$ and the observationally inferred relation from Behroozi et al.
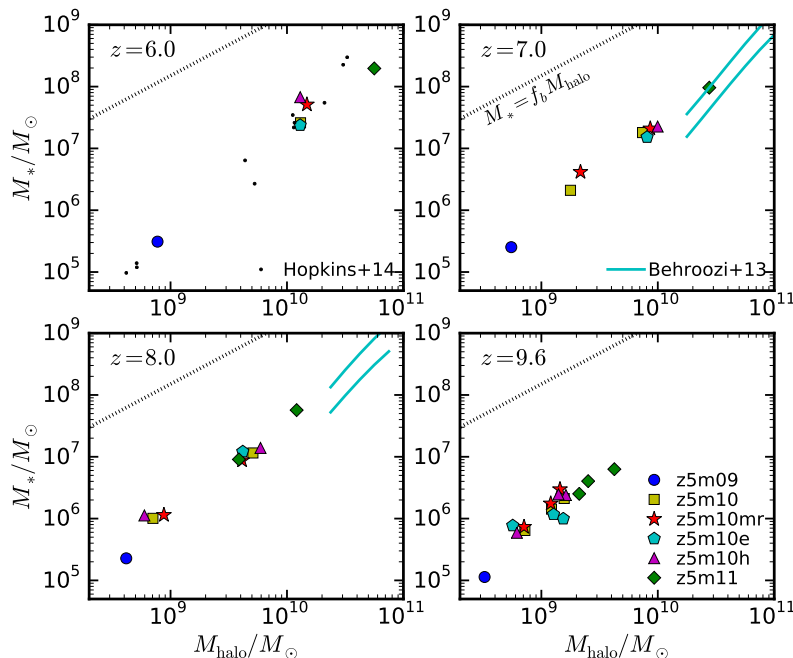
Figure 5.3: Galaxy stellar mass–halo mass relation at $z = 6, 7, 8$, and 9.6. We compare the relation with the simulations from Hopkins et al. (2014) at $z = 6$ (small black dots), and the observationally inferred relation in Behroozi et al. (2013b, $z = 7.0$ and $z = 8.0$ only, cyan lines). The black dotted lines represent the relation if all baryons turned into stars (i.e., $M_* = f_b M_{halo}$). Our simulations are broadly consistent with observations. These simulations are consistent with those in Hopkins et al. (2014), although the latter have much lower resolution. It is reassuring that the stellar mass is converged in these runs.

(2013b) at $z = 7$ and 8 (note the relation in Behroozi et al. 2013b at $z = 6$ does not overlap with the halo masses presented here). We confirm that our simulations predict stellar masses consistent with observations at these redshifts. It is also reassuring that the stellar masses in these simulations are well converged, despite those from Hopkins et al. (2014) having much poorer resolution.

In Figure 5.4, we present the relation between UV magnitude at rest-frame 1500 Å and halo mass for our simulated galaxies at $z = 6, 7, 8$, and 9.6. To obtain the UV magnitudes, we first calculate the specific luminosity at 1500 Å for each star particle by interpolating the stellar spectra tabulated from STARBURST99 as a function of age and metallicity, and then convert the galaxy-integrated luminosity to absolute AB magnitude. In Figure 5.4, we also compare with the interpolated abundance matching from Kuhlen & Faucher-Giguère (2012, dotted lines). The simulations are qualitatively consistent with the abundance matching results, and lie within the
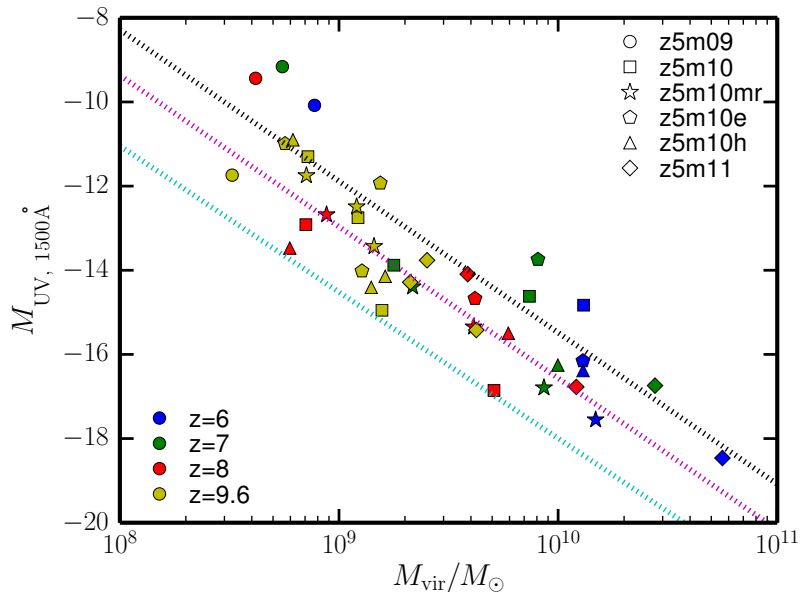
Figure 5.4: UV magnitude at 1500 Å as a function of halo mass for the simulated galaxies, color coded by redshift. Galaxies at $z =$6, 7, 8, and 9.6 are shown by blue, green, red, and yellow points, respectively. The numbers are calculated by converting the intrinsic luminosity at 1500 Å to absolute AB magnitude. Dotted lines show the abundance matching from Kuhlen & Faucher-Giguère (2012, fig 3) at $z = 4$ (black), 7 (magenta), and 10 (cyan). The simulations are qualitatively consistent with the abundance matching, and span the range of $M_{UV} = -9$ to -19 that is believed to dominate reionization.

systematic observational uncertainties. Given that in this simple calculation, we ignore the attenuation from dust inside the galaxy and along the line-of-sight in the IGM, and that the abundance matching is very uncertain at the faint end, we do not further discuss the comparison with these results. The simulated galaxies cover $M_{UV} = -9$ to -19 at these redshifts, which are believed to play a dominant role in providing ionizing photons during reionization (e.g., Finkelstein et al. 2012; Kuhlen & Faucher-Giguère 2012; Robertson et al. 2013). Most of these galaxies are too faint to be detectable in current observations; our z5m11 galaxy is, however, just above the detection limit ($M_{UV} \sim -18$) of many deep galaxy surveys beyond $z \sim 6$. Next generation space and ground-based facilities, such as the *James Webb Space Telescope* (*JWST*) and the *Thirty Meter Telescope* (*TMT*) may push the detection limit down to $M_{UV} \sim -15.5$ (e.g., Wise et al. 2014) and many of our simulated galaxies will then lie above the detection limits of future deep surveys.

Figure 5.5 shows the star formation rate–stellar mass relation at $z = 6, 7, 8$, and 9.6 for the most massive galaxy in each simulation. Our simulated galaxies agree
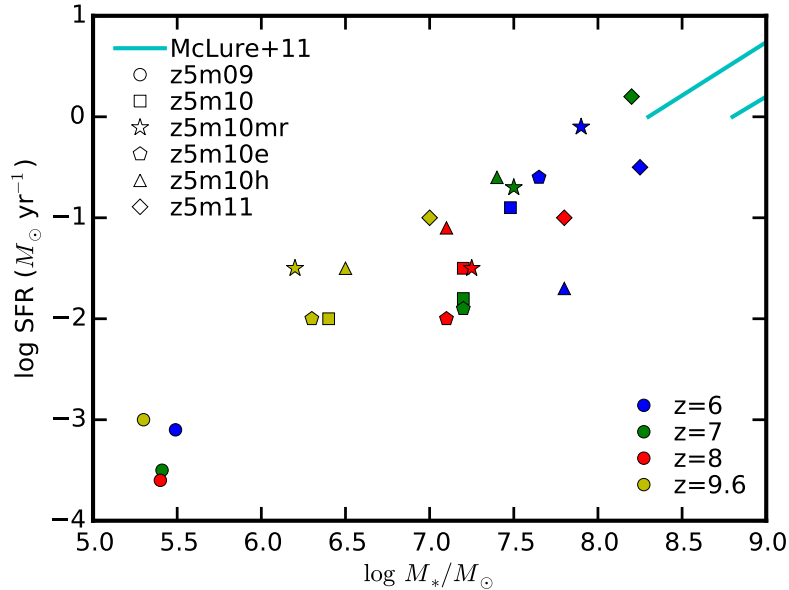
Figure 5.5: Star formation rate–stellar mass relation at $z = 6, 7, 8$, and 9.6 for the most massive galaxy in each simulation. The cyan lines illustrate the observed relation from a sample of galaxies at $z = 6$–8.7 in McLure et al. (2011). Our simulated galaxies agree with the observed relation where they connect at $\log(M_*/M_\odot) = 8.25$.

with the observed relation from a sample of galaxies at $z = 6$–8.7 in McLure et al. (2011) where they connect at $\log(M_*/M_\odot) = 8.25$. We also present the growth of galaxy stellar mass and instantaneous star formation rates (SFRs) as a function of cosmic time for these galaxies in the top two panels of Figure 5.6 (the open symbols represent the time-averaged SFR on 100 Myr time-scales). All these galaxies show significant short-time-scale variabilities in their SFRs, associated with the dynamics of fountains, feedback, and individual star-forming clouds. On larger time-scales (e.g., 100 Myr), the fluctuations in SFRs become weaker and are mostly driven by mergers and global instabilities (see the discussion in Hopkins et al. 2014).

It is worth noticing that our four z5m10x simulations have similar global galaxy properties, despite different resolutions and SF prescriptions adopted in these runs. This is because the galaxy-averaged star formation efficiency is regulated by stellar feedback (1–2% per dynamical time, e.g., Hopkins et al. 2011; Ostriker & Shetty 2011; Agertz et al. 2011; Faucher-Giguère et al. 2013), not the SF criteria (Hopkins et al. 2013b). However, SF criteria do affect the spatial and density distribution of SF. In z5m10e, the SF density threshold $n_{\rm th} = 1\,{\rm cm}^{-3}$ is comparable or slightly larger than the mean density of the ISM, so that it can be easily reached even in the

Table 5.2: Parameters used for the radiative transfer calculation.

Name	$l_{\min}$ (pc)	$N_{\max}$	l_{largest} (pc)	N_{photon}	N_{UVB}
z5m09	25	250	$\lesssim 40$	3e7	3e7
z5m10	25	300	$\lesssim 80$	3e7	3e7
z5m10mr	50	250	$\lesssim 100$	3e7	3e7
z5m10e	50	300	$\lesssim 80$	3e7	3e7
z5m10h	50	250	$\lesssim 100$	3e7	3e7
z5m11	50	300	$\lesssim 100$	4e7	4e7

(1) $l_{\min}$: the minimum cell size.
(2) $N_{\max}$: the maximum number of cells along each dimension.
(3) l_{largest}: the cell size for the largest galaxy in the last snapshot.
(4) N_{photon}: number of photon packages being transported.
(5) N_{UVB}: number of UVB packages being transported.

diffuse ISM. Also, since SF takes place at 100% efficiency per free-fall time once the gas becomes self-gravitating, many stars form just above the threshold before the gas clouds can further collapse to higher densities. As a consequence, stars are formed either in the diffuse ISM or in gas clouds of densities orders of magnitude lower than those in our standard runs. We emphasize that the z5m10e run is not realistic but is designed to mimic star formation models as adopted in low-resolution simulations where the GMCs cannot be resolved.

5.4 Escape Fraction of Ionizing Photons

We post-process every snapshot with a three-dimensional Monte Carlo radiative transfer (MCRT) code to evaluate the escape fraction of hydrogen ionizing photons from our simulated galaxies. The code is derived from the MCRT code SEDONA base (Kasen et al. 2006) and focuses specifically on radiative transfer of hydrogen ionizing photons in galaxies (see Fumagalli et al. 2011, 2014). For each galaxy, we calculate the intrinsic ionizing photon budget for every star particle within R_{vir} to obtain the galaxy ionizing photon production rate Q_{int}. We use the Padova tracks with AGB stars in STARBURST99 with a metallicity $Z = 0.0004$ ($0.02\ Z_{\odot}$, the closest available to the mean metallicity in our simulations) as our default model (also see Figure 5.13). Then we run the MCRT code to compute the rate of ionizing photons that can escape the virial radius Q_{esc}. We define the escape fraction as $f_{\text{esc}} = Q_{\text{esc}}/Q_{\text{int}}$.

5.4.1 Radiative Transfer Calculation

We perform the MCRT using a Cartesian grid. We first convert each "well-resolved" galaxy identified in our simulations to a cubic Cartesian grid of side length L and with N cells along each dimension. We center the grid at the center of the galactic halo and choose L equal to two virial radii. The size of a cell $l = L/N$ must be appropriately chosen to ensure convergence. For each simulation, we determine a minimum cell size $l_{\min}$ and a maximum $N_{\max}$ and then take $N = \min\{L/l_{\min}, N_{\max}\}$. We have run extensive tests to make sure the parameters $l_{\min}$ and $N_{\max}$ for each simulation are carefully selected to ensure convergence for every snapshot and maintain reasonable computational expenses. We show examples of convergence tests in Appendix B[6]. These parameters are listed in Table 5.2. We then calculate the gas density, metallicity, and temperature, at each cell by distributing the mass, internal energy, and metals of every gas particle among a number of cells weighted by their SPH kernel. This conserves mass and energy of gas from the simulation to the grid.

The MCRT method is similar to that described in Fumagalli et al. (2014). The radiation field is described by discrete Monte Carlo packets, each representing a large collection of photons of a given wavelength. We emit N_{star} packets isotropically from the location of the star particles, appropriately sampled by the star UV luminosities. We also emit N_{UVB} packets from the edge of the computational domain in a manner that produces a uniform, isotropic UV background radiation field with intensity given by Faucher-Giguère et al. (2009). Every photon packet is propagated until it either escapes the grid, or is absorbed somewhere in the grid. Scattering is included in the transport, i.e., we do not make the on the spot approximation.

The photon packets are used to construct estimators of the hydrogen photoionization rates in all cells. The photoionization cross-sections were taken from Verner et al. (1996), the collisional ionization rates from Jefferies (1968), and the radiative recombination rates from Verner & Ferland (1996). When calculating the rates, we use the gas temperature from the simulations instead of computing it self-consistently through the radiative transfer[7]. We use the case A recombination rates

---

[6]The MCRT calculation converges at much poorer resolution than that we use for hydrodynamics. This is because most of the sources reside in the environment where the ionizing photon optical depth is either $\tau_{\text{UV}} \gg 1$ or $\tau_{\text{UV}} \ll 1$. The MCRT calculation will converge as long as the grid captures which limit a star particle is in. However, we emphasize that the high resolution of hydrodynamics is *necessary* in order to capture the ISM structure in star-forming regions in the presence of stellar feedback. Low resolution simulations tend to over-predict escape fractions by an order of magnitude (see the discussion in Section 5.5.2).

[7]The simulations take into account many other heating sources (e.g., shocks) besides photoion-

as the transport explicitly treats photon scattering. We assume that 40% of the metals are in dust phase and adopt a dust opacity of $10^4\,\mathrm{cm^2\,g^{-1}}$ (Dwek 1998; Fumagalli et al. 2011). Since the high-redshift galaxies in our simulations tend to be extremely metal-poor, our results do not depend much on dust absorption.

We assume that the gas is in ionization equilibrium, which should be valid for all but the lowest density, highest temperature regions. Such very low density regions likely do not influence the escape fraction in any case. We use an iterative method to reach equilibrium, running the MCRT, updating the ionization state of each cell, and then repeating the transport until convergence in the ionization state and escape fraction is reached. We use up to 15 iterations to reach convergence, with typical particle counts per iteration of 3×10^7 for N_{star} and N_{UVB}. We ran tests increasing the particle counts by an order of magnitude to check that the final escape fraction did not change.

5.4.2 Instantaneous and Time-averaged Escape Fraction

In Figure 5.6, we present the instantaneous escape fractions (f_{esc}), intrinsic ionizing photon budgets (Q_{int}), and escaped photon budgets (Q_{esc}) as a function of cosmic time for the most massive galaxies in each simulation. We also average Q_{int} and Q_{esc} over 100 Myr to obtain the time-averaged escape fractions (the open symbols in Figure 5.6). The instantaneous escape fractions show significant time fluctuations, varying between $< 0.01\%$ and $> 20\%$ from time to time. In our standard runs with default star formation prescriptions, galaxies can reach high escape fractions (10–20%) only during small amounts of time. For most of the time, the time-averaged escape fractions remain below 5%. We also calculate the average escape fraction over their entire star formation history (i.e., $z = 6$–12). All our standard runs show values between 3–7%, which confirm low escape fractions on even longer time-scales. The variation in escape fractions on short time-scales is a consequence of feedback and the stochastic formation and disruption of individual star-forming regions, while long time-scale fluctuations are associated with galaxy mergers and intensive starbursts. Note that a high instantaneous escape fraction does not necessarily indicate a high contribution of ionizing photons. For example, although the main galaxy of z5m11 had an escape fraction around 20% at $z \sim 6.8$, its intrinsic ionizing photon budget

---

ization. As the radiative transfer code includes collisional ionizations, it is more realistic to take the gas temperature from the simulations than re-computing gas temperature from radiative transfer calculations (in the latter case photoionization would be the only heating source). In regions dominated by photoionization, the uncertainty due to gas temperature is very small, since the recombination rate depends only weakly on temperature.
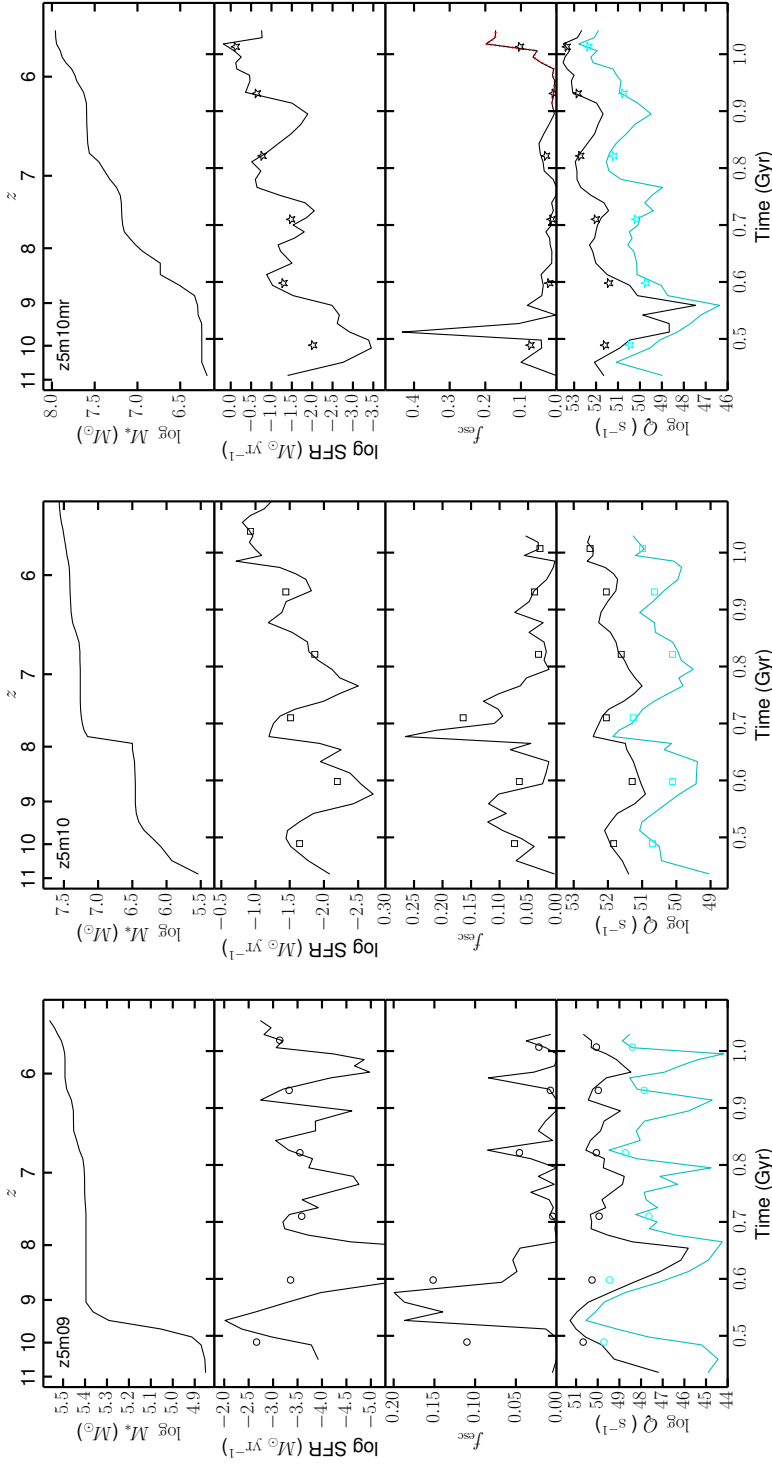
Figure 5.6: Stellar mass (top panels), star formation rate (second panels), escape fraction (third panels), and intrinsic and escaped ionizing photon budget (bottom panels, black and cyan lines, respectively) as a function of cosmic time for the most massive galaxy in each run. Open symbols show the time-averaged quantities over 100 Myr. The red dotted line in z5m10mr shows the escape fraction calculated with the UV background turned off (Section 5.5.1). Instantaneous escape fractions are highly time variable, while the time-average escape fractions (over time-scales 100–1000 Myr) are modest (∼ 5%). The intrinsic ionizing photon budgets are dominated by stellar population younger than 3 Myr, which tend to be embedded in dense birth clouds. Most of the escaping ionizing photons come from stellar populations aged 3–10 Myr, where a large fraction of sightlines have been cleared by stellar feedback. Note that the run using a common "sub-grid" star formation model (z5m10e), which allows stars to form in diffuse gas instead of in dense clouds, severely over-estimates f_{esc}.

Figure 5.7: Fig. 5.6 – continued.

Q_{int} was relatively low at that instant and the time-averaged escape fraction is only $\sim 3\%$. Recalling that many models of reionization usually require $f_{\text{esc}} \sim 20\%$ if the universe was reionized by galaxies brighter than $M_{\text{UV}} > -13$ only (e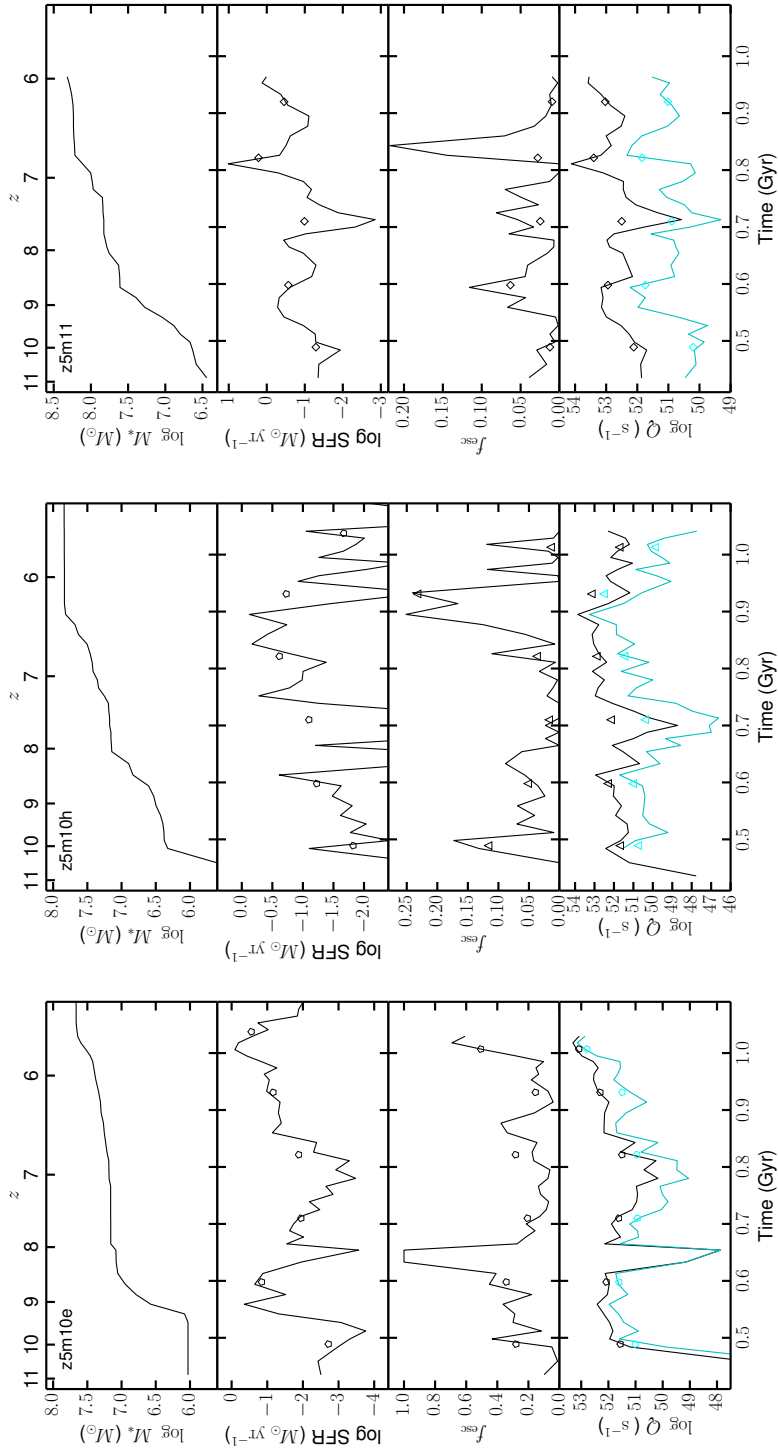.g., Finkelstein et al. 2012; Kuhlen & Faucher-Giguère 2012; Robertson et al. 2013), the escape fractions we find from our simulations are considerably lower than what those models require.

As long as we properly resolve star formation in dense birth clouds, our results are not sensitive to the details of our star formation prescription[8]. For example, in our z5m10h run where we apply $n_{\text{th}} = 1000\,\text{cm}^{-3}$, the escape fraction is very similar to the standard runs. Also, the similarity between the HR z5m10 run and the MR z5m10mr run shows that our results converge with respect to resolution[9].

However, in our z5m10e run where we allow stars form in diffuse gas, the time-averaged escape fraction exceeds 20% for most of the time. While this toy model results in higher escape fractions, we stress that such a star formation prescription is not consistent with our current understanding of star formation. As such, these predictions are likely not realistic but we include them to illustrate how escape fraction predictions depend sensitively on the ISM model, with our z5m10e run being representative of many simulations that do not have sufficient resolution to capture dense ISM structures.

For the fiducial stellar population model we adopt, the majority of the intrinsic ionizing photons are produced by the youngest star particles with age $< 3\,\text{Myr}$ (see also Figure 5.13). These stars are formed in dense, self-gravitating, molecular regions. Most of their ionizing photons are immediately absorbed by their "birth clouds" and thus cannot escape the star-forming regions (see also, e.g., Kim et al. 2013). When a star particle is older than 3 Myr, a large covering fraction of its birth cloud has been cleared by feedback and thus a significant fraction (order unity) of its ionizing photons are able to propagate to large distances (see e.g., the middle panels of Figure 5.2). Indeed, the ionizing photons that escaped in our simulations mostly come from the star particles of age between 3–10 Myr (also see Section

---

[8]Previous studies also showed that GMC lifetimes and integrated star formation efficiencies were nearly independent of the instantaneous density threshold and star formation efficiency in dense gas, as long as the clouds were resolved (Hopkins et al. 2011, 2012a).

[9]For HR runs where the mass of a star particle is only 10–100 $M_\odot$, we also test the effects of the IMF-average approximation. We randomly resample the ionizing photon budgets among individual star particles at a 1:20 ratio according to their ages and repeat the radiative transfer calculations. We find that the escape fractions are very similar. This confirms that the IMF-averaged approximation in HR runs does not affect our results.
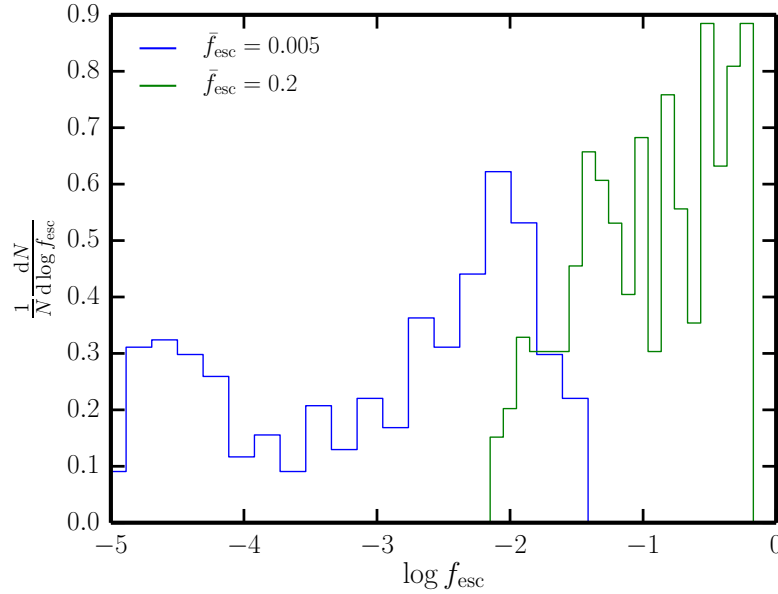
Figure 5.8: Angular distribution of escape fraction for two typical snapshots, with spatially averaged escape fraction 0.005 (blue) and 0.2 (green), respectively. Statistics are obtained from $N = 400$ uniformly sampled directions. The broad distribution implies that the ionizing photons that escape to the IGM are highly anisotropic, and that the measured escape fraction from individual galaxies can vary by more than 2 dex depending on the sightline.

5.5.4). However, the intrinsic ionizing photon budget of a star particle decreases rapidly with age above 3 Myr according to many standard stellar population models. In other words, the escape fractions are primarily determined by small-scale ISM structures surrounding young and intermediate-age star particles. The low escape fractions we find in our simulations are the consequence of the fact that the time-scale for a star particle to clear its birth cloud is comparable to the time-scale for it to exhaust a large amount of its ionizing photon budget. Only when star formation activities are intensive and can last for considerable amount of time, will the ionized regions expand and overlap and thus allow a large fraction of ionizing photons from the youngest stars to escape. For example, the high escape fractions in z5m10mr at cosmic time > 1 Gyr ($z \lesssim 6$) are due to the strong and lasting star formation during the past 100 Myr. However, such events are not common in our simulations, since further star formation activity is usually suppressed effectively by stellar feedback.

In Figure 5.8, we show the angular distribution of escape fraction as measured from $N = 400$ uniformly sampled directions. We repeat the radiative transfer calculation with ten times more photon packages than listed in Table 5.2 for two snapshots which

Figure 5.9: Time-averaged escape fraction (top panel) and escaped ionizing photon budget (bottom panel) as a function of cosmic time, color-coded by stellar mass. Different symbols represent the galaxies from different simulations. Points are the escape fraction averaged over $100\,\mathrm{Myr}$ ($Q_{\mathrm{esc}}/Q_{\mathrm{int}}$). We see no significant dependence of f_{esc} on redshift.

have spatially averaged escape fraction $f_{\mathrm{esc}} = 0.005$ and 0.2, respectively. The broad distribution of escape factions implies that the ionizing photons escaping to the IGM from galaxies are highly anisotropic. It also indicates that the observationally measured escape fraction from individual galaxies does not necessarily reflect the angle averaged escape fraction from the same object, as it can vary by roughly 2 dex depending on the sightline.

In Figures 5.9 and 5.10, we compile the time-averaged escape fraction and escaped ionizing photon budget as a function of cosmic time and stellar mass, respectively, for all the "well-resolved" galaxies in our standard runs. The symbols are color-
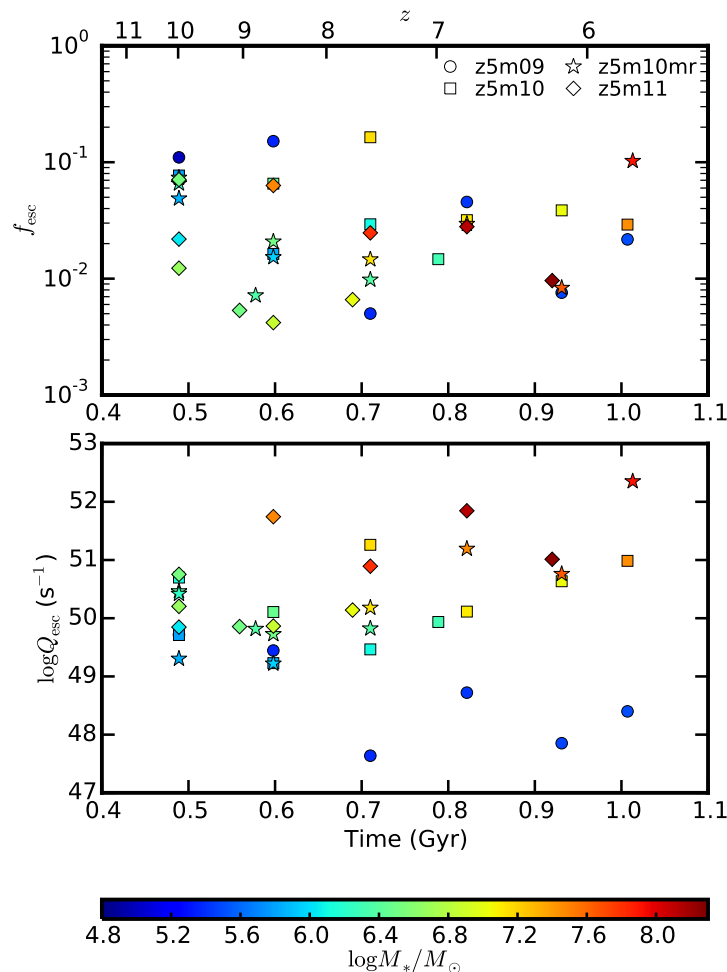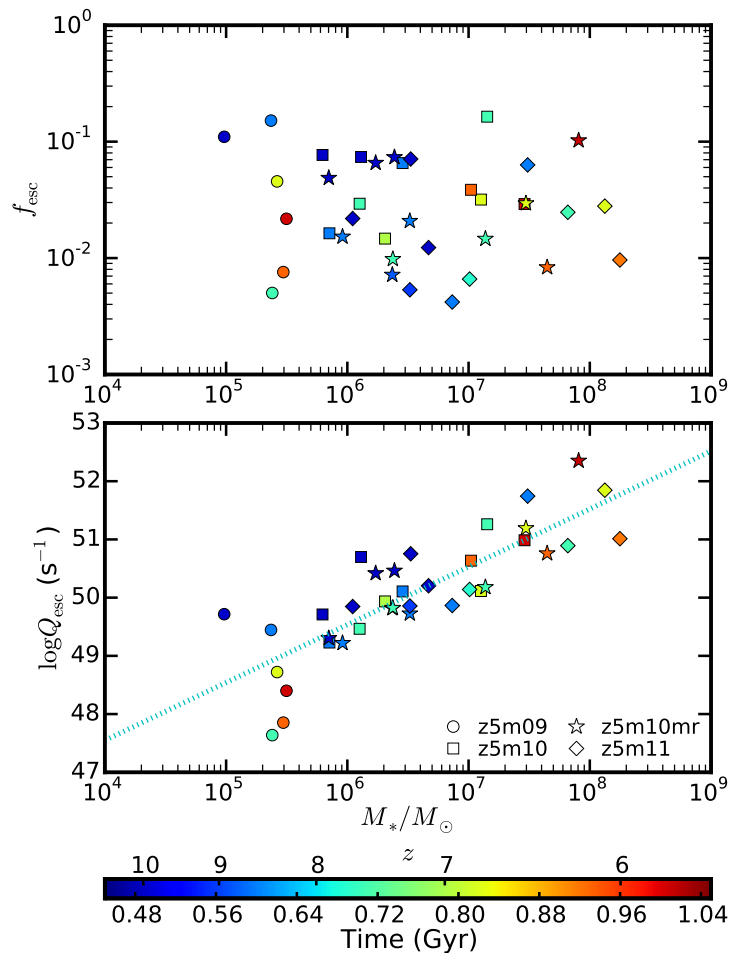
Figure 5.10: Time-averaged escape fraction (top panel) and escaped ionizing photon budget (bottom panel) as a function of stellar mass, color-coded by cosmic time. Different symbols represent the galaxies from different simulations. Points are the escape fraction averaged over 100 Myr. The cyan dotted line in the bottom panel shows the best linear fit of $\log Q_{\rm esc} = \log(M_*/{\rm M}_\odot) + 43.53$. We see no strong dependence of $f_{\rm esc}$ on M_*. The dependence of $Q_{\rm esc}$ on M_* broadly follows the SFR–M_* relation.

coded by stellar mass and cosmic time in Figure 5.9 and 5.10, respectively. Most of the points lie below $f_{\rm esc} < 5\%$. The escape fraction has a large scatter at fixed cosmic time or stellar mass. We find that there is *no* significant dependence of escape fraction on cosmic time or stellar mass. This is consistent with the argument that the escape of ionizing photons is restricted by small-scale ISM structures surrounding the young stellar populations. More simulations are required to study possible redshift and galaxy mass evolution to lower redshifts and over a wider mass interval than sampled by the simulations analyzed in this paper. We also caution that weak trends would be difficult to discern given the time variability found in our simulations and the small size of our simulation sample. The escaped ionizing photon budget depends linearly on stellar mass, with the best fit $\log Q_{\rm esc} = \log(M_*/{\rm M}_\odot) + 43.53$. This is primarily a consequence of the roughly linear dependence of SFR on stellar mass.

5.5 Discussion

We find that instantaneous escape fractions of hydrogen ionizing photons from our simulated galaxies vary between 0.01%–20% from time to time, while time-averaged escape fractions generally remain below 5%. These numbers are broadly consistent with the wide range of observationally constrained escape fractions measured from variant galaxy samples at $z = 0$–3 (e.g., Leitet et al. 2011, 2013; Cowie et al. 2009; Siana et al. 2010; Bridge et al. 2010; Iwata et al. 2009; Boutsia et al. 2011; Vanzella et al. 2012; Nestor et al. 2013).

We obtain much lower escape fractions than previous simulations with "sub-grid" ISM, star formation, and feedback models (e.g., Razoumov & Sommer-Larsen 2010; Yajima et al. 2011), but our results are more consistent with many recent simulations with state-of-art ISM and feedback models (e.g., Kim et al. 2013; Wise et al. 2014; Kimm & Cen 2014; Paardekooper et al. 2011, 2015). Below, we will show that this owes to the failure of the "sub-grid" models in resolving stellar birth clouds.

Nevertheless, the escape fractions from our simulated galaxies are still considerably lower than what requires for these galaxies to reionize the universe in many popular models. The tension can be at least partly resolved by invoking galaxies much fainter than what we study in this work, since smaller galaxies have dramatically increasing number densities and possibly much higher escape fractions (e.g., Alvarez et al. 2012; Paardekooper et al. 2013; Wise et al. 2014). Alternatively, in the rest of this section, we will discuss some physical parameters that might boost the escape

fractions in our simulated galaxies. Most of the experiments presented here are for illustrative purposes, but they are worth further exploration in future work in a more systematic and self-consistent way.

5.5.1 UV Background

We repeat the radiative transfer calculation for all the snapshots after cosmic time 0.9 Gyr ($z \sim 6$) of our z5m10mr galaxy with the UV background switched off (the red dotted line in the upper right panel of Figure 5.6). The predicted escape fractions does not differ from the previous calculation with the UV background at 0.01% level, consistent with the results in Yajima et al. (2011). This confirms that the low-density, diffused gas in the galactic halo (which is affected by the UV background) does not affect much the escape of ionizing photons[10].

5.5.2 Star Formation Criteria

In our standard simulations, we allow star formation occurs *only* in molecular, self-gravitating gas with density above a threshold $n_{th} = 100 \, cm^{-3}$. We run z5m10h where we adopt $n_{th} = 1000 \, cm^{-3}$ for a convergence study. For contrast, we intentionally design z5m10e to mimic "sub-grid" SF models, where we lower n_{th} to $1 \, cm^{-3}$ and allow extra SF at 2% efficiency per free-fall time in gas above the threshold but not self-gravitating. In Section 5.3, we have confirmed that the global galaxy properties (e.g., star formation rates, stellar masses, UV magnitudes, etc.) are very similar between these runs. However, as shown in Figure 5.6, the escape fraction from z5m10e is significantly higher than in other simulations.

To illustrate this more clearly, we compare the time-averaged (over 100 Myr timescale) escape fraction of z5m10, z5m10e, and z5m10h in Figure 5.11. The qualitative behaviors of escape fraction are very similar between z5m10, z5m10mr, and z5m10h, which further confirm that our results are converged with respect to resolution and SF density threshold (as long as it is much larger than the mean density of the ISM).

However, in z5m10e, the escape fraction is dramatically higher, since many young stars form in the diffuse ISM. Their ionizing photons can then immediately escape the galaxy. We emphasize that the z5m10e run is not realistic but mimics "sub-grid" SF models as adopted in low-resolution simulations where star formation in dense gas clouds cannot be resolved. This suggests a caution that simulations with

---

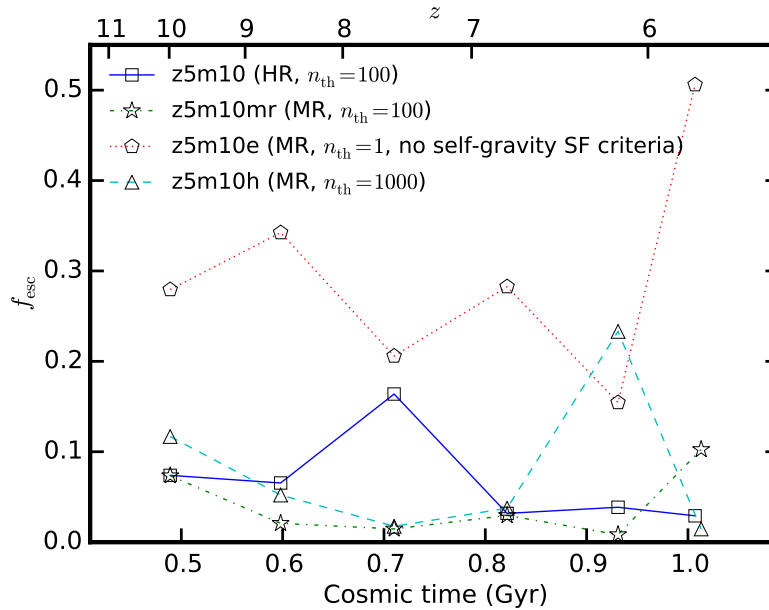[10]However, if the simulations are run without a UV background, gas accretion onto the halo itself can be modified.

Figure 5.11: Escape fraction with different star formation density prescriptions. The escape fractions averaged over 100 Myr are shown for z5m10 (n_{th} = 100 cm^{-3}, blue solid), z5m10mr (n_{th} = 100 cm^{-3}, green dotted), z5m10h (n_{th} = 1000 cm^{-3}, cyan dashed), and z5m10e (n_{th} = 1 cm^{-3}, without SF self-gravity criteria, red dotted). For n_{th} ≳ 100 cm^{-3}, our results are well-converged with respect to SF density threshold and resolution. However, if SF is allowed in diffuse gas, f_{esc} can be severely over-estimated.

"sub-grid" SF models can over-predict the escape fraction by an order of magnitude.

5.5.3 Runaway Stars

There is plenty of evidence that a considerable fraction of O and B stars have high velocities and can travel far from their birth clouds during their lifetime (the "runaway" stars, e.g., Blaauw 1961; Stone 1991; Hoogerwerf et al. 2001; Tetzlaff et al. 2011). To qualitatively illustrate the effect of these runaway stars on the escape fraction (e.g., Conroy & Kratter 2012), we move every star particle younger than 3 Myr by a distance $v_{ini}t_{age}$ along a random direction in the snapshots, and repeat the radiative transfer calculation to evaluate the escape fraction as the stars are at their new positions. Here v_{ini} is some initial kicking velocity and t_{age} is the age of the star particle. In principle, it would be more self-consistent if we re-run the whole simulation with runaway star prescription (e.g., Kimm & Cen 2014). Nonetheless, our simple experiment provides a first estimate of the effects of runaway stars on the escape fraction.
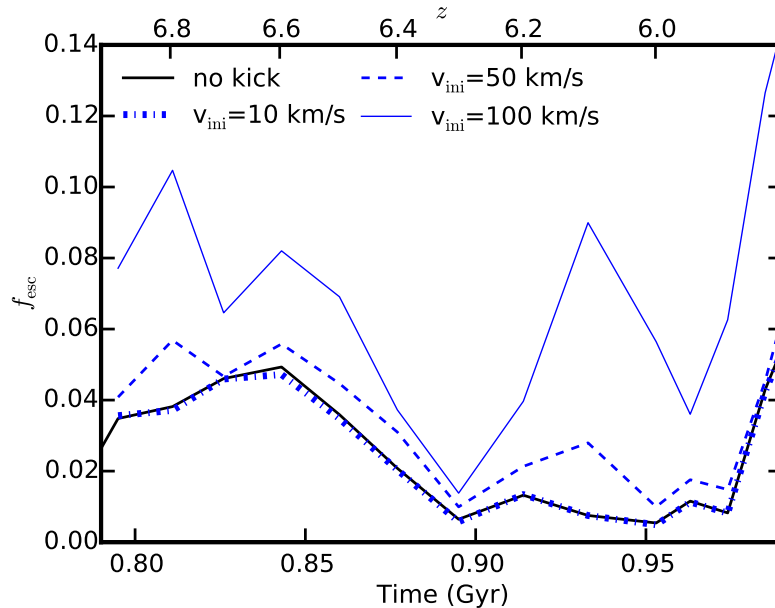
Figure 5.12: Escape fractions in presence of runaway stars. We only show z5m10mr during the cosmic time 0.8–1.0 Gyr ($z = 6$–7, but the effect in other runs would is similar). Each star particle younger than 10 Myr is kicked from its original position along a random direction with an initial velocity v_{ini}. Blue dotted, dashed, and solid lines show the results for $v_{\mathrm{ini}} = 10\,\mathrm{km\,s^{-1}}$, $50\,\mathrm{km\,s^{-1}}$, and $100\,\mathrm{km\,s^{-1}}$, respectively. The black solid line shows the escape fraction when $v_{\mathrm{ini}} = 0$ (the same as in Figure 5.6). Typical kick velocities suggested by observations ($\sim 30\,\mathrm{km\,s^{-1}}$) have only small effects on f_{esc}. Only if the velocities are very large (e.g., $\gtrsim 100\,\mathrm{km\,s^{-1}}$), and an order-unity fraction of stars have been kicked, will this be significant.

We repeat this experiment for our z5m10mr run during cosmic time between 0.8–1.0 Gyr ($z = 6$–7) with $v_{\mathrm{ini}} = 10$, 50, and 100 km s^{-1}, corresponding to a displacement of 30, 150, and 300 pc for a star particle of age 3 Myr. We show the results in Figure 5.12. A small initial velocity of $v_{\mathrm{ini}} = 10\,\mathrm{km\,s^{-1}}$ barely affects the escape fraction since the displacement of a newly formed star particle is $\lesssim 30\,\mathrm{pc}$, which is much less than the typical size of their birth clouds (see Figure 5.2 for an illustration of the ISM structure around young star particles). For $v_{\mathrm{ini}} = 50\,\mathrm{km\,s^{-1}}$, the escape fractions can be boosted by at most 1–2% (in absolute units, or 20-30% fractionally). Only for extremely high initial velocity ($\sim 100\,\mathrm{km\,s^{-1}}$), the escape fractions are enhanced by a few precent, since some young star particles are kicked out of their birth clouds. But these numbers are still somewhat lower than what many reionization models require. Note that observations suggest that only $\sim 30\%$ of the OB stars are runaway stars and that the typical velocity of runaway stars is around $30\,\mathrm{km\,s^{-1}}$ (e.g., Tetzlaff et al. 2011). Therefore, our experiments suggest that runaway stars will boost the
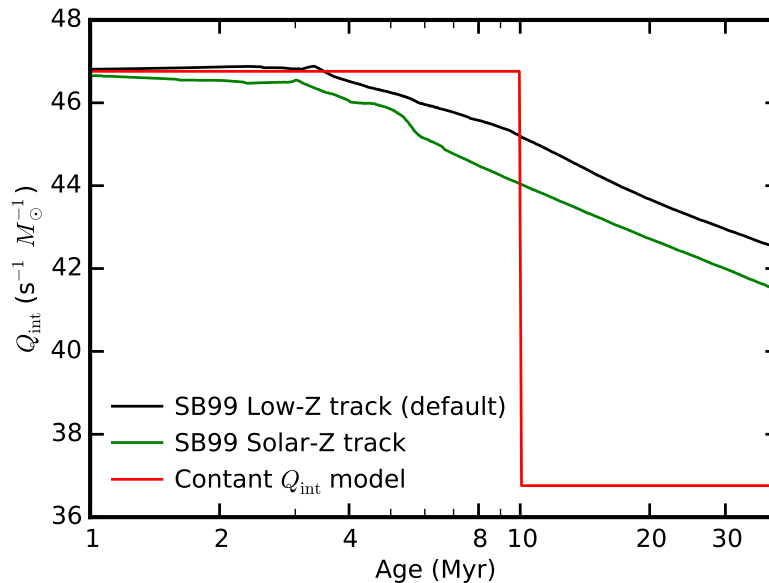
Figure 5.13: Ionizing photon budget per unit mass for a stellar population as a function of its age. The black line shows the STARBURST99 low-metallicity model (our default model). The green line shows the STARBURST99 solar-metallicity model. The red line shows a simple "constant Q_{int} model" we consider in Figure 5.14. This produces a similar number of ionizing photons in the first 3 Myr, but retains the same photon production rate to 10 Myr.

escape fractions by no more than 1% (in absolute units, or 20% fractionally)[11].

5.5.4 Stellar Population Models

So far, we have adopted the Padova+AGB stars track of metallicity $Z = 0.0004$ (0.02 $Z_\odot$) from STARBURST99 model assuming a Kroupa (2002) IMF from 0.1–100 $M_\odot$ to evaluate the intrinsic ionizing photon budget for each star particle. In this model, the ionizing photon production rate decreases rapidly when the age of a stellar population exceeds 3 Myr. However, there are good reasons to believe that these models suffer from great uncertainties. For example, Steidel et al. (2014) emphasized the importance of binary and rotating stars since these stars have high effective temperatures that are required to explain the ionization states of $z = 2$–3 star forming galaxies. Moreover, recent theoretical studies suggest that binary star interactions can produce ionizing photons in a stellar population older

---

[11]One effect not captured in our post-processing experiment which could potentially boost the escape fraction is how feedback from runaway stars would affect the structure of the ISM as they move away from their birth locations. A self-consistent modeling of runaway stars is presented in Kimm & Cen (2014). Our result is broadly consistent with theirs for halo masses $\sim 10^{10}\,M_\odot$.
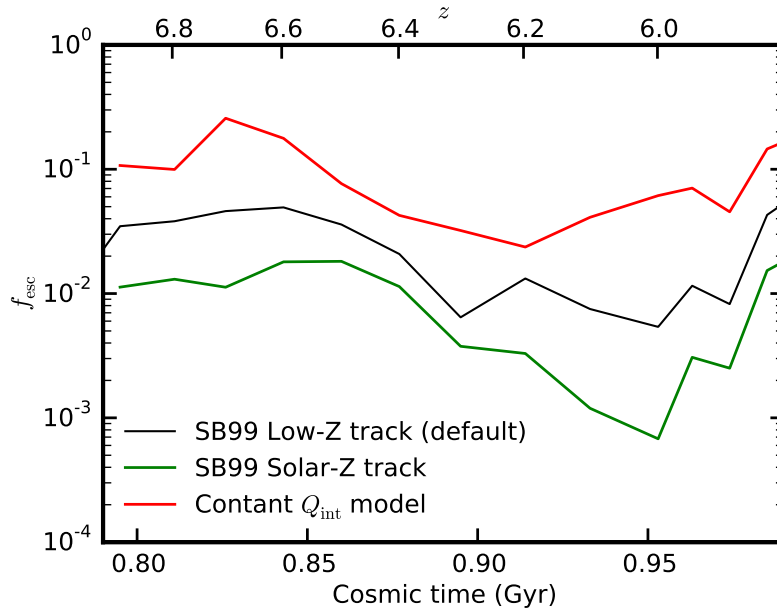
Figure 5.14: Escape fractions calculated by invoking the three different stellar population models shown in Figure 5.13. We show the results for z5m10mr during cosmic time 0.8–1.0 Gyr ($z = 6$–7, but the effect in all other runs is similar). The black line shows the results using the STARBURST99 low-metallicity model ($Z = 0.0004$, our fiducial model, the same as in Figure 5.6). The green line shows the results using STARBURST99 solar-metallicity model ($Z = 0.02$). The red line shows the results when using the "constant Q_{int} model". By extending the lifetime of photon production to 3–10 Myr, when the birth clouds have been largely cleared, large f_{esc} (10–20%) can be obtained.

than 3 Myr; such events are not uncommon (e.g., de Mink et al. 2014). While these models are very uncertain and still poorly understood, it is not unphysical to invoke more ionizing photons from these populations. To explore the effects of different stellar population models on the escape fractions, we construct a toy model which we refer to as the "constant Q_{int} model" to explore its effect on the escape of ionizing photons. In this model, the ionizing photon budget of a stellar population is $5.6 \times 10^{46}\,\mathrm{s}^{-1}\,\mathrm{M}_\odot^{-1}$ when the population is younger than 10 Myr and suddenly drops to $5.6 \times 10^{36}\,\mathrm{s}^{-1}\,\mathrm{M}_\odot^{-1}$ when the population is older than 10 Myr. For comparison, we also tabulate the ionizing photon budget using the Padova+AGB stars track of solar metallicity ($Z = 0.02$) from STARBURST99 model. We illustrate in Figure 5.13 the intrinsic ionizing photon budget as a function of stellar age for the three models we discuss. Their behaviors are very similar for stellar age < 3 Myr, after which they start to deviate heavily from each other. The solar-metallicity model has the lowest ionizing photon budget between 3–10 Myr while the constant Q_{int} model has

the highest.

We repeat the radiative transfer calculation to calculate the escape fraction assuming intrinsic ionizing photon production rate evaluated from these models. In Figure 5.14, we show the results for our z5m10mr run during cosmic time 0.8–1.0 Gyr ($z = 6$–7). The escape fractions are very sensitive to the stellar models we use. For the solar-metallicity track model, we get the lowest escape fractions. On the other hand, if we adopt the constant Q_{int} model, we find the escape fractions are enhanced by almost an order of magnitude. These results further illustrate the picture that the escaped photons come from star particles of age 3–10 Myr, where their birth clouds have been cleared by feedback. Our findings suggest that relatively older stellar populations could contribute a considerable fraction of ionizing photons during reionization, if these populations produce more ionizing photons than what standard stellar population models predict, as motivated by models that include rotation, binaries, and mergers.

5.6   Conclusions

In this work, we present a series of extremely high-resolution (particle mass 20–2000 $M_\odot$, smoothing length 0.1–4 pc) cosmological zoom-in simulations of galaxy formation down to $z \sim 6$, covering galaxy halo masses in 10^9–10^{11} $M_\odot$, stellar masses in 2×10^5–2×10^8 $M_\odot$, and rest-frame ultraviolet magnitudes $M_{UV} = -9$ to -19 at that time. This set of simulations include realistic models of the multi-phase ISM, star formation, and stellar feedback (with *no* tuned parameters), which allow us to explicitly resolve small-scale ISM structures. Cosmological simulations with these feedback models have been shown to produce reasonable star formation histories, the stellar-mass halo mass relation, the Kennicutt-Schmidt law, the star-forming main sequence, etc., at $z = 0$–6 (Hopkins et al. 2014). We post-process our simulations with a Monte Carlo radiative transfer code to evaluate the escape fraction of hydrogen ionizing photons from these galaxies. Our main conclusions include the following.

(i) Instantaneous escape fractions have large time variabilities, fluctuating from $< 0.01\%$ to $> 20\%$ from time to time. In our standard runs, the escape fractions can reach 10–20% only for a small amount of time. The time-averaged escape fractions (over time-scales 100–1000 Myr) generally remain below 5%, considerably lower than many recent models of reionization require.

(ii) As long as star formation is regulated effectively via feedback, the escape

fractions are mainly determined by small-scale ISM structures around young and intermediate-age stellar populations. According to standard stellar population models, most of the intrinsic ionizing photons are produced by newly formed star particles younger than 3 Myr. They tend to be embedded in their dense birth clouds, which prevent nearly all of their ionizing photons from escaping. The escaping ionizing photons primarily come from intermediate-age stellar populations between 3–10 Myr, where the dense birth clouds have been largely destroyed by feedback. According to "standard" stellar population models, the ionizing photon production rates decline heavily with time at these ages. This leads to the difficulty of getting high escape fractions.

(iii) The escape fractions do not change if the star formation density threshold increases from 100 to 1000 cm^{-3}, as long as stars form in resolved, self-gravitating, dense clouds. On the other hand, if we allow star formation in the diffuse ISM (with some *ad hoc* low star formation efficiency), as is adopted in most low-resolution cosmological simulations, the escape fractions can be over-predicted by an order of magnitude. We emphasize that realistic, resolved phase structure of the ISM is critical for converged predictions of escape fractions.

(iv) Applying a fraction of $\sim 30\%$ runaway OB stars to our simulations with typical velocity $\sim 30 \, \mathrm{km \, s^{-1}}$ as motivated by many observations can only enhance the escape fraction by at most 1% (in absolute values, or 20% fractionally). The effect of runaway stars would not be significant unless a large fraction of the most young stars can obtain dramatically high initial velocity in high-redshift galaxies.

(v) Stellar populations older than 3 Myr may play an important role in reionizing the universe. The escape fractions can be boosted significantly if stellar populations of intermediate ages produce more ionizing photons than what standard stellar population models predict, as suggested by many new stellar population models (e.g., models including rotations, binary interactions, and mergers).

Our simulations are limited in sample size. Also, the simple experiments we present in Section 5.5 do not treat stellar feedback consistently with varying stellar models. Our results motivate further work exploring the effects of IMF variations, stellar evolution models, runaway stars, etc., in a more systematic and self-consistent way.

Appendix A: Comparison of MCRT post-processing to on-the-fly ionization calculations

As described in Section 5.2, in our simulations, the ionization state of each gas particle at every timestep is determined from the photoionization equilibrium equations described in Katz et al. (1996), given a uniform and redshift-dependent UV background from Faucher-Giguère et al. (2009) and photon-ionization and photon-electric heating rate from local sources, assuming a local Jeans-length approximation of self-shielding. In the simulations ("on-the-fly"), we model photoionization feedback from star particles in an approximate way – we move outward from the star particle and ionize each nearest neutral gas particle until the photon budget is completely consumed. In intense star-forming regions, this allows H II regions to expand and overlap and thus approximately captures reasonable ionization states in these regions. However, if the gas distribution is highly asymmetric around an isolated star particle (see, e.g., the middle column in Figure 5.2), the gas ionization states will not be accurately captured. In this work, we follow the propagation of ionizing photons and re-compute the gas ionization state with a Monte Carlo radiative transfer code in post-processing, which will be more accurate in photoionization regions.

Figure 5.15 shows the gas neutral fractions on a slice crossing the galactic center, of a snapshot at $z = 6$ from z5m10. Figure 5.16 shows the neutral hydrogen column
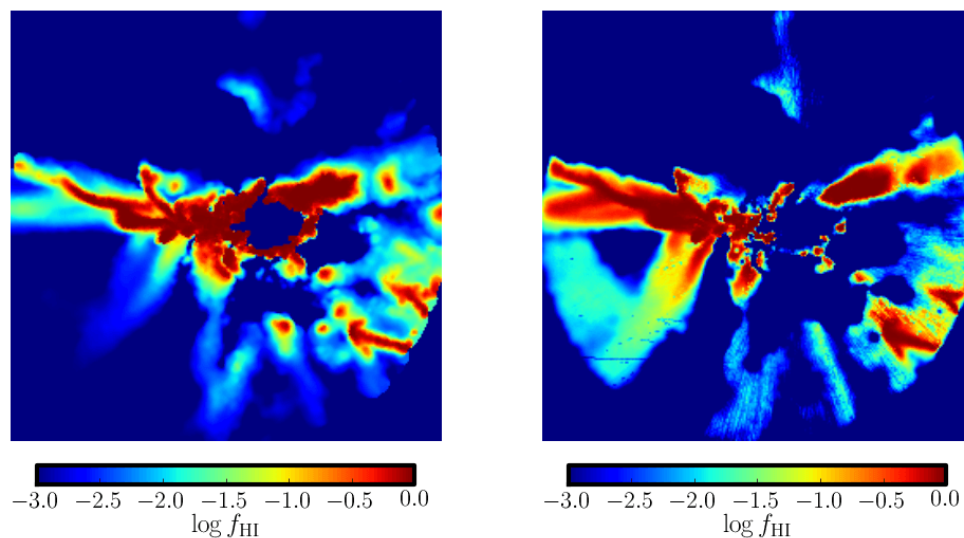
Figure 5.15: Gas neutral fraction on a slice across the galactic center. We show the snapshot at $z = 6$ from z5m10mr. *Left*: the neutral fraction directly extracted from the simulation. *Right*: the neutral fraction recomputed by radiative transfer code. The size of the box equals to two times of the virial radius and there are 250 pixels along each direction. Only regions within the virial radius are shown.
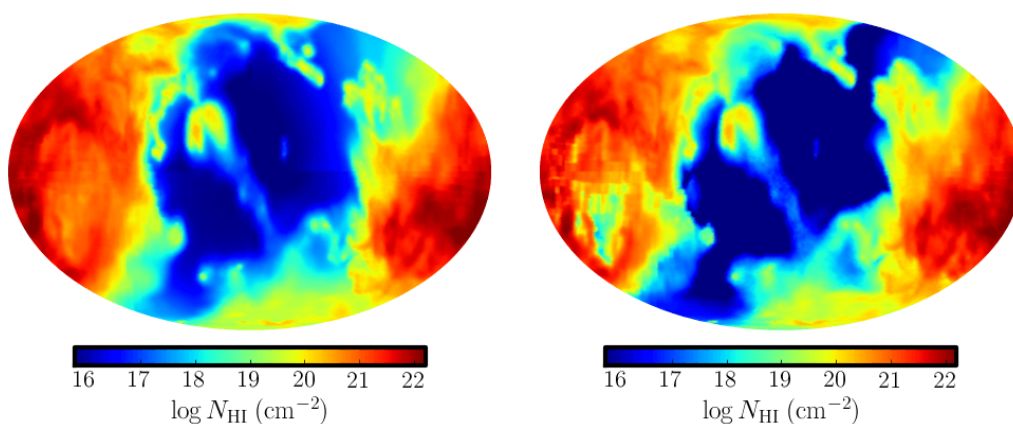
Figure 5.16: Neutral hydrogen column density as viewed from the galactic center. We show the snapshot at $z = 6$ from z5m10mr. *Left*: the neutral column density directly extracted from the simulation. *Right*: the neutral column density recomputed by radiative transfer code.
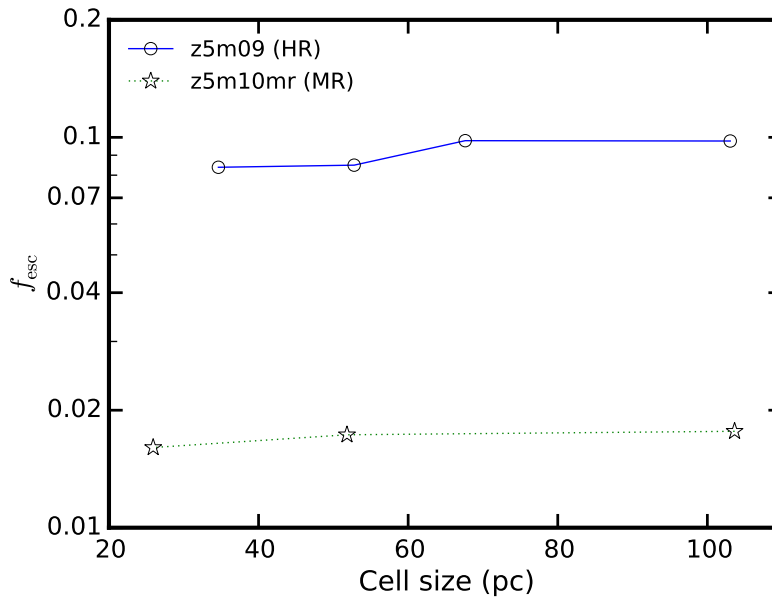
Figure 5.17: Resolution convergence of MCRT calculation. We show two examples, one from z5m09 (HR) and the other from z5m10mr (MR), where we repeat the MCRT calculation for the same galaxy but with different grid cell sizes for the RT calculation. The results are relatively insensitive to the cell size, for cell sizes varying from $l = 20$–100 pc.

density map as viewed from the center of the galaxy for the same snapshot. In both figures, the left panels are the results before post-processing and the right panels show the results from radiative transfer calculations (using ten times the standard number of photon packages listed in Table 5.2). In general, both results agree quite well on large-scale pattern of the neutral gas distribution, although radiative transfer calculations reveal more small structures in star-forming regions. None of our conclusions in this paper are changed qualitatively if we compute the escape fractions using on-the-fly ionization states in the simulations. It is reassuring, both for the present work and for previous studies that used the same approximations, that the approximations used in the simulation code predict ionization structures that are broadly consistent with post-processing radiative transfer calculations.

Appendix B: Resolution convergence for MCRT calculation

In Section 5.4.1, we describe that the MCRT calculation is performed on a cubic Cartesian grid of side length L and with N cells along each dimension. In principle, the resolution $l = L/N$ should be small enough to capture the ISM structure, but the number of cells N^3 cannot be so big that the calculation is too computationally expensive. After performing extensive convergence tests, we choose $l = 25$–100 pc

depending on the size of the galactic halo. Here we show two typical examples, one from z5m09 (HR) and the other from z5m10mr (MR), to illustrate the convergence of our MCRT calculation with respect to cell size l. As shown in Figure 5.17, we repeat the MCRT calculation for the same galaxy with resolution varying from $l = 20$–100 pc and find that the escape fractions do not change appreciably.

The MCRT calculation converges at much poorer resolution than that we adopt for hydrodynamics. This is because most of the sources reside in an environment where the ionizing photon optical depth is either $\tau_{UV} \gg 1$ or $\tau_{UV} \ll 1$. In both limits, the MCRT calculation converges even if the exact column density is not captured with great accuracy (e.g., $\tau_{UV} = 100$ and $\tau_{UV} = 10$ make little difference). However, we emphasize that the high resolution of hydrodynamics is *necessary* in order to capture the ISM structure in the presence of star formation and stellar feedback. Low resolution simulations with "sub-grid" models tend to over-predict escape fraction (see the discussion in Section 5.5.2).

Chapter 6

BINARY STARS CAN PROVIDE THE "MISSING PHOTONS" NEEDED FOR REIONIZATION

Abstract

Empirical constraints on reionization require galactic ionizing photon escape fractions $f_{\text{esc}} \gtrsim 20\%$, but recent high-resolution radiation-hydrodynamic calculations have consistently found much lower values $\sim 1\text{–}5\%$. While these models include strong stellar feedback and additional processes such as runaway stars, they almost exclusively consider stellar evolution models based on single (isolated) stars, despite the fact that most massive stars are in binaries. We re-visit these calculations, combining radiative transfer and high-resolution cosmological simulations with detailed models for stellar feedback from the Feedback in Realistic Environments (FIRE) project. For the first time, we use a stellar evolution model that includes a physically and observationally motivated treatment of binaries (the BPASS model). Binary mass transfer and mergers enhance the population of massive stars at late times ($\gtrsim 3\,\text{Myr}$) after star formation, which in turn strongly enhances the late-time ionizing photon production (especially at low metallicities). These photons are produced after feedback from massive stars has carved escape channels in the ISM, and so efficiently leak out of galaxies. As a result, the time-averaged "effective" escape fraction (ratio of escaped ionizing photons to observed $1500\,\text{Å}$ photons) increases by factors $\sim 4\text{–}10$, sufficient to explain reionization. While important uncertainties remain, we conclude that binary evolution may be critical for understanding the ionization of the Universe.

Keywords: binaries: general – stars: evolution – galaxies: formation – galaxies: high-redshift – cosmology: theory

6.1 Introduction

The escape fraction (f_{esc}) of hydrogen ionizing photons from high-redshift star-forming galaxies is perhaps the most important and yet most poorly understood parameter in understanding the reionization history. Models of cosmic reionization suggest that $f_{\mathrm{esc}} \gtrsim 20\%$ (e.g., Kuhlen & Faucher-Giguère 2012; Finkelstein et al. 2012; Robertson et al. 2013, 2015) is needed to match the optical depth of electron scattering inferred from cosmic microwave background (CMB) measurements (e.g., Hinshaw et al. 2013; Planck Collaboration et al. 2014), assuming that most of the ionizing photons come from star-forming galaxies brighter than $M_{\mathrm{UV}} = -13$.

However, such a high f_{esc} is problematic in the context of both observations and theory. From the local universe to redshift $z \sim 1$, there is no confirmed Lyman continuum (LyC) detection, neither from individual galaxies nor from stacked samples, implying upper limits of $f_{\mathrm{esc}} = 1\text{--}3\%$ (e.g., Leitet et al. 2011, 2013; Bridge et al. 2010; Siana et al. 2010). Even at $z \sim 3$, many earlier reports of LyC detection from Lyman break galaxies (LBGs) and Lyα emitters (LAEs) have proven to be contaminated by foreground sources (e.g., Siana et al. 2015) and a low f_{esc} about 5% has been derived from some galaxy samples at this redshift (e.g., Iwata et al. 2009; Boutsia et al. 2011).

Moreover, the latest generation of cosmological hydrodynamic simulations predict f_{esc} to be no more than a few percent in galaxies more massive than $10^9 \, \mathrm{M_\odot}$ in halo mass at $z > 6$ (e.g., Wise et al. 2014; Kimm & Cen 2014; Paardekooper et al. 2015; Ma et al. 2015). These simulations include detailed models of ISM physics, star formation, and stellar feedback, in contrast to early generations of simulations which tended to over-predict f_{esc} by an order of magnitude, owing to more simplistic ISM models (see Ma et al. 2015, and references therein). The low f_{esc} in these simulations is due to the fact that newly formed stars, which dominate the intrinsic ionizing photon budget, begin life buried in their birth clouds, which absorb most of the ionizing photons. By the time low column density escape channels are cleared in the ISM, the massive stars have begun to die and the predicted ionizing photon luminosity has dropped exponentially. Stellar populations older than 3 Myr have order unity photon escape fractions, but – according to single stellar evolution models such as STARBURST99 (Leitherer et al. 1999) – these stars only contribute a small fraction of the intrinsic ionizing photon budget (Ma et al. 2015).

Therefore, there appears to be a factor of $\sim 4\text{--}5$ fewer ionizing photons predicted, compared to what is needed to ionize the Universe. Several solutions have been

proposed. For example, Wise et al. (2014) suggested that tiny galaxies that are much fainter than $M_{UV} = -13$ may play a significant role in reionization, since f_{esc} increases quickly from 5% to order unity for halo mass below $10^{8.5}\,M_\odot$. However, others have noted that the required number of tiny galaxies would imply a huge population of Milky Way satellites which have not been observed (see e.g., Boylan-Kolchin et al. 2014; Graus et al. 2016). Conroy & Kratter (2012) proposed that runaway OB stars can boost f_{esc}; however, both Kimm & Cen (2014) and Ma et al. (2015) showed that in high-resolution simulations these produce a marginal effect, increasing f_{esc} systematically by a factor of only ~ 1.2 (far short of the $\gtrsim 4$ required). A more radical alternative is to invoke non-stellar sources for reionization, for example AGN (see e.g., Madau & Haardt 2015). This relies on recent observations (e.g., Giallongo et al. 2015) suggesting much higher number densities of faint AGN at high redshift than previously thought (e.g., Hopkins et al. 2007).

But there are gaps in our understanding of stellar evolution. One key factor that is usually not considered in standard stellar population models is the effect of binary interaction. Mass transfer between binary stars, and binary mergers, can effectively increase the number of high-mass stars at later times after star formation. Also, massive, rapidly-rotating stars produced via mass transfer undergo quasi-homogeneous evolution if the metallicity is sufficiently sub-solar. These stars are hotter and their surface temperature increases as they evolve (e.g., Eldridge & Stanway 2012). All of these can substantially increase the number of ionizing photons produced at late times, compared to what is expected from single-star evolution models (e.g., de Mink et al. 2014). Recently, Stanway et al. (2016) pointed out that the emissivity of ionizing photons from high-redshift galaxies, inferred from their UV luminosities, would be higher by a factor of ~ 1.5 using stellar evolution models that account for binary interaction. Furthermore, binary evolution does not just produce *more* ionizing photons, but it may also substantially increase the escape fractions (Ma et al. 2015).

In this paper, we explore in more detail the effect of binary interaction on ionizing photon production and escape by repeating the calculation described in Ma et al. (2015) using the Binary Population and Spectral Synthesis (BPASS) model of stellar population evolution[1] (Eldridge et al. 2008, 2017). These models are calibrated to observations of local stellar populations, and reproduce the observed multiplicity

---

[1]http://bpass.auckland.ac.nz

Table 6.1: Simulations analyzed in this chapter.

Name	m_b (M$_\odot$)	ϵ_b (pc)	m_{dm} (M$_\odot$)	ϵ_{dm} (pc)	M$_{halo}$ (M$_\odot$)	M$_*$ (M$_\odot$)	M$_{UV}$ (AB mag)
z5m09	16.8	0.14	81.9	5.6	7.6e8	3.1e5	-10.1
z5m10mr	1.1e3	1.9	5.2e3	14	1.5e10	5.0e7	-17.5
z5m11	2.1e3	4.2	1.0e4	14	5.6e10	2.0e8	-18.5

Notes. Initial conditions and galaxy properties at $z = 6$.
(1) Name: Simulation designation.
(2) m_b: Initial baryonic particle mass.
(3) ϵ_b: Minimum baryonic force softening. Force softening is adaptive.
(4) m_{dm}: Dark matter particle mass in the high-resolution regions.
(5) ϵ_{dm}: Minimum dark matter force softening.
(6) M$_{halo}$: Halo mass of the primary galaxy at $z = 6$.
(7) M$_*$: Stellar mass of the primary galaxy at $z = 6$.
(8) M$_{UV}$: Galaxy UV magnitude (absolute AB magnitude at 1500 Å).

distributions (Eldridge et al. 2008). Moreover, the BPASS model predicts stellar populations with a harder ionizing spectrum, which is required to explain the observed differences between various nebular emission-line properties of metal-poor, younger galaxies at $z \sim$ 2–3 and local galaxies (Steidel et al. 2014; for a more detailed study, see Steidel et al. 2016; Strom et al. 2017). In Ma et al. (2015), we performed Monte Carlo radiative transfer (MCRT) calculations on a suite of cosmological hydrodynamic simulations and showed that the time-averaged f_{esc} is about 5% for galaxies of halo masses from 10^9–10^{11} M$_\odot$ at $z = 6$ using the single-star evolution models from STARBURST99. Importantly, we showed that the results were robust to the resolution of both the radiative transfer calculation and the hydrodynamics (once sufficient resolution for convergence was reached), to variations of the star formation and stellar feedback model, and even to the inclusion of large populations of runaway stars. We will show here, however, that the inclusion of binary evolution effects increases the predicted escape fractions substantially, reconciling them with constraints on reionization. We describe the simulation and radiative transfer code in Section 6.2, present the results in Section 6.3, and conclude in Section 6.4.

We adopt a standard flat ΛCDM cosmology with cosmological parameters $H_0 = 70.2\,\mathrm{km\,s^{-1}\,Mpc^{-1}}$, $\Omega_\Lambda = 0.728$, $\Omega_m = 1 - \Omega_\Lambda = 0.272$, $\Omega_b = 0.0455$, $\sigma_8 = 0.807$ and $n = 0.961$, consistent with observations (e.g., Hinshaw et al. 2013; Planck Collaboration et al. 2014).

6.2   Method

In this work, we study the effect of binary evolution on f_{esc} using three galaxies from a suite of cosmological zoom-in simulations presented in Ma et al. (2015). The simulation and radiative transfer are identical. We *only* replace the stellar evolution model used for the post-processing radiative transfer calculations. This is likely to result in a lower limit on the impact of binaries on f_{esc}, because we do not include the enhanced radiative feedback due to binaries in our simulation. We briefly review the methodology here, but refer to Ma et al. (2015) for more details.

The simulations are part of the Feedback in Realistic Environment project[2] (FIRE; Hopkins et al. 2014). They are run using GIZMO (Hopkins 2015) in P-SPH mode, which adopts a Lagrangian pressure-entropy formulation of the smoothed particle hydrodynamics (SPH) equations that improves the treatment of fluid-mixing instabilities (Hopkins 2013). Galaxy properties at $z = 6$ for the three simulations used in this work (z5m09, z5m10mr, and z5m11) are listed in Table 6.1. Our simulations span halo masses from 10^9–10^{11} $M_\odot$ at $z = 6$. These galaxies lie on the low-mass extrapolations of the observed stellar mass–halo mass relation and SFR–stellar mass relation at $z > 6$ (Ma et al. 2015). At lower redshifts (where observations exist at these masses), the simulations have been shown to reproduce observed scaling relations and chemical abundances (Hopkins et al. 2014; Ma et al. 2016a), properties of galactic outflows and circum-galactic absorbers (Muratov et al. 2015; Faucher-Giguère et al. 2015, 2016), and abundances and kinematics of observed (local) dwarfs in this mass range (Oñorbe et al. 2015; Chan et al. 2015).

In the simulations, gas follows an ionized-atomic-molecular cooling curve from 10–10^{10} K, including metallicity-dependent fine-structure and molecular cooling at low temperatures and high-temperature metal-line cooling for 11 separately tracked species (Wiersma et al. 2009a). We do not include a primordial chemistry network nor consider Pop III star formation, but apply a metallicity floor of $Z = 10^{-4}\,Z_\odot$. At each timestep, the ionization states are determined following Katz et al. (1996) and cooling rates are computed from a compilation of CLOUDY runs, including a uniform but redshift-dependent photo-ionizing background tabulated in Faucher-Giguère et al. (2009), and an approximate model of photo-ionizing and photo-electric heating from local sources. Gas self-shielding is accounted for with a local Jeans-length approximation, which is consistent with the radiative transfer calculations in Faucher-Giguère et al. (2010). The on-the-fly calculation of ionization states is

---

[2]http://fire.northwestern.edu

consistent with more accurate post-processing radiative transfer calculations (Ma et al. 2015).

We follow the star formation criteria in Hopkins et al. (2013b) and allow star formation to take place only in dense, molecular, and self-gravitating regions with hydrogen number density above a threshold $n_{\rm th} = 50\,{\rm cm}^{-3}$. Stars form at 100% efficiency per free-fall time when the gas meets these criteria, and there is no star formation elsewhere. Because we require star-forming gas to be self-gravitating, its effective density is even higher than the fiducial density threshold we adopt in our simulations. We emphasize the importance of resolving the formation and destruction of individual star-forming regions in accurately predicting $f_{\rm esc}$, as stressed also in other studies (e.g., Kimm & Cen 2014; Paardekooper et al. 2015; Ma et al. 2015). Simulations using unphysically low $n_{\rm th}$ fail to resolve this and tend to over-predict $f_{\rm esc}$ by an order of magnitude (see Ma et al. 2015, and reference therein).

The simulations include several different stellar feedback mechanisms, including (1) local and long-range momentum flux from radiative pressure, (2) energy, momentum, mass and metal injection from SNe and stellar winds, and (3) photo-ionization and photo-electric heating. We follow Wiersma et al. (2009b) and include metal production from Type-II SNe, Type-Ia SNe, and stellar winds. Every star particle is treated as a single stellar population with known mass, age, and metallicity, assuming a Kroupa (2002) initial mass function (IMF) from 0.1–100 $M_\odot$. The feedback strengths are directly tabulated from STARBURST99.

For every snapshot, we map the main galaxy onto a Cartesian grid of side length L equal to two virial radii and with N cells along each dimension. We choose $N = 256$ for z5m09 and z5m10mr and $N = 300$ for z5m11, so that the cell size $l = L/N$ varies but is always smaller than 100 pc. This ensures convergence of the MCRT calculation (Ma et al. 2015). The MCRT code we use is derived from the MCRT code SEDONA (Kasen et al. 2006), but focuses on radiative transfer of hydrogen ionizing photons. The MCRT method is similar to that described in Fumagalli et al. (2011, 2014). $N_{\rm star} = 3 \times 10^7$ photon packets are isotropically emitted from the location of star particles, sampling their ionizing photon budgets. Another $N_{\rm UVB} = 3 \times 10^7$ photon packets are emitted from the boundary of the computational domain in a manner that produces a uniform, isotropic ionizing background with intensity given by Faucher-Giguère et al. (2009). The MCRT code includes photoionization, collisional ionization, recombination, and dust absorption and uses an iterative method to reach photoionization equilibrium. The numbers of
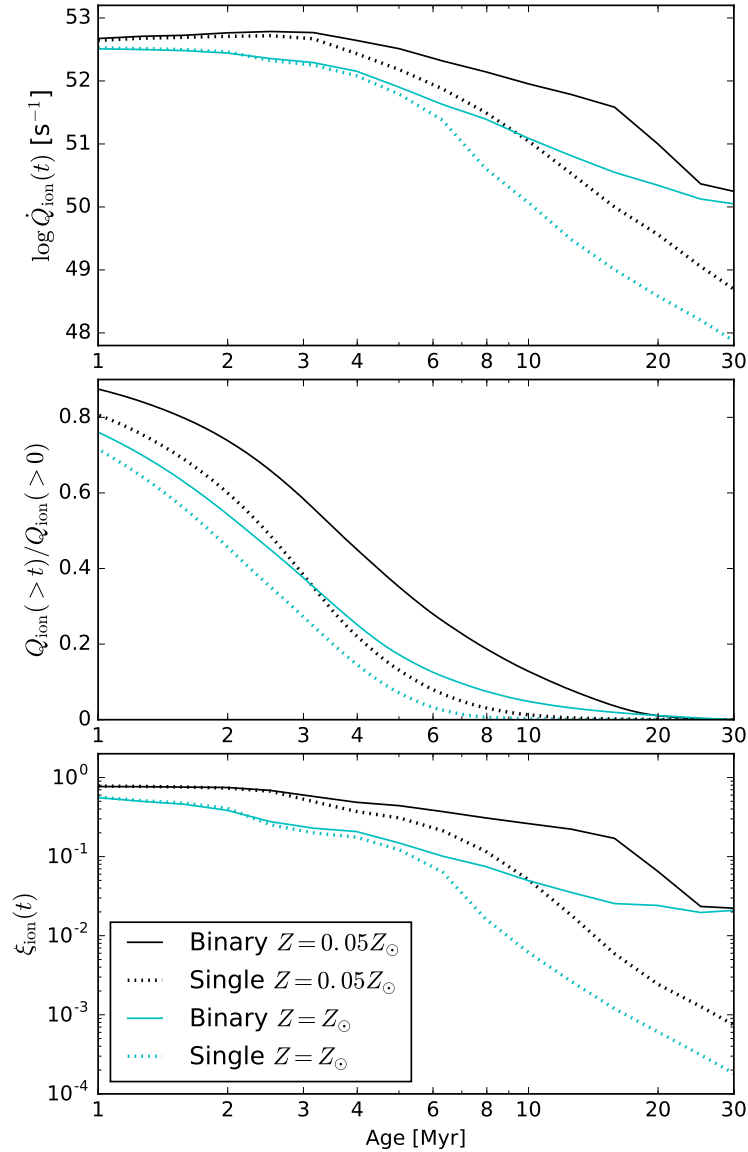
Figure 6.1: *Top:* Ionizing photon production rate, $\dot{Q}_{\mathrm{ion}}(t)$ as a function of age for a 10^6 M$_\odot$ star cluster, predicted by different stellar evolution models. *Middle:* Fraction of ionizing photons emitted after time t. *Bottom:* Ratio of ionizing luminosity to 1500 Å luminosity, ξ_{ion} as a function of age for the same star cluster. We show both single-star models (dotted) and binary models (solid) at metallicities $Z = 0.05\,Z_\odot$ (black) and $Z = Z_\odot$ (cyan), respectively. Including binaries leads to more massive stars at late times (from mass transfer and mergers), which dramatically enhances the ionizing photon production after $t \sim 3$ Myr. About 60% (20%) of the ionizing photons are emitted after 3 Myr (10 Myr) in the low-metallicity binary model, while this fraction is much lower in single-star model as well as at solar metallicity. The difference between single-star and binary models is less significant at solar metallicity. STARBURST99 models, which also ignore binaries, are nearly identical to the BPASS single-star models at both metallicities.

photon packets and iteration are selected to ensure convergence.

6.3   Results

We use $\dot{Q}_{\text{ion}}(t)$ to represent the ionizing photon production rate (number of ionizing photons produced per second) and

$$Q_{\text{ion}}(> t) = \int_{t}^{\infty} \dot{Q}_{\text{ion}}(t')\, dt' \tag{6.1}$$

to represent the number of ionizing photons produced after time t. In Figure 6.1, we show $\dot{Q}_{\text{ion}}(t)$ (upper panel), the *fraction* of ionizing photons emitted after time t, $Q_{\text{ion}}(> t)/Q_{\text{ion}}(> 0)$ (middle panel), and the ratio between ionizing luminosity and the luminosity at 1500 Å,

$$\xi_{\text{ion}} = \frac{\int_{10\,\text{Å}}^{912\,\text{Å}} L_\lambda d\lambda}{\lambda L_\lambda(1500\,\text{Å})} \tag{6.2}$$

(bottom panel), as a function of age, of an instantaneously formed star cluster of mass $10^6\,M_\odot$, for several stellar population models from BPASS. We adopt a Kroupa (2002) IMF with slopes of -1.3 from 0.1–0.5 $M_\odot$ and -2.35 from 0.5–100 $M_\odot$, consistent with that used in the simulation. We show the BPASS model at metallicity $Z = 0.001$ ($Z = 0.05\,Z_\odot$, black), the lowest metallicity available and the closest to our simulations, for both single-star evolution (dotted) and binary evolution (solid) models. We also compare those with $Z = 0.02$ ($Z = Z_\odot$, cyan) models from BPASS. We note that the starburst99 models (not shown), which are the default model in Ma et al. (2015), are nearly identical to the single-star model from BPASS at both metallicities.

The ionizing photon production rates in the single-star and binary models are very similar for the first 3 Myr, but start to differ significantly after 3 Myr at $Z = 0.05\,Z_\odot$, with the binary model producing an order of magnitude more ionizing photons by 10 Myr. Also, in the binary model, the production of ionizing photons is more extended. For example, almost 60% (20%) of the ionizing photons are produced after 3 Myr (10 Myr), while this fraction is 40% (1%) in single-star model. These late-time photons can escape more easily so one should expect them to make a big difference on f_{esc} (as confirmed by MCRT calculations below). However, at solar metallicity, these fractions are much lower and the difference between single-star and binary models is less significant.

To illustrate the effects of binaries, we run our MCRT code on the main galaxy in our z5m10mr simulation (a $\sim 10^{10}\,M_\odot$ halo at $z = 6$) and compute f_{esc} using
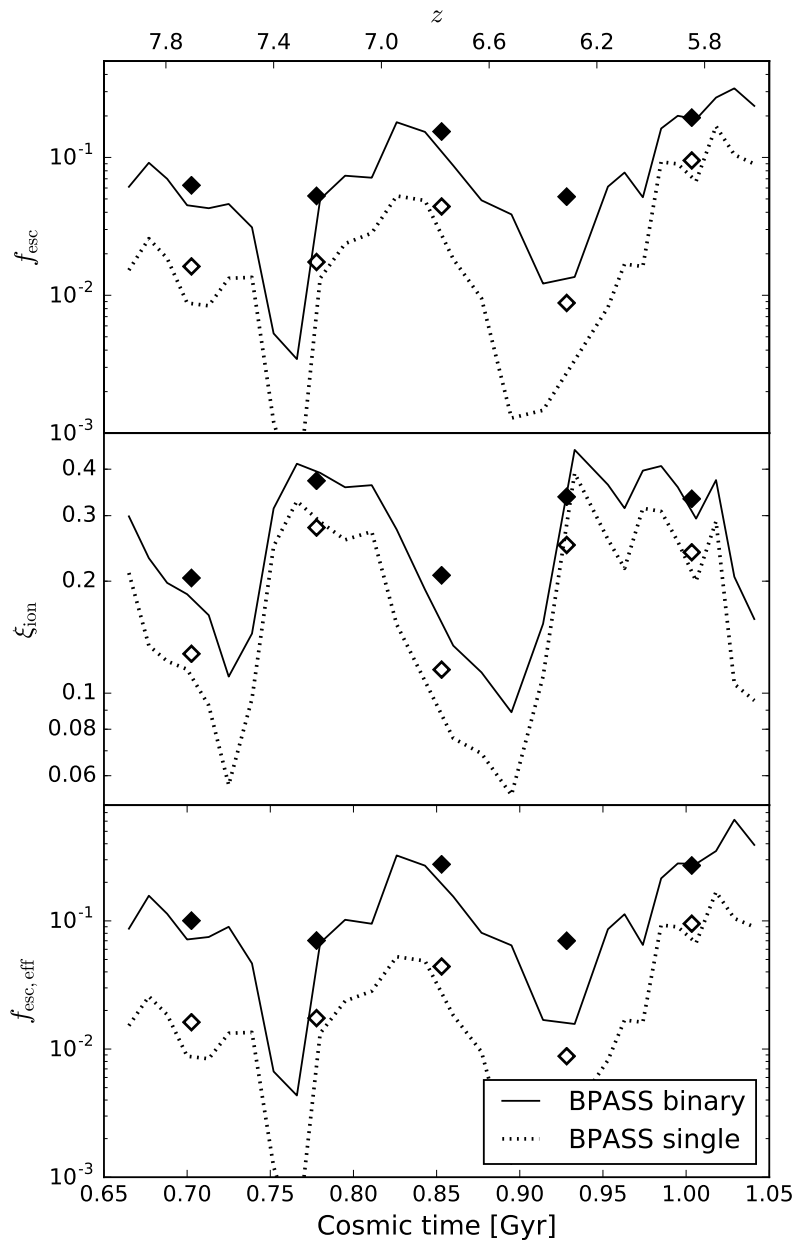
Figure 6.2: *Top:* True ionizing photon escape fraction f_{esc}, in our z5m10mr simulation (a $\sim 10^{10}$ M$_\odot$ halo at $z = 6$) as a function of redshift (or cosmic time). Lines show the instantaneous values in each snapshot, symbols are time-averaged in 100 Myr intervals. *Middle:* ξ_{ion} (as Fig. 6.1) as a function of time. *Bottom:* Effective escape fraction, $f_{esc,eff}$ (Equation 6.3) as a function of time. In the single-star model, $f_{esc} \lesssim 5\%$ most of the time, insufficient for reionization. Accounting for binary effects boosts ξ_{ion} by a factor ~ 1.5 – considerable but insufficient to explain reionization. But it also boosts f_{esc} by factors ~ 3–6 because the ionizing photons produced later (after $t \gtrsim 3$ Myr) preferentially escape, so the "effective escape fraction" $f_{esc,eff}$ is increased by factors ~ 4–10 and reaches the $\sim 20\%$ values needed to explain reionization.

both single-star and binary BPASS models with $Z = 0.05\,Z_\odot$. The results are presented in Figure 6.2. Lines and symbols show the instantaneous value and time-averaged values over $\sim 100\,\mathrm{Myr}$, respectively. Dotted lines and open symbols represent the single-star model, while solid lines and filled symbols represent the binary model. From top to bottom, the three panels show $f_{\rm esc}$ (the "true" fraction of ionizing photons that escape the galaxy virial radius), $\xi_{\rm ion}$, and the "effective" escape fraction from $z = 5.5$–8. The effective escape fraction is defined as

$$f_{\rm esc,\,eff} = f_{\rm esc} \frac{\xi_{\rm ion}}{\langle \xi_{\rm ion} \rangle_{\rm single}}, \qquad (6.3)$$

which is the ratio of the escaping ionizing flux to 1500 Å flux, relative to what would be computed using single-star models. $f_{\rm esc,\,eff}$ simply equals $f_{\rm esc}$ for single-star models, while for binary models, it also accounts for the change of $\xi_{\rm ion}$ relative to single-star models.

The instantaneous $f_{\rm esc}$ is highly time-variable, associated with stochastic formation and destruction of individual star-forming clouds (consistent with several other studies Wise et al. 2014; Kimm & Cen 2014; Paardekooper et al. 2015). For single-star models, $f_{\rm esc}$ is below 5% most of the time, because young stars are buried in their birth clouds, which prevent almost all ionizing photons from escaping. Most of the photons that escape come from stellar populations with age ~ 3–$10\,\mathrm{Myr}$, but they only contribute a very small fraction of the intrinsic ionizing photons in single-star models (Ma et al. 2015). However, at all times, the binary model predicts significantly higher (factors ~ 3–6) values for $f_{\rm esc}$. We also find that $\xi_{\rm ion}$ is boosted by a factor of ~ 1.5, consistent with Stanway et al. (2016). Multiplying the two factors, we find that the effective escape fraction is boosted by factors of ~ 4–10, with most of the contribution coming from the increased $f_{\rm esc}$. Averaged over the entire redshift range $z = 5.5$–8 that we consider here, accounting for binary effects increases the true ionizing escape fraction $f_{\rm esc}$ from 6% to 14% and increases $f_{\rm esc,\,eff}$ from 6% to $\sim 20\%$. This is consistent with what is required in empirical reionization models.

In Figure 6.3, we show the effective escape fraction as a function of time for z5m09 and z5m11 galaxies. Similar to z5m10mr (Figure 6.2), binary models boost time-averaged $f_{\rm esc,\,eff}$ by factors of ~ 4–10. In the lowest mass halo (z5m09), $f_{\rm esc,\,eff}$ is still low, because halo gas is largely neutral close to the galaxy in such low-mass systems, which consumes a large fraction of the ionizing photons. In more massive galaxies like z5m10mr and z5m11, $f_{\rm esc,\,eff}$ can reach $\gtrsim 20\%$.
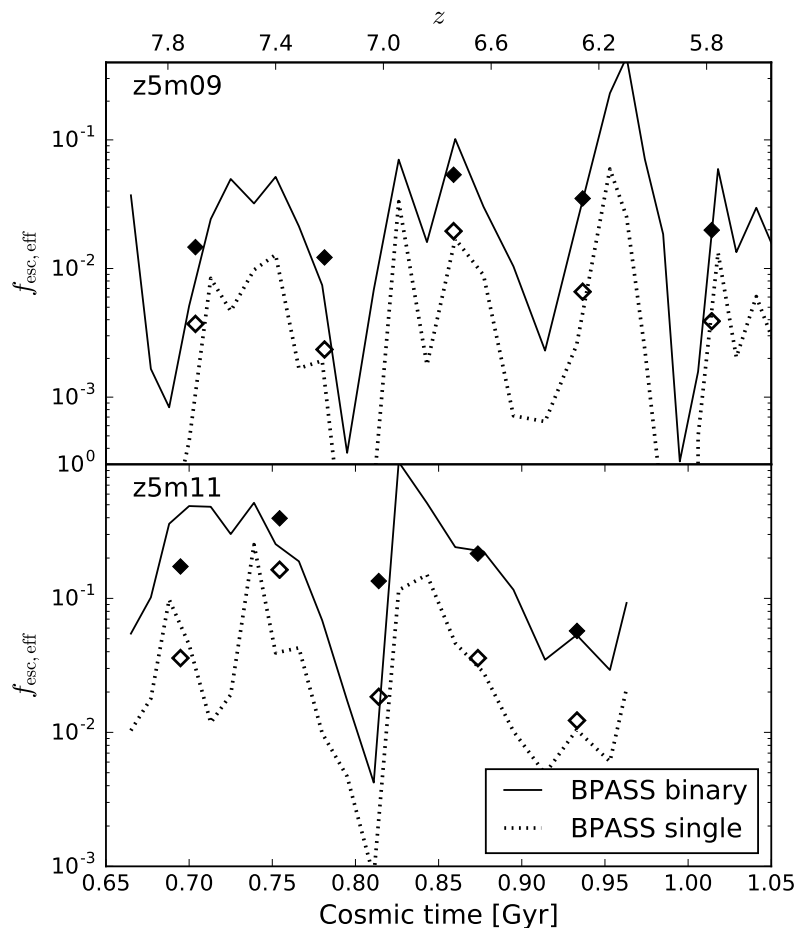
Figure 6.3: Effective escape fraction as a function time for z5m09 and z5m11. Like z5m10 (Figure 6.2), binary stellar models boost $f_{\mathrm{esc,eff}}$ by factors of $\sim$ 4–10. In more massive galaxies, the mean $f_{\mathrm{esc,eff}}$ reaches $\sim$ 20%, sufficient for reionization.

6.4 Discussion and Conclusions

In this work, we study the effect of binary evolution on ionizing photon production and escape in high-redshift galaxies, using three high-resolution cosmological simulations from the FIRE project. The simulated galaxies are around the mass estimated to dominate re-ionization (halo $M_{\mathrm{halo}} = 10^9$–$10^{11}\,M_{\odot}$ at $z = 6$). Using detailed radiative transfer calculations, we show that recent stellar evolution models which account for mass transfer and mergers in binaries (specifically, the BPASS model) produce significantly more ionizing photons for stellar populations older than 3 Myr compared to stellar evolution models ignoring binaries. These later-time photons easily escape, collectively increasing the escape fraction and ionizing photon production rate dramatically from high-redshift low-metallicity galaxies.

For single-star evolution models, we predict f_{esc} below 5% most of the time, less

than what is required ($\sim 20\%$) for cosmic reionization. However, when accounting for binary effects, f_{esc} can be boosted by factors of ~ 3–6 and ξ_{ion} can be boosted by a factor of 1.5. Therefore, the "effective" escape fraction (the ratio of escaped ionizing photon flux to 1500 Å flux) can be boosted by factors of ~ 4–10. For the more massive galaxies in our simulation, this brings them into good agreement with the values required to ionize the Universe.

We emphasize that the most important change relative to single-star models is not in the absolute photon production rate, but its time-dependence, because photons emitted after 3 Myr can much more easily escape star-forming complexes once feedback from massive stars has destroyed the dense birth cloud. Moreover, we have exhaustively tested in a previous study (Ma et al. 2015) that these results are not sensitive to our star formation and stellar feedback models. For example, increasing the strength of all feedback (radiation, stellar winds, SNe) per star particle relative to our fiducial model simply leads to self-regulation at lower star formation rates, giving an identical prediction for f_{esc}. Likewise, increasing the density threshold for star formation, re-distributing ionizing photons to fewer but more luminous particles, and increasing the ionizing photon production rate used for feedback in the code all produce similar predictions for f_{esc}.

Nevertheless, the binary fraction in high-redshift galaxies and the details of binary evolution are both uncertain, so our results are not definitive. They do, however, demonstrate the potential for binary evolution to reconcile empirical constraints on reionization by starlight with observations and simulations. In principle, these models can be confronted by the observed GRB rates at these redshifts (e.g., Kistler et al. 2009; Wyithe et al. 2010), although large uncertainties remain. In addition, the BPASS model does not include stellar rotation before binary interaction, which may also significantly increase the intrinsic ionizing photon production rate (e.g., Topping & Shull 2015). Rotation likely has a smaller effect on f_{esc} because most of the extra ionizing photons it predicts are produced less than 3 Myr after star formation.

We have repeated our radiative transfer calculation on cosmological simulations of Milky Way-mass galaxies at $z = 0$ ($Z \sim Z_\odot$) from the FIRE project (see Hopkins et al. 2014, for details). We find that binaries appear to be enhancing f_{esc} by only a factor ~ 1.5 at solar metallicity. This is expected since binary effects tend to be weaker at higher metallicities (also see Figure 6.1), for at least three reasons: (1) the number of ionizing photons decreases significantly as stellar atmospheres are cooler,

(2) quasi-homogenous evolution ceases to apply above $Z = 0.004$ ($Z = 0.2\,Z_\odot$), and (3) stellar winds become stronger, reducing the lifetime of massive stars and suppressing the mass transfered between binaries. In addition, the absolute time-averaged $f_{\rm esc}$ does not exceed $\sim 3\%$ in these galaxies, consistent with observational constraints in the local Universe (see references in Section 6.1). It appears that these galaxies are forming stars in a more "calm", less-bursty mode compared to the high-redshift dwarfs here (e.g., Sparre et al. 2017), and maintain much larger reservoirs of neutral gas in their galactic disks, which leads to much larger absorption even of photons produced by intermediate-age massive stars. A detailed study will be presented in a separate paper (Su et al. 2017a).

Acknowledgments

Chapter 7

SIMULATING GALAXIES IN THE REIONIZATION ERA WITH FIRE-2: GALAXY SCALING RELATIONS, STELLAR MASS FUNCTIONS, AND LUMINOSITY FUNCTIONS

Abstract

We present a suite of cosmological zoom-in simulations at $z \geq 5$ from the Feedback In Realistic Environments project, spanning a halo mass range $M_{halo} \sim 10^8$–$10^{12}\,M_\odot$ at $z = 5$. We predict the stellar mass–halo mass relation, stellar mass function, and luminosity function in several bands from $z = 5$–12. The median stellar mass–halo mass relation does not evolve strongly at $z = 5$–12. The faint-end slope of the luminosity function steepens with increasing redshift, as inherited from the halo mass function at these redshifts. Below $z \sim 6$, the stellar mass function and ultraviolet (UV) luminosity function slightly flatten below $M_* \sim 10^{4.5}\,M_\odot$ (fainter than $M_{1500} \sim -12$), owing to the fact that star formation in low-mass halos is suppressed by the ionizing background by the end of reionization. Such flattening does not appear at higher redshifts. We provide redshift-dependent fitting functions for the SFR–M_{halo}, SFR–M_*, and broad-band magnitude–stellar mass relations. We derive the star formation rate density and stellar mass density at $z = 5$–12 and show that the contribution from very faint galaxies becomes more important at $z > 8$. Furthermore, we find that the decline in the $z \sim 6$ UV luminosity function brighter than $M_{1500} \sim -20$ is largely due to dust attenuation. Approximately 37% (54%) of the UV luminosity from galaxies brighter than $M_{1500} = -13$ (-17) is obscured by dust at $z \sim 6$. Our results broadly agree with current data and can be tested by future observations.

Keywords: galaxies: evolution – galaxies: formation – galaxies: high-redshift – cosmology: theory

7.1 Introduction

High-redshift galaxies are believed to be the dominant sources contributing to cosmic reionization (e.g., Faucher-Giguère et al. 2008; Haardt & Madau 2012; Kuhlen & Faucher-Giguère 2012; Robertson et al. 2013, 2015; however, see Madau & Haardt 2015). Current deep surveys using the *Hubble Space Telescope* have already put reliable constraints on the $z \geq 5$ ultraviolet (UV) luminosity functions for galaxies brighter than $M_{UV} = -17$ (e.g., McLure et al. 2013; Schenker et al. 2013; Bouwens et al. 2015; Finkelstein et al. 2015a), but the faint-end behavior of the UV luminosity function remains highly uncertain. These faint galaxies contribute a non-trivial fraction of the ionizing photons needed for reionization (e.g., Finkelstein et al. 2012; Kuhlen & Faucher-Giguère 2012; Robertson et al. 2013), although their abundances are poorly understood.

Recently, Livermore et al. (2017) reported the detection of very faint galaxies of $M_{UV} = -12.5$ at $z \sim 6$ that are highly magnified by galaxy clusters in the Hubble Frontier Fields, after performing a novel analysis to remove the cluster light. They found a steep UV luminosity function down to $M_{UV} = -13$ at $z \geq 6$, implying sufficient numbers of faint galaxies to account for cosmic reionization. However, Bouwens et al. (2017c,b) later pointed out that the uncertain size distribution of high-redshift galaxies and the uncertain magnification model of the lensing clusters can have a large impact on the inferred faint-end luminosity functions in the Hubble Frontier Fields. The faint-end slope of the UV luminosity function fainter than $M_{UV} = -15$ thus remains poorly constrained.

Great efforts have also been made to measure the galaxy stellar mass functions at these redshifts (e.g., González et al. 2011; Duncan et al. 2014; Grazian et al. 2015; Song et al. 2016; Stefanon et al. 2017). The stellar masses of high-redshift galaxies are usually derived from single-band photometry using empirical relations. Such relations are calibrated against spectral energy distribution (SED) fitting using limited rest-frame optical data for a small sample of galaxies at these redshifts. These relations tend to have large intrinsic scatter and suffer from systematic uncertainties of the underlying stellar population synthesis model. Therefore, the stellar mass functions reported by different authors have considerable discrepancies (e.g., figure 9 in Song et al. 2016).

Consequently, the stellar mass–halo mass relation and the star formation efficiencies inferred from the stellar mass measurements at these redshifts are also very uncertain. For example, Finkelstein et al. (2015b) reported an increasing stellar mass to halo

mass ratio with increasing redshift, whereas Stefanon et al. (2017) found no evolution of this ratio at these redshifts. Another related question is to understand the stellar mass growth histories of galaxies at these redshifts. This is not only useful for constraining the total ionizing photon emissivity at the epoch of reionization, but also essential for understanding galaxy populations at lower redshift – both dwarf galaxy abundances in the Local Group (e.g., Boylan-Kolchin et al. 2015) and stellar mass functions in local galaxy clusters (e.g., Lu et al. 2014a).

The *James Webb Space Telescope* (JWST, scheduled for launch in 2020) and the next generation of ground-based telescopes will make it possible to study $z \geq 5$ galaxies in more detail. Future observations of galaxies in the reionization era will provide substantial data for high-spatial-resolution deep imaging at the rest-frame optical bands, as well as spectroscopic measurements probing the physical conditions of the interstellar medium (ISM) in these galaxies. This may help resolve many current open questions in the field, such as the faint-end slope of the luminosity function, more robust determination of stellar mass, understanding the stellar populations in high-redshift galaxies and their contribution to cosmic reionization (Leitherer et al. 2014; Topping & Shull 2015; Choi et al. 2017; Stanway 2017), etc. Therefore, it is necessary from a theoretical point of view to make more realistic predictions of galaxy properties at these redshifts.

Currently there are two broad categories of cosmological simulations of galaxy formation at the epoch of reionization. High-resolution cosmological radiation-hydrodynamic simulations, with a detailed set of baryonic physics, including primordial chemistry and molecular networks, can simultaneously model the formation of first stars and galaxies and the local reionization history (e.g., Wise et al. 2014; Chen et al. 2014; O'Shea et al. 2015; Paardekooper et al. 2015). Such calculations are usually computationally expensive and thus carried out in a small cosmological volume. They generally focus on the formation of Population III (Pop III) stars and low-mass galaxies (in halos below $M_{halo} \sim 10^9 \, M_{\odot}$) at relatively high redshifts ($z \gtrsim 10$). These types of simulations have been used to predict the scaling relations of high-redshift, low-mass galaxies (e.g., the stellar mass–halo mass relation, gas fraction, mass–metallicity relation, etc.; Chen et al. 2014), ionizing photon escape fractions from these small galaxies and their importance for cosmic reionization (e.g., Paardekooper et al. 2015; Xu et al. 2016), their spectral properties and detectability with *JWST* (e.g., Barrow et al. 2017), and the faint-end ($M_{UV} > -14$) UV luminosity functions at these redshifts (e.g., O'Shea et al. 2015).

On the other hand, there are also large-volume cosmological simulations at relatively low resolution using empirically-calibrated models of star formation and stellar feedback (e.g., Feng et al. 2016; Gnedin 2016; Ocvirk et al. 2016; Finlator et al. 2017; Pawlik et al. 2017). Simulations of this nature broadly reproduce the observed galaxy populations, stellar mass functions, UV luminosity functions (e.g., Gnedin 2016; Wilkins et al. 2017), and the global reionization histories (e.g., Ocvirk et al. 2016; Pawlik et al. 2017). Forward modeling of galaxies in these simulations provide large samples of mock images and spectra that can be directly confronted with *JWST* (e.g., Wilkins et al. 2016; Zackrisson et al. 2017). However, these simulations tend to have mass resolution $\gtrsim 10^5\,M_{\odot}$. Therefore, they are not able to capture the small-scale physics and the detailed structures in galaxies, which can be important for questions such as understanding the escape of ionizing photons (e.g., Ma et al. 2015). Also, some galaxy formation models calibrated to observations in the local universe struggle to reproduce observed galaxy properties at intermediate redshifts ($z \sim 2$–3), such as star formation histories, metallicities, etc. (e.g., Ma et al. 2016a; Davé et al. 2016). This is also a known problem in semi-analytic models of galaxy formation (e.g., Lu et al. 2014b).

In this work, we introduce a new suite of cosmological 'zoom-in' simulations at $z \geq 5$ in the $z = 5$ halo mass range $M_{\mathrm{halo}} \sim 10^8$–$10^{12}\,M_{\odot}$. We mainly focus on relatively massive (above the atomic cooling limit), Population II (Pop II) star-dominated galaxies in the redshift range $z = 5$–12. Our simulations cover a range of galaxies that can be well probed by future observations using JWST and next-generation ground-based telescopes. The cosmological zoom-in technique allows us to simulate galaxies in a broad mass range without being limited to a fixed simulation volume. The resolution is adaptively chosen based on the mass of the system, but always much better than that of large-volume simulations. These are not the first cosmological zoom-in simulations at $z \geq 5$: previous works using a similar technique have studied the escape fraction of ionizing photons (e.g., Kimm & Cen 2014), galaxy properties and scaling relations (e.g., Ceverino et al. 2017), and the importance of stellar feedback for shaping these galaxies (e.g., Yajima et al. 2017). Our work builds on these recent studies by increasing the resolution, expanding sample size, and most importantly including more detailed treatments for stellar feedback.

Our high-resolution cosmological zoom-in simulations use a full set of physically motivated models of the multi-phase ISM, star formation, and stellar feedback from

the Feedback in Realistic Environments (FIRE) project[1]. In a series of previous papers, these models have shown to successfully reproduce a variety of observed galaxy properties at lower redshifts (e.g., Hopkins et al. 2017, and references therein). Therefore, the new simulations presented in this paper are complementary to other state-of-the-art simulations in the field of galaxies in the reionization era.

This paper is the first in a series based on these new simulations, focusing on galaxy properties, scaling relations, stellar mass functions, and luminosity functions at $z > 5$. Our results complement previous predictions on the same topics using semi-analytic models (e.g., Clay et al. 2015; Liu et al. 2016; Cowley et al. 2018) and cosmological simulations (e.g., Jaacks et al. 2012; O'Shea et al. 2015; Yajima et al. 2015; Gnedin 2016; Ocvirk et al. 2016; Xu et al. 2016; Wilkins et al. 2017). In Sections 7.2.1 and 7.2.2, we describe the initial conditions and the physical ingredients used in the code. In Sections 7.2.3 and 7.2.4, we construct the simulated catalog. In Section 7.3, we present the general properties of our simulated galaxies. In Sections 7.4 and 7.5, we predict the stellar mass functions and luminosity functions from $z = 5$–12. We discuss our results in Section 7.6 and conclude in Section 7.7.

We adopt a standard flat ΛCDM cosmology with *Planck* 2015 cosmological parameters $H_0 = 68\,\mathrm{km\,s^{-1}\,Mpc^{-1}}$, $\Omega_\Lambda = 0.69$, $\Omega_m = 1 - \Omega_\Lambda = 0.31$, $\Omega_b = 0.048$, $\sigma_8 = 0.82$, and $n = 0.97$ (Planck Collaboration et al. 2016). In this paper, we adopt a Kroupa (2002) initial mass function (IMF) from 0.1–100 $M_\odot$, with IMF slopes of -1.30 from 0.1–0.5 $M_\odot$ and -2.35 from 0.5–100 $M_\odot$. All magnitudes are in the AB system (Oke & Gunn 1983).

7.2 The Simulations

The simulations presented in this paper form a subsample of the FIRE project (version 2.0, which we refer as FIRE-2; Hopkins et al. 2017). FIRE-2 is an updated version of the feedback implementations studied in a number of previous papers, which we refer as FIRE-1 (Hopkins et al. 2014).

All FIRE-2 simulations are run using an identical version of the GIZMO code (Hopkins 2015)[2]. We use the meshless finite-mass (MFM) method in GIZMO to solve the hydrodynamic equations. We refer to Hopkins et al. (2017) for details of the numerical methods and convergence tests of the FIRE-2 simulations, as well as their differences from FIRE-1 simulations. Other FIRE-2 simulations have already

---

[1] http://fire.northwestern.edu
[2] http://www.tapir.caltech.edu/~phopkins/Site/GIZMO.html

Table 7.1: Simulation details. Each simulation contains several galaxies in the zoom-in region. Properties below refer to the most massive (or the 'target') galaxy.

Name	M_{halo} ($z=5$) [$M_\odot$]	M_* ($z=5$) [$M_\odot$]	M_{halo} ($z=10$) [$M_\odot$]	M_* ($z=10$) [$M_\odot$]	m_b [$M_\odot$]	ϵ_b [pc]	ϵ_* [pc]	m_{DM} [$M_\odot$]	ϵ_{DM} [pc]
z5m09a	2.4e+09	8.0e+05	2.3e+08	2.3e+04	119.3	0.14	0.7	6.5e+02	10
z5m09b	2.8e+09	5.9e+05	1.5e+08	5.2e+03	119.3	0.14	0.7	6.5e+02	10
z5m10a	6.7e+09	1.0e+07	1.4e+09	3.5e+05	954.4	0.28	1.4	5.2e+03	21
z5m10b	1.2e+10	1.6e+07	1.6e+09	1.1e+06	954.4	0.28	1.4	5.2e+03	21
z5m10c	1.3e+10	1.1e+07	1.0e+09	3.5e+05	954.4	0.28	1.4	5.2e+03	21
z5m10d	1.9e+10	2.0e+07	2.9e+08	2.4e+04	954.4	0.28	1.4	5.2e+03	21
z5m10e	2.4e+10	1.7e+07	6.8e+08	3.8e+05	954.4	0.28	1.4	5.2e+03	21
z5m10f	3.2e+10	1.1e+08	1.6e+09	3.4e+05	954.4	0.28	1.4	5.2e+03	21
z5m11a	4.1e+10	2.8e+07	1.4e+09	3.3e+05	954.4	0.28	1.4	5.2e+03	21
z5m11b	4.0e+10	9.2e+07	3.3e+09	3.4e+06	890.8	0.28	1.4	4.9e+03	21
z5m11c	7.5e+10	4.5e+08	8.5e+09	1.2e+07	7126.5	0.42	2.1	3.9e+04	42
z5m11d	1.4e+11	9.9e+08	2.5e+10	1.0e+08	7126.5	0.42	2.1	3.9e+04	42
z5m11e	2.4e+11	1.1e+09	1.3e+10	5.2e+07	7126.5	0.42	2.1	3.9e+04	42
z5m12a	4.4e+11	3.0e+09	2.3e+10	4.7e+07	7126.5	0.42	2.1	3.9e+04	42
z5m12b	8.5e+11	1.5e+10	3.2e+10	1.0e+08	7126.5	0.42	2.1	3.9e+04	42

Parameters describing the initial conditions for our simulations (units are physical):

(1) Name: Simulation designation.

(2) M_{halo}: Halo mass of the target halo at $z = 5$ and its progenitor mass at $z = 10$.

(3) M_*: Stellar mass of the central galaxy in the target halo at $z = 5$ and its progenitor mass $z = 10$ (see Section 7.2.3).

(4) m_b: Initial baryonic (gas and star) particle mass in the high-resolution region. A star particle loses about 25% of its initial mass during its entire life due to mass return via supernovae and stellar winds.

(5) ϵ_b: Minimum Plummer-equivalent force softening for gas particles. Force softening for gas particles is adaptive. The gas inter-particle separation defined in Hopkins et al. (2017) is about $1.4 \, \epsilon_b$.

(6) ϵ_*: Plummer-equivalent force softening for star particles (fixed in comoving units until $z = 9$ and in physical units thereafter).

(7) m_{DM}: Dark matter particle mass in the high-resolution region.

(8) ϵ_{DM}: Plummer-equivalent force softening for high-resolution dark matter particles (fixed in comoving units until $z = 9$ and in physical units thereafter).

been presented and studied in recent papers (e.g., Wetzel et al. 2016; Fitts et al. 2017; Garrison-Kimmel et al. 2017; El-Badry et al. 2018). We describe the initial conditions of our simulated sample in Section 7.2.1 and review the baryonic physics adopted in FIRE-2 briefly in Section 7.2.2.

7.2.1 Initial conditions

We run a set of dark matter-only cosmological boxes at low resolution to $z = 5$, select target halos from the $z = 5$ snapshots, and re-simulate these halos and the regions around them at much higher resolution with baryons using the well developed multi-scale cosmological 'zoom-in' techniques (Katz & White 1993; Oñorbe et al. 2014). The initial conditions of the parent boxes and the zoom-in simulations are generated at $z = 99$ using the MUSIC code (Hahn & Abel 2011), with *Planck* 2015 cosmological parameters.

We use three dark matter-only cosmological boxes of side-length 11, 22, and 43 comoving Mpc, respectively. We use the spherical overdensity-based Amiga Halo Finder (AHF; Knollmann & Knebe 2009) to identify halos in the $z = 5$ snapshots, applying the redshift-dependent virial parameter from Bryan & Norman (1998), which leads to a virial overdensity $\Delta_{\mathrm{vir}} \approx 177$ (relative to background) for the redshift range we consider in this paper. We also checked the results against the six-dimensional phase-space halo finder ROCKSTAR (Behroozi et al. 2013a) and found good agreements in halo mass functions. We randomly select target halos in the $z = 5$ halo mass range $M_{\mathrm{halo}} = 2 \times 10^9$–$10^{12}\,M_{\odot}$, requiring that there is no more massive halo within $5R_{\mathrm{vir}}$ from the target halo. This selection excludes 1/3 of the halos in the box[3].

We identify zoom-in regions based on particles within ~ 3–$5R_{\mathrm{vir}}$ of the targeted halo, and iterate to ensure zero mass contamination from low-resolution particles within $2R_{\mathrm{vir}}$ and less than 1% contamination within $3R_{\mathrm{vir}}$ at $z = 5$. There may be more than one halo in the zoom-in region, but the target halo is the most massive one by design. In Table 7.1, we list all of our target halos studied in this paper, along with the halo mass and stellar mass of the central galaxy (see Section 7.2.3 for details) at $z = 5$ and $z = 10$, and initial particle masses and minimum Plummer-equivalent force softening lengths of baryonic and high-resolution dark matter particles.

---

[3]We also include other well-resolved halos in the zoom-in regions in our analysis (see Section 7.2.3). These halos live in the vicinity of a more massive halo (the target halo in the zoom-in region) by design. This will partially compensate the selection bias due to the isolation criteria above.

7.2.2 Baryonic physics

We briefly review the baryonic physics here, but refer to Hopkins et al. (2017, sections 2.3–2.5 and appendix B–E) for details. In the simulations, gas follows an ionized-atomic-molecular cooling curve from 10–10^{10} K, including metallicity-dependent fine-structure and molecular cooling at low temperatures and high-temperature metal-line cooling for 11 separately tracked species (H, He, C, N, O, Ne, Mg, Si, S, Ca, and Fe; see Wiersma et al. 2009a). We do not include a primordial chemistry network nor Pop III star formation, but apply a metallicity floor of $Z = 10^{-4} Z_\odot$, which corresponds crudely to the metallicity expected after enrichment by the first supernovae (SNe) from Pop III stars (e.g., Bromm et al. 2003; Wise et al. 2012). This is a reasonable treatment since we mainly focus on relatively massive galaxies at $z \lesssim 15$, which are dominated by Pop II stars. At each timestep, the ionization states and cooling rates H and He are calculated following Katz et al. (1996), and cooling rates from heavier elements are computed from a compilation of CLOUDY runs (Ferland et al. 2013), applying a uniform but redshift-dependent photo-ionizing background from Faucher-Giguère et al. (2009)[4], and an approximate model for H II regions generated by local sources. Gas self-shielding is accounted for with a local Jeans-length approximation, which is consistent with the radiative transfer calculations in Faucher-Giguère et al. (2010). The on-the-fly calculation of ionization states is broadly consistent with more accurate post-processing radiative transfer calculations (Ma et al. 2015).

We follow the star formation criteria in Hopkins et al. (2013b) and allow star formation to take place only in dense, molecular, and locally self-gravitating regions with hydrogen number density above a threshold $n_{\rm th} = 1000\,{\rm cm}^{-3}$. Stars form at 100% efficiency per free-fall time when the gas meets these criteria, and there is no star formation elsewhere. Note that star-forming particles can reach densities much higher than $n_{\rm th}$ following the self-gravitating criterion. The simulations include several different stellar feedback mechanisms, including (1) local and long-range momentum flux from radiative pressure, (2) energy, momentum, mass and metal injection from SNe and stellar winds, and (3) photo-ionization and photo-electric heating. Every star particle is treated as a single stellar population with known mass, age, and metallicity, assuming a Kroupa (2002) IMF from 0.1–100 $M_\odot$. All feedback quantities are directly calculated from STARBURST99 (Leitherer et al. 1999).

---

[4]The ionizing background starts at $z = 10.6$, with the ionization rate and heating rate increasing with time until the simulations end at $z = 5$. We note that both rates show a sharp increase just below $z \sim 7$. A tabulated version of the background is available at http://galaxies.northwestern.edu/uvb/.

Note that STARBURST99 is a single-star stellar population model[5], which assumes each star evolves independently, but most massive stars are expected to interact with a companion during their lifetimes. This will have significant effects on the SED of young populations, especially at low metallicities (e.g., Stanway 2017). It has been suggested that massive binaries can lead to high escape fractions of ionizing photons from high-redshift metal-poor galaxies, and thus have important implications for understanding the sources dominating cosmic reionization (Ma et al. 2016b; Götberg et al. 2017). Nonetheless, binarity only has weak effects on most stellar feedback quantities, such as bolometric luminosities (within 0.05 dex in the first 200 Myr since a stellar population is born) and Type-II SNe rates (e.g., Xiao & Eldridge 2015), so we do not expect binary interaction to have significant dynamical effects[6]. For these reasons, we only consider binary stellar population models in post-processing. In this paper, we use the Binary Population and Spectral Synthesis (BPASS) models (version 2.0; Eldridge et al. 2008; Stanway et al. 2016)[7] to compute the SED of each star particle from its age and metallicity. The BPASS models include both single-stellar and binary stellar population synthesis models. Their single-star models agree well with STARBURST99. Their binary models take into account mass transfer, common envelope phase, binary mergers, and quasi-homogeneous evolution at low metallicities. Also, the BPASS binary models appear to explain the nebular emission line properties observed in $z \sim 2$–3 galaxies (e.g., Steidel et al. 2016; Strom et al. 2017). In this paper, we mainly consider stellar continuum emission, while detailed modeling of dust extinction and nebular line emission will be the subject of future studies.

7.2.3   Halo selection and definitions

We run AHF on every snapshot to identify halos and subhalos in the zoom-in region. In general, most stars of the central (satellite) galaxy in a halo (subhalo) reside in $\frac{1}{3}R_{max}$ from the halo center, where R_{max} is the radius at which the maximum circular velocity V_{max} is reached (R_{max} is already computed by AHF). We thus define a galaxy by including all star particles within $\frac{1}{3}R_{max}$ after removing contributions from subhalos outside $\frac{1}{5}R_{max}$. This excludes star particles at large distances from

---

[5]Note that the stellar population models used in the simulations do not including stellar rotation, which is another key ingredient in stellar population synthesis (e.g., Leitherer et al. 2014; Choi et al. 2017) and could have important implications for reionization (e.g., Topping & Shull 2015).

[6]Binary models do produce more ionizing photons (see Section 7.6.4), which are likely to enhance photo-ionization feedback, but we checked that this only has sub-dominant effects on gas dynamics (Ma et al. 2015).
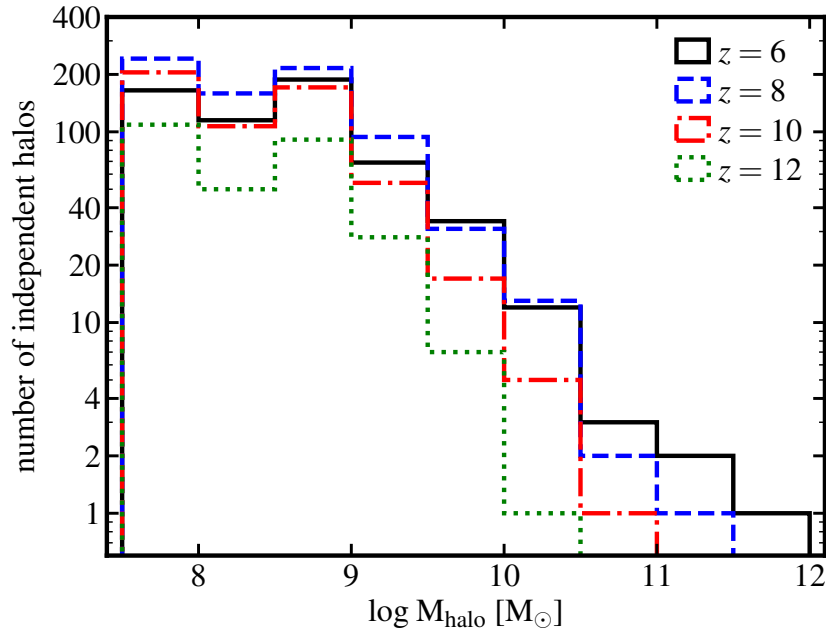
[7]http://bpass.auckland.ac.nz

Figure 7.1: Number of independent halos in the simulated catalog at several redshifts. The simulated sample includes considerably larger numbers of independent halos below $M_{halo} = 10^{11}$ $M_\odot$ at $z \sim 6$ or below $M_{halo} = 10^{10.5}$ $M_\odot$ at $z \sim 10$, where we are able to account for (at least some) halo-to-halo variance. At higher masses, our sample is limited. We can, however, study time-variability and its impact on scatter in observational properties of galaxies.

the halo center (corresponding to diffuse stellar distributions) and allow us to mask satellites. For each galaxy, we obtain a list of star particles with known position, age, and metallicity, from which we can compute a number of galaxy properties, such as stellar mass, star formation history, broad-band luminosities and magnitudes, surface brightness, galaxy size, etc. In this paper, we primarily focus on central galaxies, which dominate the stellar light: at a given stellar mass, only a few per cent of the galaxy population are satellites. We have also confirmed that they do not differ significantly from centrals at similar stellar masses in most properties we study in this paper. We restrict our analysis below to central halos that have zero contamination from low-resolution particles within R_{vir} and contain more than 10^4 particles in total[8]. Our target halos are guaranteed to meet this criteria by construction, but we also consider other halos in the zoom-in regions in our analysis.

In Figure 7.1, we show the number of halos that meet the above criteria in all zoom-in

---

[8]This excludes most halos below $M_{halo} \sim 10^{8.6}$ ($10^{7.7}$) $M_\odot$ in simulations at resolution $m_b \sim$ 7000 (900) $M_\odot$. The minimum number of dark matter particles for halos in our simulated catalog is ~ 5600.

regions at several redshifts. Our simulations are able to capture (at least some) halo-to-halo variance below $M_{halo} = 10^{11}\,M_\odot$ at $z \sim 6$ and below $M_{halo} = 10^{10.5}\,M_\odot$ at $z \sim 10$, where the simulations include a few to more than 200 halos in a given halo mass bin. Moreover, these galaxies always have 'bursty' star formation histories (see Section 7.3.3), which leads to significant time variability in their properties (e.g., Muratov et al. 2015; Sparre et al. 2017; Feldmann et al. 2017; Ma et al. 2017b; Faucher-Giguère 2018). Hence a galaxy tends to move above and below the median of certain scaling relations (see also the discussion in Section 7.3.2). To account for the scatter due to bursty star formation (as well as galaxy mergers and other time-variable phenomena), we make use of 58 snapshots saved for each simulation at redshifts $z = 5$–12 (about 20 Myr apart between two successive snapshots) to build a catalog of over 34,000 simulated halo 'snapshots'. By doing so, we sample the same halos multiple times in the catalog and treat them as statistically equal in our analysis. Figure 7.1 essentially shows the number of *independent* halos in the simulated sample. At lower masses (e.g., $M_{halo} \leq 10^{11}\,M_\odot$ at $z \sim 6$), we are able to account for the scatter both from halo-to-halo variance and time variability within single halos. A priori, it is not clear which effect dominates the scatter for a given scaling relation. At higher masses ($M_{halo} \geq 10^{11}\,M_\odot$), our sample only contains 1–2 independent halos at a given redshift, so we are only able to account for the variance due to time variability of individual galaxies. We caution that we may therefore underestimate the scatter of certain scaling relations at the high-mass end. We have also checked that excluding a randomly selected 1/2–2/3 of the snapshots from our analysis (sampling each galaxy at sparser time steps) does not change the results of this paper. In other words, our time-sampling is sufficient for statistically converged results.

7.2.4 Halo abundances

Since our simulated catalog is constructed from 15 cosmological zoom-in regions, it does not contain information about the halo abundance at a given halo mass and redshift. Therefore, we assign every simulated halo 'snapshot' a weight to recover the appropriate number density of halos at its mass and redshift in the Universe. We briefly summarize the method here and refer the readers to Appendix A for details. We use `HMFcalc` (Murray et al. 2013)[9] to calculate the halo mass functions, applying the same cosmological parameters and virial overdensities as those adopted in the simulations. We take the fitting functions from Behroozi et al. (2013b) in

---

[9]http://hmf.icrar.org

`HMFcalc`, which is a modified Tinker et al. (2008) halo mass function. It matches well with the halo mass functions directly extracted from our large-volume dark matter-only cosmological boxes in the redshift range we consider here. We bin the simulated sample in the two-dimensional $\log M_{halo}$–$\log(1 + z)$ space with bin widths $\Delta \log M_{halo} = 0.4$ from $M_{halo} = 10^{7.5}$–$10^{12} M_{\odot}$ and $\Delta \log(1+z) = 0.04$ from $z = 5$–12. We have confirmed that our results are not sensitive to the bin widths we adopt. In each bin, we count the number of halos in the simulated catalog N_{sim} and calculate the number of halos expected in the Universe N_{expect} from the halo mass function. All halos in the same bin are assigned the same weight $w = N_{expect}/N_{sim}$. In other words, by summing w over all simulated halos in certain halo mass and redshift intervals and dividing $\sum_i w_i$ by the corresponding comoving volume, one should recover the halo number densities given by the input halo mass functions. When necessary, each halo snapshot in the simulated catalog is weighted by its w. This is important when we consider statistical properties of simulated galaxies at a fixed stellar mass or magnitude, where not all galaxies have equal halo mass (e.g., Sections 7.3.3 and 7.3.4). The weights will also be used to construct stellar mass functions and luminosity functions in Sections 7.4 and 7.5.

Strictly speaking, this approach is valid only if the halos in our samples are not strongly biased. However, after an extensive check, we find no significant difference between halos in various environments (see also e.g., O'Shea et al. 2015) and at different resolution in our simulations regarding their properties studied in this paper. Although our sample is still possibly biased due to complex selection criteria – for example, all halos below $10^9 M_{\odot}$ by $z = 5$ in our sample live within a few virial radii of a more massive halo (i.e., the target halo in the zoom-in region) and we lack isolated halos at such low masses down to $z = 5$, our conclusions in this paper are likely robust.

7.3 Galaxies in the reionization era

7.3.1 Morphology

In Figure 7.2, we show the stellar $u/g/r$-composite images at $z = 5$ (left) for the central galaxy in the most massive halo in each zoom-in region. The stellar masses and halo masses are listed in Table 7.1. We use the BPASSv2.0 binary models to determine the stellar SEDs, assuming a Kroupa (2002) IMF from 0.1–100 $M_{\odot}$. Note that we only consider intrinsic stellar continuum emission, and ignore dust extinction

u/g/r-composite images ($z = 5$)
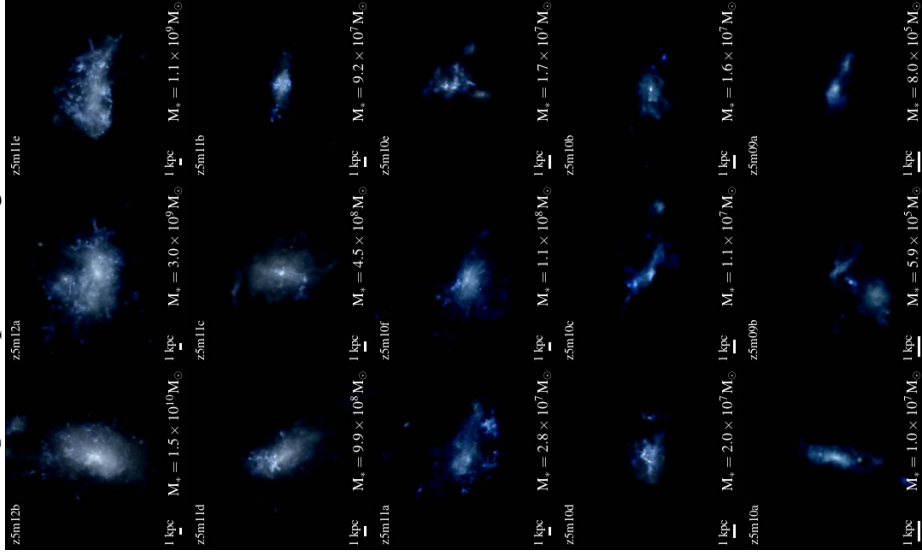
Mock JWST NIRCam F277W images ($z = 5$)
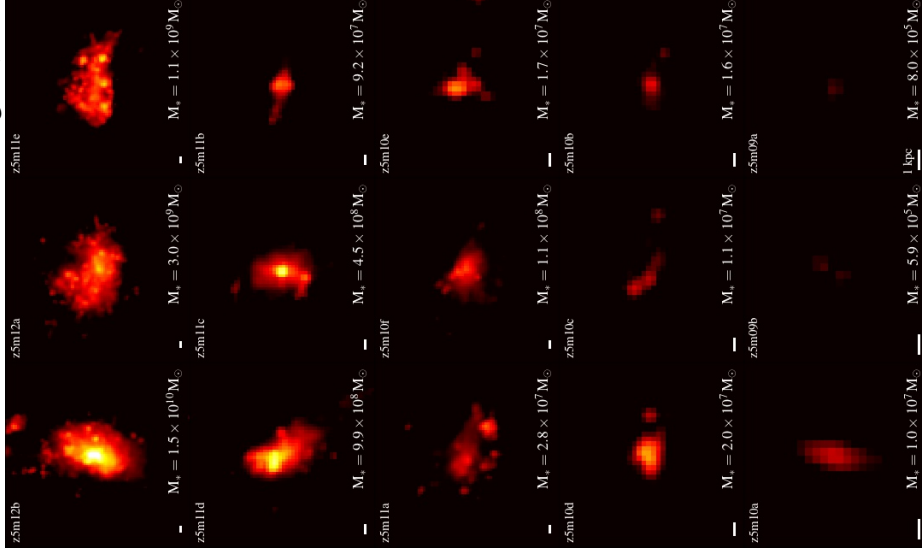
Figure 7.2: *Left*: Stellar *u/g/r*-composite images for the central galaxies of the 'target' halos from Table 7.1 at $z = 5$. *Right*: Noise-free mock JWST NIRCam F277W-band images (rest-frame 4600 Å). The pixel size is 0.065 arcsec and 0.42 kpc in physical length. The three images in the same row use the same color scale, which spans eight magnitudes in surface brightness, but the depth increases from $m_{AB} = 29.5\,\mathrm{mag\,arcsec^{-2}}$ for the most massive galaxies in the top row to 31.5 mag arcsec^{-2} for low-mass galaxies in the bottom row. We use the BPASSv2.0 binary models to determine the SED of each star particle from its age and metallicity, and then ray trace along the line-of-sight without dust attenuation. Nebular line emission is also ignored. The scale bar in each panel indicates 1 kpc (physical).

$u/g/r$-composite images ($z = 10$)

Mock JWST NIRCam F444W images ($z = 10$)
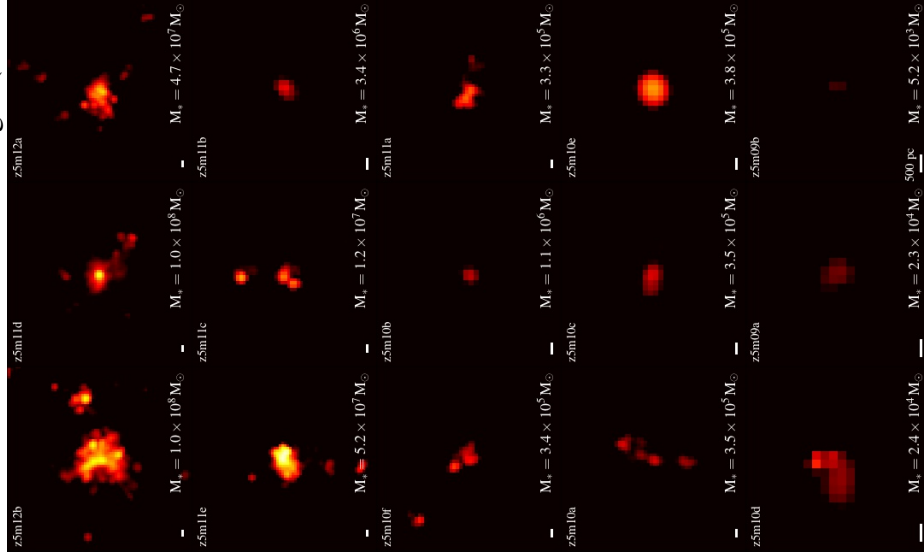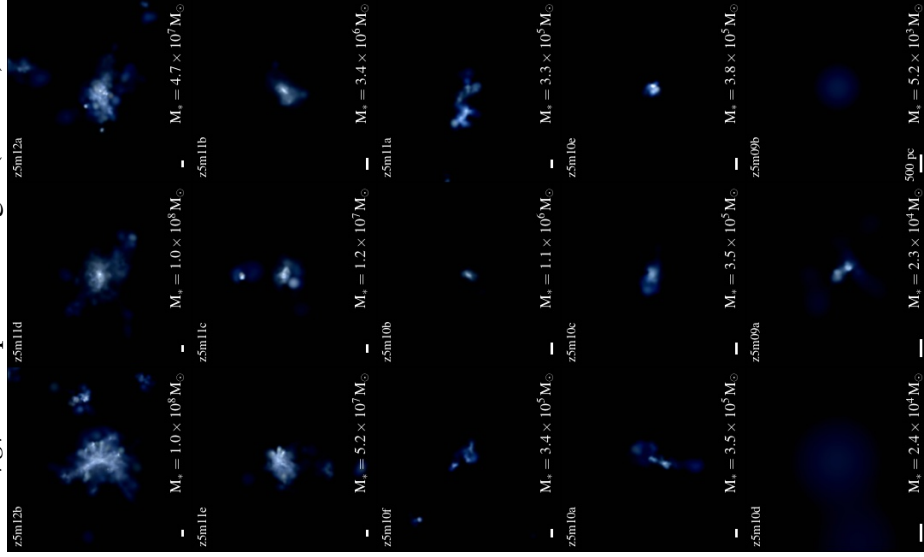
Figure 7.3: *Left:* Stellar $u/g/r$-composite images for all central galaxies at $z = 10$ (as Figure 7.2). *Right:* Noise-free mock JWST NIRCam F444W-band images (rest-frame 4000 Å). The PSF is a Gaussian function with FWHM of 2 pixels. The pixel size is 0.065 arcsec and 0.28 kpc in physical length. The three images in the same row use the same color scale, which spans eight magnitudes in surface brightness, but the depth increases from $m_{\mathrm{AB}} = 32$ mag arcsec^{-2} for the most massive galaxies in the top row to 36 mag arcsec^{-2} for low-mass galaxies in the bottom row. The scale bar in each panel indicates 500 pc (physical).

and nebular line emission at this point[10]. The right panel shows the noise-free mock images as observed by the Near Infrared Camera (NIRCam) on JWST at F277W band (rest-frame 4600 Å), applying a Gaussian point spread function (PSF) with full width half maximum (FWHM) of two pixels with pixel size 0.065 arcsec (0.42 kpc in physical length)[11]. The three images in the same row are shown using the same color scale, which spans eight magnitudes in surface brightness, but the depth increases from $m_{AB} = 29.5 \, \mathrm{mag \, arcsec^{-2}}$ in the top row to $31.5 \, \mathrm{mag \, arcsec^{-2}}$ in the bottom row (pixels below these limits are shown as black).

In Figure 7.3, we show the stellar $u/g/r$-composite images and noise-free mock JWST NIRCam F444W-band images (rest-frame 4000 Å) at $z = 10$ for the most massive galaxy in each zoom-in simulation. These images are rearranged in place to ensure a descending order in halo mass from the top-left panel to the bottom-right panel. The mock JWST images have a pixel size 0.065 arcsec and 0.28 kpc in physical length. Again, the color scale in each image spans eight magnitudes in surface brightness, but the depth increases from $m_{AB} = 32 \, \mathrm{mag \, arcsec^{-2}}$ in the top row to $36 \, \mathrm{mag \, arcsec^{-2}}$ in the bottom row.

Almost all of the simulated galaxies at $z \geq 5$ show clumpy, irregular morphologies even in rest-frame optical bands, possibly due to high merger rates and clumpy, gas-rich star formation at these redshifts. This is in contrast to galaxies at low and intermediate redshifts, which show a mix of late-type, early-type, and irregular morphologies at similar masses (e.g., Feldmann et al. 2017; El-Badry et al. 2018). Galaxies with similar stellar mass may have a variety of sizes and surface brightness, so their detectability can differ significantly. Therefore, our high-resolution simulations provide a useful database for understanding future multi-band, spatially resolved observations of $z \gtrsim 5$ galaxies, as well as determining the completeness of a flux-limited galaxy survey at these redshifts.

7.3.2 The stellar mass–halo mass relation

Figure 7.4 shows the stellar mass–halo mass relation (top panels) and the stellar baryon fraction–halo mass relation (bottom panels) for central galaxies at $z = 6, 8,$ and 10. The stellar baryon fraction is defined as $\mathrm{M}_*/(f_b \mathrm{M}_{halo})$, where $f_b = \Omega_b/\Omega_m$ is the cosmic baryonic fraction. The two-dimensional histograms represent the

---

[10]Full spectral modeling of high-redshift galaxies in cosmological simulations has been developed recently by other groups (e.g., Wilkins et al. 2016; Barrow et al. 2017; Zackrisson et al. 2017).

[11]The PSF and pixel sizes are adopted from the NIRCam pocket guide from https://jwst.stsci.edu/instrumentation/nircam.
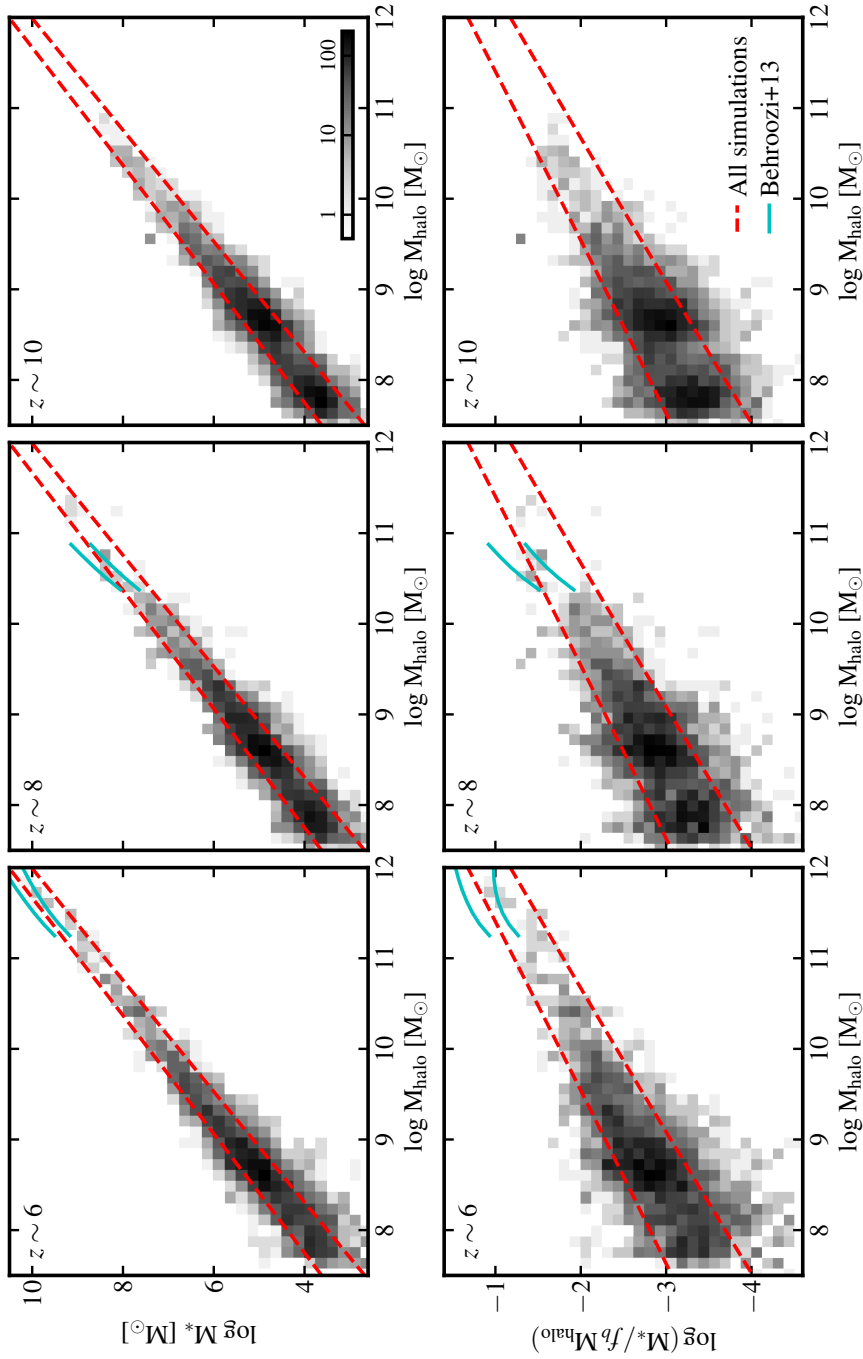
Figure 7.4: *Top:* The stellar mass–halo mass relation at $z = 6$, 8, and 10. *Bottom:* The stellar baryon fraction–halo mass relation at the same redshifts. The two-dimensional histograms represent the number of simulated halo snapshots in each pixel in logarithmic scale (as shown by the color scale). All central galaxies that meet the selection criteria described in Section 7.2.3 are included. The cyan lines show the abundance matching results at $z = 5$–8 from Behroozi et al. (2013b). The red dashed lines show the best-fit 1σ region of *all* central galaxies at $z = 5$–12 (lines are identical in all three panels, see Section 7.3.2 for details). At each redshift, the stellar mass correlates tightly with halo mass, and there is no significant evolution in the stellar mass–halo mass relation from $z = 5$–12.

number of halo snapshots in the simulated catalog (as defined in Section 7.2.3) within $\Delta z = 0.5$ (e.g., from $z = 7.5$–8.5 in the $z = 8$ panels) in each pixel in logarithmic scale (as shown by the color scale). We remind the readers that we re-sample each halo multiple times to account for time-variability in where galaxies lie on this relation, but we refer to Figure 7.1 for the number of independent halos in our sample at these redshifts (see Section 7.2.3 for details). We also show the empirical relations at $z = 6$ and 8 from Behroozi et al. (2013b, the cyan lines). At all redshifts, there is a tight correlation between stellar mass and halo mass, with the scatter increasing at the low-mass end[12]. We also examine the relation for satellite galaxies (not shown), which tend to have systematically higher stellar mass and larger scatter than central galaxies at a given halo mass, due to the fact that their halos are usually stripped. However, we note that the halo mass of a satellite depends strongly on which halo finder one uses. We find a smaller offset between central and satellite galaxies using the ROCKSTAR subhalo catalog than using the AHF catalog. Because satellite galaxies contribute no more than a few per cent of the total galaxy population at a given mass, we do not further quantify the difference in this paper.

We find little evolution in the stellar mass–halo mass relation at these redshifts, in line with recent empirical constraints (e.g., Rodríguez-Puebla et al. 2017; however, see Behroozi & Silk 2015). We will show it explicitly below. Using all halo snapshots in the simulated catalog at $z = 5$–12, we calculate the median and 1σ dispersion in $\log M_*$ at every 0.5 dex in $\log M_{\text{halo}}$ from $M_{\text{halo}} = 10^{7.5}$–$10^{12}\,M_\odot$. We assume a simple power-law relation between M_* and M_{halo}

$$\log M_* = \alpha \, (\log M_{\text{halo}} - 10) + \beta \tag{7.1}$$

and a halo mass-dependent scatter

$$\sigma_{\log M_*} = \exp \left[\gamma \, (\log M_{\text{halo}} - 10) + \delta \right], \tag{7.2}$$

and fit the median stellar mass–halo mass relation and 1σ dispersion obtained from the simulated sample as described above. We obtain the best-fit parameters as

$$(\alpha, \, \beta, \, \gamma, \, \delta) = (1.58, \, 7.10, \, -0.14, \, -1.10). \tag{7.3}$$

[12]We caution that our simulated sample have more independent galaxies at low masses than at higher masses, so we may underestimate the scatter at the high-mass end. Nonetheless, a halo mass-dependent scatter in the stellar mass–halo mass relation does exist at low redshift in both observations and FIRE-2 simulations (e.g., Garrison-Kimmel et al. 2014; Fitts et al. 2017). The current simulations are consistent with increased scatter at low masses.

These results are nearly identical to those obtained from the FIRE-1 simulations (e.g., Hopkins et al. 2014; Ma et al. 2015; Feldmann et al. 2017) at similar halo mass and redshift, despite the subtle differences in numerical details and resolution between these simulations. Our predictions also broadly agree with those in the literature (e.g., Ceverino et al. 2017). We show our best-fit 1σ stellar mass–halo mass relation in every panel in Figure 7.4 (the red dashed lines). Visual inspection implies that equations 7.1 and 7.2 describe our simulated sample reasonably well at any redshift. We also confirmed that the median relation obtained from a subsample at a given redshift does not deviate from Equation 7.1 by more than 0.1 dex at most halo masses we consider here. It is an intriguing question why the M_*–M_{halo} relation does not evolve at these redshifts. We speculate that this is probably due to feedback regulating star formation to zeroth order. A detailed analysis of the relation between halo growth rate, gas accretion rate, and stellar mass growth rate to understand the weak-evolution of the M_*–M_{halo} relation is worth future investigation.

How do galaxies evolve on the M_*–M_{halo} relation? All of our simulated galaxies experience bursty star formation because of stellar feedback. The stellar mass can grow by a factor of 2 or more during a short time period at the peak of a starburst, while it can remain almost unchanged during the troughs of its star formation history (see Section 7.3.3 and Figure 7.5 for examples). In contrast, the halo mass grows relatively smoothly via dark matter accretion, which is less affected by feedback. As a consequence, a galaxy moves vertically on the M_*–M_{halo} plane during the peak of a starburst and reaches some point above the median M_*–M_{halo} relation, while it then moves horizontally during a trough in its star formation history and reaches somewhere below the median relation until the next starburst episode. We confirmed in our simulations that the scatter in the M_*–M_{halo} relation caused by bursty star formation is a physical effect.

There are several caveats in this analysis. First, at the high-mass end ($M_{halo} \geq 10^{11}\,M_{\odot}$), our approach only captures the scatter due to bursty star formation, but the sample does not contain sufficient numbers of independent halos to account for halo-to-halo variance. Therefore, we may underestimate the scatter at these halo masses. At lower masses, our simulations include considerably larger numbers of independent halos and the scatter is reliably measured. Second, our simulations do not include more massive halos above $M_{halo} = 10^{12}\,M_{\odot}$. At these masses, slowly-cooling hot halos and feedback from supermassive black holes may play an important role. Studying early galaxy formation in such high-redshift massive
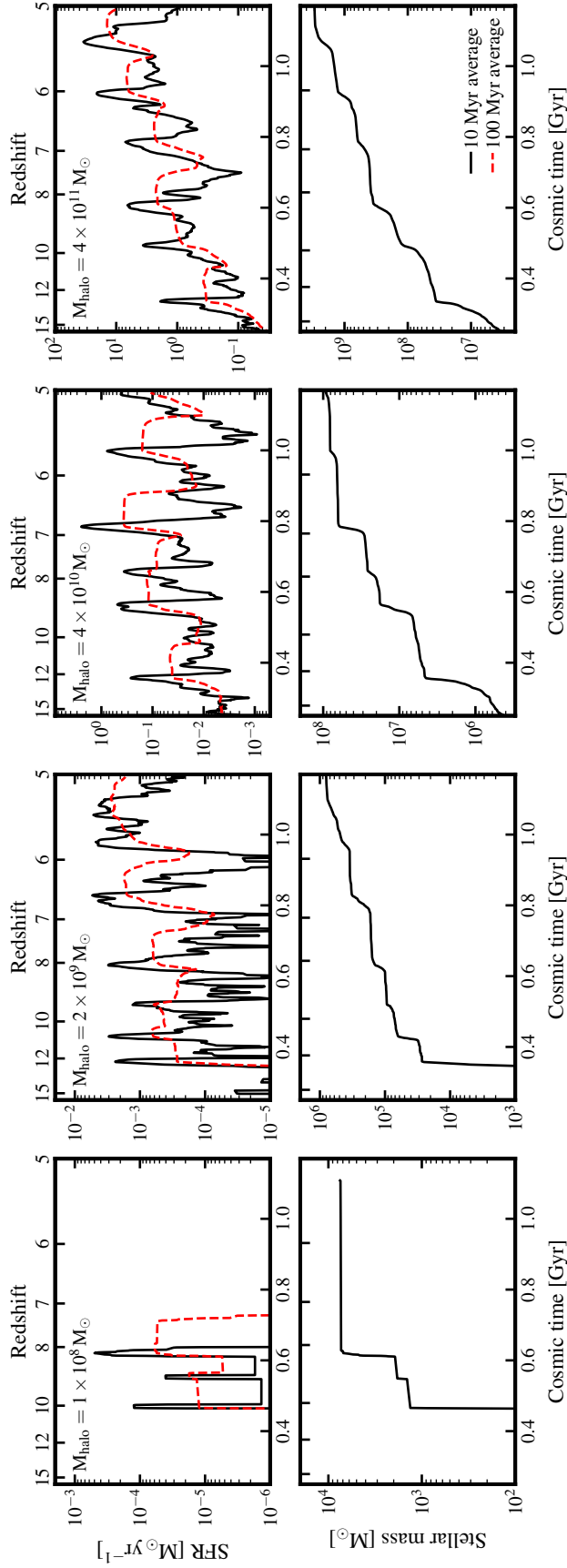
Figure 7.5: *Top:* Star formation histories averaged on 10 Myr time-scale (black solid lines) and 100 Myr time-scale (red dashed lines) for four example galaxies. The $z = 5$ halo masses are labeled in the upper-left corner. *Bottom:* Stellar mass growth histories for the same galaxies. All high-redshift galaxies show strong 'bursty' star formation histories. The least massive halo ($M_{halo} = 10^8 \, M_\odot$, left panels) does not form any stars after $z \sim 8$: the feedback following a starburst removes the majority of its gas at that time, and the ionizing background prevents fresh gas from accreting and cooling efficiently onto such low-mass halos at late times. More massive halos remain star forming until the end of the simulation at $z = 5$.

halos is beyond the scope of this paper. It may lead to a turnover in the M_*–M_{halo} relation at these redshifts similar to what is seen at lower redshifts (e.g., Behroozi et al. 2013b). We caution that our best-fit M_*–M_{halo} relation may break down at $M_{halo} > 10^{12}\,M_\odot$. Lastly, the best-fit M_*–M_{halo} relation does not apply to halos with $M_{halo} \lesssim 10^8\,M_\odot$ below $z \sim 6$. We will show in Section 7.3.3 that star formation in these low-mass halos is suppressed by the ionizing background near the end of reionization.

7.3.3 Star formation histories

Figure 7.5 shows the star formation histories (top panels) and the stellar mass growth histories (bottom panels) for four example galaxies in the $z = 5$ halo mass range $M_{halo} = 10^8$–$4 \times 10^{11}\,M_\odot$ (as labeled in each panel). The black solid lines and red dashed lines in the top panels show the star formation rates (SFRs) averaged over $10\,\mathrm{Myr}$ and $100\,\mathrm{Myr}$, respectively. These are proxies for the Hα- and UV-inferred SFRs observationally (e.g., Sparre et al. 2017). All simulated galaxies show significant 'bursty' star formation histories, with starbursts occurring on time-scales of 50–100 Myr. This feature is also seen in other cosmological zoom-in simulations with comparably high resolution and detailed physics despite different numerical methods (e.g., Kimm & Cen 2014; Ceverino et al. 2018). As discussed in Section 7.3.2, the stellar mass can grow almost instantaneously by a factor of 2 or more at the peak of a burst, while it remains nearly constant when the SFR is low. In the least massive halo ($M_{halo} = 10^8\,M_\odot$ at $z = 5$), the feedback from a starburst at $z \sim 8$ expels most of its gas. At later times, gas accretion and cooling becomes inefficient as heating from the ionizing background becomes significant for such low mass halos (e.g., Efstathiou 1992; Thoul & Weinberg 1996; Quinn et al. 1996; Okamoto et al. 2008; Faucher-Giguère et al. 2011; Noh & McQuinn 2014; Sawala et al. 2016). Star formation in these halos is thus suppressed at later times. More massive halos are able to maintain star formation until the end of our simulation at $z = 5$.

In Figure 7.6, we show the SFR (left panel) and specific SFR (sSFR, right panel) averaged over the past 100 Myr as a function of stellar mass for all galaxy snapshots in the simulated sample, color coded by their redshift. Note that the sharp upper limits at a given stellar mass in both relations are due to the fact that some galaxies form essentially all of their stellar mass in a starburst during the past 100 Myr. We also compare our results with the observed relation for $z = 6$–9 galaxies from McLure et al. (2011) (black dashed lines). Our simulations agree well with observations at
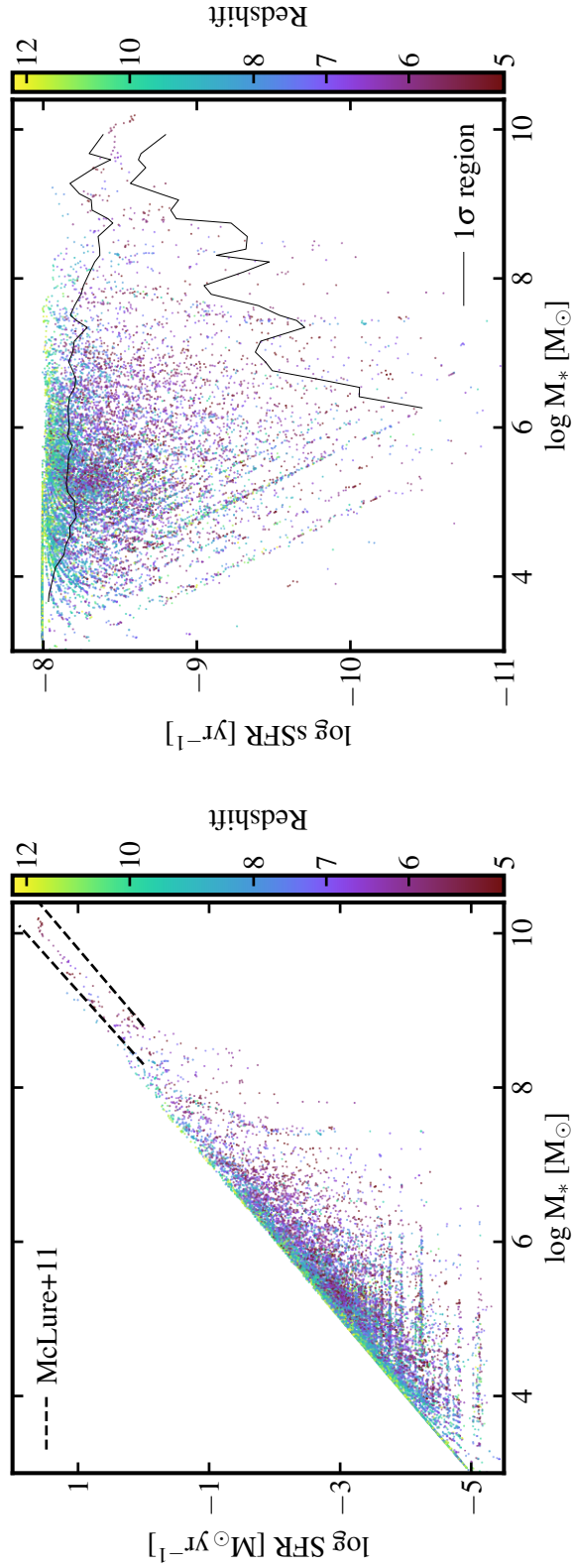
Figure 7.6: *Left*: SFR–M_* relation. *Right*: Specific SFR (sSFR)–M_* relation. Each point shows a star-forming galaxy snapshot in the simulated sample, color-coded by its redshift. The solid lines in the right panel illustrate the weighted 1σ region at $z \sim 6$. The SFR is averaged over the past 100 Myr at the time of measurement. The sharp upper limits in both relations are because these galaxies formed nearly all of their stars within the past 100 Myr. The black dashed lines show the observed relation for $z = 6$–9 galaxies from McLure et al. (2011). Our simulations agree well with observations at the most massive end. At lower masses, the scatter is large as a result of strong bursty star formation histories. Galaxies at lower redshifts have lower SFRs and larger scatter on average than galaxies at higher redshifts at a given stellar mass.

$M_* \geq 10^8 \, M_\odot$. At lower masses (where there are no observations), the scatter is larger due to stronger burstiness in their star formation histories, as illustrated by the solid lines in the right panel. Moreover, at fixed stellar mass, galaxies at lower redshifts have lower star formation rates on average than galaxies at higher redshifts. This trend is expected because the stellar mass growth time-scale (the ratio of stellar mass to star formation rate) of galaxies at a given redshift should be comparable to the Hubble time at that redshift and has also been found in previous studies (e.g., Behroozi & Silk 2015; Wilkins et al. 2017).

We now derive the weighted average SFR as a function of halo mass (or stellar mass) and redshift at every $\Delta \log M_{halo} = 0.5$ (or $\Delta \log M_* = 0.5$) and $\Delta \log(1 + z) = 0.04$ for the simulated sample. All halo snapshots are included in this calculation. We then fit the results using two-dimensional linear functions

$$\log \mathrm{SFR} = \alpha \, (\log M_{halo} - 10) + \gamma \, \log\left(\frac{1 + z}{6}\right) + \delta \qquad (7.4)$$

and

$$\log \mathrm{SFR} = \alpha' \, (\log M_* - 10) + \gamma' \, \log\left(\frac{1 + z}{6}\right) + \delta', \qquad (7.5)$$

and obtain the best-fit parameters $(\alpha, \gamma, \delta) = (1.58, 2.20, -1.58)$ and $(\alpha', \gamma', \delta') = (1.03, 2.01, 1.36)$. In Figure 7.7, we show the $\mathrm{SFR}(M_{halo}, z)$ (left panel) and $\mathrm{SFR}(M_*, z)$ (right panel) relations derived from the simulated sample. The colors represent the weighted average SFR relative to the $z = 5$ best-fit relation (in logarithmic scale, as labeled at the colorbars). This eliminates the wide dynamic range shown in the left panel of Figure 7.6 and allows us to see the evolution more clearly. Note that the white regions show the parameter space where our simulated sample contains no galaxies. At fixed halo mass or stellar mass, the average SFR increases by ~ 0.7 dex from $z = 5$–12, in broad agreement with the qualitative trend shown in Figure 7.6.

Furthermore, after $z \sim 6$, the average SFRs in low-mass galaxies (halo mass below $M_{halo} \sim 10^8 \, M_\odot$ or stellar mass below $M_* \sim 10^4 \, M_\odot$, the dark blue region in Figure 7.7) are significantly lower (by about 0.6 dex) than those inferred from the fitting functions. This is because, as mentioned above, at the end of the reionization era, the ionizing background can heat the gas in low-mass halos efficiently and prevent it from cooling and forming stars. The star formation in these galaxies is thus suppressed. We note that halos of similar masses at higher redshifts ($z \gtrsim 7$) or more massive halos ($M_{halo} \gtrsim 10^{8.5} \, M_\odot$) at any redshift are not affected and continue normal star formation.
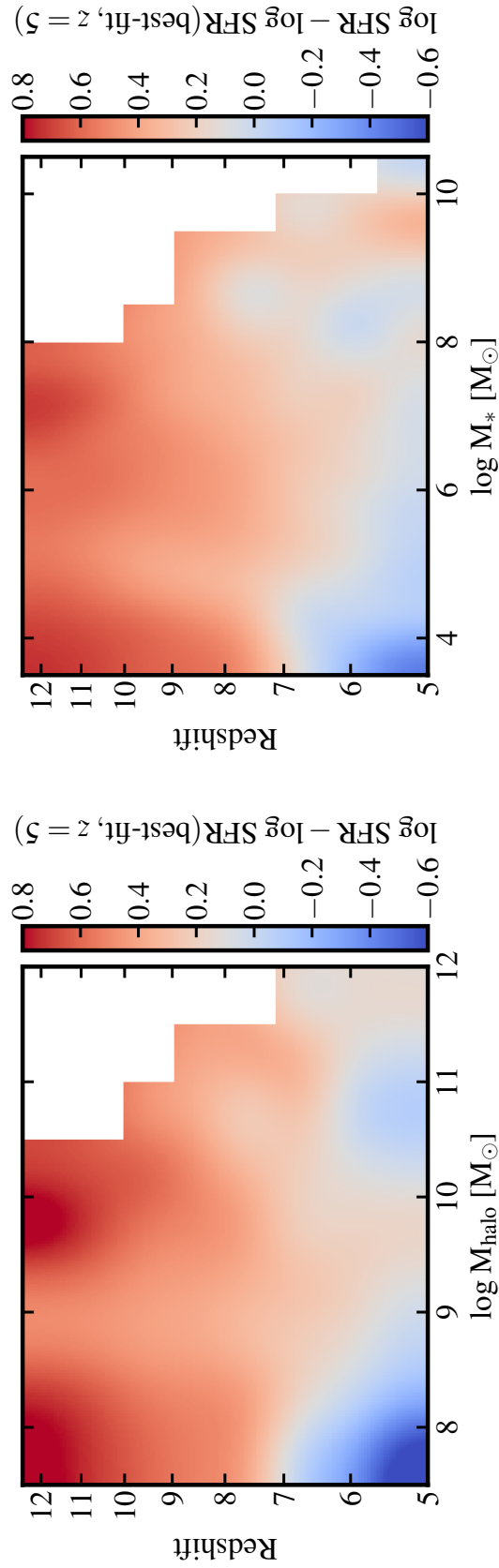
Figure 7.7: Bivariate relation between SFR, redshift, and halo mass [SFR(M_{halo}, z), left] or stellar mass [SFR(M_*, z), right]. Colors show the weighted average SFR for the simulated sample, relative to the best-fit relation at $z = 5$ (as labeled beside the colorbars). This emphasizes the dependence on redshift. The white regions represent parameter space where we have no simulations. At fixed halo mass or stellar mass, the mean SFR increases with increasing redshift, by about 0.7 dex from $z = 5$ to $z = 12$. Since $z \sim 6$, the average SFRs for galaxies below $M_{halo} \sim 10^8$ $M_\odot$ or $M_* \sim 10^4$ $M_\odot$ decrease by approximately 0.6 dex, because star formation in low-mass galaxies is suppressed by the ionizing background near the end of reionization.

In Figure 7.5, we show one example of such low-mass galaxies (the left most panel), where star formation is suppressed at lower redshifts. There are also halos at these masses which are completely 'dark' (containing no stars). The dark halo fraction is negligible for halos above $M_{halo} = 10^{8.5}\,M_\odot$ at any redshift, whereas at $M_{halo} \sim 10^8\,M_\odot$, the dark fraction increases from less than 1% at $z = 12$ to approximate 50% at $z = 5$.[13] We will show later in Sections 7.4 and 7.5 that this effect leaves an imprint in the stellar mass function and luminosity functions at $z \sim 6$.

Our findings are broadly in line with other simulations in the literature. For example, Wise et al. (2014) found no dark halos above $M_{halo} \sim 10^8\,M_\odot$ at $z > 8$. Sawala et al. (2016) found that the dark fraction decreases sharply from nearly 90% at $M_{halo} \sim 10^8\,M_\odot$ to 0% at $M_{halo} \sim 10^{8.5}\,M_\odot$ at $z \sim 10$. They also find an increasing dark fraction with decreasing redshift at a fixed halo mass. The subtle differences are likely due to different models of the ionizing background adopted in these studies, as well as to different star formation and stellar feedback physics. Wise et al. (2014) modeled the ionizing fields more self-consistently using radiative-hydrodynamic methods, while Sawala et al. (2016) adopted the uniform Haardt & Madau (2001) ionizing background at these redshifts. In addition, a dark halo only means that the expected stellar mass is lower than the mass of a few star particles. This further complicates the comparison between these results obtained at different resolutions. The effects of the ionizing radiation fields prior to complete reionization on low-mass galaxies merits future investigation.

7.3.4 Broad-band photometry

We use the BPASSv2.0 stellar population synthesis models to calculate the broad-band luminosities and magnitudes for the simulated galaxies, using the binary models with a Kroupa (2002) IMF from 0.1–$100\,M_\odot$ as our default model. We only consider intrinsic stellar continuum here, and ignore dust extinction and strong nebular line emission in the rest-frame UV and optical, as well as dust re-emission in the infrared (IR). We will explore the effect of dust attenuation in Section 7.6.2. In Figure 7.8, we show the magnitude–stellar mass relation (top panels) for our simulated sample with $M_* > 10^{3.5}\,M_\odot$ for three example redshift and band combinations. We also show the inverse relation, the stellar mass–magnitude relations for the same

---

[13]Note that the increasing dark fraction at $M_{halo} \sim 10^8\,M_\odot$ and below $z \sim 6$ indicates that the suppression of star formation in these halos is not purely due to stellar feedback but rather points to the importance of reionization.

Table 7.2: Best-fit parameters for the magnitude–stellar mass relation and the stellar mass–magnitude relation (see Section 7.3.4 for details).

Magnitude–stellar mass relation (Equation 7.6)				
Band		a	c	d
1500 Å	median	-2.81	-5.61	-22.38
1500 Å	1σ lower	-2.61	-6.83	-23.06
1500 Å	1σ upper	-2.74	-3.87	-21.42
B band	median	-2.63	-3.36	-22.46
B band	1σ lower	-2.59	-5.17	-22.89
B band	1σ upper	-2.64	-2.52	-22.05
J band	median	-2.61	-2.63	-22.69
J band	1σ lower	-2.61	-3.86	-23.20
J band	1σ upper	-2.63	-2.15	-22.31
Stellar mass–magnitude relation (Equation 7.7)				
Band		a'	c'	d'
1500 Å	median	-0.39	-2.59	8.77
1500 Å	1σ lower	-0.42	-1.65	8.38
1500 Å	1σ upper	-0.36	-2.99	9.16
B band	median	-0.38	-2.17	8.95
B band	1σ lower	-0.41	-1.59	8.66
B band	1σ upper	-0.37	-1.40	9.09
J band	median	-0.38	-1.85	8.90
J band	1σ lower	-0.41	-1.61	8.67
J band	1σ upper	-0.38	-0.90	9.01

Note: All magnitudes are derived from intrinsic stellar luminosities without accounting for dust attenuation and nebular line emission.

combinations in the bottom panels. Only galaxies brighter than $M_{AB} = -10$ are shown to ensure that our simulations are complete. The two-dimensional histogram represents the total *weight* (as defined in Section 7.2.4) of all galaxy snapshots in a pixel in logarithmic scale. This reflects the 'correct' relative number of galaxies in the Universe between pixels[14]. The red solid and dashed lines illustrate the best-fit median relation and 1σ-scatter (16–84 per cent) as obtained below.

At fixed stellar mass, the distribution of magnitudes in a specific band tends to be asymmetric, with a broader spread at the bright end. The asymmetry is driven by

---

[14]We remind the reader that we include all snapshots in the analysis to account for time variability of galaxy properties, which is important for UV luminosities, but we may underestimate the scatter for halos above $M_{halo} > 10^{11} M_{\odot}$ where our sample does not contain large number of independent halos (see Section 7.2.3 for details).
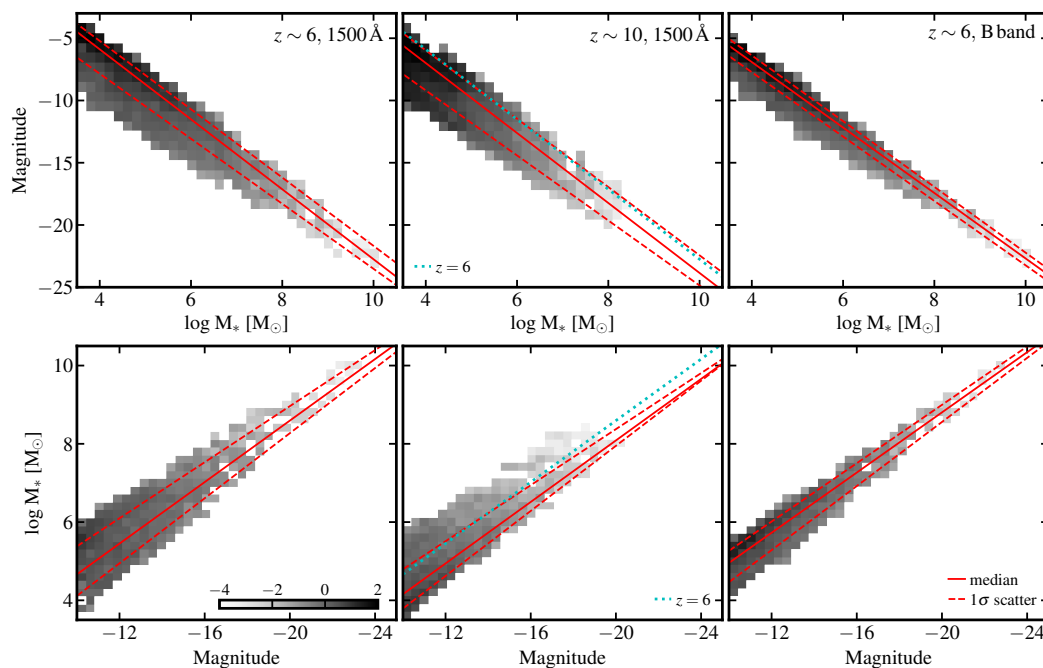
Figure 7.8: *Top:* The magnitude–stellar mass relation for rest-frame 1500 Å at $z = 6$ (left) and $z = 10$ (middle), and for rest-frame B band at $z = 6$ (right). The two-dimensional histogram represents the total *weight* of simulated galaxy snapshots in each pixel (in logarithmic scale), taking into account our simulation results and the halo mass function (see Section 7.2.4 for details). This reflects the true relative number of galaxies between pixels in the Universe. The red solid and dashed lines show the best-fit weighted median relation and 1σ scatter (see text for details). The cyan dotted line in the middle panel shows the median relation at $z = 6$ for reference. At fixed stellar mass, the distribution of magnitudes is asymmetric, with a broader spread at the bright end, and the median magnitude becomes more negative (galaxies being brighter) at higher redshifts. The scatter gets smaller from rest-frame UV to longer wavelength. *Bottom:* The stellar mass–magnitude relation for the same bands and redshifts. At fixed magnitude, the distribution of stellar mass is skewed toward low-mass galaxies, simply due to the fact that low-mass galaxies are more abundant in the Universe. The median stellar mass decreases by about 1 dex from $z = 12$ to 5.

the evolution of stellar populations: the luminosity of a stellar population declines rapidly as the most massive stars die (in about 3–30 Myr). Therefore, the luminosity of a galaxy depends not only on its total stellar mass but also on its recent star formation history. This feature is more prominent in low-mass galaxies which have significant bursty star formation histories. Figure 7.8 also shows that this effect is strongest in the rest-frame UV where young stars overwhelmingly dominate the starlight and becomes weaker at longer wavelengths, as rest-frame optical B-band relation has smaller scatter than that of rest-frame 1500 Å.

Furthermore, galaxies at higher redshifts appear brighter on average than those of similar stellar masses at lower redshifts, simply due to the fact that high-redshift galaxies have younger stellar populations and higher ongoing SFRs. We parametrize the magnitude–stellar mass relation with a linear function

$$M_{AB,\,band} = a\,(\log M_* - 10) + c\,\log\left(\frac{1+z}{6}\right) + d, \qquad (7.6)$$

where we assume a fixed slope a at any redshift but a redshift-dependent normalization to capture this feature. We fit the weighed median, 1σ lower- and upper-bound relations (above $M_* = 10^{3.5}\,M_\odot$) obtained from eight subsamples in different redshift intervals from $z = 5$–12 all together to determine the parameters for a given band. The top panels of Figure 7.8 illustrate three examples of this relationship, and we list the best-fit parameters for rest-frame 1500 Å, B band, and J band in the top half of Table 7.2.

We similarly assume a linear function for the stellar mass–magnitude relation

$$\log M_* = a'\,(M_{AB,\,band} + 20) + c'\,\log\left(\frac{1+z}{6}\right) + d', \qquad (7.7)$$

and fit the weighted median and 1σ relations for galaxies brighter than $M_{AB,\,band} = -10$ to obtain the parameters. Some examples are shown in Figure 7.8 and the best-fit parameters for rest-frame 1500 Å, B band, and J band are listed in Table 7.2 (the bottom block). We emphasize that the two relations are fundamentally different from each other – the distribution of stellar mass at fixed magnitude is biased toward low-mass galaxies, simply because they have much higher number densities in the Universe than more massive galaxies (see also Section 7.4). The stellar mass–magnitude relation is also redshift-dependent, with the median stellar mass decreasing by about 1 dex from $z = 12$ to 5 at a given magnitude.
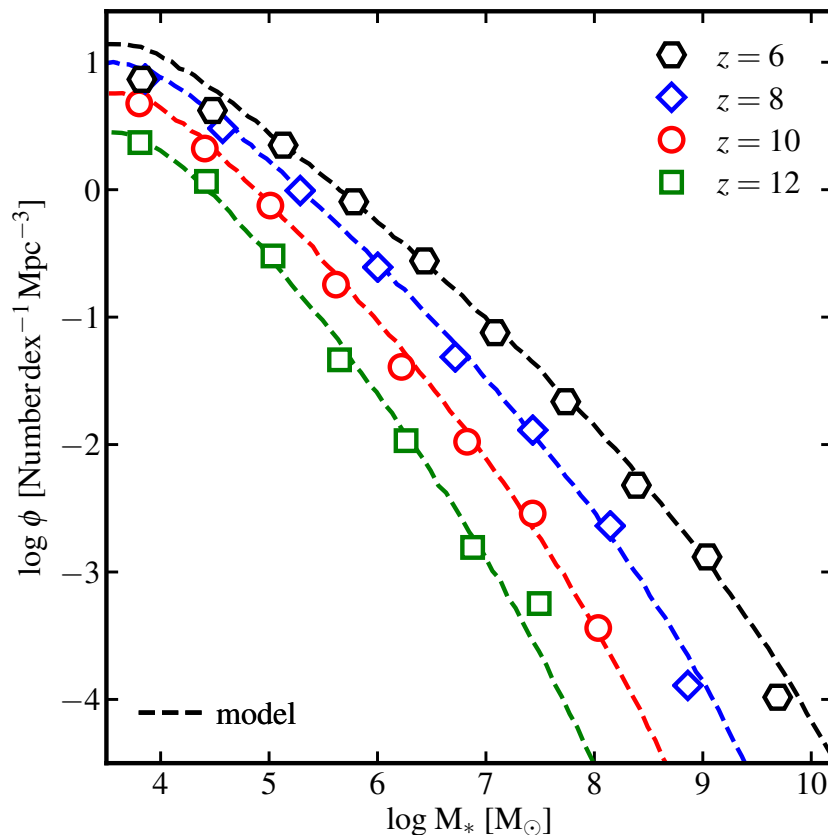
Figure 7.9: Predicted stellar mass functions above $M_* = 10^{3.5}\,M_\odot$ at $z = 6$, 8, 10, and 12. The open symbols show the results derived from the simulated sample using the weights constructed in Section 7.2.4. The dashed lines show the model stellar mass functions from convolving between the stellar mass–halo mass relation from Section 7.3.2 and the halo mass function, assuming each halo contains one central galaxy. Both methods only account for halos more massive than $M_{halo} = 10^{7.5}\,M_\odot$. The two stellar mass functions agree well with each other for a broad range of mass and redshift. The low-mass-end slope steepens with increasing redshift (from $\alpha = -1.83$ at $z \sim 6$ to $\alpha = -2.18$ at $z \sim 12$). At $z \sim 6$, the stellar mass function derived from simulations flattens and falls below the model stellar mass function by a factor of 2 below $M_* \sim 10^{4.5}\,M_\odot$, owing to the 50% fraction of dark halos around $M_{halo} \sim 10^8\,M_\odot$. A comparison with observations is shown later in Section 7.6.3 (Figure 7.14). We make our predictions publicly available (see Appendix C for details).

7.4 Stellar mass functions in the early universe

Now we calculate the stellar mass function using two distinct approaches. First, we utilize the weights constructed in Section 7.2.4: at a certain redshift, we collect all halo snapshots within $\Delta z = \pm 0.5$ from our simulated catalog. We then add the weights of galaxies in stellar mass bins and divide $\sum_i w_i$ by the comoving volume corresponding to the $\Delta z = \pm 0.5$ redshift interval. Only halos above $M_{halo} = 10^{7.5} M_\odot$ are taken into account. In Figure 7.9, we show the results in number $dex^{-1} Mpc^{-3}$ above $M_* = 10^{3.5} M_\odot$ at $z = 6, 8, 10$, and 12 with the open symbols. The data are provided in Appendix C.

Alternatively, we can model the stellar mass function by directly convolving the stellar mass–halo mass relation derived in Section 7.3.2 with the halo mass function at a given redshift. We use a Monte Carlo method: we generate a large number of mock halos more massive than $M_{halo} = 10^{7.5} M_\odot$ with number densities following the halo mass function, assign each halo a stellar mass as described below, and derive the stellar mass function from the mock catalog. We assume a) every halo hosts one galaxy (considering only central galaxies) and b) the stellar mass follows a lognormal distribution at a given halo mass, with the median and 1σ dispersion following Equations 7.1 and 7.2. In this calculation, we use Equations 7.1 and 7.2 at all redshifts and all halo masses, but we caution that uncertainties may arise at the high-mass end (see discussion in Section 7.3.2). The results are shown by dashed lines in Figure 7.9. For simplicity, we refer them as model stellar mass functions thereafter. We also make these results publicly available (see Appendix C for details). We will compare our predictions with observations later in Section 7.6.3.

We highlight the following features shown in Figure 7.9. (1) The low-mass end of the stellar mass function (asymptotic form $\phi \, d\log M_* \sim M_*^{\alpha+1} \, d\log M_*$) steepens with increasing redshift, with the slope decreasing from $\alpha = -1.80 \pm 0.02$ at $z = 6$ to $\alpha = -2.13 \pm 0.12$ at $z = 12$. The evolution of the slope is robust, although the exact slope at a given redshift may vary according to how it is computed[15]. This trend is consistent with the observed stellar mass functions (e.g., Song et al. 2016) and has been widely reproduced in cosmological simulations (e.g., Wilkins et al. 2016; Ceverino et al. 2017). Such a feature is directly inherited from the

---

[15]The slopes quoted here are obtained by fitting the stellar mass functions derived from the simulated catalog with a Schechter (1976) function. We also experiment with fitting the model mass functions in different dynamic ranges or using a double power-law function. The slope obtained at a given redshift varies systematically with method by about 0.2.

halo mass functions, which also steepen with increasing redshift at the low-mass end (e.g., Reed et al. 2003). (2) The model stellar mass functions agree well with those derived from the simulated catalog for a broad range of stellar mass and redshift. This demonstrates that the fitting functions in Section 7.3.2 describe the stellar mass–halo mass relation for the simulated sample reasonably well. (3) The discrepancies between the two stellar mass functions in the highest-mass bin is due to small numbers of galaxies in the simulated sample at the high-mass end. (4) The apparent flattening of the model stellar mass functions at $M_* \sim 10^{3.5} \, M_\odot$ is an expected artifact because we exclude all halos below $M_{halo} = 10^{7.5} \, M_\odot$.

More importantly, the $z = 6$ stellar mass function derived from the simulated sample shows a flattening below $M_* \sim 10^{4.5} \, M_\odot$ and falls below the model mass function by a factor of 2. This is caused by the 50% fraction of dark halos at $M_{halo} \sim 10^8 \, M_\odot$ at $z \sim 6$. In other words, the assumption we adopted in the model that every halo hosts one galaxy breaks down at $M_{halo} \sim 10^8 \, M_\odot$. Note that if we ignore all the 'dark halos' in the simulated catalog and repeat the exercise, the two $z = 6$ stellar mass functions agree well with each other. The large dark fraction in low-mass halos at lower redshifts is because of the suppression of star formation by the ionizing background near the end of reionization (see Section 7.3.3). The stellar mass functions at higher redshift do not show such flattening. This effect may relieve the tension between the number of low-mass galaxies in the Local Group and that needed for cosmic reionization (e.g., Bullock et al. 2000; Somerville 2002; Boylan-Kolchin et al. 2014).

7.5 Multi-band luminosity functions

We calculate the luminosity functions at several bands following the same method described in Section 7.4. Again, only halos above $M_{halo} = 10^{7.5} \, M_\odot$ are taken into account. In Figure 7.10, we show the results in number $\mathrm{mag}^{-1} \, \mathrm{Mpc}^{-3}$ at $z = 6$, 8, 10, and 12 (the open symbols). The data are also provided in Appendix C. We also model the luminosity functions using a Monte Carlo method by convolving the magnitude–stellar mass relation derived in Section 7.3.4 (Equation 7.6) with the model stellar mass functions in Section 7.4 in a similar way described above. The model luminosity functions are shown by the dashed lines in Figure 7.10. Note that we only consider intrinsic stellar continuum emission here, but we will explore the effect of dust extinction in Section 7.6.2 and compare with observations in Section 7.6.3. We do not model nebular line emission in this paper.
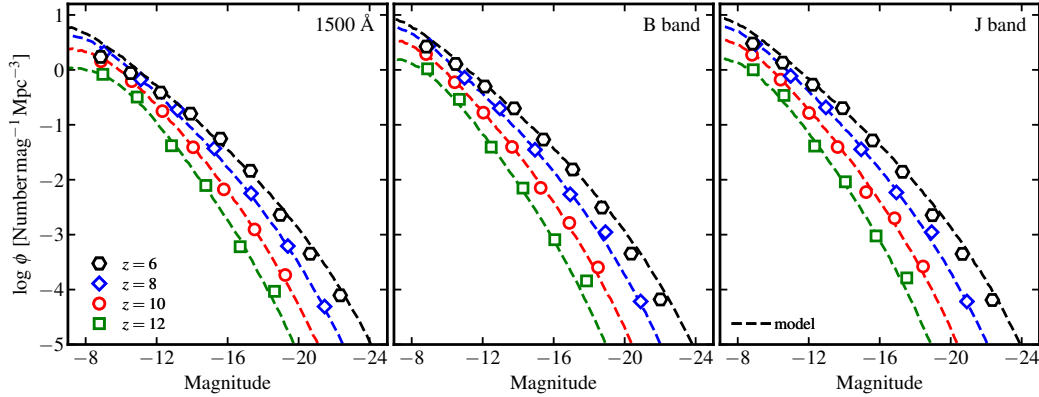
Figure 7.10: Predicted luminosity functions at rest-frame 1500 Å (left), B band (middle), and J band (right) at $z = 6$, 8, 10, and 12. All magnitudes are intrinsic without accounting for dust attenuation. The open symbols show the results derived from the simulated catalog. The dashed lines show the model luminosity functions from convolution between the magnitude–stellar mass relation in Section 7.3.4 and the model stellar mass functions in Section 7.4. As in Figure 7.9, the faint-end slope steepens with increasing redshift. The stronger flattening of the $z = 6$ luminosity functions fainter than $M_{AB} \sim -12$ is due to the suppression of star formation in halos around $M_{halo} \sim 10^8\,M_\odot$ by the strong ionizing background. We will compare our predicted UV luminosity function with observations later in Section 7.6.3 and Figure 7.14. We make our predictions publicly available (see Appendix C for details).

The luminosity functions derived from the simulations agree well with models for a broad range of magnitude and redshift. Again, the faint-end slope (asymptotic form $\phi\,dM_{AB,\,band} \sim 10^{-0.4(\alpha+1)M_{AB,\,band}}dM_{AB,\,band}$) steepens with increasing redshift (e.g., from $\alpha = -1.85 \pm 0.06$ at $z = 6$ to $\alpha = -2.17 \pm 0.10$ at $z = 12$ at 1500 Å). The trend is in good agreement with observations (e.g., Bouwens et al. 2015; Finkelstein et al. 2015a), semi-analytic galaxy formation models (e.g., Clay et al. 2015; Cowley et al. 2018), and other simulations (e.g., Gnedin 2016; Ceverino et al. 2017; Wilkins et al. 2017) at these redshifts, but the exact slopes depend largely on the fitting method. The flattening at the faintest bin at any redshift is due to the incompleteness of halos below $M_* = 10^{7.5}\,M_\odot$. Similarly, the luminosity functions show a flattening below $M_{1500\,Å} \sim -12$, $M_B \sim -12$, and $M_J \sim -12$ at $z = 6$, as seen from the fact that the luminosity functions derived from the simulated catalog fall below the model luminosity functions roughly by a factor of 2. This is caused by the large fraction of dark halos and the rapid drop in SFR at $z \sim 6$ below halo mass $M_{halo} \sim 10^8\,M_\odot$, where star formation is suppressed by the ionizing background (Figure 7.7).

7.6 Discussion

7.6.1 SFR and stellar mass densities at $z \geq 5$

We now derive the cosmic SFR density (SFRD) from $z = 5$–12 by convolving the SFR–M_{halo} relation given by Equation 7.4 (the average SFR at a given halo mass) and the halo mass function at the same redshift. In Figure 7.11, we show the results obtained by integrating over the halo mass range above $M_{halo} = 10^{7.5}\,M_\odot$ (dashed), $M_{halo} = 10^{8.5}\,M_\odot$ (solid), and $M_{halo} = 10^{9.5}\,M_\odot$ (dotted) to $M_{halo} = 10^{12}\,M_\odot$. The contributions from more massive halos are negligible at these redshifts (because they are extremely rare). In Figure 7.11, we also show observationally inferred SFRDs from Ellis et al. (2013), Oesch et al. (2013), Oesch et al. (2014), Bouwens et al. (2015), Finkelstein et al. (2015a), McLeod et al. (2016), and CLASH detections (Zheng et al. 2012; Coe et al. 2013; Bouwens et al. 2014). Data corrected (uncorrected) for dust attenuation are shown by open (filled) symbols[16]. At $z \lesssim 8$, our predictions broadly agree with data within observational uncertainties. The SFRD at $z \gtrsim 9$ are still poorly constrained observationally. These results are derived by integrating the best-fit UV luminosity functions brighter than $M_{UV} \sim -17$. This limit does not correspond to a unique halo mass, but is roughly consistent with what we obtain by integrating down to $M_{halo} = 10^{9.5}\,M_\odot$ at these redshifts (cf. Figures 7.4 and 7.8). Note that the number of galaxies in the observed $z \gtrsim 9$ sample is small, and some works are based on single galaxy detections. Our simulations suggest that the majority of star formation takes place in halos below $M_{halo} = 10^{9.5}\,M_\odot$ at $z \gtrsim 9$, but these low-mass galaxies are too faint to be detectable with current observational facilities. This may account for the apparent rapid decline in SFRD at these redshifts (e.g., Oesch et al. 2014). Future deep surveys by JWST at these redshifts are expected to put strong constraints on the $z \geq 9$ SFRD.

We also calculate the stellar mass density from $z = 5$–12 by integrating the model stellar mass functions in Section 7.4 in certain stellar mass intervals. The three lines in Figure 7.12 show the results for $M_* > 10^6\,M_\odot$ (solid), $M_* > 10^4\,M_\odot$ (dashed), and $M_* > 10^8\,M_\odot$ (dotted). At these redshifts, high-mass galaxies ($M_* > 10^{10}\,M_\odot$) only contribute a negligible fraction (less than 0.05 dex) of the total stellar mass due to their low number densities, so the total stellar mass density is insensitive to our uncertainties in the high-mass end of the stellar mass functions. In Figure 7.12, we also compare our predictions with observationally inferred results in the literature (symbols with errorbars, including González et al. 2011; Duncan et al. 2014; Oesch

---

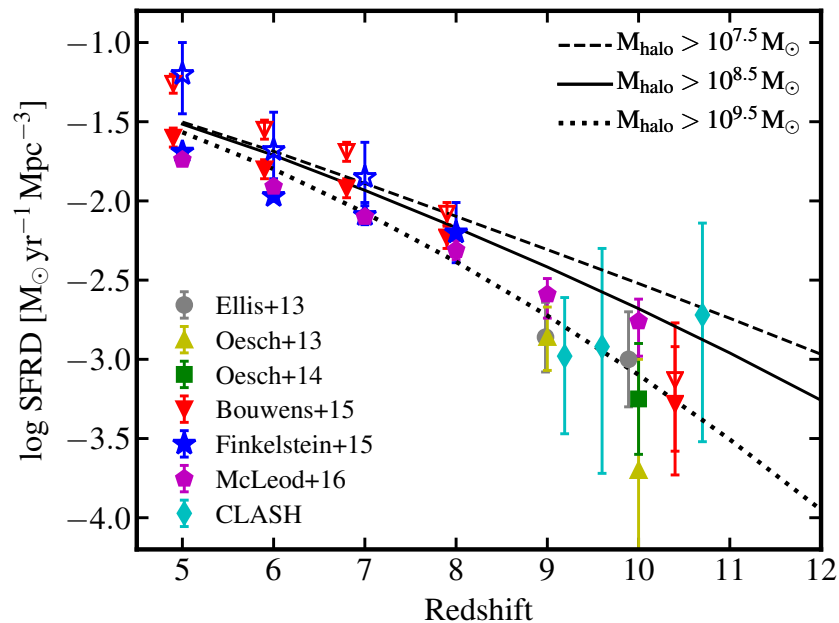[16]We note that the conversion between rest-frame UV luminosity and SFR and the amount of dust correction is still very uncertain.

Figure 7.11: Cosmic star formation rate density (SFRD) from $z = 5$–12. The lines are derived by convolving the SFR–M_{halo} relation given by Equation 7.4 and the halo mass function at the same redshift. The dashed, solid, and dotted lines show the results obtained by integrating over the halo mass range as labeled. Observationally inferred SFRDs from the literature are shown with symbols and errorbars. These results are derived by integrating the best-fit UV luminosity functions brighter than $M_{UV} \sim -17$. Data corrected (uncorrected) for dust attenuation are shown by open (filled) symbols. At $z \lesssim 8$, our predictions agree with data within observational uncertainties. The $z \gtrsim 9$ SFRD is poorly constrained due to the small size of each observational sample. Our simulations suggest that low-mass halos dominate the SFRD, due to their rapidly increasing number densities at these redshifts. This is beyond the detection limits of current observational facilities ($M_{UV} \sim -17$, roughly corresponding to halo mass $M_{halo} \sim 10^{9.5} M_{\odot}$ in our simulations). Future deep surveys by JWST will be able to put stronger constrains on the $z \gtrsim 9$ SFRD.
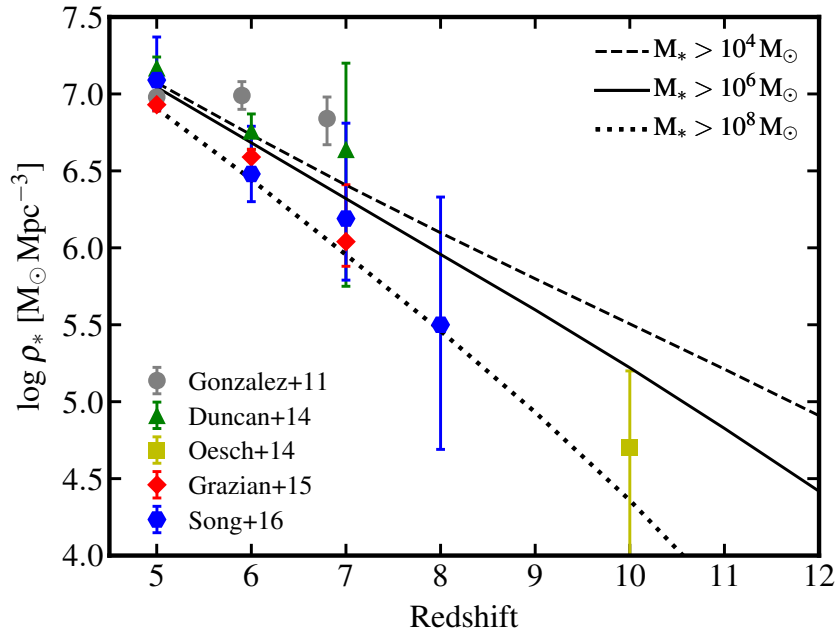
Figure 7.12: Stellar mass density from $z = 5$–12. The lines are derived by integrating the model stellar mass functions in Section 7.4 over the mass range as labeled. At high redshift, the stellar mass density is dominated by low-mass galaxies, due to the rapid steepening of the low-mass-end of the stellar mass function. Observationally inferred data from the literature are shown by filled symbols with errorbars. These observational results are derived by integrating the best-fit stellar mass functions above $M_* > 10^8\,M_\odot$. Our equivalent prediction (the dotted line) broadly agrees well with more recent studies. The discrepancies between these measurements likely originate from systematic uncertainties in stellar mass measurements.

et al. 2014; Grazian et al. 2015; Song et al. 2016). Note that these results are derived by integrating the best-fit stellar mass functions above $M_* > 10^8\,M_\odot$. Our predictions (the dotted line, which uses the same limit) broadly agree with more recent studies (Oesch et al. 2014; Grazian et al. 2015; Song et al. 2016). We note that although some groups report consistent stellar mass densities at these redshifts, their stellar mass functions do not usually agree with each other (see Section 7.6.3 or figure 9 in Song et al. 2016).

7.6.2 Dust extinction in rest-frame UV

So far we have only focused on intrinsic luminosity of our simulated galaxies, while dust obscuration can be very important in relatively massive galaxies (e.g., Cen & Kimm 2014; Cullen et al. 2017; Wilkins et al. 2017). In this section, we estimate the amount of dust extinction in the rest-frame UV band. We follow the method from Hopkins et al. (2005) and calculate the extinction by ray-tracing the emission
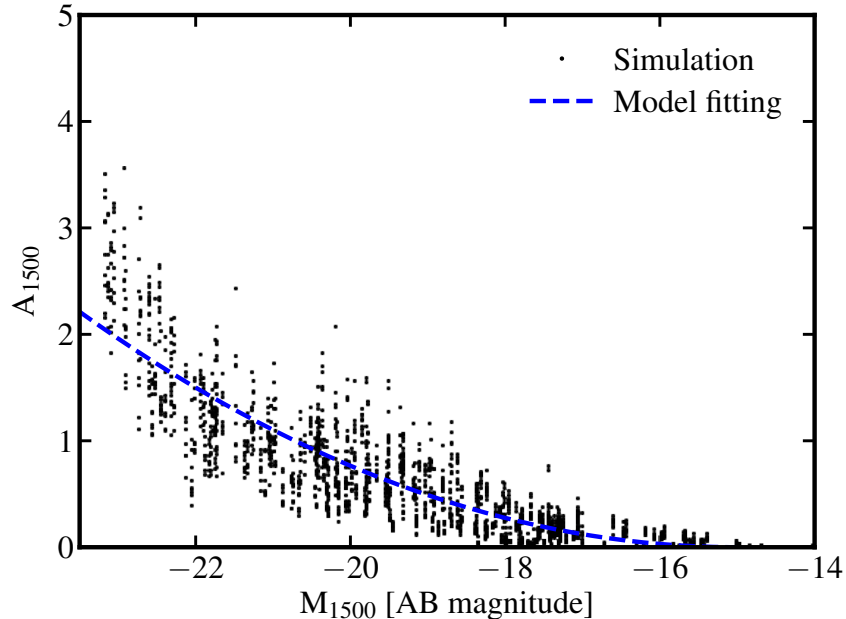
Figure 7.13: The relation between UV extinction and intrinsic UV magnitude in the simulations. The points show all simulated galaxies from $z = 5$–8, with ten different sightlines for each galaxy. We determine the dust extinction by ray-tracing and assuming a constant dust-to-metal ratio, using the distribution of gas and metals in the simulations. The blue dashed line shows the best-fit relation in Equation 7.8.

from star particles including dust attenuation self-consistently from the dust and metals in the simulation (see also Hopkins et al. 2014; Feldmann et al. 2016, 2017). We assume a canonical dust-to-metal ratio of 0.4 (Dwek 1998). Following a Small Magellanic Cloud-like extinction curve from Pei (1992), we obtain a dust opacity of $2.06 \times 10^3 \, \mathrm{cm^2 \, g^{-1}}$ at 1500 Å at solar metallicity. For each simulated galaxy, we include all gas particles within $\frac{1}{2} R_{\mathrm{max}}$ (about 1.5 times the size of the stellar component, see Section 7.2.3) and calculate the extinction by ray-tracing from every star particle to a hypothetical observer along ten different sightlines. Note that the gas in these high-redshift galaxies is clumpy, so the extinction can differ by several magnitudes between sightlines. In Figure 7.13, we show the relation between extinction $A_{1500} = -2.5 \log(F_{1500}/F_{1500,0})$ and intrinsic UV magnitude M_{1500} for all sightlines and all simulated galaxies from $z = 5$–8. We do not find significant redshift dependence in our sample, but we caution that this may be due to the small sample size at the massive end. We fit the results with a parabolic function

$$A_{1500} = (0.0306 \pm 0.0002) \, (M_{1500} + 15)^2, \tag{7.8}$$

and quote a uniformly distributed scatter with half-width $\Delta A_{1500} = -0.125\,(M_{1500} + 15)$ at $M_{1500} < -15$. A full radiative transfer calculation of dust extinction, scatter, and re-emission is beyond the scope of the current paper, but will be the subject of a future study.

7.6.3 Comparison with observations

In this section, we compare our predicted stellar mass functions and luminosity functions with observations. In the top panel in Figure 7.14, we show the $z = 6$ stellar mass function derived from the simulated catalog (open squares) and from direct convolution between the stellar mass–halo mass relation and the halo mass function (dashed lines). They are identical to those in Figure 7.9, but we only show $M_* \geq 10^7\,M_\odot$ where the observational results are available. We also show a compilation of observations from González et al. (2011), Duncan et al. (2014), Grazian et al. (2015), Song et al. (2016), and Stefanon et al. (2017) (symbols with errorbars). Above $M_* \sim 10^9\,M_\odot$, our model agrees well with Song et al. (2016) and Stefanon et al. (2017), but falls below some other results. Below $M_* \sim 10^8\,M_\odot$, we predict slightly higher number densities than Song et al. (2016).

In the bottom panel, we show the $z = 6$ UV luminosity function (rest-frame 1500 Å) from our predictions (open squares and the thin dashed line, identical to those in Figure 7.10) and from observations in Atek et al. (2015), Bowler et al. (2015), Bouwens et al. (2015), Finkelstein et al. (2015a), Bouwens et al. (2017c), and Livermore et al. (2017) (symbols with errorbars). First, we only consider the intrinsic stellar luminosities without accounting for dust extinction (the thin dashed line), which results in the fact that our model predicts higher number densities than observed at the bright end.

To quantify the effect of dust attenuation, we use a Monte Carlo method to apply the dust attenuation determined in Section 7.6.2 to the model UV luminosity function. We adopt the median attenuation from Equation 7.8, with a magnitude-dependent scatter following a uniform distribution with half-width $\Delta A_{1500} = -0.09375\,(M_{1500} + 15)$ at $M_{1500} < -15$. The model UV luminosity function after dust extinction is shown by the thick dashed line in Figure 7.14, which agrees surprisingly well with observations at the bright end. This result suggests that the bright-end of the UV luminosity function is mostly set by dust obscuration, in line with predictions from semi-analytic models (Somerville et al. 2012) and cosmological simulations (Wilkins et al. 2017). We find that dust extinction becomes significant for galaxies
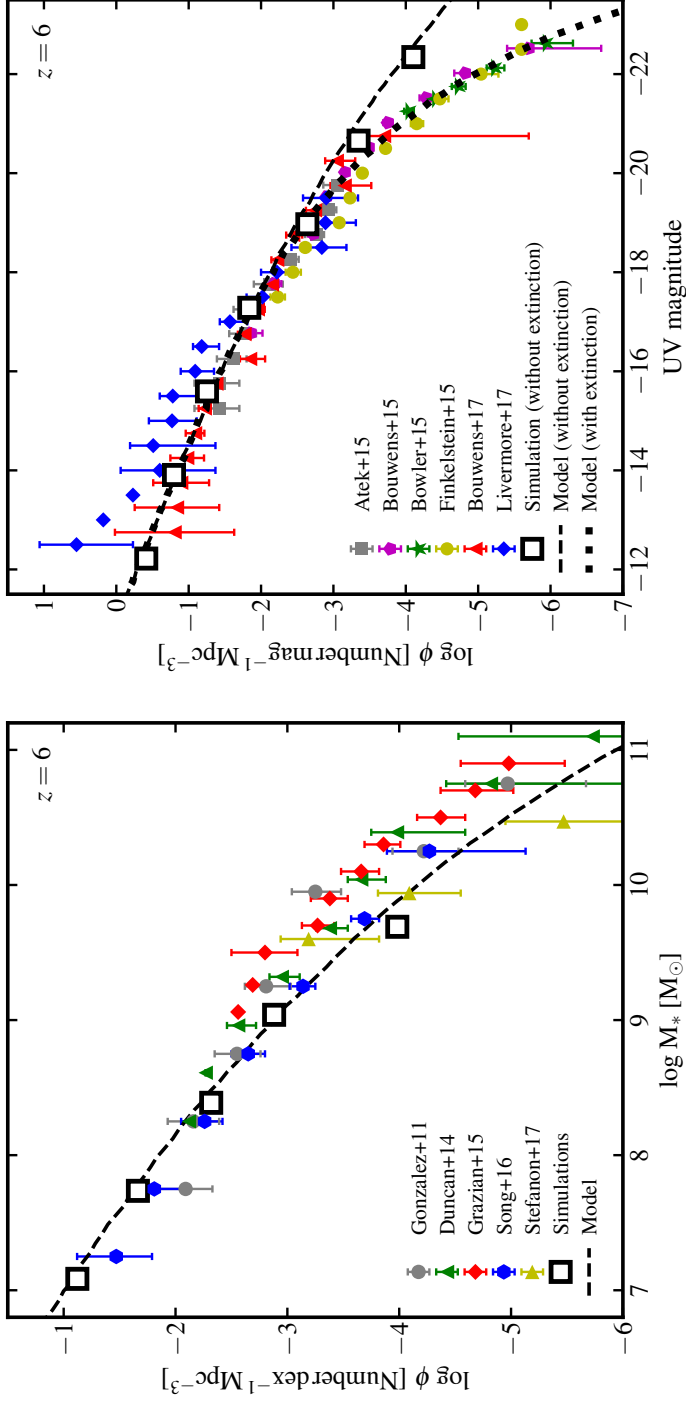
Figure 7.14: *Left:* The stellar mass function at $z = 6$. The open squares and the dashed line show the simulation-derived and the model stellar mass functions obtained in Section 7.4 (the same as in Figure 7.9). Symbols with errorbars show a compilation of observations from González et al. (2011), Duncan et al. (2014), Grazian et al. (2015), Song et al. (2016), and Stefanon et al. (2017). Our results are broadly consistent with observations. The discrepancies might be due to systematic uncertainties in deriving stellar mass from single-band magnitude, incompleteness corrections at the low-mass end, and cosmic variance at the massive end. *Right:* The UV luminosity at $z = 6$. A compilation of observations from Atek et al. (2015), Bowler et al. (2015), Finkelstein et al. (2015a), Bouwens et al. (2017c), and Livermore et al. (2017) are shown by symbols with errorbars. Using intrinsic luminosities, the model tends to predict higher number densities than observed at the bright end. The thick dashed line shows the luminosity function after accounting for the dust extinction in the simulations (see text for details). The good agreement with data suggests that the turnover at the bright-end of the UV luminosity function is largely due to dust extinction. Approximately 37% (54%) of the UV luminosity from galaxies brighter than $M_{1500} = -13$ (-17) is obscured by dust at $z \sim 6$.

with intrinsic UV magnitude brighter than $M_{1500} \sim -20$. The star formation in these galaxies cannot be fully probed in the rest-frame UV. Approximately 37% of the UV light from galaxies brighter than $M_{1500} = -13$ at $z = 6$ is obscured by dust according to our model. The obscured fraction is 54% if only galaxies brighter than $M_{1500} = -17$ are considered. These numbers are broadly in line with observational estimates of the dust obscured fraction of star formation at these redshifts (see e.g., Finkelstein et al. 2015a; Bouwens et al. 2015).

Our predicted UV luminosity function (after dust attenuation) is in good agreement with current data in a broad range of magnitudes[17], but the predicted stellar mass function shows considerable discrepancies with observational measurements. We note that the stellar mass functions from different groups also do not in general agree perfectly with each other. We discuss several systematic uncertainties that might be important in these measurements. First, a non-negligible fraction of the light from galaxies will be missed due to the finite surface brightness depth of an observational campaign. Therefore, the stellar mass of a galaxy is possibly underestimated. This effect becomes much stronger at lower masses (e.g., Ma et al. 2018). Second, the incompleteness correction at the low-mass end for a flux-limited sample is sensitive to the *a priori* distribution of magnitude at a given stellar mass. We show in Section 7.3.4 that this distribution is biased toward the faint end (top panels in Figure 7.8). One could underestimate the incompleteness if this bias is not properly accounted for. Third, measurement uncertainties in stellar mass will introduce contamination from low-mass galaxies in a given mass bin, and thereby lead to an overestimate of their number density, especially at the high-mass end where the stellar mass function is steep (e.g., Davidzon et al. 2017). In addition, cosmic variance may also lead to discrepancies at the massive end.

Nevertheless, our simulations do not include halos more massive than $M_{halo} \sim 10^{12} \, M_{\odot}$ and only include a small number of independent halos above $M_{halo} \sim 10^{11} \, M_{\odot}$. We may underestimate the scatter of certain galaxy properties at these masses. Moreover, we do not consider primordial chemistry or the ionizing background fluctuation prior to reionization, which may have important effects on halos below $M_{halo} \sim 10^8 \, M_{\odot}$. Our predictions should be tested by future observations to better understand the uncertainties in the current model.

---

[17]Note that the sample in Livermore et al. (2017) has only one galaxy in the faintest bin, and no galaxy in the next two bins (upper limits).

7.6.4 Differences between stellar population models

In this paper, we use the BPASSv2.0 binary model with a Kroupa (2002) IMF from 0.1–100 $M_\odot$ as our default stellar population model for post-processing. To illustrate the difference between stellar population models, we show the synthetic spectrum for simulation z5m12a at $z = 5$ (stellar mass $M_* = 3 \times 10^9 \, M_\odot$) in Figure 7.15 using two models in BPASSv2.0: the default binary model (black) and the single-star model with the same IMF (red). Again, the spectra only include intrinsic star light without accounting for dust attenuation and line emission. The binary models produce slightly higher luminosities in the rest-frame UV at wavelengths bluer than the Balmer break at 3648 Å, but about 0.2–0.8 mag weaker emission in the rest-frame optical and IR than single-star models. This is because of consequences of binary interaction: (a) the 'effective' IMF is changed and (b) a large fraction of red supergiants are removed and replaced with hot stripped stars (J. J. Eldridge, private communication). These effects are particularly important in stellar populations younger than 1 Gyr, which are dominant in galaxies at $z \geq 5$ when the age of the Universe is comparable and even younger. If single-star models are used, the predicted B-band and J-band magnitudes will be brighter by 0.2 dex and 0.5 dex, respectively. Future observations of high-redshift galaxies at the rest-frame optical bands will provide more hints of the stellar populations in these galaxies. Another important difference is that binary models tend to produce more ionizing photons (wavelengths shorter than 912 Å). The production of these photons even extends to 30 Myr after the formation of a stellar population (as opposed to 10 Myr in single-star models), so these photons are more likely to escape the galaxy and play an important role in cosmic reionization (Ma et al. 2016b; Götberg et al. 2017). However, ionizing photons only contribute a small fraction (less than 10%) of the bolometric luminosity. Note that the differences between different stellar evolution calculations for non-rotating, single-star models (e.g., STARBURST99 and BPASS, using the same IMF and stellar atmosphere models) are much smaller than the effects of binaries.

7.7 Conclusion

In this paper, we present a suite of cosmological zoom-in simulations at $z \geq 5$ covering the $z = 5$ halo mass range $M_{\mathrm{halo}} \sim 10^8$–$10^{12} \, M_\odot$. These are high-resolution simulations (100–7000 $M_\odot$ baryonic mass resolution) using physically motivated models of the multi-phase ISM, star formation, and stellar feedback from the FIRE-2 simulation suite of the FIRE project (Hopkins et al. 2017). These simulations
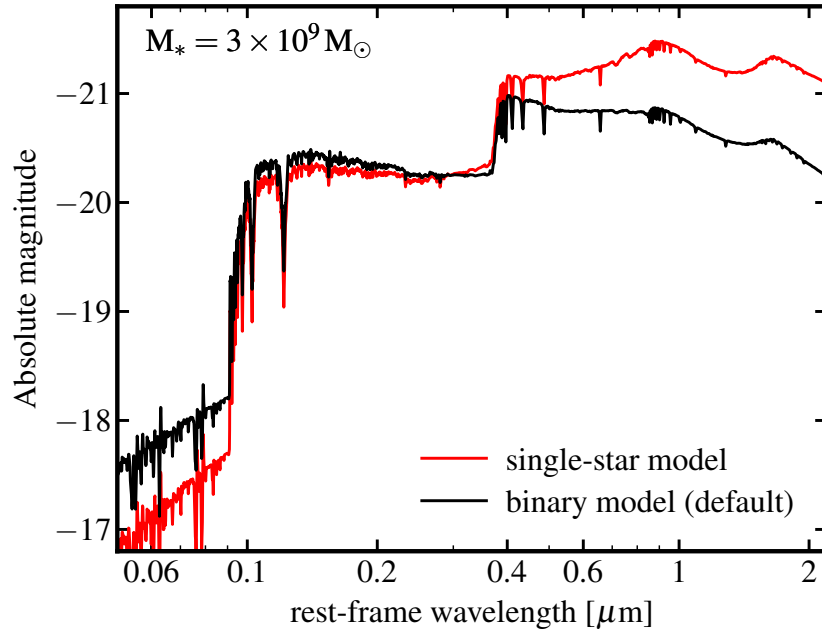
Figure 7.15: Synthetic spectrum for a $M_* = 3 \times 10^9 \, M_\odot$ galaxy (simulation z5m12a at $z = 5$) using different stellar population models. Binary models produce slightly higher rest-frame UV luminosities at 1500 Å, but approximately 0.2–0.8 mag lower rest-frame optical-to-IR luminosities than single-star models. Moreover, binary models produces more ionizing photons (wavelengths shorter than 912 Å), but these photons only contribute a small fraction of the bolometric luminosity.

provide useful guidance for future observations with JWST and next-generation ground-based telescopes. Our simulations are complementary to simulations of the first stars and low-mass galaxies at $z \gtrsim 15$ with sophisticated primordial chemistry as well as large-volume simulations using empirically calibrated star formation and feedback models at much poorer resolution.

By utilizing all properly resolved halos in each zoom-in region, we obtain a simulated sample containing hundreds of independent halos at a given redshift (Figure 7.1). We also include all snapshots (separated by about 20 Myr in time) in our analysis to account for time variability in galaxy properties. At low halo masses (e.g., $M_{halo} \leq 10^{11} \, M_\odot$ at $z \sim 6$ or $M_{halo} \leq 10^{10.5} \, M_\odot$ at $z \sim 10$), our sample includes a large number of independent halos to account for halo-to-halo variance. At higher halo masses, our sample is small, so we may underestimate the scatter of galaxy properties due to halo-to-halo variance (cf. Sections 7.2.3 and 7.3.2).

We use the BPASSv2.0 binary stellar population models with a Kroupa (2002) IMF to compute the broad-band photometry from starlight in these galaxies. We also

use analytic halo mass functions to assign each simulated galaxy a proper number density that reflects its relative abundance in the Universe. In this paper, we study the stellar mass–halo mass relation, star formation histories, the relation between broad-band magnitude and stellar mass, and stellar mass function and luminosity functions. Our main results include the following:

(i) The stellar mass–halo mass relation shows little evolution at redshift $z = 5$–12 (Figure 7.4). The best-fit median relation and 1σ-scatter are $\log M_* = 1.58 \, (\log M_{\mathrm{halo}} - 10) + 7.10$ and $\Delta \log M_* = \exp[-0.14 \, (\log M_{\mathrm{halo}} - 10) - 1.10]$ in the halo mass range $M_{\mathrm{halo}} = 10^{7.5}$–$10^{12} \, M_\odot$ (Section 7.3.2). The M_*–M_{halo} relation may bend at $M_{\mathrm{halo}} > 10^{12} \, M_\odot$ (as is inferred at lower redshifts), but this regime is not probed by our simulations.

(ii) The relation between SFR, halo mass (stellar mass), and redshift can be best described by $\log \mathrm{SFR} = 1.58 \, (\log M_{\mathrm{halo}} - 10) + 2.20 \, \log\left(\frac{1+z}{6}\right) - 1.58$ and $\log \mathrm{SFR} = 1.03 \, (\log M_* - 10) + 2.01 \, \log\left(\frac{1+z}{6}\right) + 1.36$. The slopes of the SFR–$M_{\mathrm{halo}}$ and SFR–M_* relations do not depend on redshift, but the average SFR at fixed halo mass (stellar mass) increases with increasing redshift by approximate 0.7 dex from $z = 5$ to $z = 12$ (Figure 7.7).

(iii) The mean SFR for galaxies below $M_{\mathrm{halo}} \sim 10^8 \, M_\odot$ or $M_* \sim 10^4 \, M_\odot$ below $z \sim 6$ drops significantly (Figure 7.7), because star formation is suppressed in low-mass galaxies by the ionizing background near the end of reionization (see also the left most panel in Figure 7.5). About 50% of the halos at $M_{\mathrm{halo}} \sim 10^8 \, M_\odot$ at $z \sim 6$ are dark halos that contain no stars. Halos of similar masses above $z \sim 7$ or halos more massive than $M_{\mathrm{halo}} \sim 10^{8.5} \, M_\odot$ at any redshift continue normal star formation.

(iv) We provide the median and 1σ-scatter for the magnitude–stellar mass relation and stellar mass–magnitude relation at rest-frame 1500 Å, B band, and J band (Table 7.2 and Figure 7.8). Both relations have large scatter. We emphasize that the two relations are fundamentally different from each other. At fixed stellar mass, the distribution of magnitudes is set by the range of recent star formation histories. At fixed magnitude, the distribution of stellar mass is biased toward the low-mass end, due to the higher abundance of low-mass galaxies in the Universe (Section 7.3.4).

(v) We predict the stellar mass function and luminosity functions at rest-frame 1500 Å, B band, and J band from $z = 5$–12 (Figures 7.9 and 7.10). Our results are broadly consistent with current observations (Figures 7.14) and can be tested by future observations with JWST and next-generation ground-based telescopes. We

make our predictions public for future use (see Appendix C for details).

(vi) Both the stellar mass function and luminosity functions show steepening low-mass-end or faint-end slopes with increasing redshift (from $\alpha = -1.85$ at $z \sim 6$ to $\alpha = -2.18$ at $z \sim 12$, Figures 7.9 and 7.10), as inherited from the steepening of the low-mass-end slope of the halo mass function.

(vii) The stellar mass function slightly flattens below $M_* \sim 10^{4.5}\,M_\odot$ at $z \sim 6$. This results from the high dark halo fraction at $M_{halo} \sim 10^8\,M_\odot$, due to star formation being suppressed by the ionizing background at these redshifts. Similarly, the $z = 6$ luminosity functions also show a flattening at magnitudes fainter than $M_{1500} \sim -12$, $M_B \sim -12$ and $M_J \sim -12$ (Section 7.4). There is no such flattening at higher redshifts.

(viii) We derive the star formation rate and stellar mass density at $z = 5$–12 (Figures 7.11 and 7.12). Our results are in good agreement with current observational constraints at $z \leq 8$. At higher redshifts, both are dominated by low-mass galaxies. Future JWST observations can put more robust constraints on the mass assembly histories at these redshifts by measuring galaxy number densities below $M_{UV} \sim 15$ or $M_* \sim 10^8\,M_\odot$.

(ix) Dust attenuation in the rest-frame UV becomes important for galaxies with intrinsic 1500 Å-magnitude brighter than $M_{1500} \sim -20$ (Figure 7.13). In our analysis, the bright-end shape of the UV luminosity function is primarily set by dust attenuation (Figure 7.14). Approximately 37% (54%) of the UV luminosity from galaxies brighter than $M_{1500} = -13$ ($M_{1500} = -17$) is obscured by dust at $z \sim 6$.

We note the caveat that our simulations do not include primordial chemistry and H_2 formation and dissociation, nor try to model Pop III star formation. These are important in understanding the cooling in primordial gas and metal enrichment at very high redshifts ($z \geq 15$), which may affect the star formation efficiency in halos below $M_{halo} \sim 10^8\,M_\odot$ (e.g., Wise et al. 2014; Chen et al. 2014). Furthermore, we do not model cosmic reionization self-consistently; instead, we only apply a spatially uniform, redshift-dependent ionizing background. This ignores the fact that reionization is highly inhomogeneous (e.g., Barkana & Loeb 2001; Furlanetto et al. 2004; Iliev et al. 2006; McQuinn et al. 2007) and that even after reionization the ionizing background has large spatial fluctuations (e.g., Becker et al. 2015; Davies & Furlanetto 2016; D'Aloisio et al. 2018). Preliminary results indicate that increasing the ionizing background strength by a factor of 10–100 may lower the stellar mass

in halos of $z = 5$ mass $M_{halo} \sim 10^9 \, M_\odot$ by a factor of 2. This may lead to larger scatter in the stellar mass–halo mass relation at the low-mass end that we do not capture in the current study. These questions are worth further exploration.

These simulations have many applications. In the future, we will use them to study the size evolution of high-redshift galaxies, dust attenuation and IR luminosity functions, nebular line emissions, the escape fraction of ionizing photons, [C II] and CO luminosity functions, metal-enriched absorbers in the circum-galactic medium, Lyman-α radiative transfer, globular cluster formation, and more. We will also expand the simulation suite to lower and higher masses and more extreme environments at these redshifts.
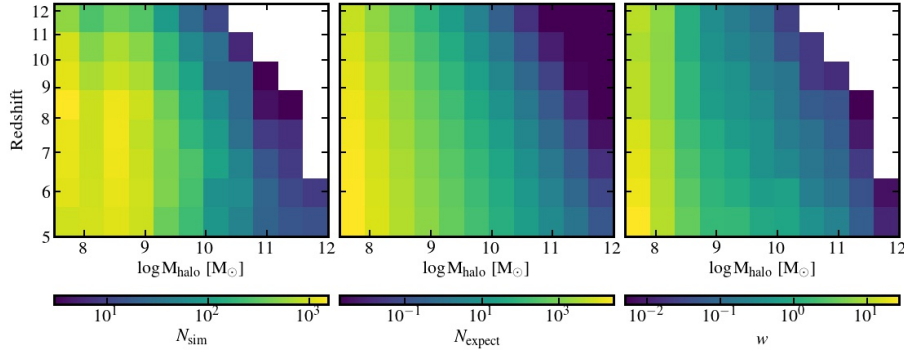
Figure 7.16: The number of halo snapshots in our simulated catalog (left), the expected number of galaxies in the Universe (on 1 arcmin^2 sky, center), and the weight assigned to each halo snapshot (right) as a function of halo mass and redshift.

Appendix A: The weighting method

In Section 7.2.4, we introduce a weighting method by assigning each halo 'snapshot' a weight w according to its halo mass and redshift to reflect its real abundance in the Universe. First, we bin our simulated catalog in $\log M_{\rm halo}$–$\log(1 + z)$ space with bin sizes $\Delta \log M_{\rm halo} = 0.4$ and $\Delta \log(1 + z) = 0.04$ and count the number of halo snapshots in each bin $N_{\rm sim}$ as shown in the left panel of Figure 7.16. Next, we compute the expected number of halos in the Universe in each bin $N_{\rm expect} = \phi \Delta \log M_{\rm halo}\Delta V_{\rm com}$, where ϕ is the halo mass function obtained from `HMFcalc` (Murray et al. 2013, number of halos per dex per comoving volume) and $\Delta V_{\rm com}$ is the comoving volume corresponding to the redshift range of each bin and 1 arcmin^2 area on the sky (this is to avoid w being too large or too small). Each halo in the same bin will then be given the same weight $w = N_{\rm expect}/N_{\rm sim}$. Therefore, summing over the weights of halos in a given bin leads to the expected number of halos in the Universe (on 1 arcmin^2 area of the sky). We show $N_{\rm expect}$ and w in the middle and right panel of Figure 7.16.

Appendix B: Resolution tests

Every zoom-in simulation presented in the paper has been run at several resolution levels. The main text shows results only from the highest-resolution runs available. In Figure 7.17, we show the stellar mass–halo mass relation in the $z = 5$ snapshots for simulations using different mass resolution (shown by different symbols). The large symbols represent the most massive halo in each simulation and smaller symbols show less massive isolated halos in the zoom-in regions with more than 10^4 particles and zero contamination. Note than we show the total stellar mass in the halo instead
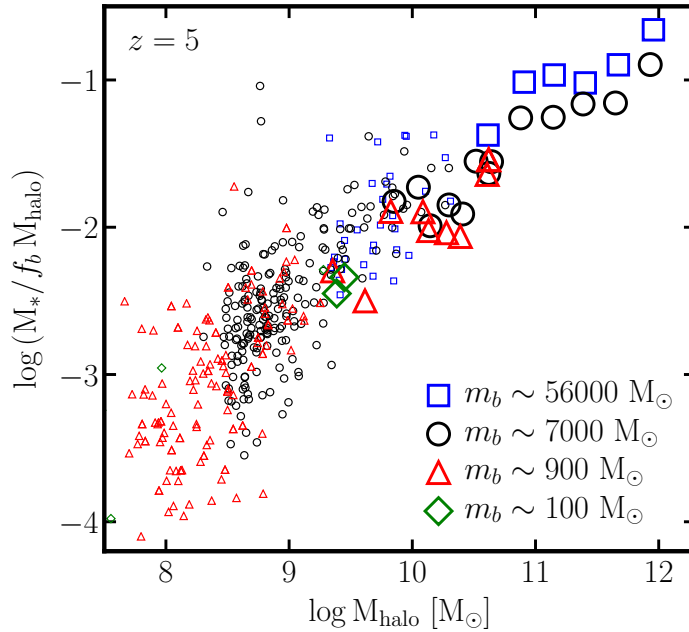
Figure 7.17: The stellar mass–halo mass relation produced by simulations at different mass resolution. Simulations at mass resolution $m_b \sim 5.6 \times 10^4 \, \mathrm{M_\odot}$ systematically produce two times more stars. Simulations at resolution $m_b \sim 7 \times 10^3 \, \mathrm{M_\odot}$ and better do not show statistically-significant systematic differences over a fairly large number of galaxies (as we are able to show below $\mathrm{M_{halo}} \sim 10^{11} \, \mathrm{M_\odot}$). The difference in the stellar mass of individual galaxy is usually due to stochastic star formation and feedback.

of the central galaxy stellar mass defined in Section 7.2.3, to reduce the effects of stochastic fluctuation in galaxy mass induced by mergers. Simulations at mass resolution $m_b \sim 5.6 \times 10^4 \, \mathrm{M_\odot}$ tend to systematically over-predict stellar mass by about a factor of two. This is also found in our previous work using ultra-high-resolution dwarf galaxy and Milky Way-mass galaxy simulations run with the same code down to $z = 0$ (see Wetzel et al. 2016; Hopkins et al. 2017). At resolution $m_b \sim 7 \times 10^3 \, \mathrm{M_\odot}$ and better, we do not find significant systematic differences in the stellar mass–halo mass relation for a fairly large sample of galaxies (as we show for $\mathrm{M_{halo}} < 10^{11} \, \mathrm{M_\odot}$). The difference in the stellar mass of individual galaxy is mainly due to stochastic effects: when and where a star particle forms and a SN occurs are stochastically sampled from the SFR and SNe rates. Any perturbations may affect the final stellar mass of each galaxy, but the statistics in the stellar mass–halo mass relation is unchanged. This is the way we define convergence for our simulations. Therefore, we adopt mass resolution $m_b \sim 7 \times 10^3 \, \mathrm{M_\odot}$ for halos above $\mathrm{M_{halo}} = 10^{11} \, \mathrm{M_\odot}$ and even better resolution for our lower mass systems for final

production runs, to ensure reasonable convergence and computational costs. For more extensive mass and spatial resolution tests, and other numerical details, see Hopkins et al. (2017).

7.8 Stellar mass functions and luminosity functions

In Sections 7.4 and 7.5, we describe the method used to compute the stellar mass functions and luminosity functions from the simulated sample. Here we provide these results at $z = 5$–12. The first two columns give the stellar mass functions above $M_* = 10^{3.5}\,M_\odot$, and the remaining columns give the luminosity functions brighter than $M_{AB} = -8$ at rest-frame 1500 Å, B, and J band, respectfully. In addition, we also make our model stellar mass function and luminosity functions public. A machine-readable version of these results is available at http://www.tapir.caltech.edu/~xchma/data/hiz_smf_lf.zip. Those derived from the simulated catalog are tabulated in files SMF_sim_zxx.txt, LF_UV_sim_zxx.txt, LF_B_sim_zxx.txt, and LF_J_sim_zxx.txt. The model stellar mass functions and luminosity functions are tabulated in files SMF_model_zxx.txt, LF_UV_model_zxx.txt, LF_B_model_zxx.txt, and LF_J_model_zxx.txt (these are shown with the dashed lines in Figures 7.9 and 7.10). The UV luminosity functions after accounting for dust attenuation are tabulated in LF_UV_red_zxx.txt. The two digits xx in all file names represent the redshift. We encourage readers to use our results and confront them with future observations and other models.

Chapter 8

SIMULATING GALAXIES IN THE REIONIZATION ERA WITH FIRE-2: MORPHOLOGIES AND SIZES

Abstract

We study the morphologies and sizes of galaxies at $z \geq 5$ using high-resolution cosmological zoom-in simulations from the Feedback In Realistic Environments project. The galaxies show a variety of morphologies, from compact to clumpy to irregular. The simulated galaxies have more extended morphologies and larger sizes when measured using rest-frame optical B-band light than rest-frame UV light; sizes measured from stellar mass surface density are even larger. The UV morphologies are usually dominated by several small, bright young stellar clumps that are not always associated with significant stellar mass. The B-band light traces stellar mass better than the UV, but it can also be biased by the bright clumps. At all redshifts, galaxy size correlates with stellar mass/luminosity with large scatter. The half-light radii range from 0.01 to 0.2 arcsec (0.05–1 kpc physical) at fixed magnitude. At $z \geq 5$, the size of galaxies at fixed stellar mass/luminosity evolves as $(1 + z)^{-m}$, with $m \sim 1$–2. For galaxies less massive than $M_* \sim 10^8\,M_\odot$, the ratio of the half-mass radius to the halo virial radius is $\sim 10\%$ and does not evolve significantly at $z = 5$–10; this ratio is typically 1–5% for more massive galaxies. A galaxy's 'observed' size decreases dramatically at shallower surface brightness limits. This effect may account for the extremely small sizes of $z \geq 5$ galaxies measured in the Hubble Frontier Fields. We provide predictions for the cumulative light distribution as a function of surface brightness for typical galaxies at $z = 6$.

Keywords: galaxies: evolution – galaxies: formation – galaxies: high-redshift – cosmology: theory

8.1 Introduction

High-redshift galaxies are thought to be the dominant source of cosmic reionization (e.g. Kuhlen & Faucher-Giguère 2012; Robertson et al. 2013, 2015). The number density of these galaxies, as described by the ultraviolet (UV) luminosity function, is well constrained for galaxies brighter than $M_{UV} = -17$ at $z \sim 6$ (e.g. McLure et al. 2013; Schenker et al. 2013; Bouwens et al. 2015; Finkelstein et al. 2015a). Recently, the Hubble Frontier Fields (HFF) program (Lotz et al. 2017), which takes advantage of strong gravitational lensing by foreground galaxy clusters, has made it possible to estimate UV luminosity functions down to $M_{UV} \sim -13$ (e.g. Bouwens et al. 2017c; Livermore et al. 2017). But one of the dominant outstanding uncertainties is the intrinsic size distribution of faint galaxies, which is necessary in order to determine the completeness of the observed sample due to surface brightness limits (Bouwens et al. 2017b).

There are only a few galaxies at these redshifts that have robust size measurements. Oesch et al. (2010) measured the sizes of galaxies brighter than $M_{UV} = -19$ at $z = 4$–8 in the Hubble Ultra-Deep Field (HUDF) and found that the half-light radii of galaxies evolve according to $(1 + z)^{-m}$, with $m \sim 1$–1.5 (see also, e.g. Bouwens et al. 2004; Ferguson et al. 2004; Ono et al. 2013; Kawamata et al. 2015). It is also expected from analytic models that galaxy size decreases with increasing redshift (Mo et al. 1998, 1999).

High-redshift galaxies tend to be intrinsically small. The half-light radii of bright galaxies ($M_{UV} < -19$) at $z \sim 6$–8 range from 0.5–1 kpc (e.g. Oesch et al. 2010). More recently, Kawamata et al. (2015) and Bouwens et al. (2017b) measured the half-light radii for a sample of fainter galaxies ($-19 < M_{UV} < -12$) from the HFF. They found that the size–luminosity relation has large scatter, with half-light radii spanning more than an order of magnitude (0.1–1 kpc) at fixed UV magnitude. A fraction of these faint galaxies have extremely small sizes from a few pc to 100 pc, although these results are very uncertain because they are far below the resolution of the *Hubble Space Telescope (HST)*.

Morphological studies have revealed that galaxies at intermediate redshifts ($z \sim 0.5$– 3) typically contain a number of star-forming clumps (e.g. Guo et al. 2015). These prominent clumps only contribute a small fraction of the total mass, however (e.g. Wuyts et al. 2012). So far, the sizes of $z \gtrsim 6$ galaxies are measured using noise-weighted stacked images over all available bands (dominated by rest-frame UV), so it is likely that the extremely small galaxy sizes in the HFF are biased by such clumps

(e.g. Vanzella et al. 2017). With the *James Webb Space Telescope* (*JWST*, scheduled to launch in 2019), one will be able to probe these faint, high-redshift galaxies with deeper imaging, higher spatial resolution, and at longer wavelengths. This makes it possible to compare galaxy morphology and sizes in different bands and to recover the stellar mass distribution using multi-band images via pixel-by-pixel spectral energy distribution (SED) modeling (e.g. Smith & Hayward 2015).

The goal of this paper is to make predictions of morphologies and sizes for $z \geq 5$ galaxies, which can be used to plan and interpret future observations. We use a suite of high-resolution cosmological zoom-in simulations from the Feedback In Realistic Environments (FIRE) project[1] (Hopkins et al. 2014). The FIRE simulations include explicit treatments of the multi-phase interstellar medium (ISM), star formation, and stellar feedback. The simulations are evolved using the FIRE-2 code (Hopkins et al. 2017), which is an update of the original FIRE code with several improvements to the numerics. These simulations predict stellar mass functions and luminosity functions in broad agreement with observations at these redshifts. When evolved to $z = 0$, simulations with the same physics have been shown to also reproduce many other observed galaxy properties (Hopkins et al. 2017, and references therein).

The paper is organized as follows. In Section 8.2, we describe the simulations briefly and the methods we use to measure galaxy sizes. We present the results in Section 8.3 and discuss their implications to observations in Section 8.4. We conclude in Section 8.5. We adopt a standard flat ΛCDM cosmology with *Planck* 2015 cosmological parameters $H_0 = 68 \, \mathrm{km \, s^{-1} \, Mpc^{-1}}$, $\Omega_\Lambda = 0.69$, $\Omega_m = 1 - \Omega_\Lambda = 0.31$, $\Omega_b = 0.048$, $\sigma_8 = 0.82$, and $n = 0.97$ (Planck Collaboration et al. 2016). We use a Kroupa (2002) initial mass function (IMF) from 0.1–100 $\mathrm{M_\odot}$, with IMF slopes of -1.30 from 0.1–0.5 $\mathrm{M_\odot}$ and -2.35 from 0.5–100 $\mathrm{M_\odot}$. All magnitudes are in the AB system (Oke & Gunn 1983).

8.2 Methods

8.2.1 The simulations

We use a suite of 15 high-resolution cosmological zoom-in simulations at $z \geq 5$ from the FIRE project, spanning a halo mass range $\mathrm{M_{halo}} = 10^8 - 10^{12} \, \mathrm{M_\odot}$ at $z = 5$. These simulations are first presented in Ma et al. (2017a). The mass resolution for baryonic particles (gas and stars) is $m_b = 100 - 7000 \, \mathrm{M_\odot}$ (more massive galaxies having larger particle mass). The minimum Plummer-equivalent force softening

---

[1]http://fire.northwestern.edu

lengths for gas and star particles are ϵ_b = 0.14–0.42 pc and ϵ_* = 0.7–2.1 pc (see table 1 in Ma et al. 2017a for details). The softening lengths are in comoving units above $z = 9$ but switch to physical units thereafter. All of the simulations are run using exactly identical code GIZMO[2] (Hopkins 2015), in the mesh-less finite-mass (MFM) mode with the identical FIRE-2 implementation of star formation and stellar feedback.

The baryonic physics included in FIRE-2 simulations are described in Hopkins et al. (2017), but we briefly review them here. Gas follows an ionized-atomic-molecular cooling curve from 10–10^{10} K, including metallicity-dependent fine-structure and molecular cooling at low temperatures and high-temperature metal-line cooling for 11 separately tracked species (H, He, C, N, O, Ne, Mg, Si, S, Ca, and Fe). At each timestep, the ionization states and cooling rates H and He are calculated following Katz et al. (1996), with the updated recombination rates from Verner & Ferland (1996), and cooling rates from heavier elements are computed from a compilation of CLOUDY runs (Ferland et al. 2013), applying a uniform but redshift-dependent photo-ionizing background from Faucher-Giguère et al. (2009), and an approximate model for H II regions generated by local sources. Gas self-shielding is accounted for with a local Jeans-length approximation. We do not include a primordial chemistry network nor Pop III star formation, but apply a metallicity floor of $Z = 10^{-4}\, Z_\odot$.

We follow the star formation criteria in Hopkins et al. (2013b) and allow star formation to take place only in dense, molecular, and locally self-gravitating regions with hydrogen number density above a threshold n_{th} = 1000 cm^{-3}. Stars form at 100% efficiency per local free-fall time when the gas meets these criteria, and there is no star formation elsewhere. The galactic-scale star formation efficiency is regulated by feedback to $\sim$ 1% (e.g. Orr et al. 2017). The simulations include the following stellar feedback mechanisms: (1) local and long-range momentum flux from radiation pressure, (2) SNe, (3) stellar winds, and (4) photo-ionization and photo-electric heating. Every star particle is treated as a single stellar population with known mass, age, and metallicity. The energy, momentum, mass, and metal returns from each stellar feedback processes are directly calculated from STARBURST99 (Leitherer et al. 1999).
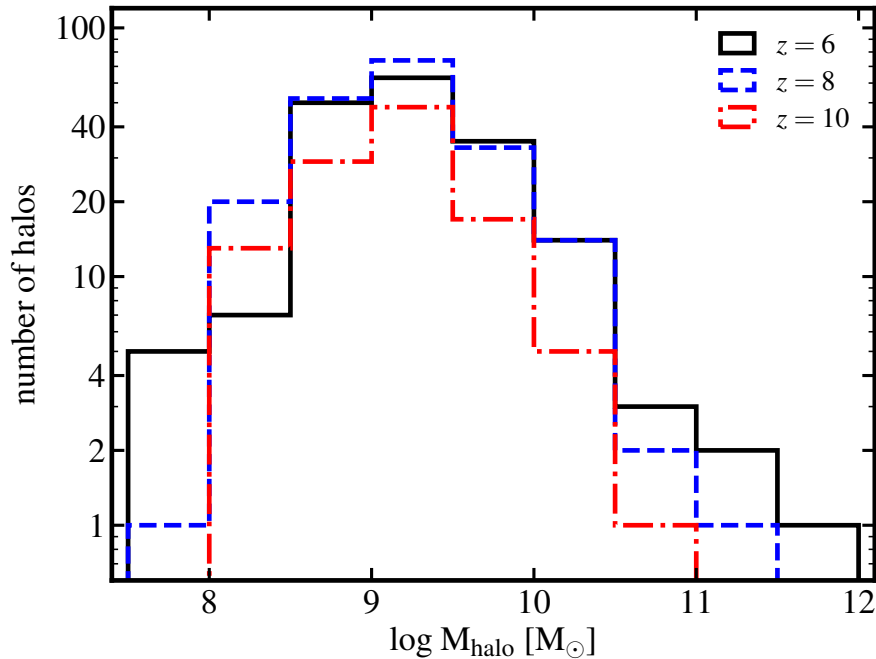
---

[2]http://www.tapir.caltech.edu/~phopkins/Site/GIZMO.html

Figure 8.1: Number of halos in our sample at $z = 6$, 8, and 10.

8.2.2 Post-processing and size definition

We use Amiga Halo Finder (AHF; Knollmann & Knebe 2009) to identify halos in our simulations. The halo mass (M_{halo}) and virial radius (R_{vir}) are computed by AHF, applying the redshift-dependent virial overdensity criterion from Bryan & Norman (1998). Each zoom-in simulation contains one central halo, which is the most massive halo of the zoom-in region. In this work, we also consider other less massive halos in the zoom-in region. We restrict our analysis to halos with zero contamination from low-resolution particles, which also having more than 100 star particles and 10^4 total particles within the virial radius. In Figure 8.1, we show the number of halos in our simulated sample at $z = 6$, 8, and 10. At a given mass, our sample includes both central halos and less massive halos in the zoom-in regions, and include simulations run with different mass resolutions. In Appendix 8.5, we show that our results converge reasonably well with resolution.

At a given redshift, we project all star particles inside the halo along a random direction onto a two-dimensional uniform grid. The pixel size of the grid is 0.0032 arcsec (3.2 mas), which equals to 1/10 of the pixel size of *JWST*'s Near-Infrared Camera (NIRCam) and corresponds to 10–20 pc in the redshift range of our interest. Each star particle is smoothed over a cubic spline kernel with a smoothing length $h = 1.5 h_n$, where h_n is its distance to the nth nearest neighbor star particle. We

adopt $n = 5$ as our default value, but varying $n = 5$–10 only makes small difference for a small fraction of our galaxies. We only consider intrinsic morphologies and sizes and do not include dust extinction in this work. The majority of galaxies (over 95%) in our sample have intrinsic UV magnitude fainter than $M_{UV} = -18$ (stellar mass $M_* < 10^8 \, M_\odot$). We find that dust attenuation has little effect on these low-mass, faint galaxies (also see Ma et al. 2017a), so most results in this paper are not affected by dust extinction.

We make projected images for stellar surface density and rest-frame UV (1500 Å) and rest-frame B-band (4300 Å) surface brightness. The rest-frame UV of galaxies at these redshifts falls in the short-wavelength channel of NIRCam (observed wavelengths 0.6–2.3 μm, spatial resolution 0.032" per pixel), in F090W band for $z = 5$ galaxies and F150W band for $z = 10$ galaxies. The rest-frame B-band falls in NIRCam's long-wavelength channel (2.4–5 μm, spatial resolution 0.065" per pixel), in F277W band for $z = 5$ galaxies and F444W band for $z = 10$ galaxies. The SED of each star particle is computed using the synthesis spectra predicted by the Binary Population and Spectral Synthesis (BPASS) models (version 2.0; Eldridge et al. 2008)[3]. We use the binary stellar population models in BPASS by default[4]. In Figure 8.2, we show example images for six galaxies labeled by A–F. Each panel is 2" (11.6 kpc) on each side. Some galaxies and structures are so small that they only occupy very few pixels, so we further smooth the images using a two-dimensional Gaussian kernel with a dispersion equal to the size of 10 pixels (0.032") only for easier visualization here.

Most galaxies in our sample show clumpy, irregular morphologies that cannot be well described by a simple profile (see also figures 2 and 3 in Ma et al. 2017a; cf. Jiang et al. 2013; Bowler et al. 2017). Therefore, we adopt a non-parametric approach to define galaxy sizes, in a way similar to Curtis-Lake et al. (2016) and Ribeiro et al. (2016). For every galaxy, we place a circular aperture of 1" in diameter, whose center is located by iteratively finding the B-band surface brightness-weighted center of all pixels within the 1"-aperture, as illustrated by the white dotted circles in Figure 8.2. We visually inspect all galaxies to ensure the apertures are reasonably

---

[3] http://bpass.auckland.ac.nz

[4] We prefer binary models to single-star models when calculating SEDs because they are able to reproduce nebular emission line features observed in high-redshift galaxies (e.g. Steidel et al. 2016; Strom et al. 2017). While we use STARBURST99 single-star models for stellar feedback calculations in our simulations, we expect BPASS binary models to give similar results in terms of feedback strengths, as bolometric luminosities and supernova rates are similar between these two models (see section 2.2 in Ma et al. 2017a, for a more detailed discussion).

located. The same aperture is used for the size measurement in stellar mass, UV, and B-band luminosity for the same galaxy as follows. We sort the pixels enclosed in the 1"-diameter aperture in descending order of surface density or surface brightness, and find the number of 'brightest' pixels that contribute 50% of the total mass or luminosity within the 1" aperture. We calculate the area spanned by these pixels S_{50} and define the 'half-mass' or 'half-light' radius as $R_{50} = \sqrt{S_{50}/\pi}$. We quote the galaxy stellar mass and luminosity as the total amount enclosed in the 1"-diameter aperture[5].

One may also measure the half-mass or half-light radius alternatively by finding the radius that encloses half of the mass or light within some larger aperture. This is close to the commonly used algorithms in observations for size measurements, such as SExtractor and galfit (e.g. Oesch et al. 2010), where concentric circular or ellipsoid apertures are usually assumed. However, this approach suffers from two main issues when applying to clumpy, irregular galaxies in our simulations. First, these galaxies do not have a well-defined center: one may use the position of intensity peak on the image or intensity-weighted center and get very different results. Second, for multi-clump systems (e.g. galaxies B, D, E, and F in the rest-frame UV, see Figure 8.2), the size defined in this way in fact represents the spatial separation between the bright clumps. The non-parametric definition we use better reflects the physical size of individual clumps. For single-component objects, such as galaxy A in Figure 8.2 and well-ordered massive galaxies at intermediate and low redshifts, both definitions should give consistent results.

Nonetheless, we note that our size measurement depends on how we smooth the star particles. In general, using a larger smoothing length results in slightly larger galaxy sizes, but the difference is usually small for most of the galaxies. We refer the readers to Appendix 8.5 for details.

8.3 Results

8.3.1 Qualitative behaviors: an overview

In Figure 8.2, we show projected images of stellar mass (left), and noise-free rest-frame UV (middle) and rest-frame B-band (right) luminosity for six galaxies at $z = 6$. These galaxies are selected to have similar UV magnitudes around $M_{UV} \sim -16.5$,

---

[5]We have checked that a 1" aperture is sufficiently large for most galaxies in our sample. The exceptions are a small number of galaxies that are in late stages of merging. In our sample, galaxy F (shown in Figure 8.2) is the object that is most strongly affected: its stellar mass and half-mass radius are underestimated by about 50% because of an ongoing merger.
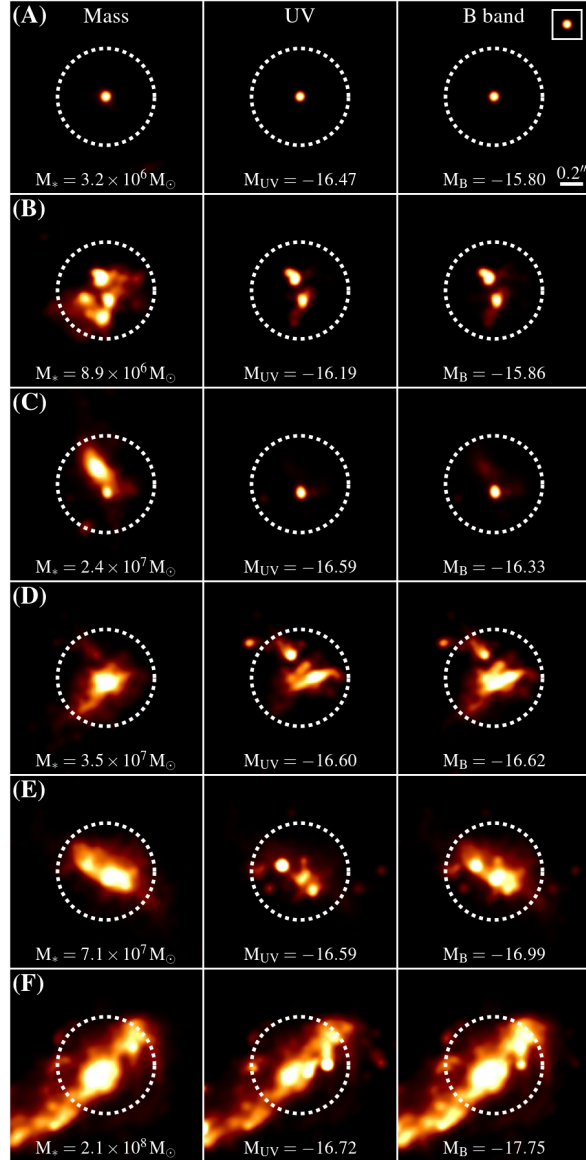
Figure 8.2: Example images for six galaxies (A–F) at $z = 6$ with rest-frame UV magnitude $M_{UV} \sim -16.5$. The left column shows stellar surface density. The middle and right columns show unattenuated, noise-free rest-frame UV and rest-frame B-band surface brightness, respectively. All images are 2" (11.6 kpc) along each side. Colors are in linear scale. These images are smoothed over a Gaussian kernel with 0.032" dispersion (10 pixels on the image) only for visualization purposes (otherwise the structures are too small to visualize on these images). The square in the top-right corner shows the appearance of a point source on these images for reference. The white dotted circles show the 1"-diameter aperture in which the sizes are measured. These galaxies span a wide range of stellar mass and B-band magnitude, and show a variety of morphologies. More massive galaxies appear to be larger than galaxies at lower masses. The UV images are largely dominated by bright, young stellar clumps, which do not necessarily trace the bulk of stars. The B-band light traces stellar mass better than the UV, but it can also be biased by the UV bright clumps. Galaxies tend to be more clumpy, more concentrated, and smaller in size from stellar mass to rest-frame optical to the UV.

in increasing order of stellar mass from the top to the bottom. The images are smoothed for visualization purposes in Figure 8.2. Our default size measurements are performed using the original images. The colors represent surface density or surface brightness in linear scale and they saturate at a level such that pixels above it contribute 10% of the total intensity on the image. The square in the top-right corner shows the appearance of a point source on these images.

Despite all galaxies having $M_{UV} \sim -16.5$, they span two orders of magnitude in stellar mass from $M_* = 3 \times 10^6$–$2 \times 10^8 \, M_\odot$. They show a wide range of morphologies in their surface density maps: galaxy A is compact; galaxies C, E, and F all have a small companion that is close (within 0.2") to the main galaxy; galaxy B is made of several clumps of comparable sizes. High-mass galaxies are generally larger than low-mass galaxies in all bands.

The UV images of these galaxies are largely dominated by one or several bright clumps, where the stellar populations are relatively young (10 Myr on average). Most of the UV clumps are intrinsically small and appear like point sources on these images. More importantly, these bright clumps do not necessarily trace the bulk of stars. In galaxy C, for example, the UV bright clump is associated with the small companion, while the larger, more massive main galaxy is very faint in the UV. In galaxy D, there are two dominant clumps in the UV image: the smaller one to the upper-left to the galaxy is not associated with any prominent stellar structure; the larger one also has a small spatial offset to the right of the stellar surface density peak. We visually inspected every galaxy in our sample and found this phenomenon to be very common in our simulated galaxies (e.g. galaxies E and F). This is consistent with the off-center star-forming UV clumps observed in intermediate-redshift galaxies ($z \sim 0.5$–2.5, e.g. Wuyts et al. 2012), which can contribute a large fraction of star formation but only a small fraction of stellar mass. These clumps are either small satellite galaxies or stars formed in individual star-forming regions (see Section 8.4.4 for more discussion)[6].

In contrast, the B-band light traces stellar mass better than the UV, although it can also be biased by the young, bright stellar clumps in some circumstances. In galaxy E, the UV bright clump associated with the companion upper-left to the central galaxy is also bright in B-band. The central galaxy also appears bright in the B-band, but it is much fainter in the UV, due to an relatively older stellar population

---

[6]Each system enclosed by a 1" aperture is counted as one galaxy in this paper even if it contains multiple clumps, as we deem such clumps to be sufficiently close that they can be classified as one galaxy.

than the UV-bright stellar clump. In galaxy C, the B-band image is dominated by the only bright clump; the main galaxy, however, is faint in the B band, because its stellar population is much older.

In general, galaxy size increases with increasing stellar mass or luminosity, following the size–mass or size–luminosity relation. From stellar mass to rest-frame optical to the UV, galaxies tend to be more clumpy, more concentrated, and smaller in size. Moreover, there is a broad distribution of galaxy UV size at fixed UV magnitude. Galaxies A–C have intrinsically small UV sizes, because nearly all of the UV light is emitted by the bright clumps. In contrast, in galaxies D–F, the more extended, low surface brightness pixels contribute a large fraction of the total UV luminosity, so they have larger half-light radius in the UV. However, we caution that low surface brightness regions may fall below the detection limit of a given observational campaign, so the observed half-light radius is consequently smaller if the imaging decreases in depth (Section 8.4.1). A better way to compare our simulations with observations is to add the background noise of an observing campaign and process the simulations with an identical pipeline for size measurement on the mock images. This is beyond the scope of the current paper, but it is worth exploring in the future.

8.3.2 Size–mass and size–luminosity relations

In Figure 8.3, we show the galaxy size–mass relation (left) and size–luminosity relation in the UV (middle) and B band (right) for our simulated sample. The points represent galaxies at $z = 6$ (black circles), 8 (blue squares), and 10 (red diamonds). We follow Bouwens et al. (2017b) and express the sizes in arcsec in this section. At any redshift, there is a correlation between galaxy size and stellar mass and/or luminosity with considerable scatter. At $M_* < 10^8 \, M_\odot$, the half-mass radius spans a factor of 3 (0.5 dex) at fixed stellar mass. The scatter is likely driven by several different effects, including halo-to-halo variance, and dynamical effects connected to mergers and strong stellar feedback (El-Badry et al. 2016), and mergers. The size–luminosity relations show larger scatter: at $M_{UV} > -18$ and $M_B > -18$, the half-light radii spans nearly one dex at fixed magnitude. Most simulated galaxies have half-light radii within 0.01–0.2", while some galaxies have even smaller half-light radii down to 0.005". In contrast, very few galaxies have half-mass radii smaller than 0.02", suggesting that galaxies with extremely small UV sizes should be larger in terms of stellar mass. This is because the bright clumps that dominate the light in these galaxies are very concentrated. At the more massive/brighter end, our simulations do not contain sufficient number of galaxies for a robust estimate
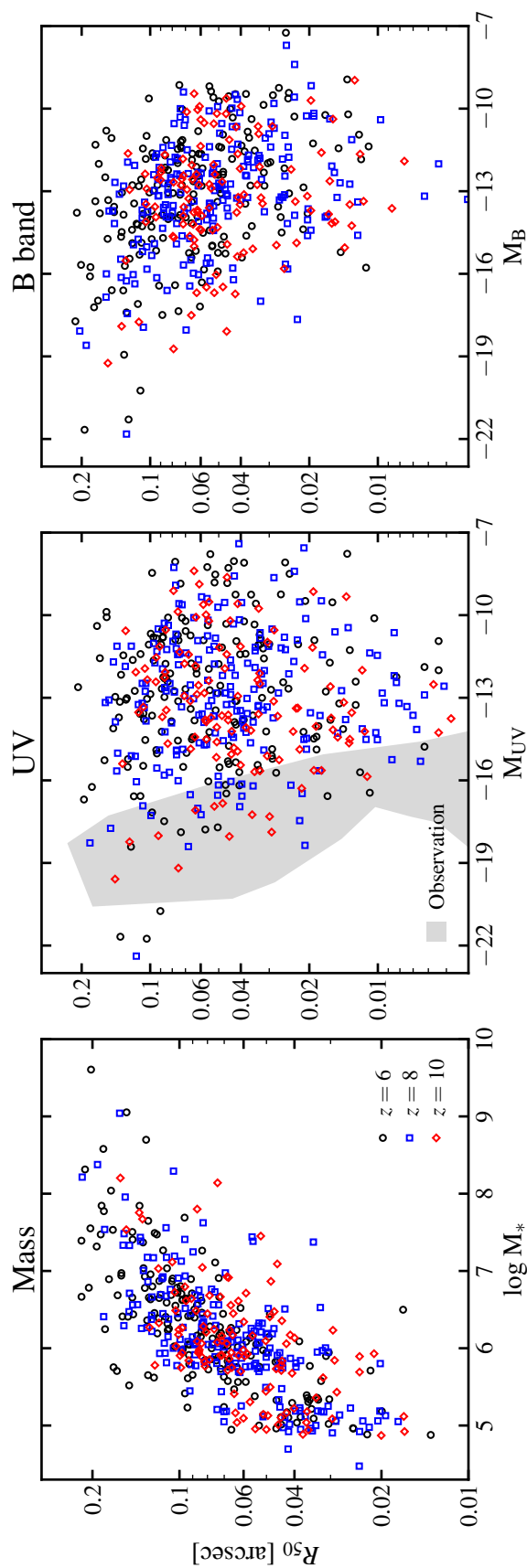
Figure 8.3: Size–stellar mass relation (left) and size–luminosity relation in the rest-frame UV (middle) and rest-frame B band (right) at $z = 6$ (black circles), 8 (blue squares) and 10 (red diamonds). At any redshift, the sizes of galaxies increase with stellar mass and/or luminosity, but all relations have considerable scatter. There is also a weak redshift evolution of galaxy sizes: high-redshift galaxies tend to have smaller sizes than low-redshift galaxies. The grey shaded region shows observational measurements from Ono et al. (2013), Kawamata et al. (2015), and Bouwens et al. (2017b), adopted from the compilation in Bouwens et al. 2017b (see Section 8.3.2 for a more detailed discussion).

of the scatter. In addition, there is a weak redshift evolution of galaxy sizes: the median angular size of galaxies decreases by 25% (physical size by a factor of two) from $z = 6$ to $z = 10$ at a fixed stellar mass and/or magnitude. This is much smaller than the intrinsic scatter of the size–mass and size–luminosity relations (see Section 8.3.3 for quantitative results).

The grey shaded region in Figure 8.3 shows the observational data taken from the compilation in Bouwens et al. (2017b) (also including the data from Ono et al. 2013 and Kawamata et al. 2015). Kawamata et al. (2015) measured the sizes of 31 lensed galaxies at $z = 6$–8 in the Abell 2744 cluster field from the HFF. The half-light radii of galaxies at $M_{UV} \sim -19.5$ in their $z \sim 6$–7 sample range from 0.1–1 kpc, corresponding to 0.02–0.2" at these redshifts. Similarly, Bouwens et al. (2017b) also found a similar range of half-light radius from 0.02–0.2" for galaxies with $M_{UV} \sim -18.5$ at $z \sim 6$ in a more complete HFF sample. Ono et al. (2013) found that $z \sim 7$–8 galaxies of $M_{UV} \sim -19$ in the HUDF also have half-light radii from 0.02–0.2" with a median of about 0.06". Brighter galaxies at $M_{UV} \sim -21$ in the HUDF have half-light radii about 0.15" at $z \sim 5$–8 (e.g. Bouwens et al. 2004; Oesch et al. 2010). The most massive galaxies in our sample broadly agree with these measurements.

So far, only a small sample of galaxies fainter than $M_{UV} \sim -18$ from the HFF have size measurements (Kawamata et al. 2015; Bouwens et al. 2017b). These galaxies are reported to have very small intrinsic sizes from 0.01–0.06", and a small fraction of them even have half-light radii down to 0.001". Some of our simulated galaxies fall in the observed range, but our sample also contains a large number of galaxies that have much larger sizes (they tend to lie above the grey shaded region at a given magnitude in Figure 8.3). We speculate two possible observational biases/uncertainties that may lead to such discrepancies. First, at fixed magnitude, larger galaxies tend to have lower surface brightness, so they are more likely to be missed in the observed sample. Second, for clumpy galaxies, one may only pick up the brightest clumps and thus the sizes are underestimated. Therefore, observations are likely biased toward intrinsically small galaxies and/or star-forming clumps (e.g. Vanzella et al. 2017). In Section 8.4.1, we will explicitly show the effect of limited surface brightness sensitivity on the observed galaxy sizes. Future deep observations on a few candidate clumpy galaxies with *JWST* can test our predictions. On the other hand, we note that our size measurements are different from those commonly used in observations (see Section 8.2.2 for a detailed discussion), which further complicates
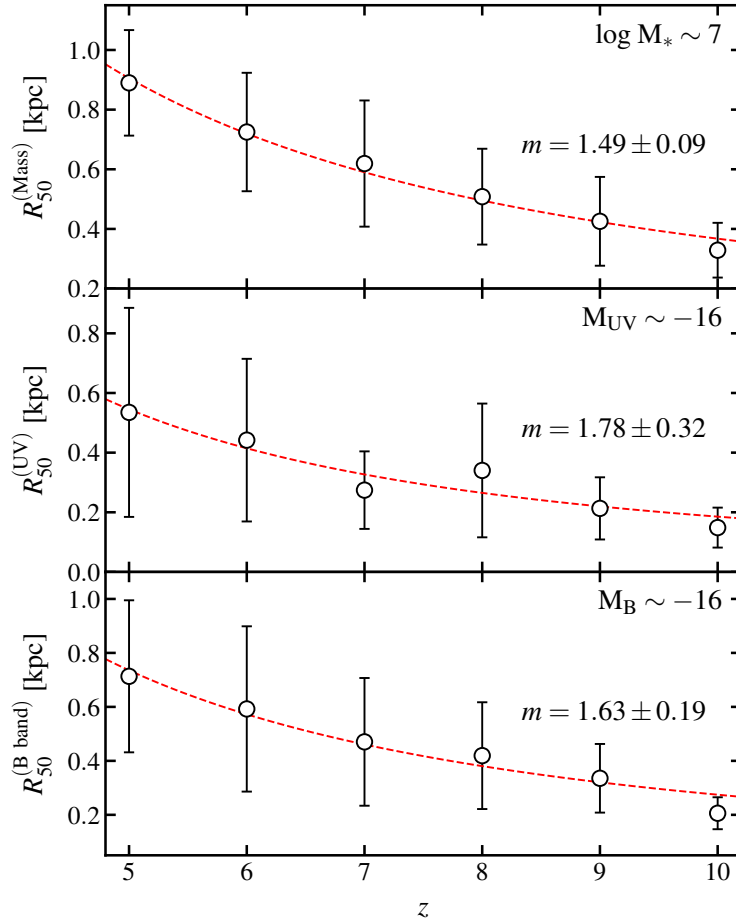
Figure 8.4: Size evolution of the simulated galaxies at $M_* \sim 10^7 \, M_\odot$ (top), $M_{UV} \sim -16$ (middle), and $M_B \sim -16$ (bottom). Points with errorbars show the mean and 1σ (16–84%) distribution of physical half-light radii (in kpc) at $z = 5$–10. The red lines show the best-fit evolution following $R_{50} \sim (1 + z)^{-m}$. The best-fit parameters are also listed in Table 8.1.

the comparison. It would be interesting to carry out more detailed comparisons with specific observational campaigns to understand the discrepancies.

8.3.3 Size evolution

In this section, we quantify the redshift evolution of galaxy sizes using the simulated sample at $z = 5$–10. At each redshift, we bin our data in stellar mass every $\Delta \log M_* = 1$ and/or in magnitude every 2 mag. In each bin, we calculate the mean and 1σ distribution (14–86 percentile) of galaxy half-mass and/or half-light radii. In Figure 8.4, we show the results at $M_* \sim 10^7 \, M_\odot$ (top), $M_{UV} \sim -16$ (middle), and $M_B \sim -16$ (bottom) (same stellar mass/magnitude at all redshifts). Note that we show the physical sizes (in kpc) instead of angular sizes (in arcsec). We fit the

evolution trend with a functional form $R_{50} \sim (1 + z)^{-m}$. The red dashed lines in Figure 8.4 show the best-fit results at these bins. In Table 8.1, we list all the best-fit parameters from $M_* \sim 10^5$–$10^8 \, M_\odot$, $-18 < M_{UV} < -12$, and $-18 < M_B < -12$. It is worth noting that the evolution of the physical sizes has power-law index $m \sim 1$–2, which is steeper than the redshift dependence of the angular diameter distance $[D_A \sim (1 + z)^{2/3}]$. This indicates that the angular sizes of galaxies also decrease with redshift, as shown in Figure 8.3.

There are some observational constraints on the size evolution. Various authors have reported $m \sim 1$–1.5 for galaxies brighter than $M_{UV} < -19$ across $z \sim 0$–8 (e.g. Bouwens et al. 2004; Oesch et al. 2010; Kawamata et al. 2015; Shibuya et al. 2015). Our results show broad agreement with these constraints (within 1σ for most mass and magnitude bins), although we mainly study galaxies at lower masses and luminosities than the observed sample, and only focus on $z \geq 5$. We note that the best-fit value of m is sensitive to the data and their uncertainties. For several stellar mass and magnitude bins, our sample only contains a small number of galaxies at some redshift. Stochastic effects in bins with small numbers of objects can strongly affect the results of fitting in those bins.

In Figure 8.5, we show the distribution of $R_{50}^{(\mathrm{Mass})}/R_{\mathrm{vir}}$ for our simulated sample at $z = 6$, 8, and 10. We find that for the entire sample, this ratio has a median of 8% and 1σ range from 5–12% (the shaded region in Figure 8.5). The median and dispersion do not strongly evolve with redshift at $z = 5$–10. This is consistent with the fact that $R_{50}^{(\mathrm{Mass})} \sim (1 + z)^{-m}$ with $m \sim 1$ at these masses (see Table 8.1), given a non-evolving stellar mass–halo mass relation at these redshifts (Ma et al. 2017a) and $R_{\mathrm{vir}} \sim (1 + z)^{-1}$ at a fixed halo mass (the virial overdensity is nearly a constant at these redshift; see Bryan & Norman 1998). For the few more massive galaxies in our sample ($M_* > 10^8 \, M_\odot$), this ratio is smaller, mostly at 1–5%: this is comparable to observational measurements for galaxies at similar masses ($\sim 3\%$, e.g. Kawamata et al. 2015; Shibuya et al. 2015). Our simulations thus predict that at these redshifts, the stellar-to-halo size ratio (as defined above) is larger for low-mass galaxies, where there are no observational constraints so far.

Our results at $z \geq 5$ should not be extrapolated to lower redshifts. Recently, Fitts et al. (2017) presented a suite of cosmological zoom-in simulations of isolated dwarf galaxies run to $z = 0$ using the same FIRE-2 code. All of their galaxies are hosted in halos of $M_{\mathrm{halo}} \sim 10^{10} \, M_\odot$ at $z = 0$. Several galaxies in their sample have stellar mass $M_* \sim 10^7 \, M_\odot$: these are all early-forming galaxies with half-mass radii
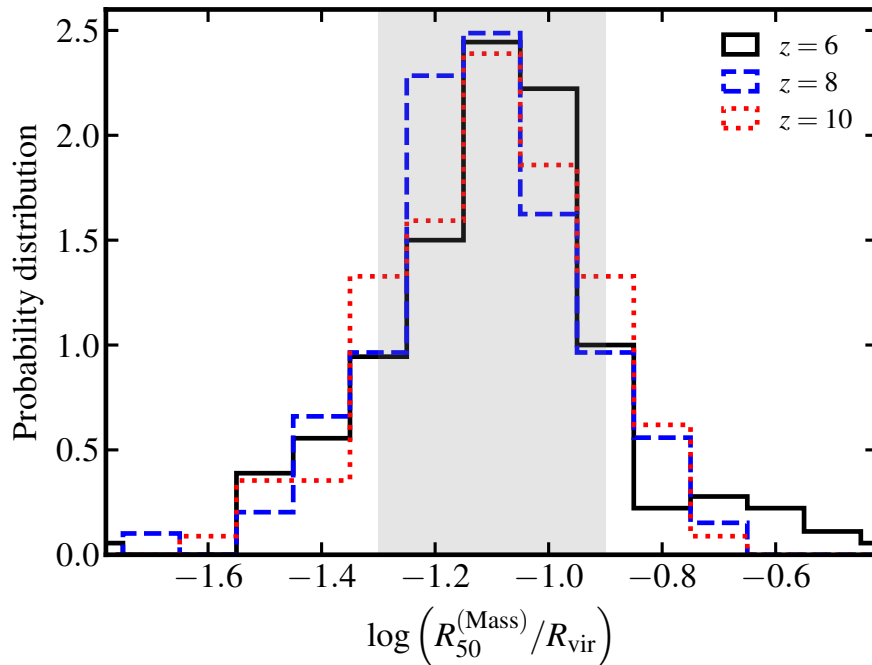
Figure 8.5: Probability distribution (normalized) of the ratio of galaxy half-mass radius to halo virial radius for the simulated sample at $z = 6, 8$, and 10. $R_{50}^{(\mathrm{Mass})}/R_{\mathrm{vir}}$ has a median value of 0.08 and 1σ range of 0.05–0.12 (the shaded region). The distribution does not evolve significantly over the redshift range considered in this figure.

around 1 kpc. This is very close to our $z = 5$ galaxy sizes at the same stellar mass, likely due to the fact that the early-forming galaxies in Fitts et al. (2017) do not grow significantly at later times. Although this is a biased sample, and $M_* \sim 10^7\,M_\odot$ galaxies may have a broad distribution of half-mass radius at $z = 0$, this suggests that the stellar-to-halo size ratio may be much at lower redshifts for low-mass galaxies (since the virial radius increases with decreasing redshift at fixed mass). This could be due, for example, to less efficient halo gas accretion at later times. For more massive galaxies, our simulations show that the stellar-to-halo size ratio at $z \geq 5$ is already comparable to that at $z \sim 0$ ($\sim 2\%$), so it may not evolve strongly at later times (e.g. Shibuya et al. 2015). A mass-dependent evolution of the stellar-to-halo size ratio is consistent with recent analysis for $z \lesssim 3$ galaxies (e.g. Somerville et al. 2018). The galaxy size and morphology evolution down to $z \sim 0$ will be studied in detail in a separate paper (Schmitz et al., in preparation).

Table 8.1: Best-fit parameters of galaxy size evolution.

	Stellar mass			Rest-frame UV			Rest-frame B band	
$\log M_*$ ($M_\odot$)	R_{50} ($z=5$) (kpc)	m	M_{UV} (mag)	R_{50} ($z=5$) (kpc)	m	M_B (mag)	R_{50} ($z=5$) (kpc)	m
8	1.09 ± 0.04	1.15 ± 0.12	-18	0.76 ± 0.08	1.87 ± 0.42	-18	0.99 ± 0.07	1.53 ± 0.25
7	0.91 ± 0.02	1.49 ± 0.09	-16	0.55 ± 0.05	1.78 ± 0.32	-16	0.74 ± 0.04	1.63 ± 0.19
6	0.52 ± 0.02	0.87 ± 0.09	-14	0.49 ± 0.01	1.78 ± 0.06	-14	0.66 ± 0.02	1.92 ± 0.11
5	0.29 ± 0.01	0.84 ± 0.11	-12	0.45 ± 0.02	1.00 ± 0.15	-12	0.46 ± 0.01	1.05 ± 0.09

Note: The size evolution of galaxies at a given stellar mass or magnitude is described as $R_{50} \sim (1 + z)^{-m}$ (see Section 8.3.3 for details). R_{50} ($z = 5$) gives the best-fit normalization at $z = 5$.

8.3.4 Galaxy sizes at different bands

In Section 8.3.1, we show examples of our simulated galaxies to illustrate that galaxies tend to be more concentrated and smaller from stellar mass to B band to the UV. The UV light is dominated by small, bright, young stellar clumps, while the B-band morphology is determined by both bright clumps and more broadly distributed stars. In Figure 8.6, we compare the half-mass (light) radii measured in one quantity against another. The green dashed lines show the $y = x$ relation. All three sizes correlate with each other, but $R_{50}^{(B\ band)}$ is systematically larger than $R_{50}^{(UV)}$, and the $R_{50}^{(Mass)}$ is larger than both $R_{50}^{(UV)}$ and $R_{50}^{(B\ band)}$. We also check the Gini coefficient (e.g. Lotz et al. 2004), which is a parameter between 0 and 1 that describes the concentration of galaxy morphology (1 being the most concentrated). We find that the Gini coefficient increases from stellar mass to B band to the UV, in line with the decreasing galaxy sizes in the sequence.

The correlation between $R_{50}^{(Mass)}$ and $R_{50}^{(UV)}$ has a larger scatter than that between $R_{50}^{(Mass)}$ and $R_{50}^{(B\ band)}$, indicating that rest-frame UV light is a relatively worse tracer of stellar mass than the B band. Furthermore, galaxies with intrinsically small UV sizes (below 0.01") mostly have small B-band sizes (below 0.02") as well, although these galaxies usually have relatively large half-mass radii (0.04–0.1"). This is because the B-band light is also biased by the small, bright clumps with high light-to-mass ratios in these galaxies (e.g. galaxy C in Figure 8.2).

8.4 Discussion

8.4.1 How do surface brightness limits affect observed galaxy sizes?

In some galaxies, a large fraction of the total UV luminosity is contributed in low surface brightness, diffuse light (pixels). These regions are dominated by relatively older stars (10–100 Myr) with lower light-to-mass ratios than those in the young, bright clumps (e.g. galaxies D–F in Figure 8.2). For a specific observing campaign, there is a surface brightness limit below which the signal-to-noise ratio is too low to be detectable: this can have a significant effect on the observed morphologies and size measurements of clump-dominated galaxies. In the top panel of Figure 8.7, we illustrate this effect using example galaxies D and F from Figure 8.2 at $z = 6$. We show the rest-frame UV half-light radii measured for the same galaxies as a function of surface brightness limit (assuming pixels below such limit have zero flux). The effect can be dramatic in some circumstances: for galaxy F, the 'observed' half-light radius decreases by over an order of magnitude (from 0.1" to 0.01") if the surface brightness depth drops from 29 to 28 mag arcsec^{-2}. In the
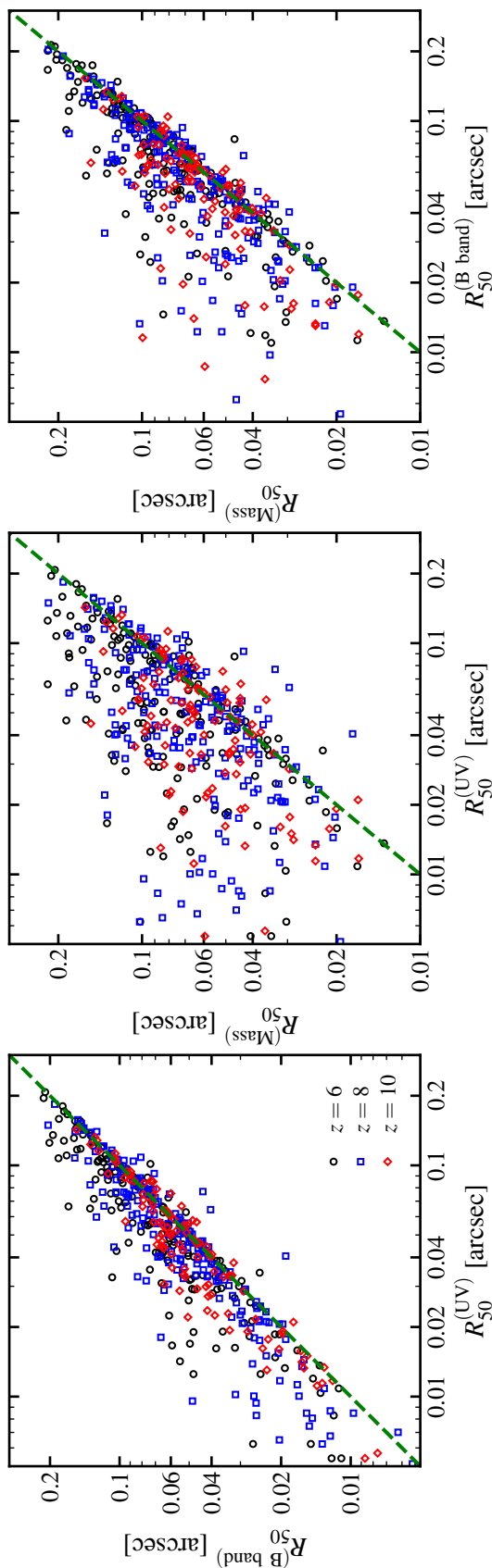
Figure 8.6: The comparison of galaxy sizes measured in stellar mass, rest-frame UV, and rest-frame B band. The half-mass (light) radii systematically decrease from stellar mass to B band to the UV, in line with a more concentrated morphology in this sequence. The $R_{50}^{(Mass)}$–$R_{50}^{(UV)}$ relation shows larger scatter than the $R_{50}^{(Mass)}$–$R_{50}^{(B\ band)}$ relation, suggesting the UV light is a relatively worse tracer of the stellar mass distribution. Galaxies with small UV sizes are also small in B band, but they usually have much larger half-mass radii, because the B-band light is biased by the bright clumps in these galaxies.

bottom panel of Figure 8.7, we further show the rest-frame UV images of galaxies D and F at three surface brightness limits. From $\mu_{\min} = 31.5$ to $28.5\,\mathrm{mag\,arcsec}^{-2}$, most of the low-surface-brightness regions become 'invisible', and the galaxy is dominated by a few clumps in the UV. Once the detection limit further drops to $\mu_{\min} = 25.5\,\mathrm{mag\,arcsec}^{-2}$, only the intrinsically small, brightest clump is dominant in these galaxies as a point source.

Now we discuss the implications of this effect on the size–luminosity relation and extremely small sizes measured for galaxies in the HFF. The typical 5σ point-source detection limit in the rest-frame UV of $z = 5$–10 galaxies is ~ 28.7–29.1 mag within a 0.4"-diameter aperture (Coe et al. 2015). This corresponds to a surface brightness limit about $\mu_{\min} \sim 26.5\,\mathrm{mag\,arcsec}^{-2}$ for extended sources if we demand the same signal-to-noise ratio within the same aperture. As a proof of concept, we perform a simple experiment on our simulated galaxies to mimic the HFF detection limit: we zero out all pixels below $26.5\,\mathrm{mag\,arcsec}^{-2}$ and re-measure the luminosities and sizes. We find that *all* galaxies intrinsically brighter than $M_{\rm UV} < -13$ are still detectable, but their 'observed' luminosities and sizes become smaller. *No* galaxies intrinsically fainter than $M_{\rm UV} > -12$ are detectable. Approximately, the fraction of light *lost* due to such surface brightness cut is a linear function of intrinsic UV magnitude, from zero at $M_{\rm UV} = -22$ to unity at $M_{\rm UV} = -12$. In Figure 8.8, we show the 'observed' size–luminosity relation in the rest-frame UV for our simulated sample. The intrinsic size–luminosity relation for the same galaxies is shown by grey points for reference (non-detectable galaxies are not shown). Most galaxies appear fainter and have much smaller 'observed' sizes. When taking into account surface brightness limits, our simulations broadly follow a $R_{50} \sim L^{0.5}$ relation (the black dashed line), as suggested in Bouwens et al. (2017b) for HFF galaxies, but this trend is affected by the $L/R^2 \sim$ constant selection for a given surface brightness limit. Nonetheless, our simple experiment is by no means a one-to-one comparison with HFF observations. Ideally, one should post-process the high-resolution images of simulated galaxies with gravitational lensing, convolve them with HST PSF, add comparable background noise, run identical source finder, and measure the luminosities and sizes using the same method (e.g. Price et al. 2017). This is beyond the scope of this paper, but is worth future exploration in parallel with JWST deep surveys.
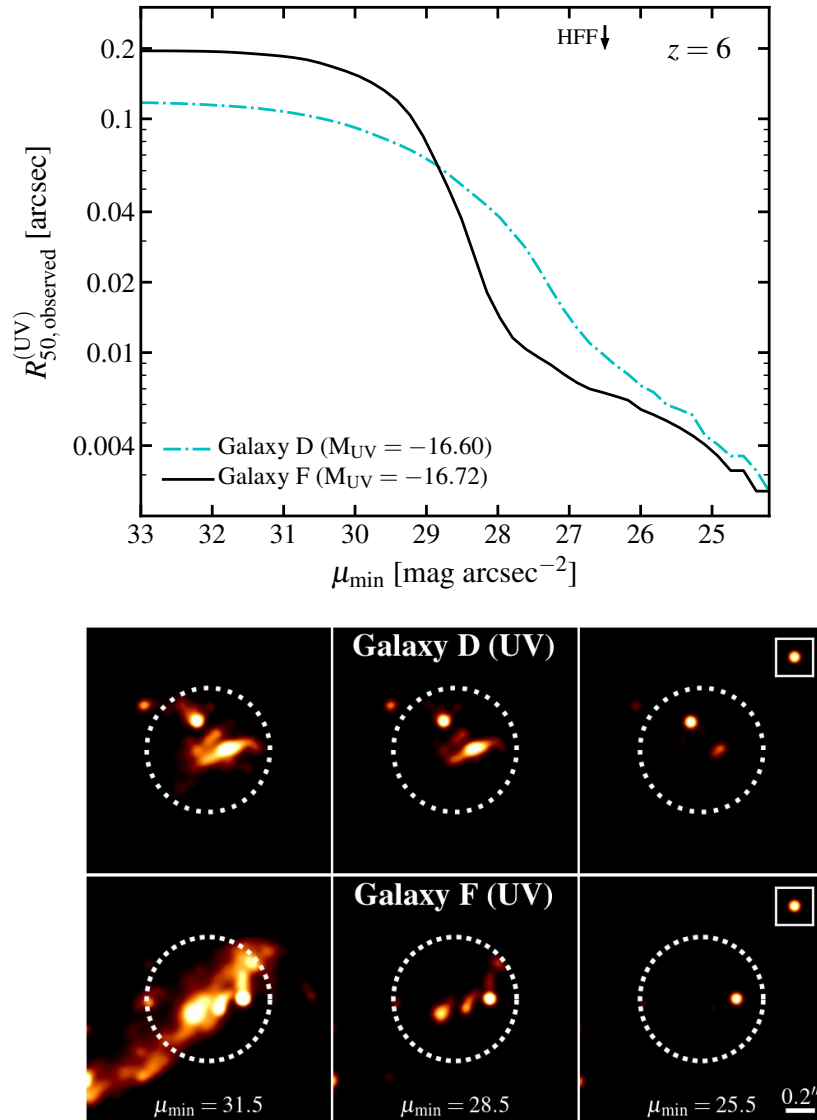
Figure 8.7: *Top:* Galaxy UV half-light radii measured assuming different surface brightness detection limits for galaxies D and F from Figure 8.2. The 'observed' size increases with the depth of imaging. *Bottom:* Appearance of galaxies D and F (Figure 8.2) at different rest-frame UV surface brightness limits. At a detection limit of $\mu_{\min} = 25.5 \, \text{mag} \, \text{arcsec}^{-2}$, the galaxies appear as point sources, and only the brightest clump is dominant.

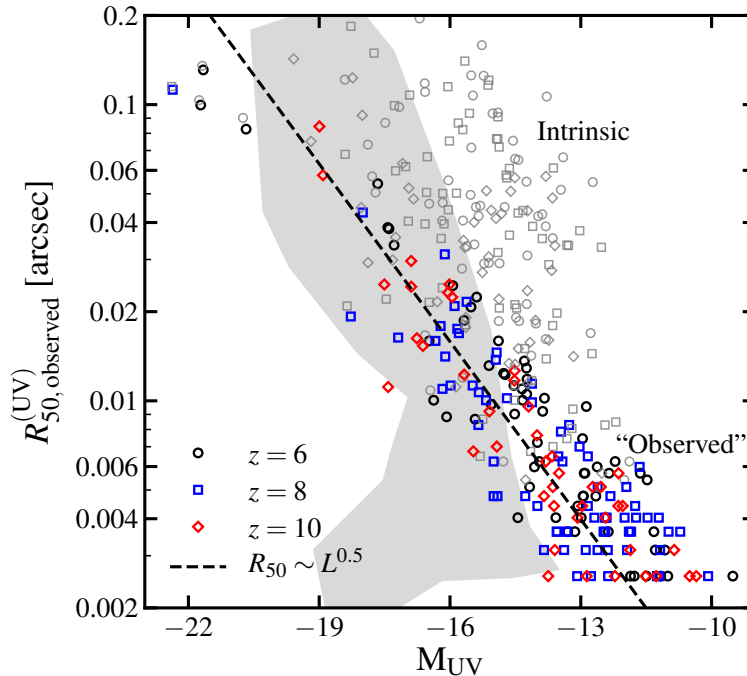Figure 8.8: The 'observed' rest-frame UV size–luminosity relation for our simulated sample after mimicking the effect of the HFF surface brightness detection limit at $\mu_{\rm min} \sim 26.5\,{\rm mag\,arcsec}^{-2}$. The grey shaded region represents the observational data as in Figure 8.3. The grey points show the intrinsic size–luminosity relation for the same galaxies (non-detectable galaxies are not shown). Most galaxies appear fainter and show much smaller 'observed' sizes. The black dashed line shows the $R_{50} \sim L^{0.5}$ scaling as suggested in Bouwens et al. (2017b) for HFF galaxies; however, such scaling is expected due to the selection effect of a surface brightness-limited sample (L/R^2 is constant).

8.4.2 Implications for the observed (faint-end) galaxy UV luminosity functions

Current observational constraints on the $z \gtrsim 6$ galaxy UV luminosity functions fainter than $M_{\rm UV} \sim -17$ come from the HFF program, which takes advantages of foreground galaxy clusters to detect strongly gravitationally lensed high-redshift galaxies. Our results in this paper have two important implications for these observations. First, our simulations show a broad distribution of galaxy sizes at fixed UV magnitude. This affects the estimated completeness correction for the observed sample: if there are more galaxies that have large sizes than expected (they cannot be detected due to low surface brightness), their number densities may be underestimated (Bouwens et al. 2017b). Second, some galaxies are dominated by a few small, bright clumps in the rest-frame UV, so they can be mis-identified as several fainter galaxies. If this is the case, the UV luminosity function can be underestimated at intermediate magnitudes, but overestimated at fainter magnitudes. It is interesting
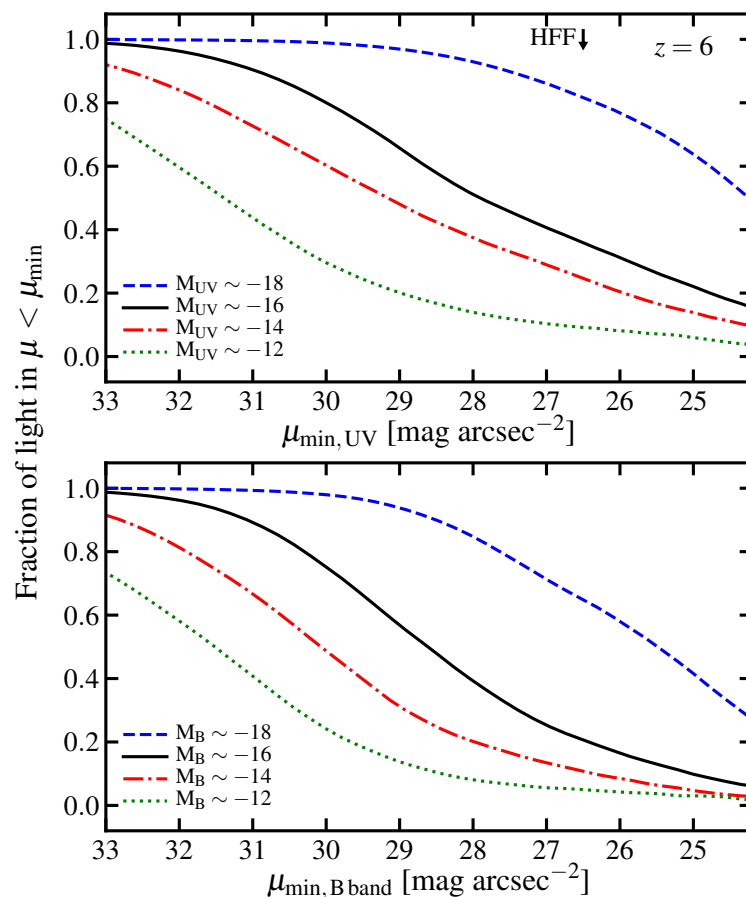
Figure 8.9: The fraction of light in pixels brighter than $\mu < \mu_{\min}$ as a function of $\mu_{\min}$, averaged over the simulated galaxies at a given intrinsic magnitude (total luminosity) in the rest-frame UV (top) and B band (bottom) at $z = 6$. These results provide predictions on what depths one needs to reach to target galaxies at a certain magnitude.

that some faint-end UV luminosity functions derived from HFF samples show a small discontinuity at the magnitude where this effect is likely to become important (although it may also be caused by other effects, e.g. Bouwens et al. 2017c; Livermore et al. 2017). A more quantitative analysis of the observational biases is worth future investigation.

8.4.3 What fraction of light come from low surface brightness regions?

In this section, we attempt to address the following question: for a given surface brightness limit, what fraction of a galaxy's light will be detected or missed? This is useful for planning future JWST deep surveys or follow-up deep imaging and understanding the completeness of an observed sample. In Figure 8.9, we show

the fraction of light in pixels brighter than $\mu < \mu_{\text{min}}$ as a function of μ_{min} for our simulated galaxies in the rest-frame UV (top) and B band (bottom) at $z = 6$. We show the results for galaxies at several intrinsic magnitudes in $-18 < M_{\text{UV}} < -12$ and $-18 < M_{\text{B}} < -12$ (averaged over all simulated galaxies at a given magnitude in our sample). Our calculation indicates that at the limits of HFF (26.5 mag arcsec^{-2}) and HUDF ($\sim$ 1 mag deeper than HFF), more than 80–90% of the rest-frame UV light from galaxies brighter than $M_{\text{UV}} < -18$ should be detected, but this fraction is much smaller for fainter galaxies. In the rest-frame B band, a larger fraction of the light is in low surface brightness regions, as expected from the fact that B-band light is more spatially extended than the UV. Figure 8.9 provides information on what depths the observations need to reach for certain targets, although in practice one also needs to account for the PSF of the observational facilities for quantitative comparison.

8.4.4   The nature of UV-bright clumps

Our simulations suggest that $z \geq 5$ galaxies are mostly irregular, with rest-frame UV images dominated by a few bright clumps. These clumps mainly have two different origins: some of them are satellite galaxies falling on to their host (e.g. galaxy C in Figure 8.2), while others are groups of young stars formed collectively from a parent cloud, i.e. massive giant molecular cloud-like complexes (galaxies D and F). The latter is similar to the clumps formed in gas-rich disks via disk instabilities in intermediate-redshift massive galaxies in simulations (e.g. Hopkins et al. 2012b; Genel et al. 2012; Moody et al. 2014; Oklopčić et al. 2017; Mandelker et al. 2017) and observations (e.g. Guo et al. 2015). These high-redshift galaxies are gas-rich and highly turbulent, in part due to rapid accretion from the intergalactic medium. The high degree of turbulent support causes the gas to fragment into large clumps, which subsequently form stars. These early galaxies often do not have well-defined, rotationally supported disks..

The two formation channels mentioned above are essentially the same as the *ex-situ* and *in-situ* clumps defined in Mandelker et al. (2017). Many clumps formed '*in-situ*' are dynamically short-lived (as seen at intermediate-redshift galaxies in Oklopčić et al. 2017). For example, the brightest clump in galaxy F (also see the top-right panel in Figure 8.7) contains a mass of $2 \times 10^5 \, M_\odot$ in stars within 100 pc (central surface density $\sim 50 \, M_\odot \, \text{pc}^{-2}$) that are formed simultaneously 6 Myr ago; the clump is unbound with a virial parameter $\alpha_{\text{vir}} \sim 2E_{\text{k}}/|E_{\text{p}}| \sim 10$, and it will be dispersed to ~ 500 pc in size within ~ 30 Myr. However, these simulations also

form long-lived bound stellar clumps that survive more than 400 Myr, after which the present simulations end. Some of these stellar clumps might survive and evolved into present-day globular clusters (Kim et al. 2018). Bound cluster are more likely to form once the initial gas surface density exceeds $\sim 500\,\mathrm{M_\odot}\,\mathrm{pc}^{-2}$ (also see Grudić et al. 2016).

Finally, we caution that these UV-bright clumps are observationally 'short-lived': they become much fainter after 30 Myr as the light-to-mass ratio decreases by more than a factor of 10 following stellar evolution and the loss of massive stars. Even the dynamically long-lived clumps are difficult to identify at later times if they only contribute a small fraction of the total stellar mass. Consequently, the rest-frame UV morphology and size of a galaxy can vary greatly on $\sim 30\,\mathrm{Myr}$ time-scale due to stellar evolution, even if the stellar mass morphology and size do not change dramatically.

8.5   Conclusions

In this paper, we use high-resolution FIRE-2 cosmological zoom-in simulations to predict galaxy morphologies and sizes during the epoch of reionization. We project the star particles onto a two-dimensional grid to make stellar surface density and UV and B-band surface brightness images, and measure the half-mass and half-light radii in UV and B band for our simulated galaxies at $z = 5$–10. Our main findings are as follows:

(i) The simulated galaxies show a variety of morphologies at similar magnitude and/or stellar mass, from compact galaxies to clumpy, multi-component galaxies to irregular galaxies. The rest-frame UV images are dominated by a few bright, small young stellar clumps that are often not always associated with a large stellar mass. The rest-frame B-band images are determined both by the bulk of stars and by the bright clumps (Section 8.3.1 and Figure 8.2).

(ii) At any redshift, there is a correlation between galaxy size and stellar mass/luminosity with large scatter. At fixed stellar mass, the half-mass radius spans over a factor of 5, while at fixed magnitude, the half-light radius (both UV and B band) spans over a factor of 20 from less than 0.01" up to 0.2" (Figure 8.3).

(iii) Galaxy morphologies and sizes in our simulations depend on the band in which they are observed. Going from the intrinsic stellar mass distribution to rest-frame B band to rest-frame UV, galaxies appear smaller and more concentrated. (Figure 8.6). The half-mass radii correlate with B-band half-light radii better than those in

the UV, suggesting that B-band light is a better tracer of stellar mass than the UV light, but it can also be strongly biased by the UV bright clumps.

(iv) At $z \geq 5$, the physical sizes of galaxies at fixed stellar mass and/or magnitude decrease with increasing redshift as $(1 + z)^{-m}$ with $m \sim 1$–2 (Figure 8.4). For galaxies below $M_* \sim 10^8 \, M_\odot$, the ratio of the half-mass radius to the halo virial radius is $\sim 10\%$ and does not evolve at $z \sim 5$–10. More massive galaxies have smaller stellar-to-halo size ratios, typically 1–5% (Section 8.3.3).

(v) The observed half-light radius of a galaxy strongly depends on the surface brightness limit of the observational campaign (Figure 8.7). This effect may account for the extremely small galaxy sizes and size–luminosity relation measured in the Hubble Frontier Fields observations (Figure 8.8), as shallower observations can be dominated by single young stellar 'clumps'. We provide the cumulative light distribution of surface brightness for typical $z = 6$ galaxies (Figure 8.9).

In this paper, we make predictions to help understand current and plan future observations of faint galaxies at $z \geq 5$. Our prediction that these galaxies have small, bright clumps on top of more extended, low surface brightness regions can be tested in the near future by high-resolution deep imaging with JWST on a typical sample of galaxies. In future work, we intend to make more realistic comparisons with specific observational campaigns to understand the sample completeness and their implications for the faint-end UV luminosity functions. We will also study the size evolution for a broad range of galaxies from $z = 0$–10 (Schmitz et al., in preparation). Moreover, it is also worth quantifying the statistical and physical properties of the UV-bright clumps in $z \geq 5$ galaxies.

Figure 8.10: Galaxy sizes measured using different smoothing approaches (see text for details). Our default size measurements are reasonably numerically robust to this choice.

Appendix A: Particle smoothing and size measurements

In this work, we adopt a non-parametric approach to define galaxy half-mass (light) radii by measuring the area spanned by the brightest pixels that contribute 50% of the total intensity within an 1"-diameter, S_{50}, and taking $R_{50} = \sqrt{S_{50}/\pi}$ (Section 8.2.2). We note that the results weakly depend on how we smooth the star particles

on the projected images. By default, each star particle is smoothed over a cubic spline kernel with a smoothing length h_5 equal to its distance to the 5$^{\text{th}}$ nearest particle. Here we discuss two alternative smoothing approaches. First, we adopt a smoothing length h_{10} (the distance to the 10$^{\text{th}}$ nearest particle) instead of h_5 (but still use the cubic spline kernel) and repeat the size measurement. In the left panel of Figure 8.10, we compare the new half-mass radii with our default results for our simulated galaxies. The green dashed line shows the $y = x$ relation. By using h_{10}, the half-mass radii only increase by less than 10% for most of the galaxies (5% difference on average), and only a small fraction (1%) of our galaxies are affected by 50% or more.

Alternatively, we further smooth our default images using a two-dimensional Gaussian function with a dispersion corresponding to the size of 10 pixels (0.032"). This equals to the pixel size of the NIRCam on JWST. This is to mimic the observed galaxy images after convolving with the PSF. A point source thus has a half-mass (light) radius of $r_{\text{psf}} = 0.038"$. Note that the example images in Figure 8.2 are generated in this way for better visualization. We repeat the non-parametric size measurement on the Gaussian-smoothed images and compare the results in the right panel of Figure 8.10. The green dashed line shows the $y = \sqrt{x^2 + r_{\text{psf}}^2}$ relation for reference: we note that this relation is also used in observations to convert apparent sizes to intrinsic sizes (e.g. Oesch et al. 2010). Nearly all of our simulated galaxies lie close to this curve (less than 20% deviation) as expected.

These experiments suggest that we obtain numerically stable galaxy half-mass radii by using a cubic spline kernel with smoothing length h_5. We find similar results for half-light radii in UV and B band: using h_{10} instead, the B-band sizes are not affected by more than 10% for the vast majority of our galaxies. The differences are slightly larger for UV sizes. 5% of our galaxies have UV half-light radii increased by a factor of 1.5–2 when using h_{10}. This is because the UV light in these galaxies is dominated by few diffuse star particles that have large inter-particle distance, so the sizes we obtain can only be treated as upper limits. Nonetheless, most galaxies in our sample are only affected by less than 20%. We conclude that our non-parametric size measurement is robust to our particle smoothing method.

Appendix B: Resolution convergence

We note that our sample includes simulations using three different mass resolutions for baryonic particles ($m_b \sim 100$, 900, and 7000 $\text{M}_\odot$). We showed in previous
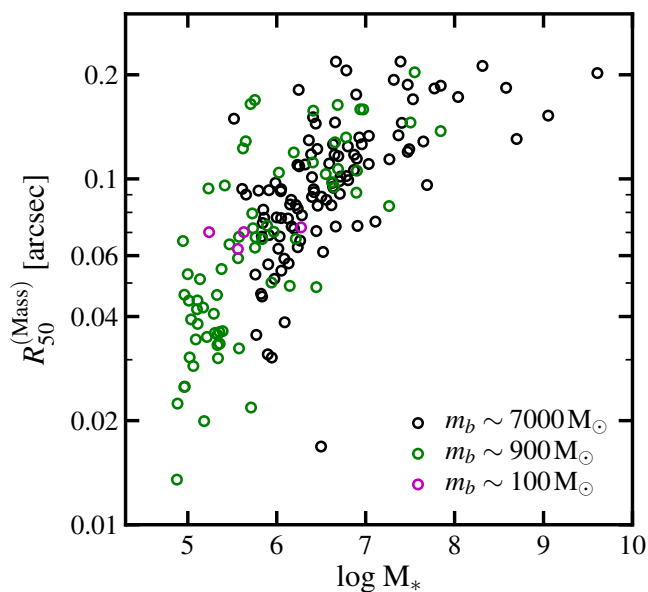
Figure 8.11: The $z = 6$ galaxy size–mass relation. Colors show simulations run with different mass resolution. Galaxy sizes converge reasonably well with resolution in our simulations.

papers that galactic scale quantities, such stellar mass, star formation rates, etc., converge reasonably well at these mass resolutions (e.g. Hopkins et al. 2017; Ma et al. 2017a). Here in Figure 8.11, we show the $z = 6$ galaxy size–mass relation for our simulated sample, where the colors represent simulations run with different mass resolution. There is no significant difference between different resolution levels in the size–mass relation, so we conclude that galaxy sizes are robust with respect to resolution in our simulations.

Chapter 9

SUMMARY AND FUTURE DIRECTIONS

In this thesis, I have investigated several questions in galaxy formation and evolution using the state-of-the-art high-resolution cosmological hydrodynamic zoom-in simulations from the FIRE suite, which includes explicit treatments of the multi-phase ISM, star formation, and stellar feedback. In particular, these simulations capture gas cooling down to 10 K, the formation of GMCs in the ISM, star formation in GMC clumps, photoionization, photo-heating, radiation pressure, stellar winds, and individual SN blastwaves. More importantly, these simulations adopt an accurate 'sub-grid' solution for SN remnants, which accounts for the momentum boost in the energy-conserving phase and injects the 'correct' amount of momentum and energy to the surrounding gas particles. These simulations naturally resolve how feedback launches galactic winds on small scales and how the wind materials propagate and recycle in large-scale galactic fountains, in contrast to low-resolution, large-volume cosmological simulations and SAMs where galactic winds are manually injected on galactic scales at an empirically motivated rate that scales to SFR and halo properties. Therefore, these detailed simulations are powerful tools for understanding the key physics governing galaxy formation and evolution and interpreting the detailed observations of galaxy properties.

The first half of this thesis presents three studies on galactic chemical evolution: (1) the shape and evolution of galaxy MZR, (2) the diversity of gas-phase metallicity gradients observed in intermediate-redshift ($z \sim 2$) galaxies, and (3) the structure, stellar age and metallicity gradients, and formation history of MW-like disk galaxies. Our findings include the following. (1) The FIRE simulations broadly agree with the observed galaxy MZR from $z = 0$–3. The shape of the MZR is largely determined by the relation between metal retention rate (the fraction of metals that still reside in the halo) and halo mass, while the amount of redshift evolution of the MZR is mostly determined by the gas fraction (or star formation efficiency) in the halo at different redshifts. (2) The FIRE simulations can reproduce the observed broad distribution of gas-phase metallicity gradients in intermediate-redshift galaxies. Such a diversity is driven by bursty star formation and feedback cycles in these galaxies. The metallicity gradient, however, only reflects the instantaneous dynamics of a galaxy. (3) There are two phases of star formation in MW-like disk galaxy assembly histories. At high

---

redshift, stars were formed in a chaotic and bursty mode, which eventually evolve to a spheroidal structure by $z = 0$. Since $z \lesssim 1$, a gas disk stabilized and stars formed in the disk thereafter. The gas disk becomes thiner at later times due to lowering gas fraction. Stars that formed earlier in the disk are kinematically heated to a thicker, flaring disk. This formation history naturally leads to the age and stellar metallicity gradients observed in the MW. The so-call 'thick disk' is only a mix of stars formed in different channels, but not an intact physical structure.

The second half of this thesis focuses on three questions on the galaxies at the epoch of reionization: (1) the escape fraction of ionizing photons from galaxies at $z \geq 5$, (2) the galaxy scaling relations, SMFs, and multi-band LFs at $z = 5$–12, and (3) the morphology and size evolution of $z \geq 5$ galaxies. Our main findings are the following. (1) Most ionizing photons are produced by the massive, young stars in the galaxy, which are still embedded in their 'birth clouds'. It takes a few Myr for feedback to clear these clouds before a large fraction of the ionizing photons are able to escape. This effect competes with stellar evolution, which determines the average $f_{\rm esc}$. In canonical stellar population models such as STARBURST99 that only include single-star evolution, the ionizing photon budget decreases very rapidly after 3 Myr, generally yielding a $f_{\rm esc}$ much lower than what is required for cosmic reionization. Binary stellar population models, on the other hand, produce much more ionizing photons at late times and thus lead to a higher $f_{\rm esc}$ than single-star models. (2) By building a new sample of high-resolution cosmological zoom-in simulations that contain thousands of $z \geq 5$ galaxies, we present the stellar mass–halo mass relation, SFR–$M_{\rm halo}$ relation, stellar mass–magnitude relation, SMFs, and multi-band LFs at $z = 5$–12. These predictions agree well with the observed SMF and UVLF at $z \sim 6$. Dust extinction is important in shaping the bright-end UVLFs even at these redshifts. (3) The rest-frame UV light from $z \geq 5$ galaxies is usually dominated by one or a few star-forming clumps that are intrinsically bright and small. Observations with finite surface brightness limits tend to only pick up intrinsically small galaxies or individual clumps but miss more diffuse light in the galaxies. This selection effect is likely to result in the extremely small sizes found for the faint galaxies in the HFFs.

Nonetheless, there are still many open questions in galaxy formation and evolution that demand more detailed theoretical understanding. Some of these questions can be naturally built upon the studies presented in this thesis. Here I briefly review two topics for future research: (1) multi-wavelength spectral modeling of our simulated galaxies at $z \geq 5$ and (2) understanding the formation and growth of SMBHs in the
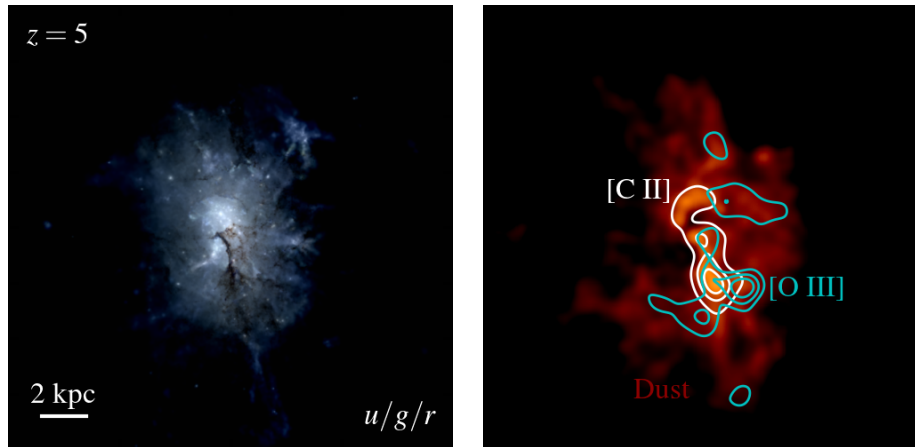
Figure 9.1: *Left*: $u/g/r$ composite image (dust extinction included) of a simulated $M_* \sim 10^{10} M_\odot$ galaxy from Ma et al. (2017a). *Right*: Dust emission (brown), cold gas [C II] emission (white), and ionized gas [O III] emission (cyan) from the same galaxy (for illustration purposes only).

early Universe and their contribution to cosmic reionization.

9.1 Multi-wavelength spectral modeling of $z \geq 5$ galaxies

Once JWST is launched in 2020, it is expected to discover many new galaxies and take thousands spectra of galaxies at the epoch of reionization over the next few years. These galaxy spectra will cover a series of rest-frame UV and optical nebular emission lines that are strong indicators of stellar populations, chemical abundances, and many other physical conditions of $z \geq 5$ galaxies (e.g., Mainali et al. 2017). In principle, these lines can also be able to probe the ionizing photon escape fraction from these galaxies. Spectroscopy observations of local and intermediate-redshift Lyman-continuum (LyC) leaking galaxies have revealed some common features of these LyC-leaking galaxies, including high [O III]/[O II] ratios, high Lyα equivalent widths (EWs), and double-peaked Lyα profile with small peak velocity separations (e.g., Izotov et al. 2016; Verhamme et al. 2017). Nonetheless, such empirical line properties seem non-exclusive to LyC leakers and may lead to inconsistent results (e.g., Jaskot & Oey 2014; Keenan et al. 2017). A detailed theoretical modeling on $f_{\rm esc}$ and its imprints on Lyα and nebular line diagnostics is demanded for finding the dominant sources and measuring the ionizing photon budget for reionization.

In future work, we will conduct Monte Carlo radiative transfer (MCRT) calculations using the SEDONA code (Kasen et al. 2006, see also Chapter 5) on the state-of-the-art cosmological hydrodynamic zoom-in simulations of $z \geq 5$ galaxies (a subsample of

these simulations has been presented in Ma et al. 2017a, see Chapter 7). By doing LyC, Lyα, and full spectral radiative transport in a self-consistent way in the same code, we expect to predict (1) f_{esc} as a function of halo mass and galaxy properties, (2) Lyα line features for a broad range of galaxies and the connection between Lyα and LyC escape fractions, and (3) a large sample of mock galaxy spectra for finding possible correlations between f_{esc} and emission line properties.

Recent observations find that dust emission in high-redshift galaxies is significantly weaker than what inferred from rest-frame UV extinction using the so-called IRX-β relation (e.g., Capak et al. 2015; Bouwens et al. 2016), but it is unclear whether this is due to a lower dust content (e.g., Dwek et al. 2014) or a higher dust temperature (e.g., Faisst et al. 2017) in these galaxies. By post-processing our simulations using dust radiative transfer code such as SKIRT (e.g., Camps & Baes 2015) with varying dust composition and dust-to-metal ratios and matching the results to observations, we expect to put constraints on these parameters and dust dust temperature in $z \geq 5$ galaxies. Moreover, it is also worth calculating cold gas emission such as [C II] and CO from our simulated galaxies, as these tracers are useful probes of star formation and AGN activities in high-redshift galaxies (e.g., Smit et al. 2018) and will be used in future intensity mapping experiments (CCAT, COMAP). These multi-wavelength mock observations are important for comparing and understanding future data (see Figure 9.1 for an illustration).

9.2   SMBHs at $z \geq 5$ and their role in reionization

As outlined in Chapter 1, the formation and growth of SMBHs and their impact on galaxies is one of the most important processes in galaxy formation and evolution. Currently, there are rapidly growing data probing the SMBH populations at $z \geq 5$: (1) a large number of AGNs and quasars at these redshifts have been discovered in recent years (e.g., Giallongo et al. 2015; Kashikawa et al. 2015; Jiang et al. 2015; Ono et al. 2018), (2) some bright $z \sim 7$ galaxies show prominent high-ionization emission line features, indicating non-thermal sources, possibly AGN activities in these galaxies (Laporte et al. 2017), and (3) recent measurements of the $z \geq 5$ IGM ionization states suggest a non-negligible contribution from rare sources to cosmic reionization (e.g., Becker et al. 2015). One plausible scenario is that AGNs play an important role, or even a dominant role in reionization (e.g., Madau & Haardt 2015; Chardin et al. 2015, 2017).

None of the simulations studied in this thesis yet include SMBHs. Recently, Anglés-
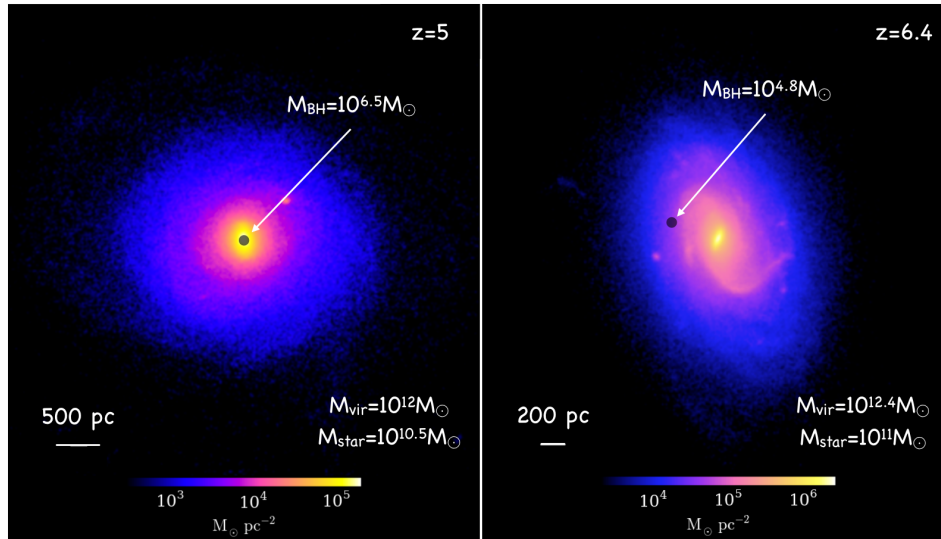
Figure 9.2: SMBH formation and growth in two massive halos at $z \geq 5$ following the BH models in Anglés-Alcázar et al. (2017b). It is not clear in what conditions the seed BHs can sink into the galactic center and accrete efficiently.

Alcázar et al. (2017b) have implemented a SMBH seeding and growth model to the FIRE simulations. In this model, a seed BH of $10^4\,M_\odot$ is placed in the most bound star clusters and then grows following the gravitational torque-driven accretion rates in Hopkins & Quataert (2011). Using four simulations of halos at $M_\odot \sim 10^{12.5}\,M_\odot$ by $z = 2$, they have found that BHs are always undermassive compared to the local M_{BH}–σ_* relation at early time, until the stellar bulge is sufficiently massive at late times so that the BH can be trapped in the galactic center and grow efficiently. This is also seen in simulations of massive halos at $z \geq 5$ (Figure 9.2). It is possible that these models generically produce too few massive BHs at high redshifts.

Nonetheless, these BH seeding and growth models are not necessarily 'correct'. In future work, we intend to explore the following questions. (1) Should we use more massive seeds above $10^5\,M_\odot$ or a larger number of low-mass seeds ($\sim 100\,M_\odot$) to produce SMBHs at $z \geq 5$? (2) What is the most reliable accretion rate estimator in highly turbulent, messy galaxies at high redshifts? The torque-drive accretion rate relies on the disk fraction and may not be applicable to high-redshift galaxies where a stable disk has not yet formed. (3) How many H, He I, and He II ionizing photons can escape from the halo given a plausible BH luminosity? Can AGNs have a non-negligible contribution to H reionization without overheating the IGM?

BIBLIOGRAPHY

Abadi M. G., Navarro J. F., Steinmetz M., Eke V. R., 2003, ApJ, 597, 21

Adibekyan V. Z. et al., 2013, A&A, 554, A44

Agertz O., Kravtsov A. V., 2015, ApJ, 804, 18

Agertz O., Kravtsov A. V., 2016, ApJ, 824, 79

Agertz O., Teyssier R., Moore B., 2011, MNRAS, 410, 1391

Allaert F. et al., 2015, A&A, 582, A18

Allende Prieto C. et al., 2008, Astronomische Nachrichten, 329, 1018

Alvarez M. A., Finlator K., Trenti M., 2012, ApJ, 759, L38

Anders F. et al., 2014, A&A, 564, A115

Andrews B. H., Martini P., 2013, ApJ, 765, 140

Anglés-Alcázar D., Davé R., Özel F., Oppenheimer B. D., 2014, ApJ, 782, 84

Anglés-Alcázar D., Faucher-Giguère C.-A., Kereš D., Hopkins P. F., Quataert E., Murray N., 2017a, MNRAS, 470, 4698

Anglés-Alcázar D., Faucher-Giguère C.-A., Quataert E., Hopkins P. F., Feldmann R., Torrey P., Wetzel A., Kereš D., 2017b, MNRAS, 472, L109

Atek H. et al., 2015, ApJ, 814, 69

Aumer M., Binney J., Schönrich R., 2016, MNRAS, 459, 3326

Barkana R., Loeb A., 2001, Physics Reports, 349, 125

Barrow K. S. S., Wise J. H., Norman M. L., O'Shea B. W., Xu H., 2017, MNRAS, 469, 4863

Becker G. D., Bolton J. S., Madau P., Pettini M., Ryan-Weber E. V., Venemans B. P., 2015, MNRAS, 447, 3402

Behroozi P. S., Silk J., 2015, ApJ, 799, 32

Behroozi P. S., Wechsler R. H., Wu H.-Y., 2013a, ApJ, 762, 109

Behroozi P. S., Wechsler R. H., Conroy C., 2013b, ApJ, 770, 57

Belfiore F. et al., 2017, MNRAS, 469, 151

Bensby T., Feltzing S., Oey M. S., 2014, A&A, 562, A71

Benson A. J., 2010, Physics Reports, 495, 33

Benson A. J., 2012, NewA, 17, 175

Bertone S., De Lucia G., Thomas P. A., 2007, MNRAS, 379, 1143

Bertschinger E., 2001, ApJS, 137, 1

Bird J. C., Kazantzidis S., Weinberg D. H., Guedes J., Callegari S., Mayer L., Madau P., 2013, ApJ, 773, 43

Blaauw A., 1961, BAN, 15, 265

Boeche C. et al., 2013, A&A, 559, A59

Boeche C. et al., 2014, A&A, 568, A71

Bothwell M. S., Maiolino R., Kennicutt R., Cresci G., Mannucci F., Marconi A., Cicone C., 2013, MNRAS, 433, 1425

Bournaud F., Elmegreen B. G., Martig M., 2009, ApJ, 707, L1

Boutsia K. et al., 2011, ApJ, 736, 41

Bouwens R. J., Cayón L., Silk J., 1997, ApJ, 489, L21

Bouwens R. J., Illingworth G. D., Blakeslee J. P., Broadhurst T. J., Franx M., 2004, ApJ, 611, L1

Bouwens R. J. et al., 2011, ApJ, 737, 90

Bouwens R. J. et al., 2014, ApJ, 795, 126

Bouwens R. J. et al., 2015, ApJ, 803, 34

Bouwens R. J. et al., 2016, ApJ, 833, 72

Bouwens R. J., van Dokkum P. G., Illingworth G. D., Oesch P. A., Maseda M., Ribeiro B., Stefanon M., Lam D., 2017a, preprint (arXiv:1711.02090)

Bouwens R. J., Illingworth G. D., Oesch P. A., Atek H., Lam D., Stefanon M., 2017b, ApJ, 843, 41

Bouwens R. J., Oesch P. A., Illingworth G. D., Ellis R. S., Stefanon M., 2017c, ApJ, 843, 129

Bovy J., Rix H.-W., Liu C., Hogg D. W., Beers T. C., Lee Y. S., 2012, ApJ, 753, 148

Bovy J., Rix H.-W., Schlafly E. F., Nidever D. L., Holtzman J. A., Shetrone M., Beers T. C., 2016, ApJ, 823, 30

Bowler R. A. A. et al., 2015, MNRAS, 452, 1817

Bowler R. A. A., Dunlop J. S., McLure R. J., McLeod D. J., 2017, MNRAS, 466, 3612

Boylan-Kolchin M., Bullock J. S., Garrison-Kimmel S., 2014, MNRAS, 443, L44

Boylan-Kolchin M., Weisz D. R., Johnson B. D., Bullock J. S., Conroy C., Fitts A., 2015, MNRAS, 453, 1503

Bridge C. R. et al., 2010, ApJ, 720, 465

Bromm V., Yoshida N., Hernquist L., 2003, ApJ, 596, L135

Brook C. B., Kawata D., Gibson B. K., Freeman K. C., 2004, ApJ, 612, 894

Brook C. B., Stinson G., Gibson B. K., Wadsley J., Quinn T., 2012a, MNRAS, 424, 1275

Brook C. B. et al., 2012b, MNRAS, 426, 690

Brook C. B., Stinson G., Gibson B. K., Shen S., Macciò A. V., Obreja A., Wadsley J., Quinn T., 2014, MNRAS, 443, 3809

Bryan G. L., Norman M. L., 1998, ApJ, 495, 80

Bullock J. S., Kravtsov A. V., Weinberg D. H., 2000, ApJ, 539, 517

Burkert A., Hartmann L., 2013, ApJ, 773, 48

Camps P., Baes M., 2015, Astronomy and Computing, 9, 20

Capak P. L. et al., 2015, Nature, 522, 455

Carlberg R. G., 1987, ApJ, 322, 59

Carrell K., Chen Y., Zhao G., 2012, AJ, 144, 185

Cen R., Kimm T., 2014, ApJ, 782, 32

Ceverino D., Klypin A., Klimek E. S., Trujillo-Gomez S., Churchill C. W., Primack J., Dekel A., 2014, MNRAS, 442, 1545

Ceverino D., Glover S. C. O., Klessen R. S., 2017, MNRAS, 470, 2791

Ceverino D., Klessen R., Glover S., 2018, preprint (arXiv:1801.10382)

Chabrier G., 2003, ApJ, 586, L133

Chan T. K., Kereš D., Oñorbe J., Hopkins P. F., Muratov A. L., Faucher-Giguère C.-A., Quataert E., 2015, MNRAS, 454, 2981

Chardin J., Haehnelt M. G., Aubert D., Puchwein E., 2015, MNRAS, 453, 2943

Chardin J., Puchwein E., Haehnelt M. G., 2017, MNRAS, 465, 3429

Chen P., Wise J. H., Norman M. L., Xu H., O'Shea B. W., 2014, ApJ, 795, 144

Cheng J. Y. et al., 2012, ApJ, 746, 149

Chiappini C., Matteucci F., Gratton R., 1997, ApJ, 477, 765

Choi J., Conroy C., Moustakas J., Graves G. J., Holden B. P., Brodwin M., Brown M. J. I., van Dokkum P. G., 2014, ApJ, 792, 95

Choi J., Conroy C., Byler N., 2017, ApJ, 838, 159

Clay S. J., Thomas P. A., Wilkins S. M., Henriques B. M. B., 2015, MNRAS, 451, 2692

Coe D. et al., 2013, ApJ, 762, 32

Coe D., Bradley L., Zitrin A., 2015, ApJ, 800, 84

Colbrook M. J., Ma X., Hopkins P. F., Squire J., 2017, MNRAS, 467, 2421

Comerón S. et al., 2011, ApJ, 729, 18

Comerón S. et al., 2012, ApJ, 759, 98

Conroy C., Kratter K. M., 2012, ApJ, 755, 123

Cowie L. L., Barger A. J., Trouille L., 2009, ApJ, 692, 1476

Cowley W. I., Baugh C. M., Cole S., Frenk C. S., Lacey C. G., 2018, MNRAS, 474, 2352

Cresci G., Mannucci F., Maiolino R., Marconi A., Gnerucci A., Magrini L., 2010, Nature, 467, 811

Croton D. J. et al., 2006, MNRAS, 365, 11

Cullen F., Cirasuolo M., McLure R. J., Dunlop J. S., Bowler R. A. A., 2014, MNRAS, 440, 2300

Cullen F., McLure R. J., Khochfar S., Dunlop J. S., Dalla Vecchia C., 2017, MNRAS, 470, 3006

Curtis-Lake E. et al., 2016, MNRAS, 457, 440

D'Aloisio A., McQuinn M., Davies F. B., Furlanetto S. R., 2018, MNRAS, 473, 560

Dalcanton J. J., 2007, ApJ, 658, 941

Davé R., Oppenheimer B. D., Finlator K., 2011a, MNRAS, 415, 11

Davé R., Finlator K., Oppenheimer B. D., 2011b, MNRAS, 416, 1354

Davé R., Finlator K., Oppenheimer B. D., 2012, MNRAS, 421, 98

Davé R., Thompson R., Hopkins P. F., 2016, MNRAS, 462, 3265

Davidzon I. et al., 2017, A&A, 605, A70

Davies F. B., Furlanetto S. R., 2016, MNRAS, 460, 1328

Dekel A., Silk J., 1986, ApJ, 303, 39

Dopita M. A., Sutherland R. S., Nicholls D. C., Kewley L. J., Vogt F. P. A., 2013, ApJS, 208, 10

Duncan K. et al., 2014, MNRAS, 444, 2960

Dwek E., 1998, ApJ, 501, 643

Dwek E., Staguhn J., Arendt R. G., Kovacks A., Su T., Benford D. J., 2014, ApJ, 788, L30

Edmunds M. G., 1990, MNRAS, 246, 678

Efstathiou G., 1992, MNRAS, 256, 43P

El-Badry K., Wetzel A., Geha M., Hopkins P. F., Kereš D., Chan T. K., Faucher-Giguère C.-A., 2016, ApJ, 820, 131

El-Badry K. et al., 2018, MNRAS, 473, 1930

Eldridge J. J., Stanway E. R., 2012, MNRAS, 419, 479

Eldridge J. J., Izzard R. G., Tout C. A., 2008, MNRAS, 384, 1109

Eldridge J. J., Stanway E. R., Xiao L., McClelland L. A. S., Taylor G., Ng M., Greis S. M. L., Bray J. C., 2017, PASA, 34, e058

Ellis R. S. et al., 2013, ApJ, 763, L7

Erb D. K., Shapley A. E., Pettini M., Steidel C. C., Reddy N. A., Adelberger K. L., 2006, ApJ, 644, 813

Fabian A. C., 2012, ARA&A, 50, 455

Faisst A. L. et al., 2017, ApJ, 847, 21

Fan X. et al., 2006, AJ, 132, 117

Faucher-Giguère C.-A., 2018, MNRAS, 473, 3717

Faucher-Giguère C.-A., Kereš D., 2011, MNRAS, 412, L118

Faucher-Giguère C.-A., Lidz A., Hernquist L., Zaldarriaga M., 2008, ApJ, 682, L9

Faucher-Giguère C.-A., Lidz A., Zaldarriaga M., Hernquist L., 2009, ApJ, 703, 1416

Faucher-Giguère C.-A., Kereš D., Dijkstra M., Hernquist L., Zaldarriaga M., 2010, ApJ, 725, 633

Faucher-Giguère C.-A., Kereš D., Ma C.-P., 2011, MNRAS, 417, 2982

Faucher-Giguère C.-A., Quataert E., Hopkins P. F., 2013, MNRAS, 433, 1970

Faucher-Giguère C.-A., Hopkins P. F., Kereš D., Muratov A. L., Quataert E., Murray N., 2015, MNRAS, 449, 987

Faucher-Giguère C.-A., Feldmann R., Quataert E., Kereš D., Hopkins P. F., Murray N., 2016, MNRAS, 461, L32

Faure C., Siebert A., Famaey B., 2014, MNRAS, 440, 2564

Federrath C., Sur S., Schleicher D. R. G., Banerjee R., Klessen R. S., 2011, ApJ, 731, 62

Feldmann R., 2013, MNRAS, 433, 1910

Feldmann R., Hopkins P. F., Quataert E., Faucher-Giguère C.-A., Kereš D., 2016, MNRAS, 458, L14

Feldmann R., Quataert E., Hopkins P. F., Faucher-Giguère C.-A., Kereš D., 2017, MNRAS, 470, 1050

Feng Y., Di-Matteo T., Croft R. A., Bird S., Battaglia N., Wilkins S., 2016, MNRAS, 455, 2778

Ferguson H. C. et al., 2004, ApJ, 600, L107

Ferland G. J. et al., 2013, RMxAA, 49, 137

Fiacconi D., Feldmann R., Mayer L., 2015, MNRAS, 446, 1957

Fielding D., Quataert E., McCourt M., Thompson T. A., 2017, MNRAS, 466, 3810

Finkelstein S. L. et al., 2012, ApJ, 758, 93

Finkelstein S. L. et al., 2015a, ApJ, 810, 71

Finkelstein S. L. et al., 2015b, ApJ, 814, 95

Finlator K., Davé R., 2008, MNRAS, 385, 2181

Finlator K. et al., 2017, MNRAS, 464, 1633

Fitts A. et al., 2017, MNRAS, 471, 3547

Ford A. B. et al., 2016, MNRAS, 459, 1745

Förster Schreiber N. M. et al., 2009, ApJ, 706, 1364

Fuhrmann K., 1998, A&A, 338, 161

Fumagalli M., Prochaska J. X., Kasen D., Dekel A., Ceverino D., Primack J. R., 2011, MNRAS, 418, 1796

Fumagalli M., Hennawi J. F., Prochaska J. X., Kasen D., Dekel A., Ceverino D., Primack J., 2014, ApJ, 780, 74

Furlanetto S. R., Zaldarriaga M., Hernquist L., 2004, ApJ, 613, 1

Gallazzi A., Charlot S., Brinchmann J., White S. D. M., Tremonti C. A., 2005, MNRAS, 362, 41

Garrison-Kimmel S., Boylan-Kolchin M., Bullock J. S., Lee K., 2014, MNRAS, 438, 2578

Garrison-Kimmel S. et al., 2017, MNRAS, 471, 1709

Genel S. et al., 2012, ApJ, 745, 11

Giallongo E. et al., 2015, A&A, 578, A83

Gibson B. K., Pilkington K., Brook C. B., Stinson G. S., Bailin J., 2013, A&A, 554, A47

Gill S. P. D., Knebe A., Gibson B. K., 2004, MNRAS, 351, 399

Gilmore G., Reid N., 1983, MNRAS, 202, 1025

Gilmore G. et al., 2012, The Messenger, 147, 25

Gnedin N. Y., 2016, ApJ, 825, L17

Gnedin N. Y., Kravtsov A. V., Chen H.-W., 2008, ApJ, 672, 765

Gómez F. A., Minchev I., O'Shea B. W., Beers T. C., Bullock J. S., Purcell C. W., 2013, MNRAS, 429, 159

González V., Labbé I., Bouwens R. J., Illingworth G., Franx M., Kriek M., 2011, ApJ, 735, L34

Götberg Y., de Mink S. E., Groh J. H., 2017, A&A, 608, A11

Grand R. J. J., Kawata D., 2016, Astronomische Nachrichten, 337, 957

Grand R. J. J., Springel V., Gómez F. A., Marinacci F., Pakmor R., Campbell D. J. R., Jenkins A., 2016, MNRAS, 459, 199

Graus A. S., Bullock J. S., Boylan-Kolchin M., Weisz D. R., 2016, MNRAS, 456, 477

Grazian A. et al., 2015, A&A, 575, A96

Gregersen D. et al., 2015, AJ, 150, 189

Grogin N. A. et al., 2011, ApJS, 197, 35

Grudić M. Y., Hopkins P. F., Faucher-Giguère C.-A., Quataert E., Murray N., Kereš D., 2016, preprint (arXiv:1612.05635)

Guo Q., White S., Angulo R. E., Henriques B., Lemson G., Boylan-Kolchin M., Thomas P., Short C., 2013, MNRAS, 428, 1351

Guo Y. et al., 2015, ApJ, 800, 39

Haardt F., Madau P., 2001, in Neumann D. M., Tran J. T. V., eds, Clusters of Galaxies and the High Redshift Universe Observed in X-rays. preprint (arXiv:astro-ph/0106018)

Haardt F., Madau P., 2012, ApJ, 746, 125

Hafen Z. et al., 2017, MNRAS, 469, 2292

Hahn O., Abel T., 2011, MNRAS, 415, 2101

Hayden M. R. et al., 2014, AJ, 147, 116

Hayward C. C., Hopkins P. F., 2017, MNRAS, 465, 1682

Haywood M., Di Matteo P., Lehnert M. D., Katz D., Gómez A., 2013, A&A, 560, A109

Henriques B. M. B., White S. D. M., Thomas P. A., Angulo R. E., Guo Q., Lemson G., Springel V., 2013, MNRAS, 431, 3373

Henriques B. M. B., White S. D. M., Thomas P. A., Angulo R., Guo Q., Lemson G., Springel V., Overzier R., 2015, MNRAS, 451, 2663

Henry A., Martin C. L., Finlator K., Dressler A., 2013a, ApJ, 769, 148

Henry A. et al., 2013b, ApJ, 776, L27

Hinshaw G. et al., 2013, ApJS, 208, 19

Ho I.-T., Kudritzki R.-P., Kewley L. J., Zahid H. J., Dopita M. A., Bresolin F., Rupke D. S. N., 2015, MNRAS, 448, 2030

Hoogerwerf R., de Bruijne J. H. J., de Zeeuw P. T., 2001, A&A, 365, 49

Hopkins P. F., 2013, MNRAS, 428, 2840

Hopkins P. F., 2015, MNRAS, 450, 53

Hopkins P. F., Quataert E., 2010, MNRAS, 407, 1529

Hopkins P. F., Quataert E., 2011, MNRAS, 415, 1027

Hopkins P. F., Hernquist L., Martini P., Cox T. J., Robertson B., Di Matteo T., Springel V., 2005, ApJ, 625, L71

Hopkins P. F., Richards G. T., Hernquist L., 2007, ApJ, 654, 731

Hopkins P. F., Hernquist L., Cox T. J., Younger J. D., Besla G., 2008, ApJ, 688, 757

Hopkins P. F., Cox T. J., Dutta S. N., Hernquist L., Kormendy J., Lauer T. R., 2009, ApJS, 181, 135

Hopkins P. F. et al., 2010, ApJ, 724, 915

Hopkins P. F., Quataert E., Murray N., 2011, MNRAS, 417, 950

Hopkins P. F., Quataert E., Murray N., 2012a, MNRAS, 421, 3522

Hopkins P. F., Kereš D., Murray N., Quataert E., Hernquist L., 2012b, MNRAS, 427, 968

Hopkins P. F., Cox T. J., Hernquist L., Narayanan D., Hayward C. C., Murray N., 2013a, MNRAS, 430, 1901

Hopkins P. F., Narayanan D., Murray N., 2013b, MNRAS, 432, 2647

Hopkins P. F., Kereš D., Oñorbe J., Faucher-Giguère C.-A., Quataert E., Murray N., Bullock J. S., 2014, MNRAS, 445, 581

Hopkins P. F., Torrey P., Faucher-Giguère C.-A., Quataert E., Murray N., 2016, MNRAS, 458, 816

Hopkins P. F. et al., 2017, preprint (arXiv:1702.06148)

Iliev I. T., Mellema G., Pen U.-L., Merz H., Shapiro P. R., Alvarez M. A., 2006, MNRAS, 369, 1625

Illingworth G. D. et al., 2013, ApJS, 209, 6

Iwamoto K., Brachwitz F., Nomoto K., Kishimoto N., Umeda H., Hix W. R., Thielemann F.-K., 1999, ApJS, 125, 439

Iwata I. et al., 2009, ApJ, 692, 1287

Izotov Y. I., Schaerer D., Thuan T. X., Worseck G., Guseva N. G., Orlitová I., Verhamme A., 2016, MNRAS, 461, 3683

Izzard R. G., Tout C. A., Karakas A. I., Pols O. R., 2004, MNRAS, 350, 407

Jaacks J., Choi J.-H., Nagamine K., Thompson R., Varghese S., 2012, MNRAS, 420, 1606

Jaskot A. E., Oey M. S., 2014, ApJ, 791, L19

Jefferies J. T., 1968, Spectral line formation

Jiang L. et al., 2013, ApJ, 773, 153

Jiang L., McGreer I. D., Fan X., Bian F., Cai Z., Clément B., Wang R., Fan Z., 2015, AJ, 149, 188

Jones T., Ellis R., Jullo E., Richard J., 2010, ApJ, 725, L176

Jones T., Ellis R. S., Richard J., Jullo E., 2013, ApJ, 765, 48

Jones T. et al., 2015, AJ, 149, 107

Kalberla P. M. W., Kerp J., Dedes L., Haud U., 2014, ApJ, 794, 90

Kasen D., Thomas R. C., Nugent P., 2006, ApJ, 651, 366

Kashikawa N. et al., 2015, ApJ, 798, 28

Katz N., White S. D. M., 1993, ApJ, 412, 455

Katz N., Weinberg D. H., Hernquist L., 1996, ApJS, 105, 19

Kawamata R., Ishigaki M., Shimasaku K., Oguri M., Ouchi M., 2015, ApJ, 804, 103

Kazantzidis S., Bullock J. S., Zentner A. R., Kravtsov A. V., Moustakas L. A., 2008, ApJ, 688, 254

Keenan R. P., Oey M. S., Jaskot A. E., James B. L., 2017, ApJ, 848, 12

Kennicutt Jr. R. C., 1998, ARA&A, 36, 189

Kereš D., Hernquist L., 2009, ApJ, 700, L1

Kereš D., Katz N., Weinberg D. H., Davé R., 2005, MNRAS, 363, 2

Kewley L. J., Ellison S. L., 2008, ApJ, 681, 1183

Kewley L. J., Geller M. J., Barton E. J., 2006, AJ, 131, 2004

Kewley L. J., Rupke D., Zahid H. J., Geller M. J., Barton E. J., 2010, ApJ, 721, L48

Kewley L. J., Zahid H. J., Geller M. J., Dopita M. A., Hwang H. S., Fabricant D., 2015, ApJ, 812, L20

Kim J.-h., Krumholz M. R., Wise J. H., Turk M. J., Goldbaum N. J., Abel T., 2013, ApJ, 775, 109

Kim J.-h. et al., 2014, ApJS, 210, 14

Kim J.-h. et al., 2018, MNRAS, 474, 4232

Kimm T., Cen R., 2014, ApJ, 788, 121

Kirby E. N., Martin C. L., Finlator K., 2011, ApJ, 742, L25

Kirby E. N., Cohen J. G., Guhathakurta P., Cheng L., Bullock J. S., Gallazzi A., 2013, ApJ, 779, 102

Kistler M. D., Yüksel H., Beacom J. F., Hopkins A. M., Wyithe J. S. B., 2009, ApJ, 705, L104

Knebe A. et al., 2018, MNRAS, 475, 2936

Knollmann S. R., Knebe A., 2009, ApJS, 182, 608

Kordopatis G. et al., 2015, A&A, 582, A122

Kroupa P., 2002, Science, 295, 82

Kuhlen M., Faucher-Giguère C.-A., 2012, MNRAS, 423, 862

Laporte N., Nakajima K., Ellis R. S., Zitrin A., Stark D. P., Mainali R., Roberts-Borsani G. W., 2017, ApJ, 851, 40

Lee H., Skillman E. D., Cannon J. M., Jackson D. C., Gehrz R. D., Polomski E. F., Woodward C. E., 2006, ApJ, 647, 970

Leethochawalit N., Jones T. A., Ellis R. S., Stark D. P., Richard J., Zitrin A., Auger M., 2016, ApJ, 820, 84

Leethochawalit N., Kirby E. N., Moran S. M., Ellis R. S., Treu T., 2018, ApJ, 856, 15

Leitet E., Bergvall N., Piskunov N., Andersson B.-G., 2011, A&A, 532, A107

Leitet E., Bergvall N., Hayes M., Linné S., Zackrisson E., 2013, A&A, 553, A106

Leitherer C. et al., 1999, ApJS, 123, 3

Leitherer C., Ekström S., Meynet G., Schaerer D., Agienko K. B., Levesque E. M., 2014, ApJS, 212, 14

Lilly S. J., Carollo C. M., Pipino A., Renzini A., Peng Y., 2013, ApJ, 772, 119

Liu C., Mutch S. J., Angel P. W., Duffy A. R., Geil P. M., Poole G. B., Mesinger A., Wyithe J. S. B., 2016, MNRAS, 462, 235

Livermore R. C., Finkelstein S. L., Lotz J. M., 2017, ApJ, 835, 113

Loebman S. R., Roškar R., Debattista V. P., Ivezić Ž., Quinn T. R., Wadsley J., 2011, ApJ, 737, 8

Longair M. S., 2008, Galaxy Formation

López-Corredoira M., Molgó J., 2014, A&A, 567, A106

Lotz J. M., Primack J., Madau P., 2004, AJ, 128, 163

Lotz J. M. et al., 2017, ApJ, 837, 97

Lu Y., Kereš D., Katz N., Mo H. J., Fardal M., Weinberg M. D., 2011, MNRAS, 416, 660

Lu Z., Mo H. J., Lu Y., Katz N., Weinberg M. D., van den Bosch F. C., Yang X., 2014a, MNRAS, 439, 1294

Lu Y. et al., 2014b, ApJ, 795, 123

Lu Y., Mo H. J., Lu Z., 2015a, preprint (arXiv:1504.02109)

Lu Y., Blanc G. A., Benson A., 2015b, ApJ, 808, 129

Lynden-Bell D., Kalnajs A. J., 1972, MNRAS, 157, 1

Ma X., Kasen D., Hopkins P. F., Faucher-Giguère C.-A., Quataert E., Kereš D., Murray N., 2015, MNRAS, 453, 960

Ma X., Hopkins P. F., Faucher-Giguère C.-A., Zolman N., Muratov A. L., Kereš D., Quataert E., 2016a, MNRAS, 456, 2140

Ma X., Hopkins P. F., Kasen D., Quataert E., Faucher-Giguère C.-A., Kereš D., Murray N., Strom A., 2016b, MNRAS, 459, 3614

Ma X. et al., 2017a, preprint (arXiv:1706.06605)

Ma X., Hopkins P. F., Feldmann R., Torrey P., Faucher-Giguère C.-A., Kereš D., 2017b, MNRAS, 466, 4780

Ma X., Hopkins P. F., Wetzel A. R., Kirby E. N., Anglés-Alcázar D., Faucher-Giguère C.-A., Kereš D., Quataert E., 2017c, MNRAS, 467, 2430

Ma X. et al., 2018, MNRAS,

Maciel W. J., Costa R. D. D., Uchida M. M. M., 2003, A&A, 397, 667

Madau P., Dickinson M., 2014, ARA&A, 52, 415

Madau P., Haardt F., 2015, ApJ, 813, L8

Madau P., Haardt F., Rees M. J., 1999, ApJ, 514, 648

Mainali R., Kollmeier J. A., Stark D. P., Simcoe R. A., Walth G., Newman A. B., Miller D. R., 2017, ApJ, 836, L14

Maiolino R. et al., 2008, A&A, 488, 463

Mandelker N., Dekel A., Ceverino D., DeGraf C., Guo Y., Primack J., 2017, MNRAS, 464, 635

Mannucci F., Della Valle M., Panagia N., 2006, MNRAS, 370, 773

Mannucci F. et al., 2009, MNRAS, 398, 1915

Mannucci F., Cresci G., Maiolino R., Marconi A., Gnerucci A., 2010, MNRAS, 408, 2115

Mannucci F., Salvaterra R., Campisi M. A., 2011, MNRAS, 414, 1263

Maoz D., Sharon K., Gal-Yam A., 2010, ApJ, 722, 1879

Martig M., Minchev I., Flynn C., 2014a, MNRAS, 442, 2474

Martig M., Minchev I., Flynn C., 2014b, MNRAS, 443, 2452

Martig M., Minchev I., Ness M., Fouesneau M., Rix H.-W., 2016, ApJ, 831, 139

Martizzi D., Faucher-Giguère C.-A., Quataert E., 2015, MNRAS, 450, 504

Matteucci F., Brocato E., 1990, ApJ, 365, 539

McConnell N. J., Ma C.-P., 2013, ApJ, 764, 184

McLeod D. J., McLure R. J., Dunlop J. S., 2016, MNRAS, 459, 3812

McLure R. J. et al., 2011, MNRAS, 418, 2074

McLure R. J. et al., 2013, MNRAS, 432, 2696

McQuinn M., Lidz A., Zahn O., Dutta S., Hernquist L., Zaldarriaga M., 2007, MNRAS, 377, 1043

Mikolaitis Š. et al., 2014, A&A, 572, A33

Minchev I., Famaey B., 2010, ApJ, 722, 112

Minchev I., Quillen A. C., 2006, MNRAS, 368, 623

Minchev I., Famaey B., Combes F., Di Matteo P., Mouhcine M., Wozniak H., 2011, A&A, 527, A147

Minchev I., Famaey B., Quillen A. C., Dehnen W., Martig M., Siebert A., 2012, A&A, 548, A127

Minchev I., Chiappini C., Martig M., 2013, A&A, 558, A9

Minchev I., Chiappini C., Martig M., 2014, A&A, 572, A92

Minchev I., Martig M., Streich D., Scannapieco C., de Jong R. S., Steinmetz M., 2015, ApJ, 804, L9

Minchev I., Steinmetz M., Chiappini C., Martig M., Anders F., Matijevic G., de Jong R. S., 2017, ApJ, 834, 27

Miranda M. S. et al., 2016, A&A, 587, A10

Mo H. J., Mao S., White S. D. M., 1998, MNRAS, 295, 319

Mo H. J., Mao S., White S. D. M., 1999, MNRAS, 304, 175

Mo H., van den Bosch F. C., White S., 2010, Galaxy Formation and Evolution

Momany Y., Zaggia S., Gilmore G., Piotto G., Carraro G., Bedin L. R., de Angeli F., 2006, A&A, 451, 515

Moody C. E., Guo Y., Mandelker N., Ceverino D., Mozena M., Koo D. C., Dekel A., Primack J., 2014, MNRAS, 444, 1389

Moster B. P., Naab T., White S. D. M., 2013, MNRAS, 428, 3121

Muratov A. L., Kereš D., Faucher-Giguère C.-A., Hopkins P. F., Quataert E., Murray N., 2015, MNRAS, 454, 2691

Muratov A. L. et al., 2017, MNRAS, 468, 4170

Murray N., Quataert E., Thompson T. A., 2010, ApJ, 709, 191

Murray S. G., Power C., Robotham A. S. G., 2013, Astronomy and Computing, 3, 23

Naab T., Ostriker J. P., 2017, ARA&A, 55, 59

Nestor D. B., Shapley A. E., Kornei K. A., Steidel C. C., Siana B., 2013, ApJ, 765, 47

Nicholls D. C., Dopita M. A., Sutherland R. S., Kewley L. J., Palay E., 2013, ApJS, 207, 21

Nidever D. L. et al., 2014, ApJ, 796, 38

Noh Y., McQuinn M., 2014, MNRAS, 444, 503

Nomoto K., Tominaga N., Umeda H., Kobayashi C., Maeda K., 2006, Nuclear Physics A, 777, 424

Nordström B. et al., 2004, A&A, 418, 989

Oñorbe J., Garrison-Kimmel S., Maller A. H., Bullock J. S., Rocha M., Hahn O., 2014, MNRAS, 437, 1894

Oñorbe J., Boylan-Kolchin M., Bullock J. S., Hopkins P. F., Kereš D., Faucher-Giguère C.-A., Quataert E., Murray N., 2015, MNRAS, 454, 2092

O'Brien J. C., Freeman K. C., van der Kruit P. C., 2010, A&A, 515, A62

O'Shea B. W., Wise J. H., Xu H., Norman M. L., 2015, ApJ, 807, L12

Obreja A., Brook C. B., Stinson G., Domínguez-Tenreiro R., Gibson B. K., Silva L., Granato G. L., 2014, MNRAS, 442, 1794

Ocvirk P. et al., 2016, MNRAS, 463, 1462

Oesch P. A. et al., 2010, ApJ, 709, L21

Oesch P. A. et al., 2013, ApJ, 773, 75

Oesch P. A. et al., 2014, ApJ, 786, 108

Okamoto T., Gao L., Theuns T., 2008, MNRAS, 390, 920

Oke J. B., Gunn J. E., 1983, ApJ, 266, 713

Oklopčić A., Hopkins P. F., Feldmann R., Kereš D., Faucher-Giguère C.-A., Murray N., 2017, MNRAS, 465, 952

Olling R. P., 1995, AJ, 110, 591

Ono Y. et al., 2013, ApJ, 777, 155

Ono Y. et al., 2018, PASJ, 70, S10

Oppenheimer B. D., Davé R., 2009, MNRAS, 395, 1875

Oppenheimer B. D., Schaye J., 2013, MNRAS, 434, 1043

Oppenheimer B. D., Davé R., Kereš D., Fardal M., Katz N., Kollmeier J. A., Weinberg D. H., 2010, MNRAS, 406, 2325

Orr M. et al., 2017, preprint (arXiv:1701.01788)

Ostriker E. C., Shetty R., 2011, ApJ, 731, 41

Ouchi M. et al., 2009, ApJ, 706, 1136

Paardekooper J.-P., Pelupessy F. I., Altay G., Kruip C. J. H., 2011, A&A, 530, A87

Paardekooper J.-P., Khochfar S., Dalla Vecchia C., 2013, MNRAS, 429, L94

Paardekooper J.-P., Khochfar S., Dalla Vecchia C., 2015, MNRAS, 451, 2544

Padoan P., Nordlund Å., 2011, ApJ, 730, 40

Pawlik A. H., Rahmati A., Schaye J., Jeon M., Dalla Vecchia C., 2017, MNRAS, 466, 960

Peeples M. S., Pogge R. W., Stanek K. Z., 2009, ApJ, 695, 259

Peeples M. S., Werk J. K., Tumlinson J., Oppenheimer B. D., Prochaska J. X., Katz N., Weinberg D. H., 2014, ApJ, 786, 54

Pei Y. C., 1992, ApJ, 395, 130

Pettini M., Pagel B. E. J., 2004, MNRAS, 348, L59

Pilkington K. et al., 2012, A&A, 540, A56

Pillepich A. et al., 2018, MNRAS, 473, 4077

Planck Collaboration et al., 2014, A&A, 571, A16

Planck Collaboration et al., 2016, A&A, 594, A13

Press W. H., Schechter P., 1974, ApJ, 187, 425

Price D. J., Monaghan J. J., 2007, MNRAS, 374, 1347

Price S. H., Kriek M., Feldmann R., Quataert E., Hopkins P. F., Faucher-Giguère C.-A., Kereš D., Barro G., 2017, ApJ, 844, L6

Purcell C. W., Kazantzidis S., Bullock J. S., 2009, ApJ, 694, L98

Purcell C. W., Bullock J. S., Tollerud E. J., Rocha M., Chakrabarti S., 2011, Nature, 477, 301

Qu Y., Di Matteo P., Lehnert M. D., van Driel W., 2011, A&A, 530, A10

Queyrel J. et al., 2012, A&A, 539, A93

Quinn P. J., Hernquist L., Fullagar D. P., 1993, ApJ, 403, 74

Quinn T., Katz N., Efstathiou G., 1996, MNRAS, 278, L49

Razoumov A. O., Sommer-Larsen J., 2010, ApJ, 710, 1239

Recio-Blanco A. et al., 2014, A&A, 567, A5

Reda F. M., Proctor R. N., Forbes D. A., Hau G. K. T., Larsen S. S., 2007, MNRAS, 377, 1772

Reed D., Gardner J., Quinn T., Stadel J., Fardal M., Lake G., Governato F., 2003, MNRAS, 346, 565

Ribeiro B. et al., 2016, A&A, 593, A22

Rix H.-W., Bovy J., 2013, A&ARv, 21, 61

Robertson B. E. et al., 2013, ApJ, 768, 71

Robertson B. E., Ellis R. S., Furlanetto S. R., Dunlop J. S., 2015, ApJ, 802, L19

Rodríguez-Puebla A., Primack J. R., Avila-Reese V., Faber S. M., 2017, MNRAS, 470, 651

Roškar R., Teyssier R., Agertz O., Wetzstein M., Moore B., 2014, MNRAS, 444, 2837

Rupke D. S. N., Kewley L. J., Barnes J. E., 2010a, ApJ, 710, L156

Rupke D. S. N., Kewley L. J., Chien L.-H., 2010b, ApJ, 723, 1255

Saha K., Tseng Y.-H., Taam R. E., 2010, ApJ, 721, 1878

Salpeter E. E., 1955, ApJ, 121, 161

Sánchez-Blázquez P., Forbes D. A., Strader J., Brodie J., Proctor R., 2007, MNRAS, 377, 759

Sánchez-Blázquez P. et al., 2014, A&A, 570, A6

Sánchez S. F. et al., 2012, A&A, 546, A2

Sánchez S. F. et al., 2014, A&A, 563, A49

Sanders R. L. et al., 2015, ApJ, 799, 138

Savaglio S. et al., 2005, ApJ, 635, 260

Sawala T. et al., 2016, MNRAS, 456, 85

Scannapieco C. et al., 2012, MNRAS, 423, 1726

Schaye J. et al., 2015, MNRAS, 446, 521

Schechter P., 1976, ApJ, 203, 297

Schenker M. A. et al., 2013, ApJ, 768, 196

Schmidt M., 1963, ApJ, 137, 758

Schönrich R., Binney J., 2009a, MNRAS, 396, 203

Schönrich R., Binney J., 2009b, MNRAS, 399, 1145

Searle L., 1971, ApJ, 168, 327

Searle L., Sargent W. L. W., 1972, ApJ, 173, 25

Sellwood J. A., Binney J. J., 2002, MNRAS, 336, 785

Sellwood J. A., Carlberg R. G., 1984, ApJ, 282, 61

Shapley A. E., Steidel C. C., Pettini M., Adelberger K. L., Erb D. K., 2006, ApJ, 651, 688

Shapley A. E. et al., 2017, ApJ, 846, L30

Shen S., Wadsley J., Stinson G., 2010, MNRAS, 407, 1581

Shibuya T., Ouchi M., Harikane Y., 2015, ApJS, 219, 15

Siana B. et al., 2010, ApJ, 723, 241

Siana B. et al., 2015, ApJ, 804, 17

Silk J., Mamon G. A., 2012, Research in Astronomy and Astrophysics, 12, 917

Smit R. et al., 2018, Nature, 553, 178

Smith D. J. B., Hayward C. C., 2015, MNRAS, 453, 1597

Somerville R. S., 2002, ApJ, 572, L23

Somerville R. S., Davé R., 2015, ARA&A, 53, 51

Somerville R. S., Hopkins P. F., Cox T. J., Robertson B. E., Hernquist L., 2008, MNRAS, 391, 481

Somerville R. S., Gilmore R. C., Primack J. R., Domínguez A., 2012, MNRAS, 423, 1992

Somerville R. S. et al., 2018, MNRAS, 473, 2714

Song M. et al., 2016, ApJ, 825, 5

Sparre M. et al., 2015, MNRAS, 447, 3548

Sparre M., Hayward C. C., Feldmann R., Faucher-Giguère C.-A., Muratov A. L., Kereš D., Hopkins P. F., 2017, MNRAS, 466, 88

Spitzer Jr. L., Schwarzschild M., 1951, ApJ, 114, 385

Spitzer Jr. L., Schwarzschild M., 1953, ApJ, 118, 106

Springel V., 2005, MNRAS, 364, 1105

Springel V., Hernquist L., 2003, MNRAS, 339, 289

Springel V. et al., 2005a, Nature, 435, 629

Springel V., Di Matteo T., Hernquist L., 2005b, ApJ, 620, L79

Stanway E. R., 2017, preprint (arXiv:1702.07303)

Stanway E. R., Eldridge J. J., Becker G. D., 2016, MNRAS, 456, 485

Stark D. P., 2016, ARA&A, 54, 761

Stefanon M., Bouwens R. J., Labbé I., Muzzin A., Marchesini D., Oesch P., Gonzalez V., 2017, ApJ, 843, 36

Steidel C. C., Pettini M., Adelberger K. L., 2001, ApJ, 546, 665

Steidel C. C. et al., 2014, ApJ, 795, 165

Steidel C. C., Strom A. L., Pettini M., Rudie G. C., Reddy N. A., Trainor R. F., 2016, ApJ, 826, 159

Steinmetz M. et al., 2006, AJ, 132, 1645

Stinson G. S., Brook C., Macciò A. V., Wadsley J., Quinn T. R., Couchman H. M. P., 2013a, MNRAS, 428, 129

Stinson G. S. et al., 2013b, MNRAS, 436, 625

Stone R. C., 1991, AJ, 102, 333

Stott J. P. et al., 2014, MNRAS, 443, 2695

Strom A. L., Steidel C. C., Rudie G. C., Trainor R. F., Pettini M., Reddy N. A., 2017, ApJ, 836, 164

Su K.-Y. et al., 2017a, preprint (arXiv:1712.02795)

Su K.-Y., Hopkins P. F., Hayward C. C., Faucher-Giguère C.-A., Kereš D., Ma X., Robles V. H., 2017b, MNRAS, 471, 144

Swinbank A. M., Sobral D., Smail I., Geach J. E., Best P. N., McCarthy I. G., Crain R. A., Theuns T., 2012, MNRAS, 426, 935

Talbot Jr. R. J., Arnett W. D., 1971, ApJ, 170, 409

Tetzlaff N., Neuhäuser R., Hohle M. M., 2011, MNRAS, 410, 190

Thompson T. A., Quataert E., Murray N., 2005, ApJ, 630, 167

Thoul A. A., Weinberg D. H., 1996, ApJ, 465, 608

Tinker J., Kravtsov A. V., Klypin A., Abazajian K., Warren M., Yepes G., Gottlöber S., Holz D. E., 2008, ApJ, 688, 709

Topping M. W., Shull J. M., 2015, ApJ, 800, 97

Torrey P., Cox T. J., Kewley L., Hernquist L., 2012, ApJ, 746, 108

Torrey P., Vogelsberger M., Genel S., Sijacki D., Springel V., Hernquist L., 2014, MNRAS, 438, 1985

Torrey P., Hopkins P. F., Faucher-Giguère C.-A., Vogelsberger M., Quataert E., Kereš D., Murray N., 2017, MNRAS, 467, 2301

Tremonti C. A. et al., 2004, ApJ, 613, 898

Tumlinson J. et al., 2011, Science, 334, 948

Vanzella E., Siana B., Cristiani S., Nonino M., 2010, MNRAS, 404, 1672

Vanzella E. et al., 2012, ApJ, 751, 70

Vanzella E. et al., 2017, MNRAS, 467, 4304

Vázquez-Semadeni E., Banerjee R., Gómez G. C., Hennebelle P., Duffin D., Klessen R. S., 2011, MNRAS, 414, 2511

Veilleux S., Cecil G., Bland-Hawthorn J., 2005, ARA&A, 43, 769

Vera-Ciro C., D'Onghia E., Navarro J., Abadi M., 2014, ApJ, 794, 173

Verhamme A., Orlitová I., Schaerer D., Izotov Y., Worseck G., Thuan T. X., Guseva N., 2017, A&A, 597, A13

Verner D. A., Ferland G. J., 1996, ApJS, 103, 467

Verner D. A., Ferland G. J., Korista K. T., Yakovlev D. G., 1996, ApJ, 465, 487

Vila-Costas M. B., Edmunds M. G., 1992, MNRAS, 259, 121

Villalobos Á., Helmi A., 2008, MNRAS, 391, 1806

Vogelsberger M., Genel S., Sijacki D., Torrey P., Springel V., Hernquist L., 2013, MNRAS, 436, 3031

Vogelsberger M. et al., 2014, MNRAS, 444, 1518

Wang L., Dutton A. A., Stinson G. S., Macciò A. V., Penzo C., Kang X., Keller B. W., Wadsley J., 2015, MNRAS, 454, 83

Wang X. et al., 2017, ApJ, 837, 89

Wetzel A. R., Hopkins P. F., Kim J.-h., Faucher-Giguère C.-A., Kereš D., Quataert E., 2016, ApJ, 827, L23

Wheeler C. et al., 2017, MNRAS, 465, 2420

Wiersma R. P. C., Schaye J., Smith B. D., 2009a, MNRAS, 393, 99

Wiersma R. P. C., Schaye J., Theuns T., Dalla Vecchia C., Tornatore L., 2009b, MNRAS, 399, 574

Wilkins S. M., Feng Y., Di-Matteo T., Croft R., Stanway E. R., Bunker A., Waters D., Lovell C., 2016, MNRAS, 460, 3170

Wilkins S. M., Feng Y., Di Matteo T., Croft R., Lovell C. C., Waters D., 2017, MNRAS, 469, 2517

Wise J. H., Cen R., 2009, ApJ, 693, 984

Wise J. H., Turk M. J., Norman M. L., Abel T., 2012, ApJ, 745, 50

Wise J. H., Demchenko V. G., Halicek M. T., Norman M. L., Turk M. J., Abel T., Smith B. D., 2014, MNRAS, 442, 2560

Woosley S. E., Weaver T. A., 1995, ApJS, 101, 181

Wuyts S. et al., 2012, ApJ, 753, 114

Wuyts E. et al., 2016, ApJ, 827, 74

Wyithe J. S. B., Hopkins A. M., Kistler M. D., Yüksel H., Beacom J. F., 2010, MNRAS, 401, 2561

Xiao L., Eldridge J. J., 2015, MNRAS, 452, 2597

Xu H., Wise J. H., Norman M. L., Ahn K., O'Shea B. W., 2016, ApJ, 833, 84

Yabe K. et al., 2014, MNRAS, 437, 3647

Yajima H., Choi J.-H., Nagamine K., 2011, MNRAS, 412, 411

Yajima H., Shlosman I., Romano-Díaz E., Nagamine K., 2015, MNRAS, 451, 418

Yajima H., Nagamine K., Zhu Q., Khochfar S., Dalla Vecchia C., 2017, ApJ, 846, 30

Yanny B. et al., 2009, AJ, 137, 4377

Yates R. M., Henriques B., Thomas P. A., Kauffmann G., Johansson J., White S. D. M., 2013, MNRAS, 435, 3500

Yoachim P., Dalcanton J. J., 2006, AJ, 131, 226

Yuan T.-T., Kewley L. J., Swinbank A. M., Richard J., Livermore R. C., 2011, ApJ, 732, L14

Yurin D., Springel V., 2015, MNRAS, 452, 2367

Zackrisson E. et al., 2017, ApJ, 836, 78

Zahid H. J., Kewley L. J., Bresolin F., 2011, ApJ, 730, 137

Zahid H. J., Bresolin F., Kewley L. J., Coil A. L., Davé R., 2012, ApJ, 750, 120

Zahid H. J., Geller M. J., Kewley L. J., Hwang H. S., Fabricant D. G., Kurtz M. J., 2013, ApJ, 771, L19

Zahid H. J., Dima G. I., Kudritzki R.-P., Kewley L. J., Geller M. J., Hwang H. S., Silverman J. D., Kashino D., 2014, ApJ, 791, 130

Zaritsky D., Kennicutt Jr. R. C., Huchra J. P., 1994, ApJ, 420, 87

Zheng W. et al., 2012, Nature, 489, 406

de Mink S. E., Sana H., Langer N., Izzard R. G., Schneider F. R. N., 2014, ApJ, 782, 7

van Zee L., Salzer J. J., Haynes M. P., O'Donoghue A. A., Balonek T. J., 1998, AJ, 116, 2805

van de Voort F., Quataert E., Hopkins P. F., Kereš D., Faucher-Giguère C.-A., 2015, MNRAS, 447, 140